

# Time-lapse high-resolution microscopy to study the morphogenesis of microorganisms

Présentée le 25 septembre 2020

à la Faculté des sciences et techniques de l'ingénieur  
Laboratoire de bio- et nano-instrumentation  
Programme doctoral en biotechnologie et génie biologique

pour l'obtention du grade de Docteur ès Sciences

par

**Mélanie Thérèse Marie HANNEBELLE**

Acceptée sur proposition du jury

Prof. A. Oates, président du jury  
Prof. G. Fantner, Prof. J. McKinney, directeurs de thèse  
Prof. P. Tomancak, rapporteur  
Prof. F. Lafont, rapporteur  
Prof. M. Blokesch, rapporteuse



# Acknowledgements

First, I would like to thank my parents and my sisters, brother, and my whole family for their unconditional support, no matter what I choose to do or where I choose to go.

Many thanks to Profs. Georg Fantner and John McKinney for welcoming me in their respective laboratory, LBNI and UPKIN, and supervising this work. I knew I could always go knock on your door to get some help and advice, or to discuss crazy ideas. Being at LBNI or at UPKIN, nothing is too impossible to be done, which makes sense when you are mentored by open minded and creative PIs who built labs with a fantastic level of expertise.

I would also like to thank Profs. Andrew Oates, Melanie Blokesch, Frank Lafont and Pavel Tomancak for accepting to devote some of their time to be part of my thesis committee.

During this PHD, I had the chance to be surrounded by amazing colleagues. Thanks to Oliver Peric, who welcomed me in the lab and introduced me to my first bacteria and AFMs. Thanks to Pascal Odermatt, Joelle Ven and Alex Eskandarian, with whom I shared the adventure of working with AFM on mycobacteria. Thanks to Adrian Nievergelt, for always being available to give a hand and share his expertise. Thanks to Vivek Thacker for the exciting biophysics discussions in the coffee room. Many thanks to Esther Rath and Samuel Leitao for their help with the openSIM project. I would like to thank sincerely each of my colleagues from both side of the bio-engineering *röstigraben*: Jonathan Adams, Blake Erickson, Maja Dukic Pjanic, Nahid Hosseini, Chen Yang, Samuel Leitao, Santiago Andany, Matthias Neuenschwander, Mustafa Kangul, Charlene Brillard, Bahareh Gandhiani, Yusuke Sakiyama, Navid Asmir, Esther Rath, Neeraj Dhar, Francois Signorino-Gelo, Katrin Schneider, Chiara Toniolo, Gaelle Thurre-Vuaridel, Kunal Sharma, Thomas Simonet, Sofia Von Schultz, Julius Winter, Frederic Normandeau, Ophelie Rutschmann: life would not have been the same without all the coffees, barbecues and ski days with you! Thanks to our admins Tamina Sissoko, Ingrid Margot, Anouk Hein and Suzanne Balharry: your warm support, regarding admin matters or not, is such an important contribution to our work and our well-being in the lab. I would also like to thank the students I got the chance to work with during an internship, bachelor or master

thesis: Camille Roche, Nicolas Bichon, Clara Bonnet, Clement Chenevas-Paule and Florian Lemarignier.

Thanks to Prof. Theo Lasser for sharing his knowledge of optical design in his office full of microscopes. Many thanks to Prof. Philippe Renaud for his precious advice during this thesis. It is also important to mention Chantal Mellier, Kristin Becker van Slooten and my mentor for the incredible FLP program. Thanks as well to our deans, presidents and administrators of institutes, committees and doctoral programs, and all those who chose to give some of their time for the rest of us to work in the best possible conditions.

Thanks to all the people who make sure that the EPFL campus is a nice place to work: thanks for keeping the campus clean and safe, with food to eat at lunch, buildings to work in and a salary at the end of the month. Special thanks to Frank, Manu and Ben at the *centre nautique* for sharing their positive energy and passion for sailing.

Zouka, Nicolae, Traian, Vetuta: thanks for the good time we shared together every week. I cannot begin to realize all the life lessons that you have taught me. Many thanks to the Lausanne Santegidio team, which makes everything possible: Anne-Catherine, Camille, Lorenz, Nore, Megane, Sylvain, Daniel, Pierre-Luc, Axelle and the numerous people who contributed.

Many thanks to Daniel, with whom I have shared all of the adventure a PHD is, inside and outside EPFL. I knew I could always find you to share a coffee and discuss crazy theories, go windsurfing, start snowboarding... or organize a concert. Many, many thanks. Thanks as well to Samuel and Audrey for their support in hard and in good times. Life outside the lab would have been a lot less fun without my fantastic friends, flatmates and neighbors. Florian, Laurent, Santiago, Marina, Lorenz, Francesco, Louisa, Bru: thanks for the evenings on the balcony, the cambio games, all the hikes, climbs and ski tours to our secret mountain paradise.

To all of you, I would like to say one more wholehearted *Thanks, Danke, or Merzi*; I wish you all the best for the future!



# Résumé

*Mycobacterium tuberculosis*, l'agent étiologique de la tuberculose, est un pathogène bactérien qui infecte environ un quart de la population humaine mondiale. La tuberculose est la première cause de décès parmi les maladies infectieuses et elle est la plus répandue dans les populations à faible revenu. Beaucoup de choses restent inconnues sur la façon dont ces bactéries se développent, se divisent et parviennent à persister dans l'hôte même pendant des traitements antibiotiques de plusieurs mois.

Les bactéries sont généralement à la limite de la résolution spatiale que les techniques conventionnelles de microscopie optique peuvent offrir. De nouveaux outils sont donc nécessaires pour étudier les sous-structures bactériennes avec une résolution nanométrique. Nous avons développé une plateforme automatisée de microscopie optique et de microscopie à force atomique (AFM) afin d'étudier la morphogenèse des mycobactéries.

Quelle est la dynamique de croissance des mycobactéries? Des modèles opposés coexistent dans la littérature pour la dynamique de croissance polaire des mycobactéries: le modèle unipolaire et le modèle bipolaire. Nous montrons que la dynamique de croissance des mycobactéries suit un nouveau modèle, *NETO*. Il existe une similitude surprenante entre la dynamique de croissance *NETO* des mycobactéries et de la levure à fission, ce qui interroge sur l'existence de mécanismes communs pour la croissance polaire dans des organismes éloignés sur l'arbre phylogénétique.

Comment les organismes à croissance polaire conservent-ils leur forme grâce à l'insertion de nouveau matériau cellulaire au pôle ? Pour explorer davantage la morphogenèse de la croissance polaire, nous avons développé une méthode d'imagerie avec AFM du pôle d'un bacille. Nous avons observé la formation d'un maillage fibreux rigide sur le pôle des cellules de levure à fission, et montré que ce maillage est étiré à mesure que la cellule se développe et insère du nouveau matériau de paroi cellulaire au pôle.

Comment les mycobactéries se divisent-elles? Un autre aspect essentiel de la morphogenèse des bacilles est la division d'une cellule mère en deux cellules sœurs. À l'aide de l'AFM, nous

avons mesuré les contributions relatives des forces mécaniques et des mécanismes moléculaires à l'origine du processus de division chez les mycobactéries. Nous avons montré qu'il y avait une concentration de contraintes mécaniques au futur site de division, en utilisant une combinaison de modélisation par éléments finis COMSOL et de mesures AFM tout en modulant la pression de turgescence des cellules. L'accumulation de stress mécanique, combinée à une activité enzymatique, conduit finalement à une fracture mécanique et à la séparation des bactéries.

Les techniques de microscopie optique conventionnelles ont tendance à avoir une résolution faible et une vitesse élevées, tandis que les AFM conventionnels ont une résolution élevée et une vitesse faible. Nous avons conçu et construit un module d'éclairage structuré imprimé en 3D, l'openSIM, qui peut être ajouté aux microscopes à fluorescence. Il fournit un éclairage structuré pour obtenir des images SIM avec une résolution plus élevée. Dans le but d'améliorer la vitesse d'imagerie de l'AFM, nous avons mis en œuvre un actionnement photothermique dans une tête AFM à balayage de pointe et quantifié les contraintes de conception pour l'imagerie haute-vitesse avec actionnement photothermique hors résonance.

L'AFM est le plus souvent utilisé pour acquérir des images haute résolution d'un échantillon. Sa précision nanométrique en fait un outil unique pour d'autres applications. Nous avons combiné une tête AFM avec une sonde en forme de volcan pour les mesures d'électrogramme, et démontré l'enregistrement simultané des potentiels de champ extracellulaire et de la contraction de la cellule. Ce nouvel outil ouvre la voie à de futures études explorant les liens intrigants entre la mécanobiologie et l'électrophysiologie, avec une résolution unicellulaire.

## **Mots-clés**

Microscopie à force atomique, mycobactéries, croissance polaire, dynamique de croissance, morphogenèse, division bactérienne, microscopie à fluorescence, imagerie time-lapse, microscopie à éclairage structuré, superrésolution

# Abstract

*Mycobacterium tuberculosis*, the etiological agent for the tuberculosis disease, is a bacterial pathogen thought to infect about a quarter of the global human population. It is the first cause of death among infectious diseases, and is most prevalent in low-income populations. Much remains unknown about how these bacteria grow, divide, and manage to persist in the host even during month-long antibiotic treatments.

Bacteria are typically at the edge of the spatial resolution that conventional optical microscopy techniques can offer, and so new tools are required to study bacterial substructures or surface morphologies with nanometer resolution. We developed a platform for automated optical microscopy and atomic force microscopy (AFM) in order to study the morphogenesis of mycobacteria.

What is the growth dynamics of mycobacteria? Opposite models coexist in the literature for the pole growth dynamics of mycobacteria: the unipolar model and the bipolar model. Revising previous observations on mycobacterial growth, we show that the growth dynamics of mycobacteria follows a *new end take off* NETO model. There is a surprising similarity between the NETO growth dynamics of mycobacteria and of fission yeast, which hints at shared mechanisms for pole growth in evolutionarily distant pole growing organisms.

How do pole-growing organisms maintain their shape through insertion of new cell wall material at the tip? To explore further pole growth morphogenesis, we developed a method for imaging with AFM the pole of a growing rod-shaped microorganism. We observed the formation of a stiff fibril mesh on the pole of fission yeast cells, and showed that this mesh is stretched as the cell grows and insert new cell wall material at the tip.

How do mycobacteria divide into two sibling cells? Another essential aspect of morphogenesis of rod-shaped cell is the division of a mother cell into two sibling cells. Using AFM, we measured the relative contributions of mechanical forces and molecular mechanisms driving the division process in mycobacteria. We showed that there is a concentration of mechanical stress at the future division site, using a combination of COMSOL finite element modeling and AFM measurements while controlling the cell

turgor pressure. The accumulation of mechanical stress, in combination of enzymatic activity, ultimately leads to mechanical fracture and separation of the sibling bacteria.

Conventional optical microscopy techniques tend to have low resolution and high speed, while conventional AFMs have comparatively high resolution and low speed. We designed and built a 3D-printed structured illumination (SIM) module, the openSIM, as an add-on for fluorescence microscopes. It provides structured illumination to obtain SIM images with higher resolution. With the aim of improving the imaging speed of AFM, we implemented photothermal actuation in a tip-scanning AFM head, and quantified the design constraints for high-speed photothermal off-resonance tapping imaging.

AFM is most often used to scan and acquire high-resolution images of a sample. Its nanometer precision make it a unique tool for other applications. We combined an AFM head with a volcano-shaped probe for electrogram measurements, and demonstrated simultaneous recording of extracellular field potentials and contraction of the cell. This new tool opens the way for future studies exploring the intriguing links between mechanobiology and electrophysiology, with single-cell resolution.

## **Keywords**

Atomic force microscopy, mycobacteria, pole growth, growth dynamics, morphogenesis, bacterial division, fluorescence microscopy, time-lapse imaging, structured illumination microscopy, superresolution

# Table of content

<b>Acknowledgements .....</b>	<b>3</b>
<b>Résumé .....</b>	<b>5</b>
<b>Abstract .....</b>	<b>7</b>
<b>Table of content .....</b>	<b>9</b>
<b>Table of figures.....</b>	<b>14</b>
<b><i>Chapter A</i>    <b>General introduction.....</b></b>	<b>19</b>
A.1. Imaging mycobacteria with single-cell resolution.....	19
Tuberculosis .....	19
Importance of phenotypic heterogeneity .....	19
Growth in mycobacteria.....	19
Time-lapse microscopy for studying bacterial growth and division.....	20
Resolution limit in optical microscopy .....	20
A.2. Correlated atomic force microscopy and optical microscopy .....	22
A.3. Increasing the resolution of optical microscopy.....	25
Superresolution techniques .....	25
Structured illumination microscopy .....	26
A.4. General objectives of the research.....	28
<b>Part I    AFM time-lapse imaging of growth and division in pole growing microorganisms .....</b>	<b>29</b>
<b><i>Chapter B</i>    <b>A biphasic growth model for cell pole elongation in mycobacteria</b></b>	<b>31</b>
B.1. Preamble .....	31
B.2. Abstract.....	31
B.3. Introduction .....	32
B.4. Results.....	33
Measurement of pole elongation with time-lapse AFM.....	33

Pole elongation follows “new end take off” (NETO) dynamics.....	34
NETO is not due to release of physical constraints on poles.....	37
Delayed accumulation of Wag31 at the new cell pole.....	38
Wag31 relocalizes from old poles to new poles .....	40
NETO timing does not scale with the interdivision time.....	40
B.5. Discussion .....	43
B.6. Methods.....	45
Bacterial strains and growth conditions.....	45
Time-lapse optical microscopy.....	46
Time-lapse atomic force microscopy (AFM).....	46
Processing of AFM images .....	47
Photo-conversion of Wag31-Dendra2.....	47
Pole elongation measurement with time-lapse AFM.....	47
Pole elongation measurement with time-lapse phase microscopy .....	47
Bilinear fitting of pole elongation data.....	48
Calculation of cell wall age distribution in a microcolony .....	48
B.7. Acknowledgements.....	48
B.8. Author contributions.....	48
B.9. Supplementary Figures .....	48
 <b>Chapter C Mapping the topography and mechanical properties during pole</b>	
<b>growth of a rod-shaped microorganism .....</b>	<b>57</b>
C.1. Preamble.....	57
C.2. Introduction.....	57
C.3. Results.....	60
Vertical trapping of live rod-shaped cells in agarose microwells for AFM imaging..	60
AFM imaging of cell poles of live fission yeast cells .....	62
AFM time lapse imaging of the pole of a growing yeast cell.....	62
Radial displacement during growth of the fibrils visible on the yeast cell pole.....	63
Deformation of the fibril mesh as it migrates from the tip to the sides of the cell...	65
C.4. Discussion .....	66
C.5. Materials and methods .....	68
Yeast strains and growth conditions .....	68
Agarose microwells .....	68
Trapping.....	68
AFM Imaging.....	68

<b>Chapter D</b>	<b>Overlapping and essential roles for molecular and mechanical mechanisms in mycobacterial cell division.....</b>	<b>71</b>
D.1.	Preamble .....	71
D.2.	Introduction .....	71
D.3.	Results .....	72
D.4.	Discussion .....	80
D.5.	Author contributions: .....	81
D.6.	Acknowledgements: .....	81
D.7.	Materials and methods.....	82
	Bacterial culture conditions.....	82
	<i>M. smegmatis</i> RipA depletion strain.....	82
	Coverslips for AFM imaging .....	82
	Attachment of bacteria on coverslips.....	82
	AFM imaging .....	82
	Correlated AFM and fluorescence imaging.....	83
	Membrane staining.....	83
	AFM data processing.....	84
	Finite-element model of a dividing cell.....	84
D.8.	Supplementary figures .....	84
<b>Part II</b>	<b>Instrumentation developments for increasing resolution, speed or measurement modalities of combined AFM-optical microscopes .....</b>	<b>95</b>
<b>Chapter E</b>	<b>openSIM: a 3D printed microscope add-on for structured illumination microscopy.....</b>	<b>97</b>
E.1.	Preamble.....	97
E.2.	Introduction.....	97
E.3.	Results.....	98
	Structured illumination microscopy: principle.....	99
	openSIM design .....	101
	openSIM interface.....	102
	openSIM imaging .....	103
E.4.	Discussion.....	105
E.5.	Materials and methods .....	106
	Optical components for the openSIM.....	106
	Mechanical components for the openSIM.....	107
	Electronic components for the openSIM .....	107
	Labview interface and openSIM control .....	107

Sample preparation.....	107
Combined SIM/SICM microscopy.....	109
 <b>Chapter F Photothermal Actuation for Tip-Scanning Atomic Force</b>	
<b>Microscopy 111</b>	
F.1. Preamble .....	111
F.2. Introduction .....	111
F.3. Results .....	112
F.4. Discussion .....	119
F.5. Materials and methods.....	122
AFM.....	122
Collagen sample .....	122
PORT simulation.....	122
 <b>Chapter G Volcano-shaped SPM probe for combined force-electrogram</b>	
<b>recordings from excitable cells.....</b>	<b>125</b>
G.1. Preamble .....	125
G.2. Abstract.....	125
G.3. Introduction .....	126
G.4. Results .....	127
Microfabrication .....	128
Force and electrical measurements on neonatal rat cardiomyocytes .....	130
Recording of cardiomyocyte contraction displacements using the nanovolcano	
probe.....	131
Simultaneous recording of contraction displacements and electrogram from	
cardiomyocytes using the nanovolcano probe.....	133
G.5. Discussion .....	134
G.6. Conclusion.....	136
G.7. Materials and methods.....	137
Microfabrication .....	137
Interfacing.....	138
Electrodeposition of platinum-black.....	139
Isolation and culture of primary rat cardiomyocytes .....	139
Device functionalization.....	139
Combined AFM-optical-electrical setup and recordings .....	139
Electrophysiology.....	140
G.8. Acknowledgments.....	140
G.9. Authors contribution .....	140



G.10. Supplementary information .....	141
Custom cantilever holder .....	141
Setup for simultaneous optical imaging, force, and electrical recordings.....	141
Electrode-electrolyte interface.....	142
Cell-electrode interface .....	144
Long-term characterization.....	144
Force-controlled impedance measurements .....	144
Contraction displacement measurements.....	145
Electrogram measurements .....	145
<b>Chapter H Conclusion.....</b>	<b>147</b>
H.1. Main contributions of the thesis .....	147
How do mycobacteria grow? .....	147
Measuring the topography and local mechanical properties of a growing pole with atomic force microscopy .....	147
How do mycobacteria divide? .....	148
Designing a SIM add-on for fluorescence microscopes .....	148
Adding photothermal actuation capability to a tip-scanning AFM head .....	148
Adding live-cell electrical measurement capability to an AFM.....	149
H.2. Possibilities for future development of the work presented in the thesis.....	149
Is there a link between NETO and the other events of the cell cycles in mycobacteria?.....	149
Tip-growth morphogenesis: surprising similarities between evolutionarily distant organisms and potential insights on mycobacteria to be gained from analogous tip- growing organisms .....	149
What is the relationship between tip-growth and infection? .....	151
Future developments for the openSIM .....	153
<b>References .....</b>	<b>155</b>
<b>Curriculum Vitae .....</b>	<b>179</b>

# Table of figures

Figure 1: Modes of bacterial growth.....	20
Figure 2: Link between resolution, numerical aperture and noise level.....	21
Figure 3: The resolution of an image is lower than the diffraction limit if the signal-to-noise ratio is low .....	22
Figure 4: Comparison between the typical size of a mycobacterium and a wavelength of light.....	22
Figure 5: Combined AFM and optical microscope setup .....	23
Figure 6: Measuring topography and mechanical properties with AFM in off-resonance tapping (ORT) mode.....	24
Figure 7: Combined AFM and optical microscope for automated time-lapse imaging ...	25
Figure 8: Relationship between spatial frequencies, the image domain and the Fourier domain .....	27
Figure 9: Principle of structured illumination .....	27
Figure 10: Increase in resolution with SIM.....	28
Figure 11: Measurement of <i>M. smegmatis</i> pole elongation dynamics using AFM.....	34
Figure 12: Biphasic pole growth: NETO and cell division are independent events. ....	35
Figure 13: Unipolar, bipolar, and NETO pole growth models in mycobacteria.....	36
Figure 14: The pre-NETO phase is not due to physical constraints on new cell poles... 38	
Figure 15: Wag31 relocates from the old to the new pole during the pre-NETO phase. ....	39
Figure 16: Species-specific NETO dynamics impart different patterns of asymmetry. ...	42
Figure 17: Sample immobilization methods for atomic force microscopy.....	59
Figure 18: Vertical trapping of live fission yeast for AFM imaging of the cell pole .....	61
Figure 19: Procedure for loading fission yeast cells into agarose microwells using a lab centrifuge.....	61
Figure 20: Mechanical properties measurement on the pole of a live fission yeast cell ...	62
Figure 21: Time-lapse imaging of the pole growth of a fission yeast cell.....	63
Figure 22: Displacement of stiff fibrils during tip growth .....	64
Figure 23: Deformation of the stiff mesh during pole growth.....	65
Figure 24: Artistic representation of the fission yeast cell wall components, as seen with electron microscopy during cell wall formation.....	67
Figure 25. The pre-cleavage furrow (PCF) is a nanoscale cell-surface feature that marks the future division site in <i>M. smegmatis</i> . ....	74

Figure 26. Daughter cell cleavage occurs with millisecond kinetics by rupture around the PCF. ....	75
Figure 27. Turgor pressure drives cell cleavage through stress concentration at the PCF. ....	76
Figure 28. AFM-applied local stress on the PCF can substitute for an essential cell division enzyme (RipA). ....	78
Figure 29: Principle of structured illumination .....	99
Figure 30: Principle of structured illumination microscopy reconstruction.....	100
Figure 31: Design and assembly of the openSIM microscope add-on .....	102
Figure 32: Increase in resolution and optical sectioning when using the openSIM compared to wide field illumination .....	104
Figure 33: openSIM images of fluorescent biological samples.....	105
Figure 34: Implementation of photothermal actuation in a tip-scanning AFM .....	114
Figure 35: Photothermal cantilever actuation .....	115
Figure 36: Imaging in air with photothermal actuation in tapping mode.....	116
Figure 37: Measuring topography and mechanical properties with AFM in off-resonance tapping (PORT) mode .....	117
Figure 38: Impact of the tracking error for PORT .....	118
Figure 39: Imaging in air in photothermal off-resonance tapping (PORT) mode.....	119
Figure 40: Estimated photothermal actuation bandwidth for several commercial cantilevers.....	121
Figure 41: Concept and microfabrication of the nanovolcano probe.....	129
Figure 42: Force and electrical measurements on neonatal rat cardiomyocytes.....	131
Figure 43: Recording of contraction displacements from primary rat cardiomyocytes. ....	132
Figure 44: Simultaneous recording of cardiomyocyte contraction displacements electrograms.....	133
Figure 45: Combined AFM-fluorescence imaging of live <i>M. smegmatis</i> bacteria.....	147
Figure 46: Convergent evolution of analog traits between evolutionary distant organisms .....	150
Figure 47: <i>M. tuberculosis</i> bacteria form intercellular cord structures and deform their environment during infection .....	152
Figure S 1: Surface nanostructures resolved by AFM can be used as fiducial markers....	49
Figure S 2: Absolute measurement of pole elongation with AFM using surface nanostructures as fiducial markers. ....	49
Figure S 3: Precision of single-cell measurements using AFM.....	50

Figure S 4: Model for pole elongation dynamics. ....	50
Figure S 5: Measurement of pole elongation by phase-contrast microscopy requires a fiducial marker and accurate detection of cell division. ....	51
Figure S 6: The AFM cantilever tip can be used to lyse or displace cells. ....	52
Figure S 7: NETO is associated with an accumulation of Wag31-GFP at the new pole. ....	53
Figure S 8: Relocalization of Wag31-Dendra2 from old to new poles measured using photo-conversion fluorescence microscopy. ....	53
Figure S 9: NETO growth dynamics are observed in fast-growing and slow-growing <i>Mycobacterium</i> species. ....	54
Figure S 10: The duration of the pre-NETO phase does not scale in proportion to the interdivision time in <i>Mycobacterium</i> species. ....	55
Figure S 11: The pre-cleavage furrow (PCF) precedes the Wag31-GFP cytokinesis marker at the future cell division site. ....	84
Figure S 12: AFM scan line across the PCF during cleavage. ....	85
Figure S 13: Height data of millisecond cell cleavage measured at 1 kHz rate (shown in Figure 26e). ....	85
Figure S 14: Cell cleavage measured at 1 millisecond time resolution. ....	85
Figure S 15: Overview height images of cell before (left) and after (right) cleavage shown in Figure 26f-h. ....	86
Figure S 16: AFM force curves at the PCF of two representative cells over time. ....	86
Figure S 17: Comparison of stiffness values obtained from QNM DMT modulus imaging channel and analysis of the individual force-distance curves. ....	87
Figure S 18: Stiffness at the PCF measured by repeatedly scanning across the PCF. ....	88
Figure S 19: Height images of cells before and after deflation induced by piercing with a sharp AFM cantilever tip. ....	88
Figure S 20: Height images of cells corresponding to stiffness maps shown in Figure 28. ....	89
Figure S 21: Cell cleavage can be induced prematurely by increasing the mechanical stress on the PCF. ....	89
Figure S 22: Premature cleavage can be induced by AFM force curves or AFM scanning along the PCF. ....	90
Figure S 23: Cells forced to undergo premature cleavage continue to grow and divide. ....	90
Figure S 24: RipA-depleted cells form chains of cells that grow only at the free cell poles. ....	91
Figure S 25: Height and stiffness changes of chained RipA-depleted cells. ....	91
Figure S 26: Cell wall failure of centrally located cells of RipA-depleted cell chains occurs in between the flanking PCFs. ....	92

Figure S 27. Finite element modeling of the PCF in a dividing cell. ....	92
Figure S 28: Mechanical and electrical interfacing of the nanovolcano probe.....	141
Figure S 29: Description of the custom AFM-optical system. ....	142
Figure S 30: Electrochemical characterization of the nanovolcano probe. ....	143
Figure S 31: Recording of a cardiomyocyte electrogram using the nanovolcano probe.	146



# *Chapter A* General introduction

## **A.1. Imaging mycobacteria with single-cell resolution**

### **Tuberculosis**

*Mycobacterium tuberculosis*, the etiological agent for the tuberculosis disease, is a bacterial pathogen thought to infect about a quarter of the global human population<sup>1</sup>. Among infectious diseases it is responsible for the largest amount of annual death and is most prevalent in low-income populations<sup>1</sup>. Much remains unknown about how these bacteria grow, divide, and manage to persist in the host even during month-long antibiotic treatments<sup>2,3</sup>, information that is all the more relevant given the sharp increase in the prevalence of multi-drug-resistant strains<sup>3</sup>.

### **Importance of phenotypic heterogeneity**

While studies at the population level provide significant insights on the global behavior of bacteria, it does not capture the diversity of phenotypes within the bacterial population<sup>4</sup>. Indeed, the average phenotype of a population is not necessarily a good representation of the phenotype of any bacterium within that population<sup>4</sup>. Conversely, a diverse population is often more capable to evolve and adapt when exposed to environmental changes; phenotypic diversity increases the probability that at least a sub-population of bacteria will be more suited to survive in the new environment<sup>4</sup>.

Such phenotypic diversity has been observed in mycobacteria. In a small microcolony of genetically identical bacteria, epigenetic factors generate a certain diversity in gene expression<sup>5</sup>, cell size<sup>6–8</sup>, and age<sup>7</sup>, which in turn impacts the ability of the colony to survive under drug exposure<sup>5,7,9</sup>.

### **Growth in mycobacteria**

At each generation, new daughter bacteria inherit the same growth potential as the mother cells (Figure 1a). However, we still have poor understanding of the processes involved in the preservation of cell shape and function during growth and division. The precise growth dynamics of mycobacteria is important for its potential contribution to cell-to-cell phenotypic heterogeneity and drug susceptibility<sup>7,9</sup>. In some rod-shape bacteria such as *Escherichia Coli*, new cell wall is synthesized along the cell sidewalls (Figure 1b). In contrast, Actinobacteria, including the medically relevant genus *Mycobacterium tuberculosis*, are

extending by inserting new cell wall material at the pole<sup>10</sup> (Figure 1b). Diverging descriptions of pole growth co-exist in mycobacteria, such as the unipolar<sup>7,10</sup> and the bipolar model<sup>6</sup> (Figure 1c). Motivated by this intriguing discrepancy, we show that the growth dynamics of mycobacteria follows a *new end take off* NETO model<sup>11</sup> (Figure 1c).

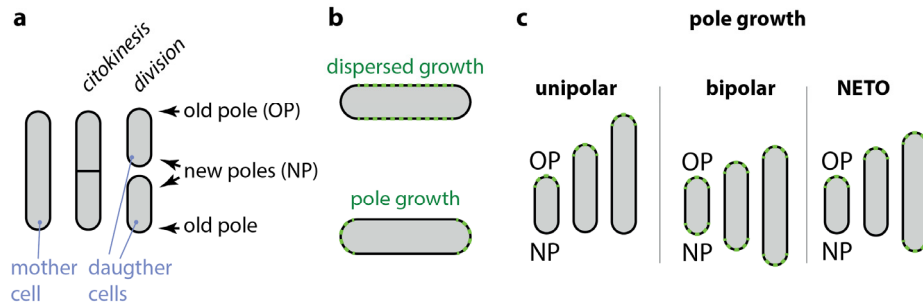


**Figure 1: Modes of bacterial growth**

(a) Schematic representation of bacterial division. A mother cell divides in two daughter cells. Each daughter cell inherits a pole of the mother cell (old pole) and a new pole, formed at the division site. (b) Schematic representation of two modes of bacterial growth: dispersed growth and pole growth. Inserted new cell wall material is represented by a green dotted line. Some species (e.g. *E. Coli*) grow by insertion of new cell wall material on the sides of the cell (dispersed growth) while for others the insertion of new material is restricted to the cell pole. (c) Three models proposed for the pole growth dynamics of mycobacteria: unipolar growth<sup>7</sup>, bipolar growth<sup>6</sup>, and the model introduced in this work, biphasic NETO growth<sup>11</sup>.

### Time-lapse microscopy for studying bacterial growth and division

Automated microscopes for time-lapse imaging of mycobacterial growth are essential for seeing bacterial diversity. They typically combine a motorized microscope, a high-performance camera, a sample stage, a temperature control system, a microfluidic system to renew the growth medium continuously, and a software control to coordinate these hardware elements<sup>5,7</sup>. This type of instrument was key for determining the size distribution of individual mycobacteria<sup>6,7</sup>, the location of the division site relative to the middle of the mother cell<sup>6</sup>, the age of cell poles<sup>7</sup>, and the gene expression of individual cells<sup>5</sup>.

### Resolution limit in optical microscopy

Because of the diffraction of light in the optical microscope, objects close to each other cannot always be resolved. Abbe<sup>12</sup> showed that a microscope cannot resolve objects separated by a distance smaller than  $d = \frac{\lambda}{2 \cdot n \cdot \sin(\theta)} = \frac{\lambda}{2 \cdot NA}$ , where  $\lambda$  is the wavelength of light,  $n$  is the refractive index of the medium between the microscope objective and the sample,  $\theta$  is the half of the collection angle of the objective, and  $NA = n \cdot \sin(\theta)$  is the



numerical aperture of the objective (Figure 2a,b). In other words, there is a limit to the smallest details that are visible through an optical microscope, depending on the numerical aperture of the microscope objective (Figure 2b,c). The optical components of a microscope determine the value of the diffraction limit. In practice, the diffraction limit is about 200nm for conventional optical microscopes<sup>13</sup>.

The diffraction limit sets a low boundary to the smallest distance that can be resolved with a given microscope (using conventional microscopy techniques). Depending on the noise level compared to the signal (usually quantified as signal-to-noise ratio), the actual resolution of the image might not reach the diffraction limit (Figure 2d, Figure 3). For fluorescence microscopy, the signal-to-noise ratio depends on several factors, such as the numerical aperture of the objective, the sensitivity and noise performance of the camera, the density and brightness of the individual fluorophores in the imaging plane, the density and brightness of fluorophores in out-of-focus planes, and the intensity of the light used for fluorescence excitation. This last point is crucial when imaging live cells, because of phototoxic effects<sup>14</sup>. The total amount of light that can be used to illuminate a given sample without a major toxic impact is often referred to as the *photon budget*<sup>14</sup>. For live-cell imaging, there is thus a compromise to be made between light-induced damage, signal-to-noise-ratio (hence spatial resolution) and temporal resolution<sup>15</sup>.

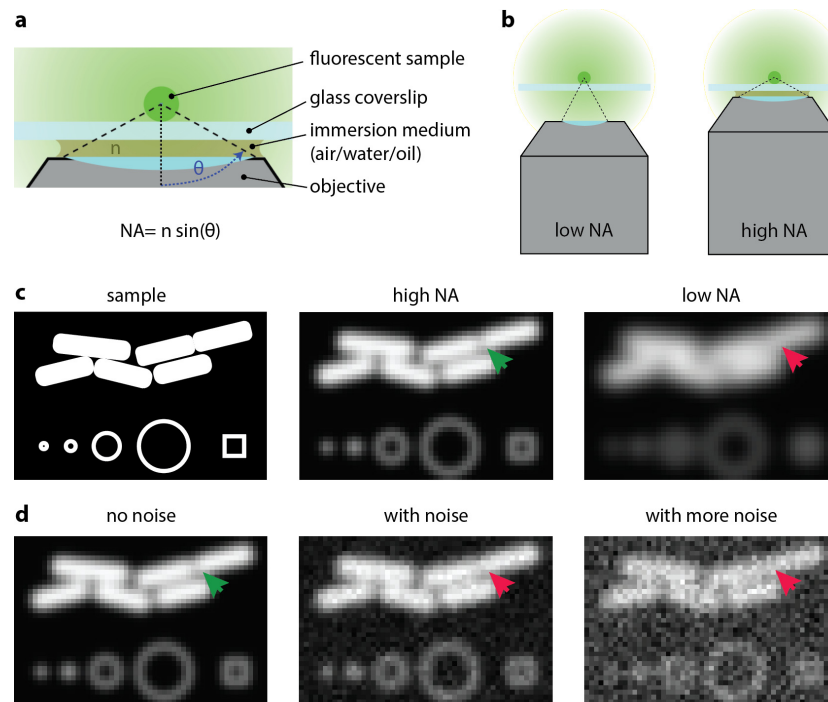
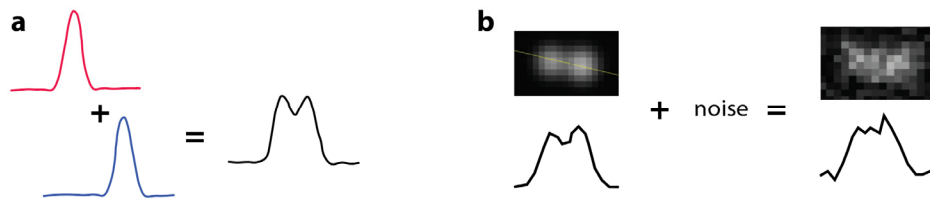


Figure 2: Link between resolution, numerical aperture and noise level

(a) Illustration of the components determining the numerical aperture (NA) of a microscope objective. The numerical aperture is equal to the product of the refractive index of the medium between the objective and the sample and the sinus of the aperture angle. (b) Schematic representation of a low NA objective (left), without immersion medium and with a low aperture angle and a high NA objective (right), with oil immersion medium and a high aperture angle. (c) Simulated image of a sample, when using a high NA objective (center) or a low NA objective (right). (d) Simulated image of a sample (sample defined in (c)), when there is no noise (left), some noise (center) or more noise (right). (c-d) An arrow indicates when two bacteria close to each other are correctly resolved as being two separated bacteria (green arrow) or mistaken for a single long bacterium (red arrow).



**Figure 3: The resolution of an image is lower than the diffraction limit if the signal-to-noise ratio is low**

(a) Illustration of the intensity profile for two point sources close to each other. Here, the two peaks are close, but clearly separated: the two point sources are properly resolved. (b) Illustration of the impact of noise on resolution: adding noise makes the two peaks indiscernible and the two point sources are no longer resolved, even if they are separated by a distance larger than the diffraction limit.

## A.2. Correlated atomic force microscopy and optical microscopy

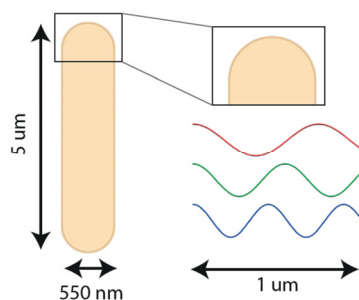


**Figure 4: Comparison between the typical size of a mycobacterium and a wavelength of light**

Given the micrometric size of bacteria, many subtle details involved in their growth and division are typically at the edge of the spatial resolution that conventional optical microscopy techniques can offer (Figure 4). It is therefore important in microbiology to explore alternative techniques with higher resolution.

Atomic force microscopy (AFM) is a technique that does not rely on light to image a sample and is therefore not limited by diffraction. The atomic force microscope is a scanning probe instrument, invented in 1986 to image non-conductive samples, and it can reach nanometer resolution on live biological samples<sup>16–18</sup>. Additionally, AFM imaging has

no reported toxic effect on live bacteria, which continue to grow and divide normally during the scan<sup>11,16,18</sup>.

An AFM requires a nanometer-sharp tip made by microfabrication technology at the free end of a flexible cantilever (Figure 5). The deflection of the cantilever is measured with a laser and a four-quadrant photodiode. A piezoelectric actuator moves the cantilever in XY (for scanning) and Z (for tracking the sample topography during scanning).

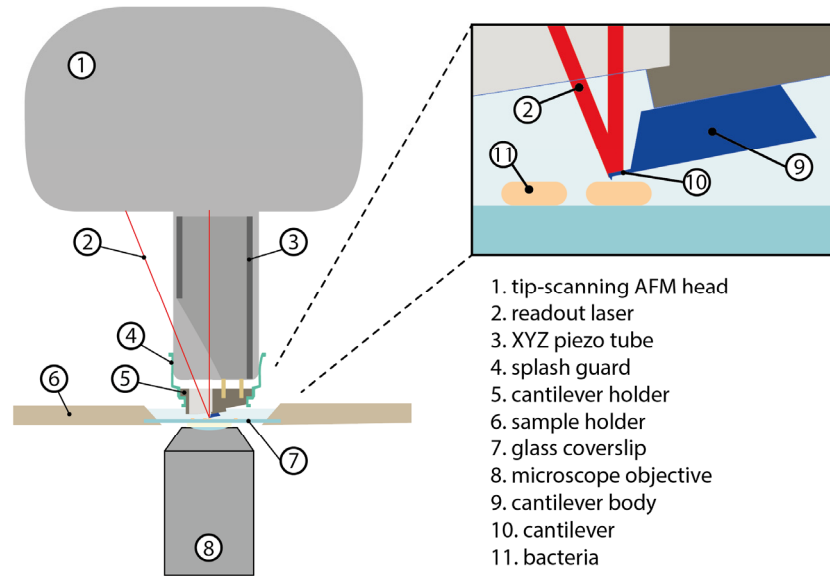


**Figure 5: Combined AFM and optical microscope setup**

The sample (e.g. bacteria in this schematic) is attached to a glass coverslip and covered in cell medium. The sample holder heats the cell medium to the optimal temperature. An inverted optical microscope allows us to get fluorescence images of the sample. For AFM imaging, the deflection of a microfabricated cantilever is measured using a readout laser. The force applied to the sample is calculated in real time based on the cantilever deflection, as well as calibration parameters such as cantilever spring constant and deflection sensitivity. The piezo tube translates the cantilever to scan the sample in XY, while adjusting the vertical Z position with a feedback loop to apply a constant (low) force to the sample. *This diagram is not to scale.*

When the cantilever interacts with a sample (Figure 6a), it is possible to calculate the vertical position of the sample, as well as the local mechanical properties, such as stiffness and adhesion (Figure 6b). The ORT AFM imaging mode<sup>19</sup> (also called Pulsed Force mode<sup>20</sup>, PeakForce QNM<sup>21</sup>, HybriD mode, etc.) is a method for measuring the topography and the local mechanical properties simultaneously at high speed. At each point of the sample surface, the local interaction curve is calculated by subtracting the cantilever dynamics (free deflection). The applied peak force is deduced (Figure 6c), as are the local mechanical properties, and the applied force is compared to the force setpoint (typically

1nN for imaging mycobacteria). The difference is set as the input of a proportional integral controller (PI controller), to calculate the voltage to apply to the piezoelectric actuator and reduce the error. This feedback loop ensures that the applied force remains close to the setpoint while scanning (Figure 6d). The motion of the piezoelectric actuator required to do so corresponds to the topography of the sample (Figure 6d), and is the output data of AFM.

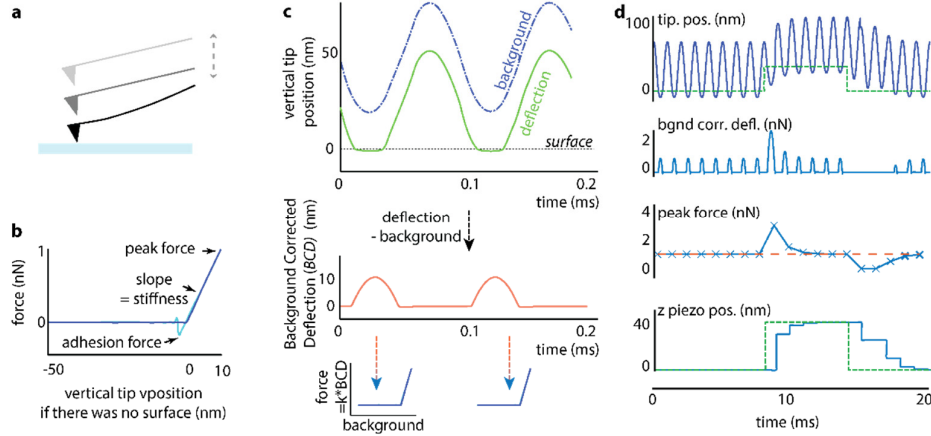


**Figure 6: Measuring topography and mechanical properties with AFM in off-resonance tapping (ORT) mode**

(a) Illustration of the cantilever (black) being deflected when it is in contact with the sample surface (light blue). (b-d) are numerical simulations made with a custom MATLAB script, based on Newton's law, assuming linear interaction forces, and transferred in the discrete temporal domain with Euler approximation. (b) Simulated force curve, from which sample mechanical properties (stiffness, adhesion) are deduced. In ORT, interaction curves are obtained by plotting the cantilever deflection (multiplied by the cantilever spring constant) as a function of the background (i.e. free deflection). As long as the cantilever is away from the surface, no force is applied. When the cantilever touches the surface, the force applied increases with the indentation, proportionally to the sample stiffness. (c) Simulated ORT measurement of the sample mechanical properties without scanning. During ORT, the cantilever is actuated with a sine wave signal. When the cantilever is away from the surface, the cantilever motion is therefore a sine wave (dotted blue line, background). When the cantilever is brought closer to the surface, the cantilever motion deviates from a sine wave (green line). The difference between the free deflection and the deflection signal in contact gives the background corrected deflection signal (orange), from which interaction curves are calculated (blue).  $k$ : cantilever stiffness. (d) Simulated ORT measurement of the sample topography and mechanical properties while scanning a line of a sample. The topography of the simulated sample is a step represented by a green dotted line. The background corrected deflection is calculated in real time to determine the peak force applied. The peak force is compared to the force setpoint (1nN here, indicated by the red dotted line). The controller adapts the voltage sent to the piezoelectric actuator to keep applying a

constant force. The position of the piezoelectric actuator (“z piezo pos.”) reflects the topography of the sample and is our output, i.e. one line of the AFM image.

An atomic microscope provides nanometer resolution information about the surface of a sample without requiring a labeling step, and a fluorescence microscope provides information on specific labelled structures of the cells (usually with diffraction-limited resolution). The combination of such complementary techniques is gaining increasing popularity for biological applications, to integrate high-resolution information about the cell surface with specific data on the inside of the cell<sup>17</sup> (Figure 5). We developed an automated platform for combined AFM-optical microscopy (Figure 5, Figure 7) to record correlated images of the growth and division of mycobacteria over several generations<sup>11</sup>.

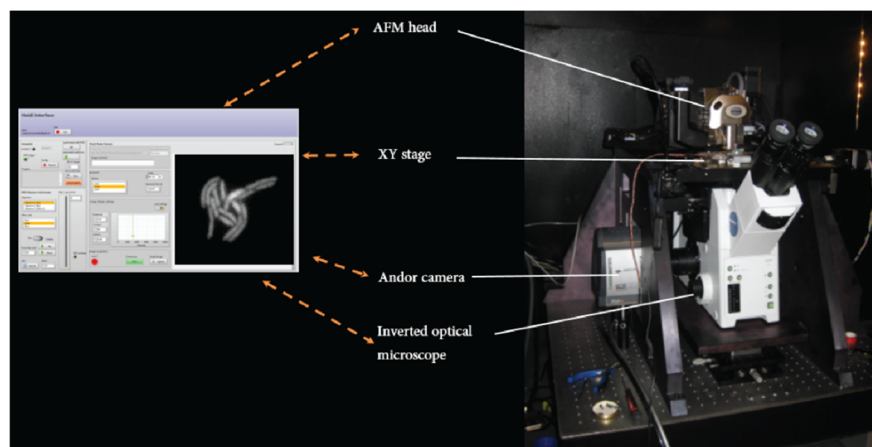


Figure 7: Combined AFM and optical microscope for automated time-lapse imaging

### A.3. Increasing the resolution of optical microscopy

#### Superresolution techniques

The diffraction limit was long believed to be impossible to overcome. However, there has been recent developments in superresolution fluorescence microscopy, achieving resolution one or two orders of magnitude higher than the diffraction limit.

Superresolution microscopy techniques divide into two categories: superresolution with patterned excitation (STED<sup>22,23</sup>, SIM<sup>24</sup>, MINFLUX<sup>25</sup>), and superresolution without patterned excitation (PALM<sup>26</sup>, STORM<sup>27</sup>, SOFI<sup>28</sup>, SRRF<sup>29</sup>,...).

For STED microscopy, a doughnut shaped beam deactivates the fluorophores, while a focused beam activates them<sup>22</sup>. When the two beams are precisely aligned, only the fluorophores at the very center of the excitation beam emit light. Scanning the sample with the beams results in a superresolution image.

Single molecule localization microscopy techniques (SMLM, such as PALM<sup>26</sup> and STORM<sup>27</sup>) relies on a very different principle. It takes advantage of the reversible switch of fluorophores between an “on” and an “off” state. At a given time, only a small fraction of the fluorophores are emitting light, and it is consequently possible to localize each with high precision. Several hundreds or thousands of images are recorded to generate a final superresolved image.

Both STED and SMLM techniques require high excitation intensity and are too toxic to be compatible with long term time-lapse imaging<sup>15</sup>. Structured illumination microscopy (SIM) on the other hand gives a moderate resolution improvement (two-fold improvement in lateral resolution for 2D linear SIM<sup>24</sup>), but has been gaining a wide interest because of its high speed<sup>30,31</sup> and low phototoxicity<sup>15</sup>. For this reason, we chose to focus on the SIM superresolution technique as a mean to increase the resolution for time-lapse imaging of live cells.

### **Structured illumination microscopy**

SIM relies on operations on spatial frequency domain of the images.

Figure 8 illustrates what are the low and high spatial frequency components of an image. In short, an image without the high spatial frequency components looks blurred and loses the sharp details. In the Fourier domain, the distance from the origin is directly related to the frequency in the real space (Figure 8): low frequencies lay close to the origin, whereas high ones are farther from it.

Because of the diffraction limit, a microscope blurs the image, i.e. it blocks the high spatial frequency components of the image (with a frequency cut-off equal to  $\frac{1}{2\pi} \frac{2 \cdot NA}{\lambda}$ ). In the Fourier domain, this corresponds to filtering out all the spatial frequencies laying outside of a disk of radius  $R = \frac{1}{2\pi} \frac{2 \cdot NA}{\lambda}$ , and blocking the high-frequency information outside that disk. Structured illumination is a method to translate high frequency components into the diffraction-limited disk of the microscope.

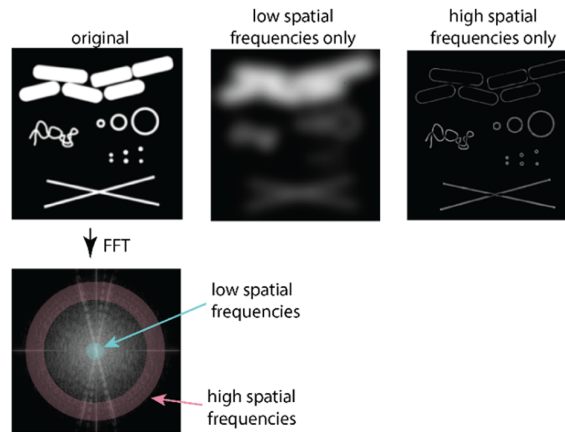


**Figure 8: Relationship between spatial frequencies, the image domain and the Fourier domain**

The Fourier transform (FFT) of an image gives information about its content in terms of special frequencies: an image which contains only the low spatial frequency looks blurred (center), while an image with high spatial frequencies (right) mainly contains edges and small details. In the Fourier space, low (respectively, high) frequencies lay close to (respectively, far from) the origin.

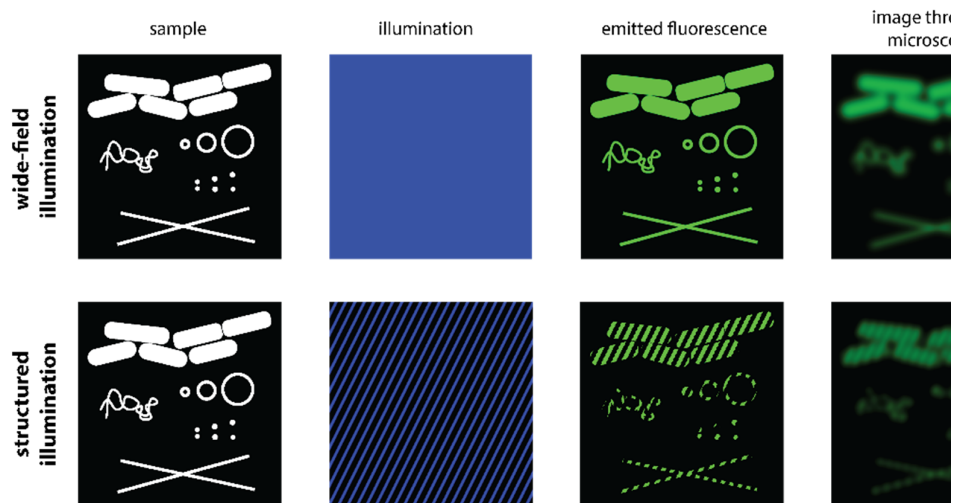


**Figure 9: Principle of structured illumination**

Illustration of the principle of wide field illumination compared to structured illumination. For wide field illumination, the field of view is illuminated with a constant excitation intensity, in response to which the fluorescent areas of the sample emit light. Due to the diffraction limit, a “blurred” version of the emitted fluorescence reaches the camera. For structured illumination, the excitation light is patterned, meaning that not all the areas of the sample are excited and emit light. In mathematical terms, the emitted fluorescence is the product of the fluorescent area of the sample and the excitation pattern. The emitted fluorescence image is “blurred” due to the diffraction limit in an identical manner as for wide field microscopy.

A structured illumination microscope illuminates the sample with a predefined pattern (usually lines, Figure 9, Figure 10a), instead of a constant illumination over the whole field of view (wide field illumination, Figure 9). Several images with different illumination patterns are combined to build an artificial superresolved image with a computational algorithm<sup>32,33</sup> (Figure 10).

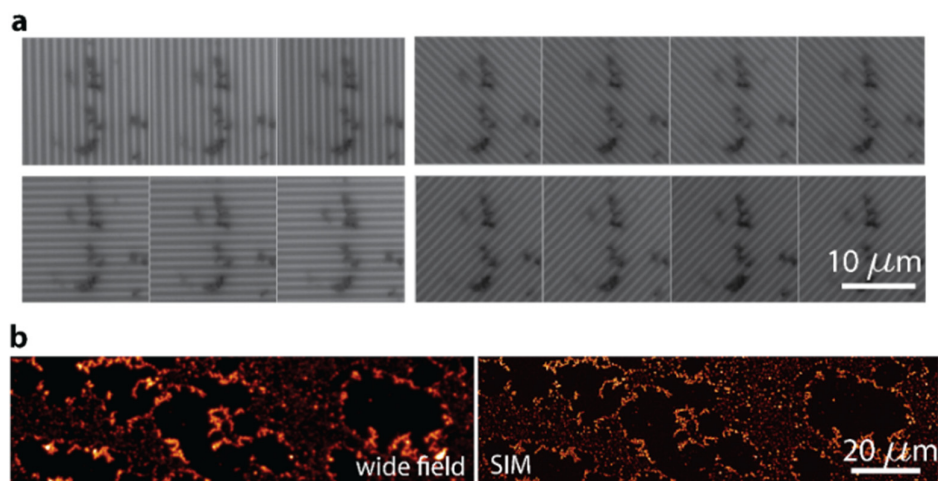


**Figure 10: Increase in resolution with SIM**

(a) Example of patterned illumination on a thin fluorescent film. Here, 14 different patterns are used corresponding to 4 different angles. (b) Comparison between an image of beads with wide field illumination compared to the SIM image.

#### A.4. General objectives of the research

The first objective of this thesis was to understand some of the biophysical mechanisms enabling mycobacteria to grow and divide: determining the growth dynamics of pole elongation (Chapter B), and highlighting the role of mechanical stress concentration during bacterial cell division (Chapter D). This research was made possible thanks to previous and new developments in instrumentation for time-lapse optical and AFM microscopy, by our group and by others.

The second objective of this research was to develop new tools for live-cell microscopy, which will facilitate future research on mycobacteria and living organisms in general, by our group and by others. To do so, I developed a protocol for AFM imaging of the growing tip of a pole-growing microorganism (Chapter C), introduced a design for photothermal actuation in a tip-scanning AFM to increase AFM imaging speed (Chapter F), designed and built a microscope add-on for SIM microscopy to increase optical resolution (Chapter E), and collaborated with another group<sup>34</sup> to develop an AFM setup for simultaneous optical, mechanical and electrical recordings on live cells (Chapter G).



## **Part I**

AFM time-lapse imaging of growth  
and division in pole growing  
microorganisms



# ***Chapter B*** A biphasic growth model for cell pole elongation in mycobacteria

## **B.1. Preamble**

Opposite models coexist in the literature for the growth dynamics of mycobacteria<sup>6,7</sup>. Motivated by this intriguing discrepancy, we show, thanks to time-lapse AFM images, that the growth dynamics of mycobacteria follows a *new end take off* NETO model.

This is a verbatim copy of an article that has been published in a peer reviewed journal<sup>11</sup>. Permission is granted by the publisher to reproduce the article in this thesis dissertation.

Hannebelle, M. T. M., Ven, J. X. Y., Toniolo, C., Eskandarian, H. A., Vuaridel-Thurre, G., McKinney, J. D.\* & Fantner, G. E\*. A biphasic growth model for cell pole elongation in mycobacteria. *Nat. Commun.* **11**, (2020).

\* contributed equally

My contribution to this work consist in the assembly and automation of the combined AFM-optical microscope used in this study. I also acquired the AFM time-lapse images and analyzed the data.

## **B.2. Abstract**

Mycobacteria grow by inserting new cell wall material in discrete zones at the cell poles. This pattern implies that polar growth zones must be assembled *de novo* at each division, but the mechanisms that control the initiation of new-pole growth are unknown. Here, we combine time-lapse optical and atomic force microscopy to measure single-cell pole growth in mycobacteria with nanometer-scale precision. We show that single-cell growth is biphasic due to a lag phase of variable duration before the new pole transitions from slow to fast growth. This transition and cell division are independent events. The difference between the lag and interdivision times determines the degree of single-cell growth asymmetry, which is high in fast-growing species and low in slow-growing species. We propose a biphasic growth model

that is distinct from previous unipolar and bipolar models and resembles “new end take off” (NETO) dynamics of polar growth in fission yeast.

### B.3. Introduction

At the single-cell level, the spatial pattern of cell growth and division is remarkably diverse, even among organisms that are morphologically similar<sup>35</sup>. Among rod-shaped bacteria, some species grow by insertion of new material into the sidewalls with little or no growth at the poles (e.g., *Escherichia coli*, *Bacillus Subtilis*)<sup>35</sup>, while others show the opposite pattern, growing by insertion of new material at the poles with little or no growth at the sidewalls (e.g., *Mycobacterium* species)<sup>35</sup>. *Mycobacterium* is a medically relevant genus that includes important pathogenic species such as *M. tuberculosis* and *M. leprae*.

To characterize the pattern of growth of a bacterium at the single-cell level, both temporal and spatial information are required with sufficiently high resolution. Several methods have been developed over the past decades for measuring the pattern of single-cell growth, but the conclusions have varied between studies. Two main models have been proposed for bacteria that grow by extension of the sidewalls, such as *E. coli* or *B. subtilis*: a linear model in which cells grow at a constant speed<sup>36</sup>, and an exponential model in which the speed of growth is proportional to cell size<sup>37</sup>. More recently, the exponential growth pattern has been confirmed for *B. subtilis* by a pioneering study using a suspended microchannel resonator to measure the buoyant mass of individual cells over time<sup>38</sup>.

Compared to our understanding of the growth pattern of sidewall-growing organisms, our understanding of polar growth is incomplete<sup>8</sup>. Time-lapse optical microscopy combined with microfluidics has become a tool of choice for measuring the pattern of polar growth in mycobacteria<sup>5–7,9,10</sup>. Despite a consensus that mycobacteria grow exclusively at the poles, it remains controversial whether their pattern of single-cell growth follows unipolar (asymmetric) or bipolar (symmetric) dynamics<sup>6–10,39</sup>. According to the *unipolar model*, the new cell pole grows very slowly or not at all between birth and division, when it becomes the old pole of the newborn cell and transitions to fast growth (Figure 11a). According to the *bipolar model*, both poles, new and old, grow at the same rate between birth and division (Figure 11a).

We sought to reexamine this controversy regarding the pattern of single-cell growth in mycobacteria using time-lapse microscopy with high spatial resolution. The spatial resolution of optical microscopy is limited by diffraction to approximately half the wavelength of light, which corresponds in size to the radius of a bacterium. Super-resolution optical microscopy

can overcome the diffraction limit<sup>22,26,27</sup>, but most super-resolution techniques are not compatible with long-term time-lapse imaging due to phototoxicity<sup>15</sup>. Atomic force microscopy (AFM) is emerging as a powerful tool for microbiology, as it allows nanometer resolution imaging of live cells in liquid cultures<sup>40,41</sup>. AFM has been successfully used to study cell wall nanostructure<sup>42–44</sup>, cell growth<sup>42,43</sup>, and the nanoscale effects induced by drug exposure<sup>44,45</sup>. In addition, developments in AFM technology have enabled imaging of bacterial processes at high temporal resolution<sup>46–48</sup>. Recently, we developed methods for long-term time-lapse AFM to observe mycobacteria growing and dividing through multiple generations with nanometer resolution<sup>16</sup>. AFM time-lapse images revealed morphological landmarks on the mycobacterial cell surface, which appear up to two generations in advance and correspond to future sites of division<sup>16</sup>. Using AFM nanomechanical mapping, we found that mycobacterial division is driven by a combination of peptidoglycan hydrolytic activity and accumulation of mechanical stress at the septum, which culminates in abrupt division in a timeframe of milliseconds<sup>18</sup>.

Here, we use a combination of time-lapse AFM and optical microscopy to characterize the spatial and temporal pattern of single-cell growth in fast- and slow-growing *Mycobacterium* species. We show that single-cell growth of mycobacteria follows biphasic polar dynamics distinct from the previously proposed unipolar and bipolar models.

## **B.4. Results**

### **Measurement of pole elongation with time-lapse AFM**

We imaged cell growth and division of *Mycobacterium smegmatis* with time-lapse AFM, which provides nanometer-resolution three-dimensional topographical data of the cell surface (Supplementary Movie 1). Cell division is visible in the AFM images as a sudden drop in height at the nascent division site<sup>16,18</sup>. Upon cell division, two newly formed sibling cells often remain closely apposed at their new poles and may therefore appear to be a single non-divided cell by optical microscopy while being resolvable as two distinct cells by AFM (Figure 11b). Moreover, AFM reveals nanoscale structures on the cell surface, such as wave-troughs<sup>16</sup>, division scars<sup>49</sup>, and protruding blebs, which may represent microvesicles<sup>50</sup> (Figure 11; Figure S 1). These surface structures are spatially immobile over time because they are outside the polar growth zones (Figure S 1), which validates them as fiducial markers that can be used to measure the growth of each cell pole individually. By repeatedly measuring the distance between cell-surface fiducial markers and the cell poles, we were able to quantify pole elongation in absolute terms (Figure 11c; Figure S 2) with ~50nm precision (Figure S 3).

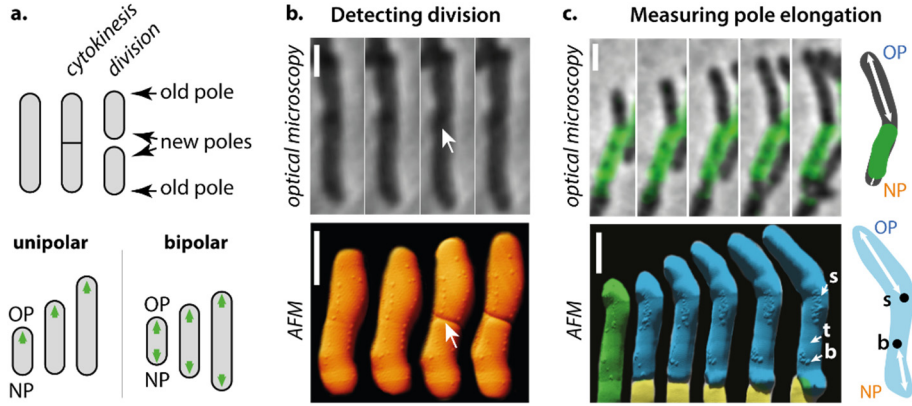


**Figure 11: Measurement of *M. smegmatis* pole elongation dynamics using AFM.**

(a) Schematic of unipolar<sup>7</sup> and bipolar<sup>6</sup> elongation models. OP, old pole. NP, new pole. (b) Comparison between phase-contrast and AFM time-lapse images of dividing cells measured on different instruments. Arrows indicate the division site in the first frame following the division event. For phase-contrast microscopy data, the division event was detected using the method described in Figure S 5. Scale bar, 1  $\mu\text{m}$ . Time between consecutive images is 10 minutes for phase-contrast microscopy data and 13 minutes on average for AFM data. (c) Absolute measurement of pole elongation using fluorescence pulse-chase labelling and AFM-resolved surface nanostructures as fiducial markers. Scale bar, 1  $\mu\text{m}$ . Top: combined phase-contrast and fluorescence images of an elongating cell. Time between consecutive images is 30 minutes. The schematic illustrates how fluorescently labeled cell wall (green) can be used as a fiducial marker to measure pole elongation (white arrows). Bottom: AFM time-lapse images of a mother cell (green) and its two daughter cells (blue and yellow). Surface nanostructures used as fiducial markers are indicated with a white arrow: division scar (s), protruding bleb (b), trough (t). The schematic illustrates how surface nanostructures (black circles) are used as fiducial markers to measure pole elongation over time. Time between two images is 1.25 hours on average.

### Pole elongation follows “new end take off” (NETO) dynamics

We observed that a newly born cell pole initially grows slowly (or not at all) before transitioning to a constant rate of fast growth (Figure 12a), reminiscent of the unipolar model<sup>7</sup>. However, close inspection of our AFM data reveals that, in most cases, the new pole transitions from slow to fast growth prior to the subsequent cell division (Figure 12a). Rather than unipolar<sup>7,10</sup> or bipolar<sup>6</sup> growth, this pattern (Figure 12b; Figure S 4) instead resembles the “new end take off” (NETO) model of biphasic pole growth described previously in the eukaryotic fission yeast *Schizosaccharomyces pombe*<sup>51</sup>. Although mycobacteria and fission yeast are separated by more than a billion years of evolution, we will use the descriptive term “NETO” in reference to the dynamics of polar growth in mycobacteria as well (Figure 12c).

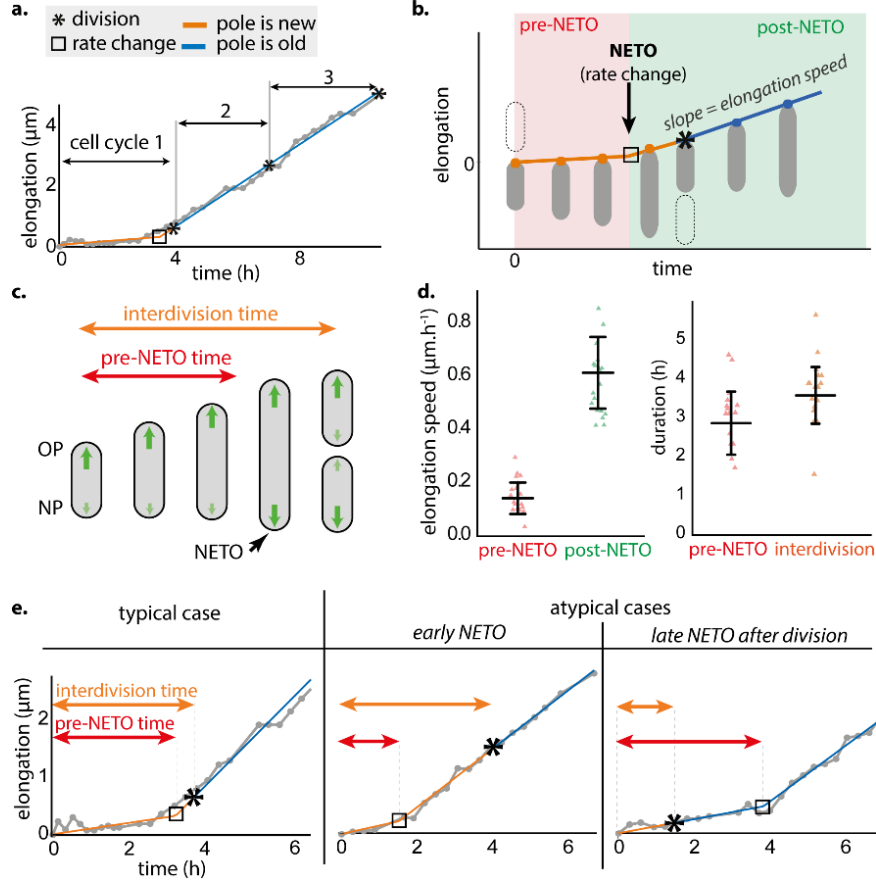


**Figure 12: Biphasic pole growth: NETO and cell division are independent events.**

(a) Elongation of a representative newborn pole through three generations measured by time-lapse AFM. Grey: AFM data; orange/blue: bilinear fit. See Figure S 4. (b) Schematic of biphasic growth of a newborn pole with a rate change (NETO). (c) Schematic of biphasic NETO growth of a cell over one cell cycle. (d) Left: elongation speeds of newborn poles during the pre-NETO phase (slow or no growth) and the post-NETO phase (fast growth). Right: pre-NETO time and interdivision time. Data from time-lapse AFM images (20 poles). Bars indicate averages and standard deviations. (e) Typical elongation curve of a newborn cell pole (left) and atypical curves with early NETO before division (center) and late NETO after division (right). Each curve corresponds to one of the data points in (d). Grey: AFM data; orange/blue: bilinear fit.

We found that the lag phase between new-pole formation and the transition from slow growth (average  $\sim 0.15 \pm 0.06$  μm per hour) to fast growth ( $\sim 0.61 \pm 0.13$  μm per hour) is variable with an average duration of  $2.9 \pm 0.8$  hours in cells growing with an average interdivision time of  $3.6 \pm 0.7$  hours (Figure 12d). In the majority ( $> 80\%$ ) of cells, NETO occurs between birth and the next cell division (Figure 12e). However, in a minority ( $< 20\%$ ) of cells, NETO occurs after the next cell division (Figure 12e), which rules out the possibility that division *per se* is the

trigger that causes a cell pole to switch from slow to fast growth. We conclude that NETO and cell division are temporally distinct events in terms of their relative order and timing. The NETO pattern of growth is distinct from the bipolar growth model<sup>6</sup>, according to which fast pole growth is initiated immediately at pole birth (Figure 12). The NETO pattern of growth is also distinct from the unipolar growth model<sup>7,10</sup>, according to which fast pole growth is initiated at cell division, when the new pole becomes an old pole (Figure 13).

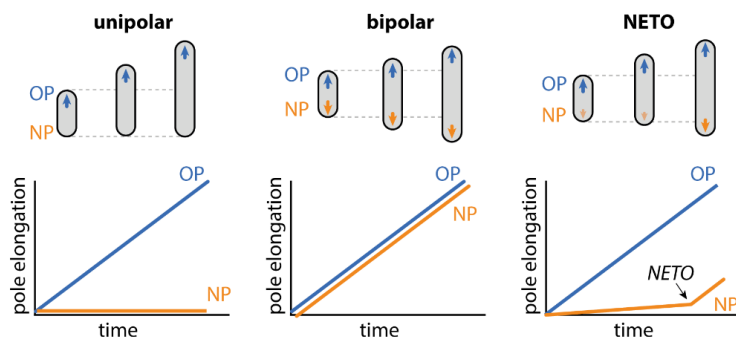


**Figure 13: Unipolar, bipolar, and NETO pole growth models in mycobacteria.**

Schematic representation of the elongation curves for the old pole (OP, blue) and the new pole (NP, orange) of a cell from birth (division of the mother cell) to division, according to the unipolar<sup>7</sup>, bipolar<sup>6</sup>, and NETO models.

We investigated whether NETO growth dynamics might be an artifact caused by the experimental conditions we used for time-lapse AFM. As a comparison, we analyzed data obtained by phase-contrast microscopy of bacteria growing in a microfluidic device using the same experimental conditions under which bipolar growth was previously reported<sup>6</sup>. In this device, the cells are sandwiched between a glass coverslip and a semipermeable membrane, which constrains them to grow in the imaging plane while providing a continuous supply of nutrients. Separation of newly divided sibling cells can be difficult to observe in diffraction-limited phase-contrast microscopy images. However, time-lapse AFM images revealed that division was accompanied by an abrupt snapping movement of the sibling cells away from each other by  $\sim 100$  nm on average (Figure S 5a). Based on the insights provided by our AFM experiments, we developed an algorithm using differential image processing to identify the snapping separation of sibling cells in phase-contrast microscopy images by measuring the differences between consecutive frames (Figure S 5b). We then used morphological features that were visible by phase-contrast microscopy on a minority of cells (e.g., bent cells, constrictions) as low-precision fiducial markers to measure the elongation of individual cell poles (Figure S 5c). Our results with phase-contrast microscopy confirmed that newborn cell



poles grow with biphasic NETO dynamics, in agreement with the results we obtained in AFM time-lapse experiments (Figure S 5d). We conclude that NETO growth dynamics are not an artifact caused by the experimental conditions that we use for time-lapse AFM imaging. Moreover, our AFM time-lapse data allowed us to validate a new and more accurate method to measure pole elongation from birth to division using diffraction-limited optical time-lapse images.

### **NETO is not due to release of physical constraints on poles**

We hypothesized that the lag phase between birth and NETO might result from spatial constraint inhibiting growth of the new cell pole, since newborn cells remain in physical contact for some time after cell division (Figure 14a). We relieved this spatial constraint by using the AFM cantilever tip to mechanically lyse or physically displace one cell in a pair of siblings (Figure S 6). Neither of these manipulations eliminated the lag phase between new-pole birth and NETO (Figure 14b,c). Conversely, inverting the orientation of a cell in order to bring its old pole into physical contact with another cell pole (Figure S 6) had no impact on the growth dynamics of the old pole, which continued to elongate at the same rate (Figure 14d). We conclude that the spatial constraint imposed by end-to-end physical contact between newborn sibling cells is not responsible for the slow rate of new-pole elongation during the pre-NETO phase.

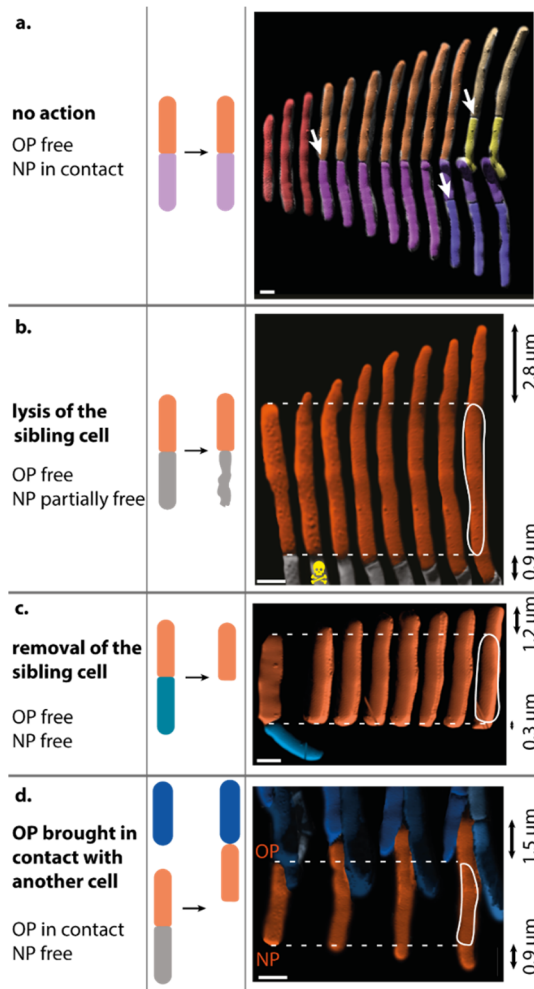


**Figure 14: The pre-NETO phase is not due to physical constraints on new cell poles.**

(a-d) Schematics and corresponding time-lapse AFM of growing *M. smegmatis* cells. Black arrows indicate the cumulated elongation of the old pole (OP) and the new pole (NP). Scale bar, 1  $\mu\text{m}$ . (a) Close contact of new poles of newborn sibling cells is maintained after division of the mother cell (white arrows). (b) Elongation of cell poles after the new pole was partially freed by ablating the turgor pressure in one of the sibling cells using the sharp AFM tip (skull). (c) Elongation of cell poles after the new pole was freed by removal of one of the sibling cells using the AFM cantilever. (d) Elongation of cell poles after the new pole was freed and the old pole was physically obstructed by moving it into contact with other cells using the AFM cantilever.

### Delayed accumulation of Wag31 at the new cell pole

Since the pre-NETO phase is not due to physical constraints on the new cell poles, we investigated whether recruitment of the machinery required for cell wall biogenesis might occur with a delay similar to the duration of the pre-NETO phase. We focused on the Wag31 protein (also known as DivIVa) because it preferentially binds to the cell poles<sup>10,52,53</sup> and functions as a scaffold for recruitment of enzymes responsible for cell wall biogenesis<sup>10</sup>. We measured the progressive accumulation of Wag31 at new cell poles using a strain of *M. smegmatis* expressing a fusion of Wag31 to green fluorescent protein (Wag31-GFP)<sup>6</sup>. Starting from a low level at the time of cell division (about 10% of the final intensity), Wag31-GFP fluorescence at the new cell poles gradually increases before stabilizing, with an average time constant of 2.4 hours (representative curve: Figure 15a; average of 20 poles: Figure S 7; Supplementary Movie 2). On average, Wag31-GFP accumulates to about 70% of its final value before NETO occurs (Figure 15b; Figure S 7).

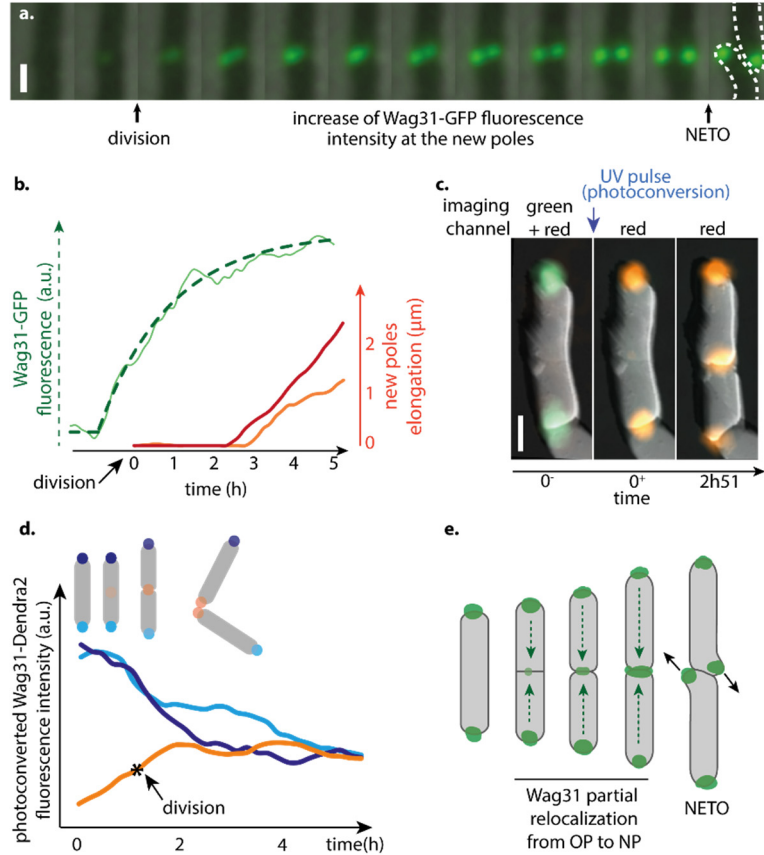


**Figure 15: Wag31 relocalizes from the old to the new pole during the pre-NETO phase.**

(a) Combined time-lapse phase-contrast and fluorescence microscopy of *M. smegmatis* expressing Wag31-GFP. Zoom on the division site showing progressive formation of two elongating new poles. Time between consecutive images is 20 minutes. Scale bar, 1 μm. (b) New-pole elongation curves of two sibling cells (red and orange) and the average of their Wag31-GFP intensities (green). Data are representative of 20 poles (Figure S 7). The *average* intensity rather than *individual* intensity of the two new poles is plotted because their physical proximity precluded individual measurements. Wag31-GFP intensity over time was fitted with an asymptotic exponential function (dotted green line) with a time constant of 1.9 hours (confidence interval 0.26 at 95%), adjusted  $R^2 = 0.98$ . The confidence interval and  $R^2$  value indicate the quality of the fit to the fluorescence curve. (c) Combined time-lapse fluorescence and atomic force microscopy of *M. smegmatis* expressing Wag31-Dendra2 before (0-), just after (0+), and 2 hours 51 minutes after (2h51) UV-induced photoconversion. Scale bar, 1 μm. (d) Evolution of photo-converted Wag31-Dendra2 signal at the new and old cell poles during cell division. Each sibling cell has a new pole (orange) and an old pole (light or dark blue) inherited from the mother cell. (e) Schematic representation of Wag31 relocalization from the old pole to the new pole during and after cell division.

### **Wag31 relocates from old poles to new poles**

Accumulation of Wag31 at the new cell pole during the pre-NETO phase could be due to localization of newly synthesized protein, relocation of existing protein from the old pole to the new pole, or both. To distinguish between these possibilities, we constructed a strain of *M. smegmatis* expressing a fusion of the Wag31 protein to the photo-convertible fluorescent protein Dendra2 (Wag31-Dendra2). We imaged the cells before and after exposure to a pulse of UV light, which irreversibly converts Dendra2 fluorescence emission from green to red<sup>54</sup> (Figure S 8a). Cells born after photo-conversion showed a gradual accumulation of photo-converted (red) Wag31-Dendra2 at the new poles, which was accompanied by a gradual decrease of photo-converted Wag31-Dendra2 at the old poles (Figure 15c,d). These observations suggest that Wag31 partially relocates from the old pole to the new pole in newborn cells. In parallel, non-photo-converted (green) Wag31-Dendra2 gradually accumulated at both the new and old cell poles, presumably due in part to recruitment of newly synthesized protein (Figure 15c,d). As a consequence of these dynamics, the total amount of Wag31-Dendra2 increased over time at new cell poles while remaining more or less constant at old cell poles. In subsequent generations, photo-converted Wag31-Dendra2 continued to redistribute between the old and new cell poles (Supplementary Movie 3). Non-dividing cells exhibited a relatively stable signal of photo-converted Wag31-Dendra2 over time, which confirms that the amount of photo-bleaching was low. In contrast, dividing cell lineages exhibited a lower photo-converted Wag31-Dendra2 signal per pole due to repartition of photo-converted Wag31-Dendra2 between a larger number of poles (Figure S 8b,c). We conclude that Wag31 partially relocates from the old pole to the new pole during the pre-NETO phase (Figure 15e).

### **NETO timing does not scale with the interdivision time**

In *M. smegmatis*, cell division and NETO are independent events characterized by different time intervals, although on average the pre-NETO time is only slightly shorter than the interdivision time (Figure 12). We asked whether NETO dynamics are also characteristic of other mycobacterial species and whether the pre-NETO time scales with the interdivision time. Due to biosafety constraints, we were unable to use AFM to measure single-cell growth in pathogenic mycobacteria. As discussed above, we used AFM-based imaging of *M. smegmatis* to develop a differential image processing method to interpret diffraction-limited optical time-lapse images with improved accuracy (Figure S 5). We used this method to measure polar growth of pathogenic mycobacteria with optical time-lapse microscopy.

The interdivision time of the human pathogen *M. tuberculosis* is, on average, about six times longer than the interdivision time of *M. smegmatis*<sup>6,55</sup>. Similar to *M. smegmatis*, we found that new-pole growth in *M. tuberculosis* displays NETO growth dynamics, with an initial slow-growth phase of variable duration followed by a fast-growth phase (Figure 16a). We also observed NETO dynamics (Figure S 10) in *M. abscessus* and *M. marinum*. In *M. smegmatis*, most poles (70%) initiate NETO during the second half of the cell cycle (Figure 6c). In a small minority of poles (10%), NETO occurs early, in the first half of the cell cycle. Since the pre-NETO time is only slightly smaller on average than the interdivision time in *M. smegmatis*, NETO occurs after division for a minority of cells (about 20%), when the pole is no longer “new”. In the slow-growing mycobacteria *M. marinum* and *M. tuberculosis*, the pre-NETO time is much smaller than the interdivision time, and NETO always occurs before division (Figure 16b,c).

Unexpectedly, the duration of the lag phase between birth and NETO is only twice as long in *M. tuberculosis* compared to *M. smegmatis*: on average,  $6.2 \pm 2.2$  hours in a population of cells growing with an average interdivision time of  $16.3 \pm 3.1$  hours (Figure S 10). As a consequence, *M. smegmatis* exhibits asymmetric polar growth during 80% of the cell cycle on average, whereas *M. tuberculosis* grows asymmetrically during only 40% of the cell cycle on average (Figure 16c). Similarly, NETO occurs in the second half of the cell cycle (60% on average) in fast-growing *M. abscessus*, and in the first half of the cell cycle (30% on average) in slow-growing *M. marinum* (Figure 16c). We conclude that the lag phase between pole birth and NETO does not scale strictly with the interdivision time in mycobacteria (Figure 16b,c; Figure S 9; Figure S 10), and the ratio between the pre-NETO time and the interdivision time is variable and determines the degree of growth asymmetry in different species.

Bacterial cells are composed of a combination of newly synthesized material and material inherited from previous generations. We calculated the spatial distribution of aged cell wall material within a cell, and its progression during growth of a microcolony of *M. smegmatis*, based on time-lapse phase-contrast microscopy. Figure 6d shows a microcolony with the cell surface false-colored based on the age of the cell wall (see Methods for details). We found that the composition of aged cell wall material is heterogeneous within the population: some cells are composed mostly of new cell wall material (e.g., cell A in Figure 16d), while other cells are composed mostly of older material (e.g., cell B in Figure 16d). Based on NETO growth dynamics measured in *M. smegmatis* and *M. tuberculosis* (Figure 16c) and assuming symmetric division for simplicity, we calculated the repartitioning of aging cell wall material in the two

species. Based on our calculations, we predict that sibling cells of *M. smegmatis* exhibit greater cell-to-cell heterogeneity in the composition of aged cell wall material compared to *M. tuberculosis* sibling cells (Figure 16e). We conclude that the ratio between the pre-NETO time and the interdivision time affects the cell-to-cell heterogeneity of cell wall age distribution.

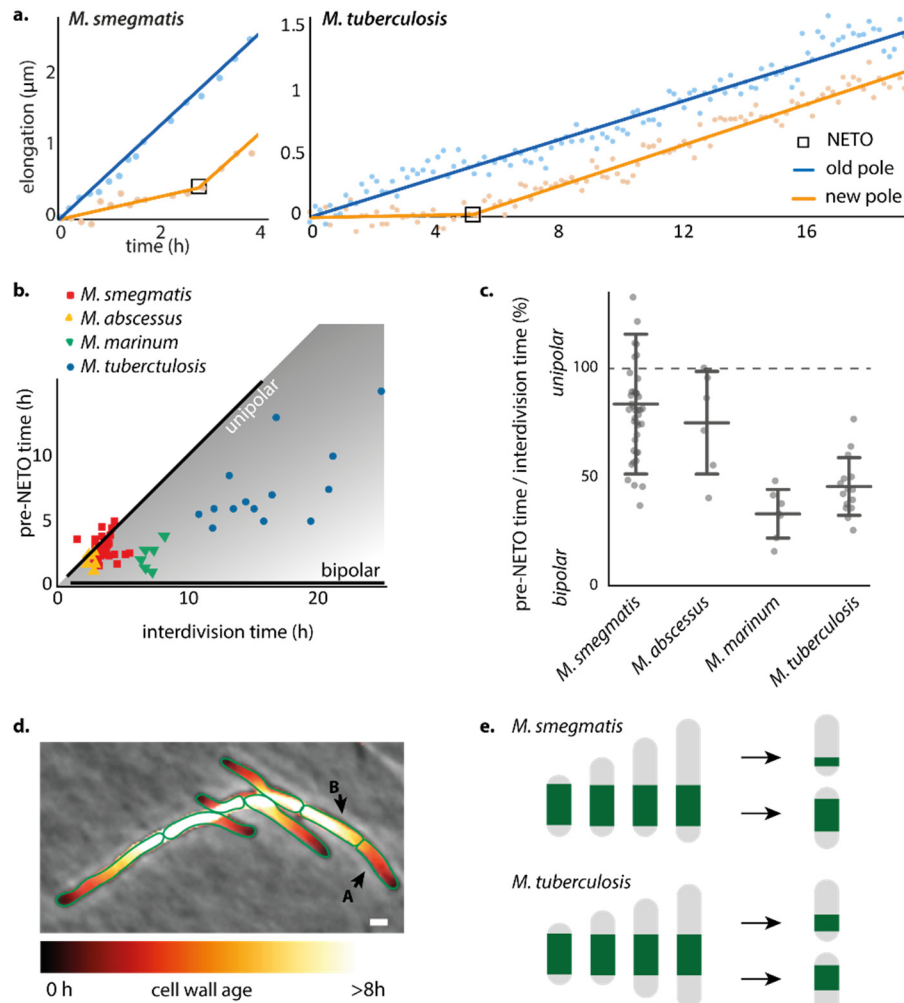


**Figure 16: Species-specific NETO dynamics impart different patterns of asymmetry.**

(a) Elongation dynamics of representative old and new cell poles of *M. smegmatis* and *M. tuberculosis* between birth and division. Points: phase-contrast microscopy data. Lines: linear fit (blue) or bilinear fit (orange). (b) Pre-NETO phase vs. interdivision time in *M. smegmatis* (38 poles), *M. tuberculosis* (14 poles), *M. abscessus* (6 poles), and *M. marinum* (6 poles). Each symbol represents a new cell pole. Black lines indicate the expected pre-NETO time and interdivision time corresponding to unipolar growth or bipolar growth. (c) Asymmetry of old-pole and new-pole growth between birth and division in individual cells of *M. smegmatis*, *M. abscessus*, *M. marinum*, and *M. tuberculosis*, expressed as the ratio (pre-

NETO time)/(interdivision time). Bars indicate averages and standard deviations. (d) Calculated spatial pattern of cell wall age for individual cells within a microcolony of *M. smegmatis* based on time-lapse phase-contrast microscopy. (e) Calculation of the partitioning of cell wall material inherited by the daughter cells from the original mother cell in *M. smegmatis* (top) and *M. tuberculosis* (bottom), based on the average values calculated from the experimental data in panel (c) and assuming symmetric division for simplicity.

## B.5. Discussion

Two models of single-cell growth have previously been proposed in mycobacteria: a unipolar model, in which the new cell pole grows slowly (or not at all) between birth and division, and a bipolar model in which both poles (old and new) grow at the same rate after birth<sup>8</sup>. By measuring the growth of each cell pole with unprecedented precision using time-lapse AFM, we find that single-cell growth is neither strictly unipolar nor bipolar; rather, we find that new-pole growth follows biphasic NETO (“new end take off”) dynamics, in which the new pole initiates fast growth after a delay.

In a recent study, Botella et al. used pulse-labeling with fluorescent peptidoglycan precursors and snapshot microscopy to measure the amount of peptidoglycan synthesis at cell poles as a function of cell length, on the assumption that cell length corresponds roughly with cell cycle position<sup>39</sup>. In *M. smegmatis*, they reported a fast rate of peptidoglycan synthesis at one of the cell poles and a slow rate of synthesis at the other cell pole across the whole range of cell lengths. In contrast, they reported that, in *M. tuberculosis*, the rate of peptidoglycan synthesis is lower at one of the cell poles for short cells but is similar at both poles for long cells. Based on this analysis, they proposed that *M. smegmatis* and *M. tuberculosis* exhibit different modes of pole elongation, as reflected in their distinct spatiotemporal dynamics of cell wall peptidoglycan synthesis, although they did not measure cell growth *per se*, nor could they distinguish between old and new cell poles<sup>39</sup>. Our results using time-lapse AFM and optical microscopy to measure cell growth directly are partly consistent with their findings. In *M. tuberculosis*, smaller cells are more likely to be at an earlier time point in the cell division cycle, and therefore the new pole is more likely to be in the pre-NETO phase and to grow slowly. In *M. smegmatis*, NETO occurs, on average, only shortly before division; thus, in the majority of cells one pole (the old pole) grows rapidly for the entire duration of the cell division cycle, while the other pole (the new pole) grows rapidly for only a fraction of the cell cycle just before division. However, we found that NETO in *M. smegmatis* can, in rare cases, occur long before division or, conversely, after division. These results establish that NETO and division are

temporally distinct events in both *M. smegmatis* and *M. tuberculosis*. Comparing the dynamics of pole growth in fast-growing and slow-growing *Mycobacterium* species, we conclude that the dynamics of pole growth are fundamentally the same and we propose a unifying model based on our observation that all of the four species we tested display NETO pole dynamics with a pre-NETO lag phase of variable duration.

Biphasic NETO dynamics seem to be a general characteristic of single-cell growth in mycobacteria. The question arises, why do mycobacteria initiate growth of a newly formed pole only after a lag phase? One possibility is that the lag phase corresponds to a period required for “maturation” of the new pole before it can initiate growth<sup>39</sup>. It is, however, unlikely that the maturation phase is an absolute requirement, as initiation of growth from a newly formed pole has been observed immediately after division in a morphologically abnormal strain of *M. smegmatis*<sup>10</sup>. It has been proposed that asymmetric growth has evolved by natural selection because it increases cell-to-cell phenotypic heterogeneity, which may increase overall evolutionary fitness<sup>56</sup>. Consistent with this idea, it was recently shown that deletion of the *lamA* gene in *M. smegmatis* decreases the asymmetry of polar growth as well as survival during exposure to the antibiotic rifampicin<sup>9</sup>. However, we find that polar growth is less asymmetric in slow-growing species (e.g., *M. tuberculosis*) compared to fast-growing species (e.g., *M. smegmatis*), because the pre-NETO time does not scale in proportion to the duration of the cell cycle.

What is the mechanistic basis for NETO pole growth dynamics? In fission yeast, it has been shown that application of a high external mechanical force on the cell poles can counteract the forces driving pole extension, thereby inducing growth arrest<sup>57</sup>. We considered the possibility that pole-to-pole contact forces remaining after cell division might inhibit mycobacterial new-pole extension during the pre-NETO phase. However, we find that physical separation of daughter cells immediately after division of the mother cell, using the AFM cantilever, does not eliminate the lag phase. These results rule out the possibility that pole-to-pole contact forces alone are responsible for NETO growth dynamics in mycobacteria.

In fission yeast, it is thought that NETO might reflect the initiation of repartitioning of Cdc42 from the old pole to the new pole<sup>58,59</sup>, although the actual determinants of elongation speed remain unknown<sup>60</sup>. In mycobacteria, polar insertion of new cell wall material is thought to be directed by Wag31, and it has been proposed that accumulation of Wag31 at the new cell pole may be rate-limiting for pole growth<sup>10,61,62</sup>. Consistent with this idea, we found that Wag31



gradually accumulates at the new cell pole prior to NETO due, in part, to relocalization of Wag31 from the old pole to the new pole. However, it remains to be proven whether Wag31 accumulation above a certain threshold actually serves as a trigger for NETO. In other bacteria, relocalization of proteins from one pole to the other can occur on fast timescales. For example, proteins of the Min system in *E. coli* oscillate from one pole to the other with a periodicity of about 50 seconds<sup>63</sup>, and pole-to-pole equilibration of the Wag31 homolog DivIVa in *B. subtilis* takes only about five minutes<sup>64</sup>. These kinetics are much faster than the rate of Wag31 equilibration between the old and new cell poles in *M. smegmatis*, which is about three hours on average, as shown here. This striking difference suggests that *M. smegmatis* Wag31 and *B. subtilis* DivIVa might have different intrinsic dissociation constants at the poles, or that species-specific regulatory proteins might control the rate of dissociation from the old pole or association to the new pole, such as PonA1<sup>65</sup> and LamA<sup>9</sup> in *M. smegmatis*. It has been shown recently that deleting the lamA gene decreases growth asymmetry between the two cell poles and increases recruitment of Wag31 to the division septum (and, therefore, to the future new cell poles)<sup>9</sup>. As LamA localizes to the septum<sup>9</sup>, it might reduce the association constant of Wag31 to the new pole, thereby slowing recruitment of Wag31 from the old pole to the new pole.

This study has revealed an unexpected similarity of pole growth dynamics between mycobacteria and fission yeast, which are separated by billions of years of evolution<sup>66</sup>. It seems unlikely *a priori* that this striking similarity reflects the conservation of molecular mechanisms that evolved prior to the divergence of these organisms. This raises the intriguing possibility that NETO growth dynamics may reflect underlying biophysical and mechanical constraints associated with polar growth of rod-shaped organisms that divide by binary fission. In the future, it will be interesting to determine whether NETO growth dynamics are a general characteristic of pole-growing microorganisms, which are found in taxonomically diverse phyla including the Actinobacteria, Proteobacteria, and Ascomycota<sup>35,51</sup>.

## B.6. Methods

### Bacterial strains and growth conditions

*Mycobacterium smegmatis* mc<sup>2</sup>155 (wild-type), *Mycobacterium tuberculosis* Erdman (wild-type), *Mycobacterium abscessus* DSM2 (wild-type), *Mycobacterium marinum* M (wild-type), and derivative strains were grown in Middlebrook 7H9 liquid medium (Difco) supplemented with 0.5% albumin, 0.2% glucose, 0.085% NaCl, 0.5% glycerol, and 0.05% Tween-80. Cultures were grown at 37°C (30°C for *M. marinum*) to mid-exponential phase, corresponding to an optical

density at 600 nm (OD<sub>600</sub>) of ~0.5. Aliquots were stored in 15% glycerol at -80 °C and thawed at room temperature before use; individual aliquots were used once and discarded. The strain expressing a Wag31-GFP fusion protein has been described previously<sup>6</sup>. The reporter strain expressing a Wag31-Dendra2 fusion protein was constructed using the Gibson assembly NEBuilder HiFi DNA Assembly Master Mix (New England Biolabs) according to the manufacturer's protocol. The *dendra2* open reading frame, minus the start codon, was PCR-amplified from pGEX6P-1-Dendra2 (a gift from Periklis Pantazis; Addgene plasmid # 82436<sup>67</sup>) using primers *dendra2\_wo\_STARTF* (AGT TCA ACC GCG GCA ACA ACA ACA CCC CGG GAA TTA ACC) and *dendra2\_wo\_STARTR* (GGC CAT TGC GAA GTC ATT ATT TAC CAC ACC TGG CTG GG) and joined by Gibson assembly to the integrative plasmid pIS220<sup>6</sup>, which was PCR-amplified using primers *pIS220\_wag\_F* (ATA ATG ACT TCG CAA TGG CCA AG) and *pIS\_wag\_R* (GTT GTT GCC GCG GTT GAA C). The resulting plasmid was confirmed by restriction digestion and DNA sequencing. The Wag31-Dendra2-expressing plasmid was integrated at the chromosomal *attB* site by electroporating a wild-type strain of *M. smegmatis* with 1–2 µg of plasmid DNA and selecting transformants on 7H10 plates containing 50 µg ml<sup>-1</sup> kanamycin.

### **Time-lapse optical microscopy**

For time-lapse optical microscopy, bacteria were cultured in a custom-made microfluidic device with a continuous flow of 7H9 medium<sup>5,6</sup>. Bacteria were imaged with a DeltaVision personalDV microscope (Applied Precision) equipped with a 100X oil immersion objective and an environmental chamber maintained at 37°C (30°C for *M. marinum*). Images were recorded on phase-contrast and fluorescence channels (490/20-nm excitation filter and 528/38-nm emission filter for GFP, 575/25-nm excitation filter and 632/60-nm emission filter for mCherry) with a CoolSnap HQ2 camera.

### **Time-lapse atomic force microscopy (AFM)**

An aliquot from an exponential-phase culture of *M. smegmatis* was pipetted onto a PDMS-coated glass coverslip<sup>16</sup>, mounted in a custom-made coverslip holder with a built-in heating unit<sup>17</sup>, and incubated at 37°C without agitation for ~15 minutes to allow attachment. Unattached bacteria were removed by rinsing the coverslip surface with 7H9 before imaging. The sample was maintained at 37°C during imaging using the coverslip heating holder controlled by a TC200 temperature controller (Thorlabs). AFM images were recorded using a customized Icon AFM (Bruker) that was mounted above an inverted optical microscope.

Images were recorded at  $\approx 0.5$  Hz line rate using ScanAsyst Fluid cantilevers (Bruker) with a nominal spring constant of  $0.7 \text{ N m}^{-1}$  in PeakForce quantitative nanomechanical mode (QNM) at an oscillation rate of 1 kHz and a force setpoint  $< 2 \text{ nN}$ . Fluorescence images were acquired with an EMCCD iXon Ultra 897 camera (Andor) mounted on an IX81 inverted optical microscope (Olympus) equipped with a 100X oil immersion objective. Illumination was provided by a mercury lamp (U-HGLGPS, Olympus). The AFM was mounted above the inverted microscope and the AFM laser was switched off while acquiring fluorescence images.

### **Processing of AFM images**

Standard scanning probe software (Gwyddion<sup>68</sup>, Nanoscope Analysis) was used to process AFM images. Images were scaled and aligned using Fiji<sup>69</sup> and the StackReg plugin<sup>70</sup>. The area of interest was cropped, and a montage was generated from the time-series stacks to show consecutive images side by side. A false color was assigned to the background and to each individual bacterium with Photoshop. 3D renderings were made using Fiji, using the AFM height channel for topography and the AFM error channel as an overlay.

### **Photo-conversion of Wag31-Dendra2**

Photo-conversion of Wag31-Dendra2 was induced with UV light using the excitation channel of a DAPI filter cube (417-477 nm) with 500 milliseconds of exposure time. Subsequent imaging was performed only in the red channel unless specified otherwise, to avoid additional photo-conversion over time.

### **Pole elongation measurement with time-lapse AFM**

For obtaining pole elongation curves from AFM data, the distance between the pole and the closest immobile surface structure (fiducial marker) was manually measured using Fiji (Figure 11c; Figure S 2). When the reference was changed from one fiducial marker to another, the distance between the old and the new fiducial markers was added as an offset to subsequent values. As the surface structures are inherited by the daughter cells from the mother cell, elongation of a given pole can be measured over several generations.

### **Pole elongation measurement with time-lapse phase microscopy**

The timing of sibling-cell separation was defined in the phase-contrast microscopy data by identifying the abrupt (frame-to-frame) displacement of the two sibling cells along their longitudinal axes (Figure S 5). StackReg<sup>70</sup> was used to align individual bacteria over time using

cell shape. Pole elongation was measured with a similar method as with AFM data, using details in cell shape as a fiducial marker instead of the surface nanostructures resolved by AFM (Figure S 5).

#### **Bilinear fitting of pole elongation data**

Pole elongation data were fitted with a bilinear curve with a custom MATLAB (R2018a) script, using the MATLAB *fminsearch()* function with four fitting parameters: the timing of the NETO event, the growth speed before NETO, the growth speed after NETO, and an offset.

#### **Calculation of cell wall age distribution in a microcolony**

To compute the cell wall age distribution, we chose a microcolony of bacteria that did not move relative to each other over time. A threshold was applied to separate the cells from the background with Fiji<sup>69</sup>. The binary images were summed to obtain a 2D intensity map indicating the cell wall age distribution for each bacterium within the microcolony.

### **B.7. Acknowledgements**

This research was supported in part by grants to G.E.F. from the Swiss National Science Foundation (205321\_134786 and 205320\_152675), from the European Union FP7/2007-2013/ERC under Grant Agreement No. 307338-NaMic, from the Commission for Technology and Innovation under CTI no. 18330.1 PFNM-NM, and by a grant to J.D.M. from the Swiss National Science Foundation (310030B\_176397). H.A.E. was supported by an EMBO Long Term Fellowship (191-2014) and an EMBO Advanced Long Term Fellowship (750-2016). C.T. was supported by funding from the European Union's Horizon 2020 research and innovation program under the Marie Skłodowska-Curie grant agreement No. 665667.

### **B.8. Author contributions**

M.T.M.H., J.D.M., G.E.F. conceptualized the study. M.T.M.H., H.A.E. developed imaging protocols. M.T.M.H., J.D.M., G.E.F. designed the experiments. M.T.M.H., J.X.Y.V., C.T., G.V. performed the experiments. M.T.M.H. analyzed the data. M.T.M.H., H.A.E., J.D.M., G.E.F. wrote the manuscript.

### **B.9. Supplementary Figures**

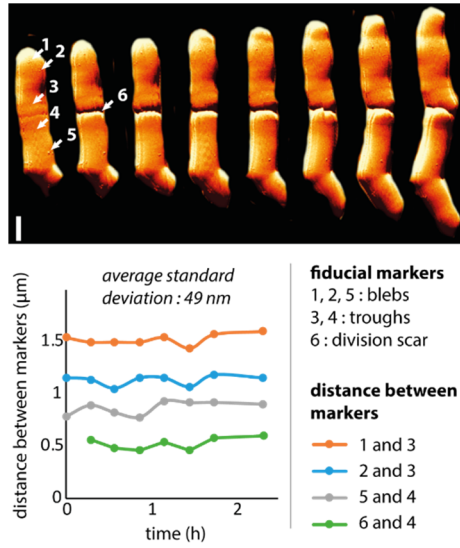


**Figure S 1: Surface nanostructures resolved by AFM can be used as fiducial markers.**

Top panel: AFM time-lapse images of a mother cell and its two daughters. Arrows point to surface nanostructures: blebs (markers 1, 2, 3), wave-troughs (markers 3, 4), and a division scar (marker 6). Scale bar, 1 μm. Bottom panel: Distance between several cell-surface markers and an arbitrarily chosen marker on the same cell (point 3 for the top cell, point 4 for the bottom cell). The distance between markers on the same cell remains constant over time (average standard deviation: 49 nm).

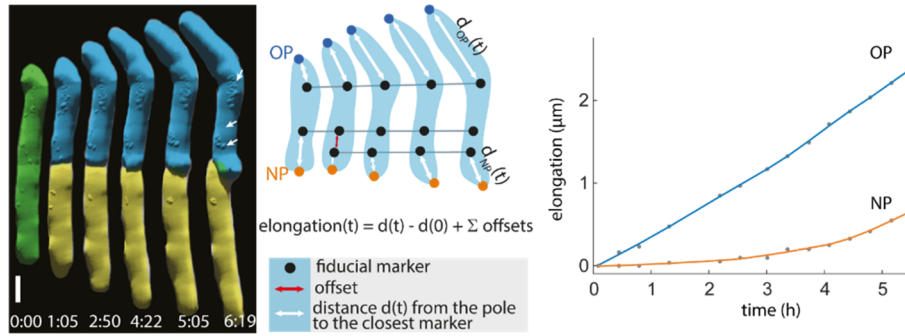


**Figure S 2: Absolute measurement of pole elongation with AFM using surface nanostructures as fiducial markers.**

Left panel: AFM time-lapse images of a mother cell (green) and its two daughters (blue and yellow). Scale bar, 1 μm. Center panel: Schematic representation of the methodology used for measuring pole elongation over time using surface nanostructures as fiducial markers. The elongation of a given pole  $d(t)$  is equal to the distance between the pole and the closest fiducial marker (white arrows), plus the cumulated offsets (red arrow) to compensate for switching between different fiducial markers when necessary, minus the initial distance between the pole and the closest marker. Right panel: Corresponding elongation curves for the old pole (OP) and the new pole (NP).

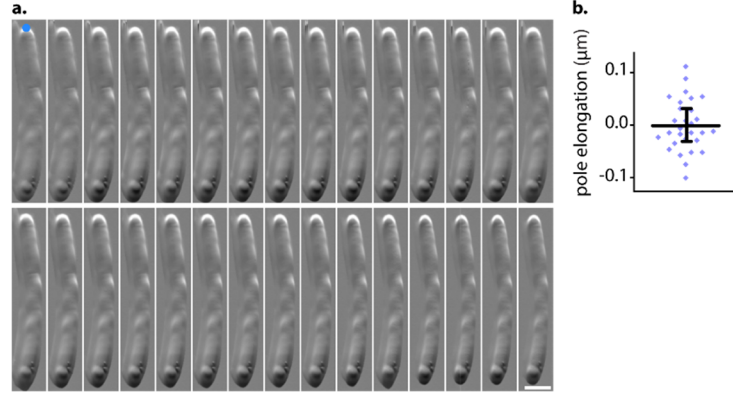


**Figure S 3: Precision of single-cell measurements using AFM.**

(a) AFM time-lapse images of a non-growing cell over 15 hours. Blue point: Cell pole used for the measurement. Scale bar, 1  $\mu\text{m}$ . (b) Distribution of the measured pole elongation. Each blue point corresponds to a time point in (a). Bars indicate the average and the standard deviation. Standard deviation: 49 nm.

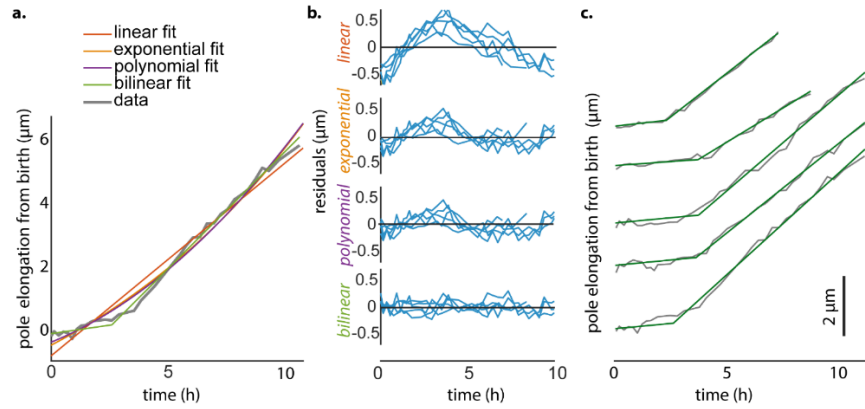


**Figure S 4: Model for pole elongation dynamics.**

(a) Elongation of a pole measured from pole birth (grey) fitted with a linear model (red, equation:  $y=a \cdot x+b$ ), an exponential model (orange,  $y=a+b \cdot \exp(c \cdot x)$ ), a polynomial model (purple,  $y=a \cdot x^2+b \cdot x+c$ ), or a bilinear model (green). (b) Residuals (difference between data and fit) for the four fitting models introduced in (a) and for the elongation of five representative cell poles measured with AFM from pole birth over at least seven hours. Residuals that are systematically positive or systematically negative for much of the data range indicate that the model is a poor fit to the data. Residuals that appear randomly scattered around zero indicate that the model describes the data well<sup>71</sup>. (c) Pole elongation of five representative poles measured with AFM (grey), fitted with a bilinear model (green).

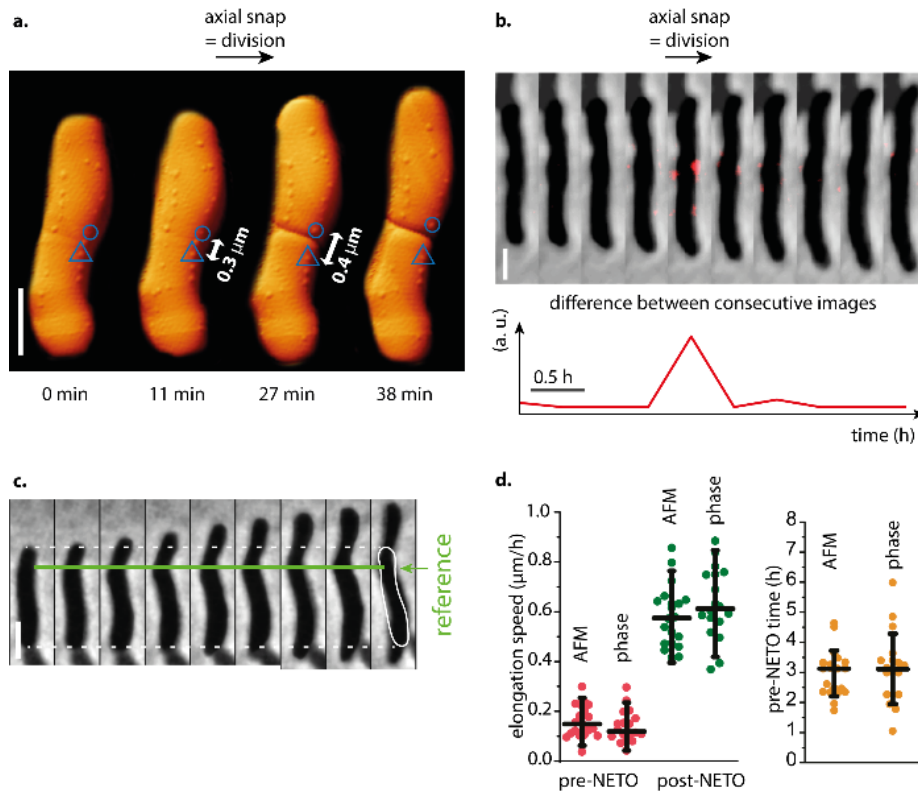


**Figure S 5: Measurement of pole elongation by phase-contrast microscopy requires a fiducial marker and accurate detection of cell division.**

(a) Time-lapse AFM illustrating cell division. Blue shapes indicate two surface nanostructures, one inherited by each sibling cell, used as fiducial markers to reveal the axial snap during division. Scale bar, 1  $\mu\text{m}$ . (b) Time-lapse phase-contrast microscopy (top panel) and corresponding graph (bottom panel) of the differences between consecutive images (red), revealing the axial snap associated with division. Scale bar, 1  $\mu\text{m}$ . (c) Time-lapse phase-contrast microscopy of a single cell from birth (first image) to division (last image). Images were aligned using a kink in cell shape as a fiducial marker (green line), which was used to measure absolute pole elongation over time as for AFM data in Figure 1. Division was detected using the axial snap, as defined in panel (b). Scale bar, 1  $\mu\text{m}$ . (d) Elongation speed before and after NETO and duration of the pre-NETO phase measured with AFM (20 poles) or phase-contrast microscopy (18 poles). Bars indicate average values and standard deviations. The differences between AFM and phase-contrast microscopy measurements are not statistically significant (two-sided t-test; at 0.05 level, when equal variance is not assumed, the difference is not statistically different from 0).

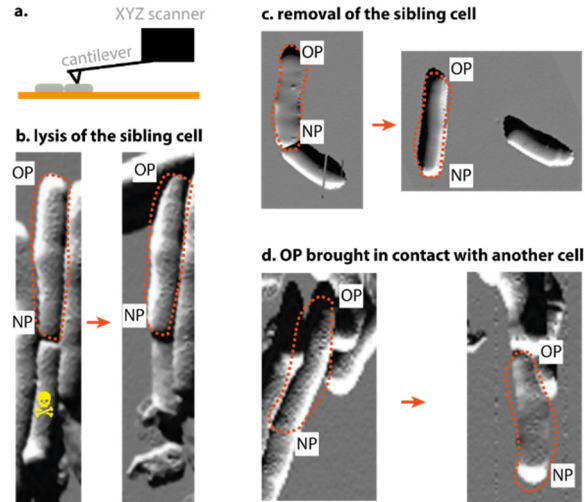


**Figure S 6: The AFM cantilever tip can be used to lyse or displace cells.**

(a) Schematic of the AFM cantilever applying a force to a mycobacterial cell surface and demonstrating the use of an AFM cantilever as a nano-mechanical manipulating tool. (b-d) AFM images, error channel. The observed cell is highlighted with a dotted orange line. (b) Lysis of one of the sibling cells (marked with a skull). See Figure 4b. (c) Displacement of one sibling cell. See Figure 4c. (d) Inversion of the orientation of one of the sibling cells in relation to its neighbors. The old pole (OP) is brought into contact with other cells while the new pole (NP) is removed from contact with other cells. See Figure 4d.



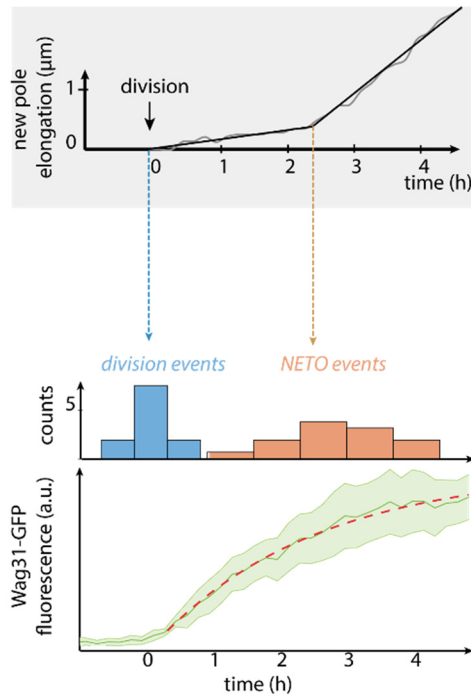


**Figure S 7: NETO is associated with an accumulation of Wag31-GFP at the new pole.**

Elongation measured by time-lapse phase-contrast and fluorescence microscopy of *M. smegmatis*. Top panel: Representative example of new pole elongation dynamics. Middle panel: Binned cell division events and NETO events, extracted from pole elongation curves (20 poles). Bottom panel: Median and standard deviation of the accumulation of Wag31-GFP over time at new poles (20 poles). Dotted red line is an exponential fit of the median values. Time constant ( $\tau$ ) = 2.4 hours. Adjusted  $R^2$  = 0.99.

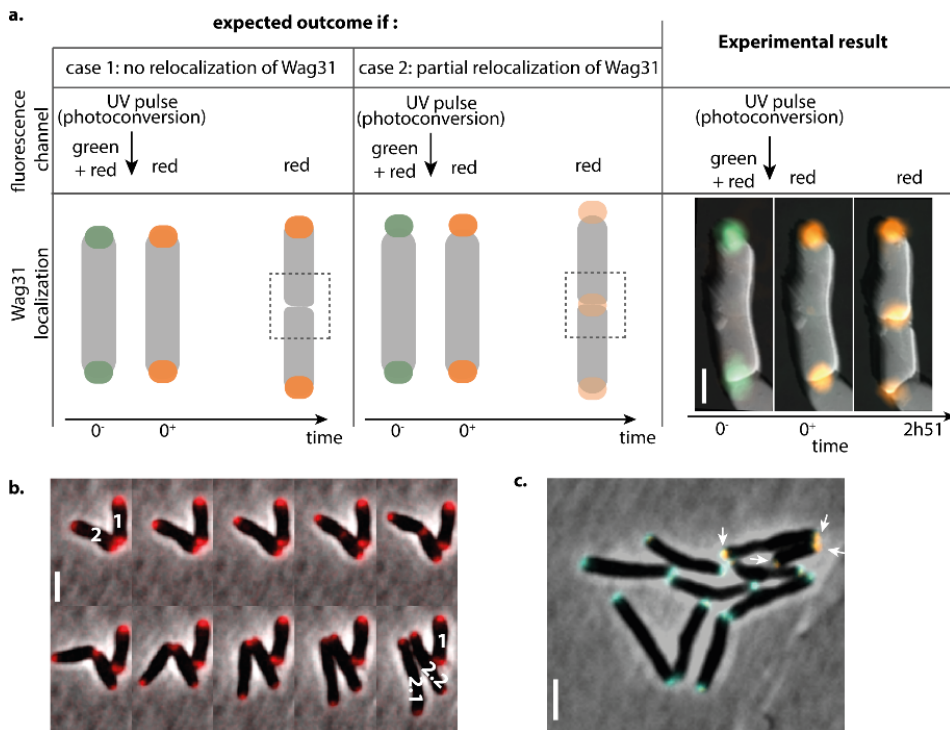


**Figure S 8: Relocalization of Wag31-Dendra2 from old to new poles measured using photo-conversion fluorescence microscopy.**

(a) Schematic of the expected experimental results if Wag31 is initially present at the old pole and remains there (case 1), or if Wag31 relocates from the old to the new pole (case 2). Comparison with the experimental results obtained by correlated fluorescence and atomic force microscopy (see Figure 5c). Scale bar, 1  $\mu\text{m}$ . (b) Combined phase-contrast and fluorescence time-lapse imaging of photo-converted Wag31-Dendra2 (red) in dividing (cell 2) and non-dividing (cell 1) sibling cells. The photo-converted signal remains relatively stable over time in the non-dividing sibling, suggesting that the gradual decrease of the photo-converted signal in the dividing sibling is due to dilution rather than photo-bleaching. Scale bar, 2  $\mu\text{m}$ . (c) Snapshot of combined phase-contrast and fluorescence microscopy from a time-lapse series. The poles marked with white arrows belong to two daughters of a mother cell that grew slowly after photo-conversion. The green poles belong to eight great-granddaughters of a mother cell that grew normally after photo-conversion. Photo-converted (red) signal at the poles depends on the dilution over the generations and is not necessarily proportional to the non-photo-converted (green) signal. Scale bar, 2  $\mu\text{m}$ .

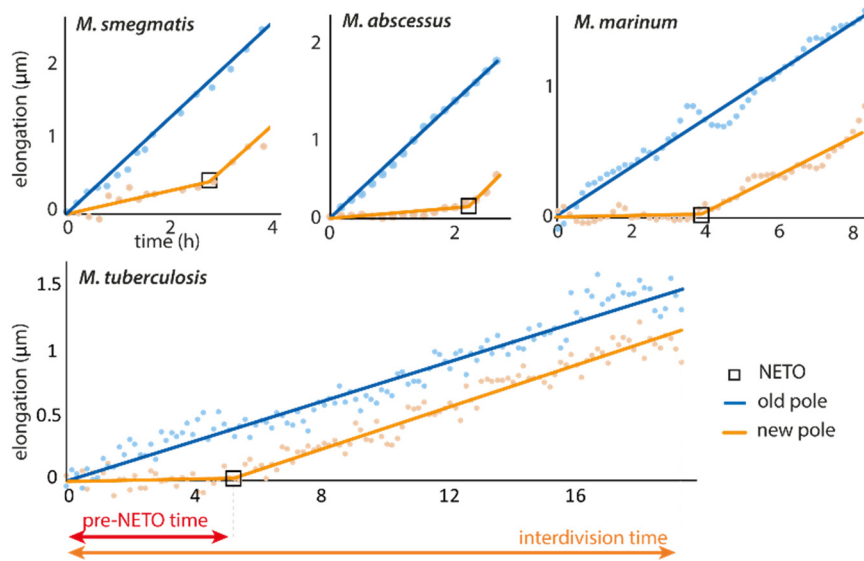


**Figure S 9: NETO growth dynamics are observed in fast-growing and slow-growing *Mycobacterium* species.**

Representative elongation curves for the old pole (blue) and new pole (orange) of a cell between birth and division. NETO (black square) was observed in the four tested species, which include both fast-growers (*M. smegmatis* and *M. abscessus*) and slow-growers (*M. marinum* and *M. tuberculosis*). Points: phase-contrast microscopy data. Blue lines: linear fit. Orange lines: bilinear fit.

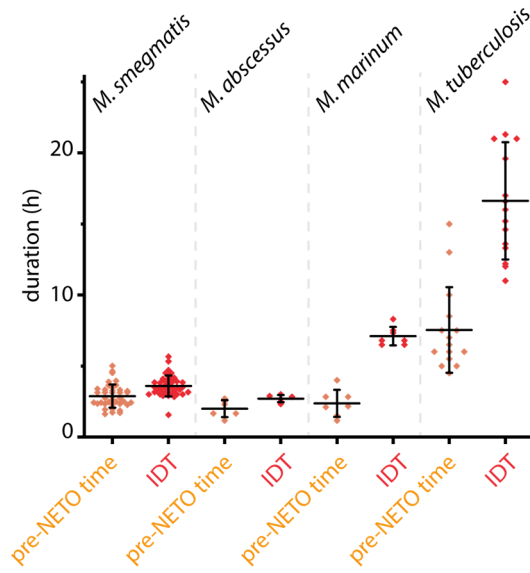


**Figure S 10: The duration of the pre-NETO phase does not scale in proportion to the interdivision time in *Mycobacterium* species.**

Distributions of the duration of the pre-NETO phase and the interdivision time (IDT) for fast-growing (*M. smegmatis* and *M. abscessus*) and slow-growing (*M. marinum* and *M. tuberculosis*) mycobacteria. Each point corresponds to a single pole. Bars indicate averages and standard deviations.



# ***Chapter C*** Mapping the topography and mechanical properties during pole growth of a rod-shaped microorganism

## **C.1. Preamble**

In the previous chapter (Chapter B), we report a surprising similarity between the growth dynamics of mycobacteria and fission yeast, which hints at shared mechanisms for tip growth in evolutionarily distant pole growing organisms. With the current protocol developed for imaging mycobacteria used in Chapter B, the cells are imaged from the side, and we do not have images of the pole itself, which is the site where new material is inserted for cell growth.

In this chapter, we develop a method for imaging the pole of a growing rod-shaped microorganism, and show time-lapse AFM images of the topography and local mechanical properties of a growing fission yeast pole.

My contribution to this chapter is the general idea of vertical trapping for pole imaging with AFM and part of the supervision of the project. The protocol was developed by Camille Roche, as her master thesis, and myself, based on a similar method for optical imaging of vertical fission yeast<sup>72</sup> and bacteria<sup>73</sup>. Camille Roche and I imaged the growing poles with AFM and processed the data.

I would like to thank Prof. Sophie Martin and Veneta Gerganova for providing the yeast cells and growth medium, for general support for working with fission yeast cells, as well as for useful discussion.

## **C.2. Introduction**

Numerous living organisms form elongated structures by growing from their tip: root hairs and pollen tubes in plants, axons of neuron in animals, yeast cells, bacterial cells. Some of the tip-growing genus are highly medically relevant, such as Mycobacteria, among which *M. tuberculosis*, which is thought to infect more than 20% of the world population and causing the highest number of death among infectious diseases<sup>74</sup>, and Streptomyces, from which come a large portion of the antibiotics we know<sup>75</sup>. *Schizosaccharomyces pombe* (also called fission yeast) is another tip-growing species, and a widely studied model organisms for cell biology, particularly

for the genetic analysis of cell morphogenesis<sup>76</sup>. We chose to study the poles of fission yeast cells, as a model for pole-growing micro-organisms in general.

Many questions remain about the morphogenesis of tip growing microorganisms, because of the challenges associated with microscopy at sub-micron scale. How do these organisms regulate the time and place for insertion of new material while preserving cell integrity? What controls the NETO transition from slow to fast pole growth in fission yeast<sup>51</sup> and mycobacteria<sup>11</sup>?

Conventional optical microscopy techniques are limited in resolution to 0.2  $\mu\text{m}$  because of fundamental constraints associated to the diffraction of light<sup>77</sup>. The resolution limit of conventional optical microscopes (0.2  $\mu\text{m}$ ) is comparable to the diameter of a bacterium (about 0.8  $\mu\text{m}$ ), which means that higher resolution techniques are desirable for microbiology. Superresolution microscopy techniques can achieve higher resolution, but are often toxic for the cells<sup>15</sup>. With electron microscopy techniques, sub-nanometer resolution images of yeast cell surfaces<sup>78</sup> and bacterial cell envelopes<sup>79</sup> can be obtained. However, electron microscopy is not compatible with live cell imaging because it requires fixing or freezing the sample.

Atomic Force Microscopes (AFM) can image cells surfaces with a nanometer resolution and is compatible with liquid environment and live-cell imaging<sup>80</sup>. Like scanning electron microscopy (SEM), AFM has the advantage of being a label-free technique. Additionally, new AFM modes such as off-resonance tapping (ORT, also called jumping mode and peak force tapping) have been developed to quantify the local mechanical properties of the sample, opening new roads for a better understanding of the physical and mechanical phenomena at play in living organisms<sup>47,81,82</sup>. One can wonder why AFM is not used more frequently compared to scanning electron microscopy. It is possible that the complexity of the instrument plays a role. A major other factor is the difficulty of sample immobilization on a surface<sup>40,83</sup>, which is essential for high resolution AFM imaging. If the sample immobilization is not sufficiently strong, the lateral forces applied during AFM imaging drag the sample during the scanning motion (Figure 1a), resulting in a poor-quality image (Figure 1b). Appropriate immobilization of the sample is therefore essential for AFM imaging.

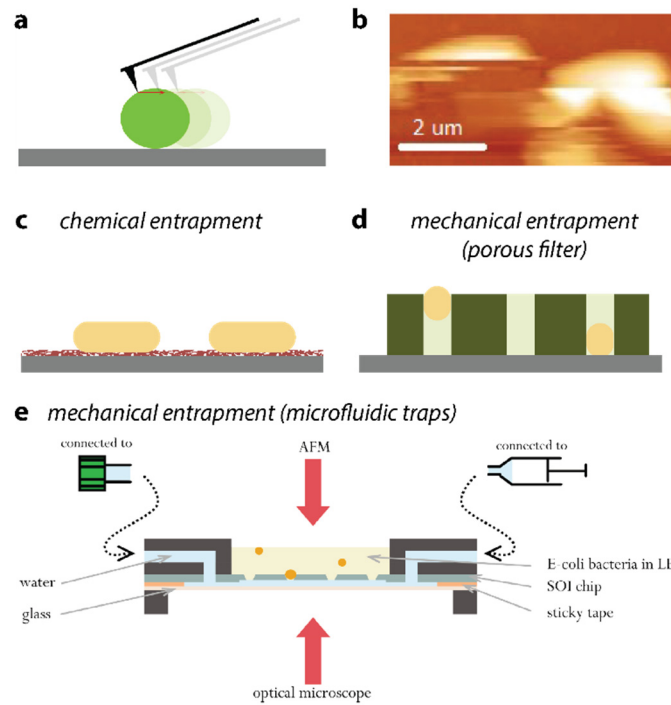


**Figure 17: Sample immobilization methods for atomic force microscopy**

(a) Schematic representation illustrating how the lateral forces applied while scanning can displace a loosely immobilized sample. (b) AFM image of a loosely immobilized sample (*E. Coli*). The sample was scanned from top to bottom. The stripes are due to the motion of the bacteria. (c) Schematic illustrating chemical immobilization<sup>84</sup> of bacteria (yellow) via a coating of the surface (grey) with an adhesive chemical (red). (d) Schematic illustrating mechanical entrapment<sup>85</sup> of bacteria (yellow) in a porous filter (green). (e) Schematic illustrating the immobilization of bacteria with an active microfluidic system<sup>86</sup>.

Several methods have been developed to hold a microorganism while imaging. A coating of poly-L-lysine, cell-tak or other chemical compounds can be used to generate adhesive bonds to the sample<sup>84</sup> (Figure 17c). Chemical immobilization techniques require minimal sample preparation, but are often toxic for the cells: these methods are suited for imaging during a short amount of time, but unsuited for long time-lapse during a whole or several cell cycles. One notable exception is the use of a thin film of PDMS as an adhesive layer to immobilize mycobacteria, which has no observable impact on the bacterial growth rate, possibly because the adhesion is not chemical but due to hydrophobicity<sup>11,16</sup>. Alternatively, mechanical traps are being used to hold the sample during imaging and prevent lateral motion (Figure 17d). The most frequently used mechanical entrapment techniques rely on porous filters<sup>85</sup>. Our group has introduced a more complex method to trap bacteria with a microfluidic chip, allowing for sequential trapping, imaging, and release of bacteria<sup>86</sup> (Figure 17e).

Here we introduce a method for imaging the pole of growing microorganisms with nanometer resolution, and demonstrate its use to study the topography and mechanical properties during the growth of a fission yeast pole.

### **C.3. Results**

#### **Vertical trapping of live rod-shaped cells in agarose microwells for AFM imaging**

To image fission yeast cells poles with AFM, the yeast cells need to be held in a vertical position. We propose a mechanical immobilization method for AFM imaging of cell poles, with agarose microwells. The agarose microwells would need to have a cylindrical shape similar to the shape of a fission yeast cell held vertically (3 to 4  $\mu\text{m}$  in diameter and 7 to 14  $\mu\text{m}$  in length). A very similar method has been developed for optical imaging of fission yeast<sup>72</sup> and bacteria<sup>73</sup>. Because lateral forces are applied during AFM imaging, the diameter of the microwell traps has to be optimized to make sure that the cell remains trapped and immobile while scanning.

We used photolithography and deep reactive ion etching to create vertical cylindrical pillars on a silicon wafer (Figure 18a), with 10 $\mu\text{m}$  height and a diameter of 2.5 $\mu\text{m}$ , 3 $\mu\text{m}$ , 3.8 $\mu\text{m}$  and 4.5  $\mu\text{m}$ . Liquid agarose was poured onto the micropatterned silicon wafer (Figure 18a) to obtain vertical cylindrical microwells (Figure 18a). A lab centrifuge was used to push the fission yeast cells into the agarose traps (Figure 18b, Figure 19). Because the diameter of the wells (2.5 to 4.5  $\mu\text{m}$ ) is similar in size to the average diameter of a cell (3 to 4  $\mu\text{m}$ ), but much smaller than the average length of a cell (7 to 14  $\mu\text{m}$ ), all the trapped cells stand vertically, leaving one of their poles exposed.

Upon loading, half of the accessible poles are old poles (of variable age), and the other half are new poles. To ensure consistency in the results, we chose to image new poles only. After 4 hours of incubation at 32C, the trapped cell will have divided at least once. Because the height of the microwell is smaller than the length of two cells, one of the sibling cell is released in the liquid medium, while the other remains trapped. This ensures that the pole imaged with AFM is a new pole.

Magnets clamp the agarose microwells to a glass slide, which was placed in a custom sample holder for AFM imaging (Figure 18c)<sup>16</sup>. Trapped fission yeast cells were visible on the AFM image (Figure 18d). The cell immobilization was ideal for AFM imaging when the diameter of the well was 3 $\mu\text{m}$ . Smaller wells had a very low loading efficiency. Larger wells were loaded with yeast cells, but the cells were moving during imaging.



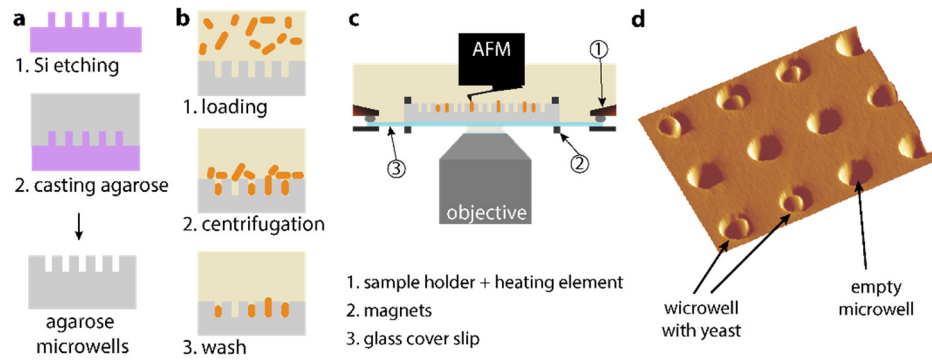


**Figure 18: Vertical trapping of live fission yeast for AFM imaging of the cell pole**

(a) Simplified representation of the process flow for making agarose microwells. (b) Fission yeast loading process into the agarose microwells. (c) Schematic representation of the setup holding the live vertical yeast cells for imaging with a combined AFM-optical setup. (d) 3D AFM image of trapped fission yeast cells. image size: 35x26  $\mu\text{m}$ .

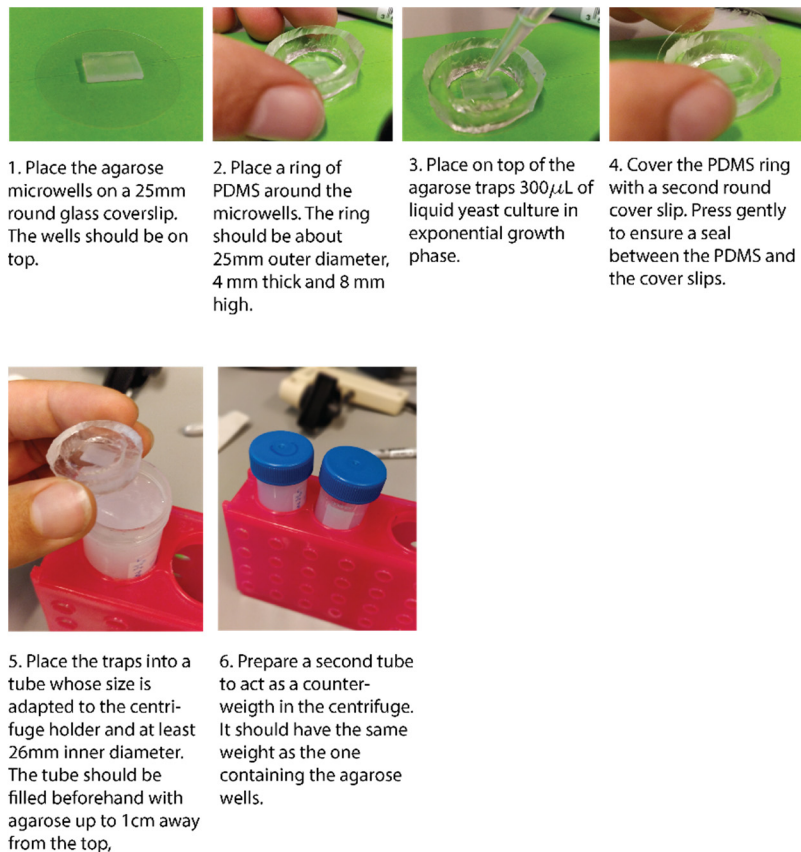


**Figure 19: Procedure for loading fission yeast cells into agarose microwells using a lab centrifuge**

### AFM imaging of cell poles of live fission yeast cells

AFM measures surface topography (*height channel*, *error channel*), but also local mechanical properties using the ORT mode (Figure 20). When imaging a new pole with a force setpoint of 1nN, a round, smooth surface was visible on the topography channel (Figure 20a,b,c). In comparison, the stiffness channel is more contrasted (Figure 20d). In particular, stiff fibril structures are visible, forming a mesh covering the whole pole (Figure 20d). This mesh is barely visible in the error channel (Figure 20c). These fibrils do not have an evident preferred orientation.

These fibrils are also visible as less adherent areas in the adhesion channel (Figure 20e). However, it is possible that the cell is not actually less adhesive in these areas: because the cell wall is stiffer, less indentation is required to apply the force setpoint of 1nN; therefore, there is less contact area between the AFM cantilever tip and the sample surface, which in turn could reduce the total adhesion force. Consequently, if we show the adhesion image here for the sake of completeness, we did not explore further the adhesion data in this report.

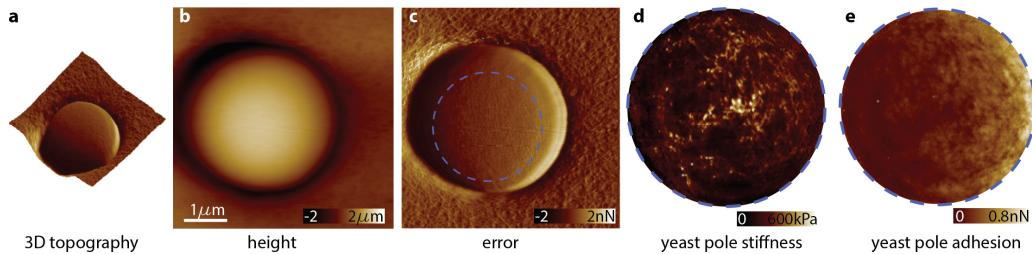


**Figure 20: Mechanical properties measurement on the pole of a live fission yeast cell**

(a) 3D topography render of the pole of a live yeast cell. Topography: AFM height image; overlay: AFM error image. (b) AFM height image. (c) AFM error image. (d) AFM stiffness map of the yeast pole (DMT modulus), corresponding to the circular area highlighted with a dotted blue line in (c). The area outside of the blue circle has been excluded because the stiffness image is dominated by edge effects at the transition between the yeast and the agarose microwell, and does not represent the actual stiffness of the surface. (e) AFM adhesion map of the yeast pole, corresponding to the circular area highlighted with a dotted blue line in (c).

### AFM time lapse imaging of the pole of a growing yeast cell

The fission yeast cells are trapped in agarose, which is a material with no known impact on the growth of fission yeast, and is routinely used as a covering pad for optical time-lapse imaging<sup>87</sup>. Our trapping system with microwells should therefore be compatible with live-cell imaging. Additionally, AFM is demonstrated to work well in normal liquid cell growth media<sup>80</sup>. We

successfully imaged a new pole of a fission yeast cell during cell growth and over several hours (Figure 21). The cell pole was imaged during more than 3 hours, after which the cell separated, releasing one of the sibling cells in the growth medium.

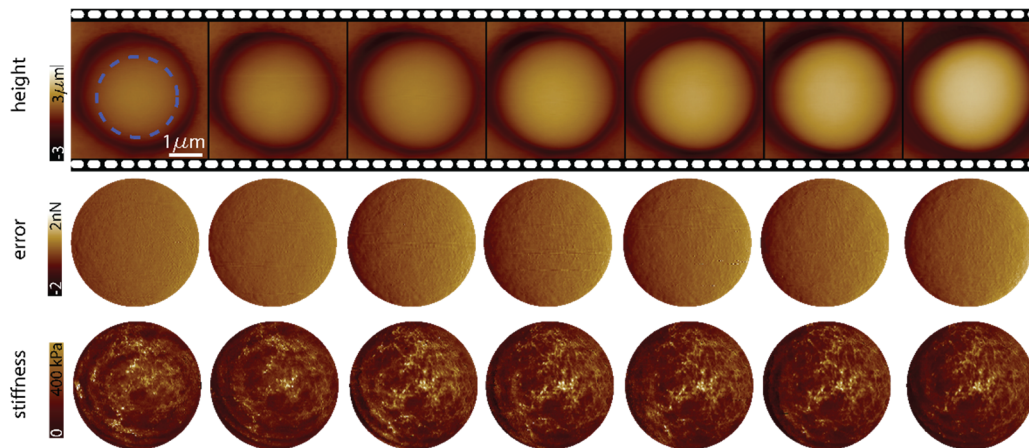


**Figure 21: Time-lapse imaging of the pole growth of a fission yeast cell**

AFM height, error and stiffness images of the pole of a growing fission yeast cell, immersed in growth medium at 25°C. A dotted blue circle highlights on the AFM height image the area corresponding to the error and stiffness images. Time between consecutive images: 20 minutes.

### Radial displacement during growth of the fibrils visible on the yeast cell pole

The stiff fibrils described in Figure 20 are also visible on the time-lapse images of the new pole, and there is a good spatial correspondence between the strands visible in consecutive time points (Figure 21). It was therefore possible to track the position of single fibrils over time (Figure 22a,b). The trajectory of each fibril is a line going outwards from a central area, to which we will refer as the *center of growth*. The distance between the position of the fibril and the center of growth was calculated at each time point, using the AFM stiffness channel to locate the strand, and the height channel to measure the 3D coordinates of the strand and of the center of growth (Figure 22c). The linear fit of the experimental data of the translation speed as a function of the distance to the center of growth shows a statistically significant positive slope. In other words, fibrils which are close to the center of growth move slowly (about 0.15  $\mu\text{m}/\text{h}$  for strands at 0.25  $\mu\text{m}$  of the center of growth), while fibrils which are further away translates faster (about 0.3  $\mu\text{m}/\text{h}$  for strands at 1  $\mu\text{m}$  of the center of growth). It should be noted that this result applies only to the fibrils in the vicinity of the center of growth (less than 1  $\mu\text{m}$  away), we did not measure for fibrils located further away. Based on the linear model of the experimental velocity data (Figure 22c), we deduce an exponential model for the

position of a fibril over time as it translates radially away from the center of growth (Figure 22d).

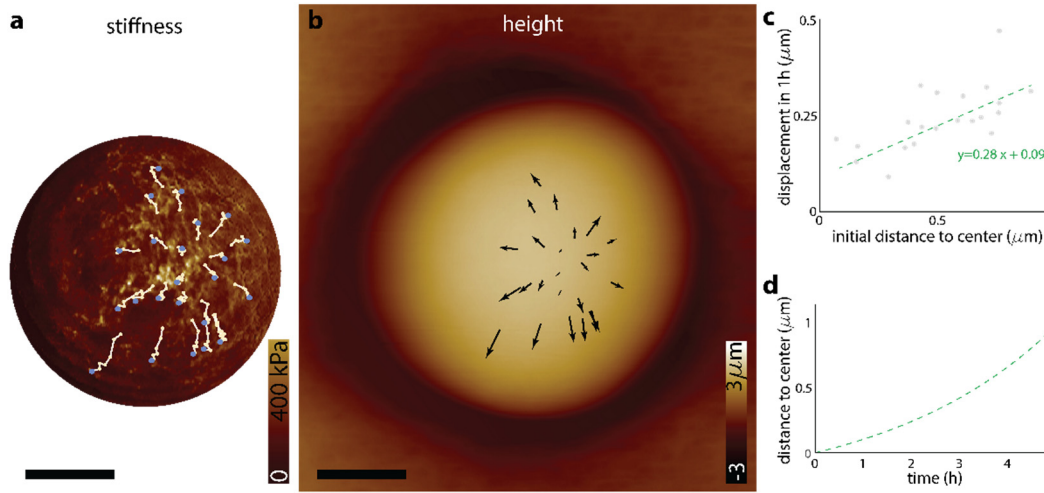


**Figure 22: Displacement of stiff fibrils during tip growth**

(a) Stiffness map of a fission yeast pole with, as an overlay, the position of surface markers over time (yellow). The stiff fibril structures were used as fiducial surface markers. The position of the surface markers was measured from a time-series of AFM stiffness images acquired every 20 minutes. The surface markers corresponding to the image being displayed are in blue. Scale bar: 1 μm. (b) Displacement of surface markers on the surface of a fission yeast pole determined from (a), overlaid on an AFM topography image. Black arrows are proportional to the displacement of surface markers over one hour. Scale bar: 1 μm. (c) Displacement of surface markers in one hour, as a function of their initial position relative to the center of growth. Dotted green line: linear fit showing an increase of the displacement speed for markers further away from the center of growth. The slope of the linear fit is significantly different from zero ( $p=0.002$ ). (d) Model for the displacement over time of new material originating on the pole from the center of growth, and migrating to the sides of the cells. The model was calculated based on the linear fit of the experimental data from (c),  $y=0.28x+0.09$ , and the solution of the first order differential equation  $dx/dt-0.28x-0.09=0$ .

### Deformation of the fibril mesh as it migrates from the tip to the sides of the cell

In the time-lapse AFM images, we see that the stiff fibrils migrate radially as the pole grows. Because the radial displacement speed is not constant but increases, we expect the distance between nearby fibrils to increase over time, as the cell grows. This would mean that the fibril mesh is deformed and stretched as it moves away from the tip. To test this hypothesis, we tracked the local shape of the mesh over time (Figure 23a). As expected from Figure 5, the mesh translates radially outwards (Figure 23b). If we subtract the translation movement, the deformation of the mesh itself become clearly visible (Figure 23c): the mesh stretches as it moves away from the tip of the cell.

The projection of the spherical topography of the pole as a 2D AFM image could account for some of the observed mesh deformation (it would make the mesh look compressed in the radial direction). For this reason, we tracked the local mesh deformation in Figure 23 over a short translation only (less than 200nm). Given that the radius of the yeast cell is approximately  $1.5\mu\text{m}$ , the projection artefact for a translation of 200nm would be of  $1 - \cos\left(\frac{0.2\mu\text{m}}{1.5\mu\text{m}}\right) = 0.9\%$ , which is negligible compared to the observed deformations Figure 23 (stretch in the radial direction: 17% for the top panel and 25% for the bottom panel).

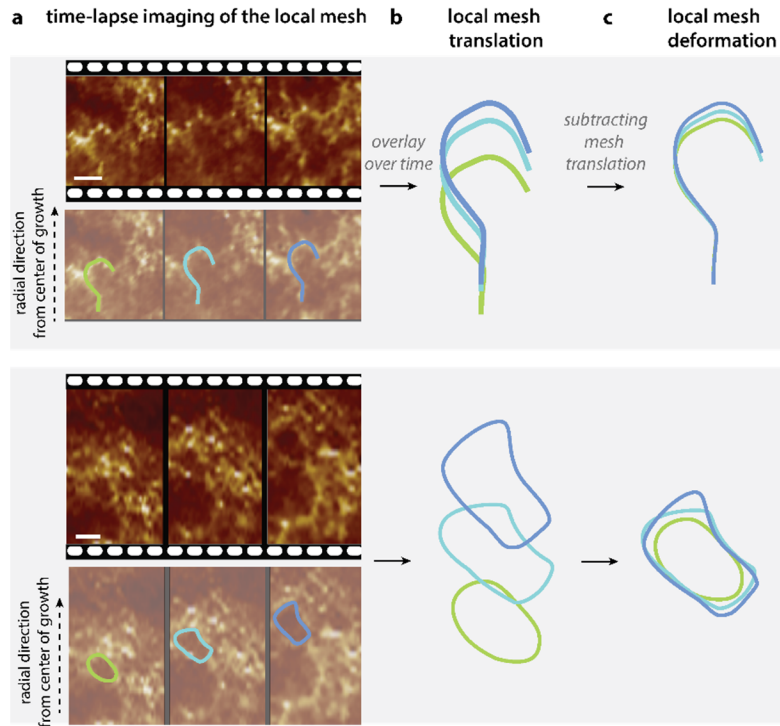


Figure 23: Deformation of the stiff mesh during pole growth

(a) Zoom on two areas of the fibril mesh visible in the stiffness channel of Figure 4. Time between consecutive images: 20 minutes. Top panel: original image. Bottom image: manual selection of a mesh structure easily identifiable over time. Scale bar: 100 nm. (b) Overlay of the mesh structures over time, as it migrates radially outwards. (c) Subtraction of the mesh translation highlights the local mesh deformation. The radial mesh deformation is 17% for the top panel, and 53% for the bottom panel.

#### C.4. Discussion

Vertical trapping and time-lapse AFM pole imaging represents a new strategy to understand how pole-growing microorganisms incorporate new cell wall material at the pole without disrupting the structural integrity of the pole. In this study, we propose a protocol for immobilizing live rod-shaped fission yeast cells using microfabricated vertical agarose microwells for AFM imaging. Using this method, we obtained high-resolution AFM time-lapse imaging of growing yeast cell poles.

We measured the translation and deformation of a stiff fibril mesh within a 2  $\mu\text{m}$  diameter area centered on the pole tip. Within this area, we showed that the radial velocity of the fibrils increases linearly with the distance to the pole. Because fission yeast are pole growing cells, we expect the fibril velocity to become constant and equal to the overall pole growth speed once it has reached the sides of the pole. Abenza et al. used quantum dots bound to the cell wall of growing fission yeast, and measured the position of the quantum dots over time<sup>88</sup>. Our result on the displacement and deformation of the fibril mesh is in coherence with their observations: they show a linear increase of the quantum dot velocity with meridional position, until it transitions to a constant velocity when it reaches the sides of the cell<sup>88</sup>.

While the topography of the pole is a relatively smooth surface (Figure 21a,b), the stiff fibrils are visible in the stiffness channel and form a mesh covering the whole pole (Figure 21c). The fact that the fibrils are more visible on the stiffness channel could be explained if they were covered with a softer material. In that case, the topography would correspond to the outer layer of soft material, while the underneath fibrils would be “felt” as stiffer areas. SEM images of cell wall formation from a protoplast state could support this hypothesis<sup>89</sup>. Osumi et al. reported that the first step of the formation of a new cell wall is visible on electron microscopy images as the formation of a mesh on top of the cell membrane<sup>89</sup> (Figure 24a). This mesh is identified as being constituted of  $\beta$ -glucan fibrils, with a selective enzymatic digestion experiment<sup>89</sup>. In a later stage, the  $\beta$ -glucan fibrils get covered by a layer of amorphous  $\alpha$ -



galactomannan particles<sup>89</sup> (Figure 24b). The underlying mesh of  $\beta$ -glucan fibrils is no longer visible on the electron microscopy images<sup>89</sup>. It is likely that the stiff fibrils observed with AFM correspond to the  $\beta$ -glucan fibrils observed with electron microscopy, since they have the same appearance and since no other fibrillary mesh is visible in cross section of the cell wall observed with electron microscopy<sup>78,89</sup>. These  $\beta$ -glucan fibrils would be seen as stiffer areas in the stiffness channel of the AFM, but not clearly visible in the topography channel because they are covered with  $\alpha$ -galactomannan particles and other proteins.

#### cell wall formation from protoplast as observed with SEM

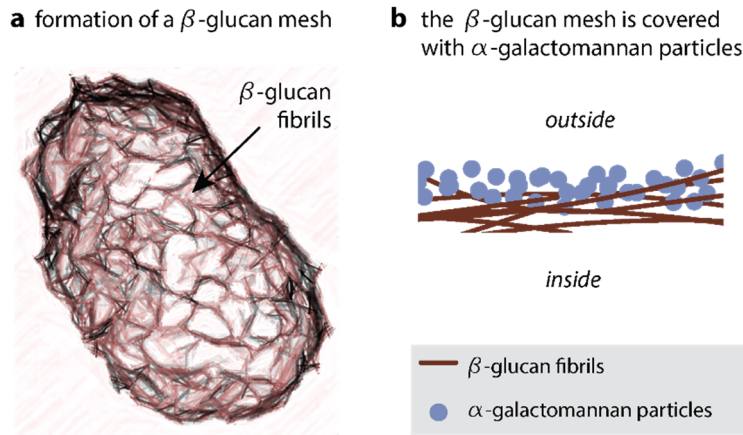


**Figure 24: Artistic representation of the fission yeast cell wall components, as seen with electron microscopy during cell wall formation**

(a) Artistic rendering. During the first 5 hours after incubation of a fission yeast protoplast, a fibrillary network of fibrils of  $\beta$ -glucan is formed on top of the cell membrane. For the original SEM image, see Osumi et al.<sup>78</sup> (b) In a second step, the fibrils are covered progressively with amorphous particles of  $\alpha$ -galactomannan<sup>78</sup>. The fixed cells were observed by Osumi et al. using SEM, and the composition of the fibrils and particles was determined using electron-immunolabelling and selective enzymatic digestion<sup>78</sup>.

Fibrillary meshes of glycans have also been observed with AFM in other microbial species<sup>90</sup>, on live cells such as *Staphylococcus aureus*<sup>45</sup> and *Bacillus subtilis*<sup>91</sup>, and on extracted cell sacculus of *Escherichia coli*<sup>92</sup>. These meshes are directly visible in the topography image of live *S. aureus*<sup>45</sup> and *B. subtilis*<sup>86</sup> but not for *E. coli*<sup>86</sup>. This is expected given that *S. aureus* and *B. subtilis* are Gram-positive, while Gram-negative bacteria such as *E. coli* have their peptidoglycan mesh covered with the outer membrane and cell wall proteins. In mycobacteria, we have published images of the stiffness of the cell wall, revealing a stiff mesh of fibers<sup>18</sup>. Like for the fission yeast images that we reported here, these fibers were not clearly visible in the topography channel<sup>18</sup>,

very likely because the peptidoglycan layer is covered with mycolic acids. AFM stiffness measurements of the cell wall surface offers the opportunity to “feel” the underlying glycan structures directly on live cells, even in cases where the glycan mesh is covered with other proteins and therefore clearly visible.

## **C.5. Materials and methods**

### **Yeast strains and growth conditions**

A volume of 370  $\mu$ L of a frozen stock of *Schizosaccharomyces pombe* stored at -80°C was incubated at 30°C in 12mL of Edinburgh minimal media (EMM) with supplements (ALU). After 15h of incubation, the optical density of cell culture was between 0.3 and 0.4 and fission yeast cells were harvested.

### **Agarose microwells**

Pillars on a silicon wafer were fabricated in the EPFL CMi clean room facility by using photolithography and etching. First, the wafer was coated with a 1.3  $\mu$ m thick layer of AZ1512 positive resin. The areas to be etched were exposed with ultraviolet light from the MLA150 mask aligner, and developed. After this step, the diameters of the pillars were measured to be 2.5  $\mu$ m, 3 $\mu$ m, 3.8  $\mu$ m, 4.5  $\mu$ m. Deep Reactive Ion Etching (DRIE) was used to etch around the pillars. An oxygen plasma process removed the remaining resin.

Liquid agarose was prepared by heating a mixture of 0.4 gram of agarose and 10 ml of EMM without boiling (for about 1 minute) with a 530 Watt microwave oven. 1 mL of liquid agarose was poured onto the microfabricated wafer to imprint microwells into the agarose. After solidification, this agarose mold was gently lifted from the silicon wafer.

### **Trapping**

The setup for centrifuging the yeast cells into the agarose microwells is described in Figure 19. The centrifuge was set to 1000 rom for 10 minutes. Non-trapped yeast cells were removed by rinsing away 3 times with EMM medium.

### **AFM Imaging**

During AFM imaging, the fission yeast cells were covered with EMM medium. AFM images were recorded with a Dimension Icon microscope in peak force mode at room temperature using a ScanAsyst-Fluid cantilever. The AFM was combined with an ix81 Olympus optical



microscope equipped with a 60x objective to align the cantilever tip with a trapped yeast cell before scanning it.



# ***Chapter D* Overlapping and essential roles for molecular and mechanical mechanisms in mycobacterial cell division**

## **D.1. Preamble**

In Chapter B and in Chapter C we studied the morphogenesis of rod-shaped microorganisms from the perspective of growth and insertion of new cell wall material. Another essential aspect of the morphogenesis of a rod-shaped cell is the division of a mother cell into two sibling rod-shaped cells.

This chapter describes the relative contributions of mechanical forces and molecular mechanisms driving the division process in mycobacteria.

This is a verbatim copy of an article that has been published in a peer reviewed journal<sup>18</sup>. Permission is granted by the publisher to reproduce the article in this thesis dissertation.

Odermatt, P. D., Hannebelle, M. T. M., Eskandarian, H. A., Nievergelt, A. P., McKinney, J. D.\* & Fantner, G. E. \* Overlapping and essential roles for molecular and mechanical mechanisms in mycobacterial cell division. *Nat. Phys.* (2019). doi:10.1038/s41567-019-0679-1

\* contributed equally

My contribution in this chapter is the finite element simulation of stress concentration at the future cell division site, the tracking over time of topographical features revealing material stretching at the future division site, the AFM experiment showing that the increased stiffness measured on the septum corresponds to a turgor-pressure driven stress concentration, and the AFM images showing that RipA-depleted cells grow only at the free cell poles.

## **D.2. Introduction**

Mechanisms to control cell division are essential for cell proliferation and survival<sup>93</sup>. Bacterial cell growth and division require the coordinated activity of peptidoglycan synthases and hydrolytic enzymes<sup>94–96</sup> to maintain mechanical integrity of the cell wall<sup>97</sup>. Recent studies

suggest that cell separation is governed by mechanical forces<sup>98,99</sup>. How mechanical forces interact with molecular mechanisms to control bacterial cell division in space and time is poorly understood. Here, we use a combination of atomic force microscope (AFM) imaging, nanomechanical mapping, and nanomanipulation to show that enzymatic activity and mechanical forces serve overlapping and essential roles in mycobacterial cell division. We find that mechanical stress gradually accumulates in the cell wall concentrated at the future division site, culminating in rapid (millisecond) cleavage of nascent sibling cells. Inhibiting cell wall hydrolysis delays cleavage; conversely, locally increasing cell wall stress causes instantaneous and premature cleavage. Cells deficient in peptidoglycan hydrolytic activity fail to locally decrease their cell wall strength and undergo natural cleavage, instead forming chains of non-growing cells. Cleavage of these cells can be mechanically induced by local application of stress with AFM. These findings establish a direct link between actively controlled molecular mechanisms and passively controlled mechanical forces in bacterial cell division.

### D.3. Results

Marked morphological changes occur when a microbial cell divides to form two daughter cells<sup>93</sup>. In *Escherichia coli* this process involves gradual constriction of the cell envelope and structural remodeling of the new cell poles<sup>94–96</sup>. In contrast, other microbial species build a septum without gradual constriction of the cell envelope<sup>100,101</sup>. Instead, the cell wall connecting the two daughter cells remains intact and separation of daughter cells occurs only after completion of the septum, with division scars appearing next to the new poles<sup>102,103</sup>. The final stages of cell separation involve enzymatic digestion of peptidoglycan, which is thought to be the main tensile stress bearing component of the cell wall<sup>104</sup>. Spatial and temporal control of peptidoglycan hydrolytic enzymes is indispensable in order to maintain structural integrity of the cell wall<sup>97</sup>.

In the past decade the atomic force microscope (AFM) has become a powerful tool for structural and mechanical studies in microbiology, with wide-ranging applications covering multiple magnitudes of length-scales (from single molecules to biofilms) and time-scales (from milliseconds to days)<sup>41</sup>. Force spectroscopy experiments have shed light on interaction forces between bacteria and specific biomolecules or surfaces of different chemistries<sup>105,106</sup>, while imaging and mechanical mapping of cell wall components and live cells<sup>42,107,108</sup> have provided detailed insights into the structural architecture of peptidoglycan as well as growth and division mechanisms<sup>16,109–111</sup>. Here, we use AFM to elucidate the complementary roles of peptidoglycan

hydrolytic activity and mechanical mechanisms on cell division in *Mycobacterium smegmatis*, a relative of the pathogen that causes tuberculosis in humans.

The earliest morphological feature of a nascent division event detected by AFM imaging is the “pre-cleavage furrow” (PCF), a constriction of  $\sim 50$  nm width and 5-10 nm depth circumscribing the cell’s short axis (Figure 1a). The PCF appears  $52 \pm 9$  minutes ( $n=15$ ) before cell cleavage and co-localizes with the FtsZ contractile ring. Subsequently, the PCF is the site of septum formation (Figure 1b) and localization of Wag31-GFP, a marker of cytokinesis<sup>6</sup> (Figure S 11). We investigated the nature of the PCF by performing finite element analysis on a simplified model of the bacterial cell wall with a double septum. When this structure is under increased turgor pressure, a PCF-like depression occurs between the two septal walls (Figure 25a). However, other causes for the PCF are conceivable, such as pre-tension in the septum.

At the time of cell cleavage, hemispherical poles flanked by division scars appear abruptly where the PCF was formerly located (Figure 25c-d and Extended data Movie S1). This morphological transition (Figure 26a-d and Figure S 12) occurs within a few milliseconds (Figure 26e, Figure S 13 and Figure S 14). Rather than gradual enzymatic reshaping of the cell wall, millisecond cell cleavage and elastic deformation of the septal walls to hemispherical poles, inflated by turgor pressure, indicate a circumferential mechanical fracture along the PCF.

To elucidate the fracture mechanism of cell cleavage, we used nanoscale topographical features on either side of the septum as fiducial markers to monitor local cell wall deformations while continuously scanning the same line across the PCF (Figure 26f-h and Figure S 15). These measurements revealed that just before cleavage occurs, features on opposite sides of the PCF move apart by more than 10 nm, presumably due to stress exerted along the cell’s longitudinal axis.

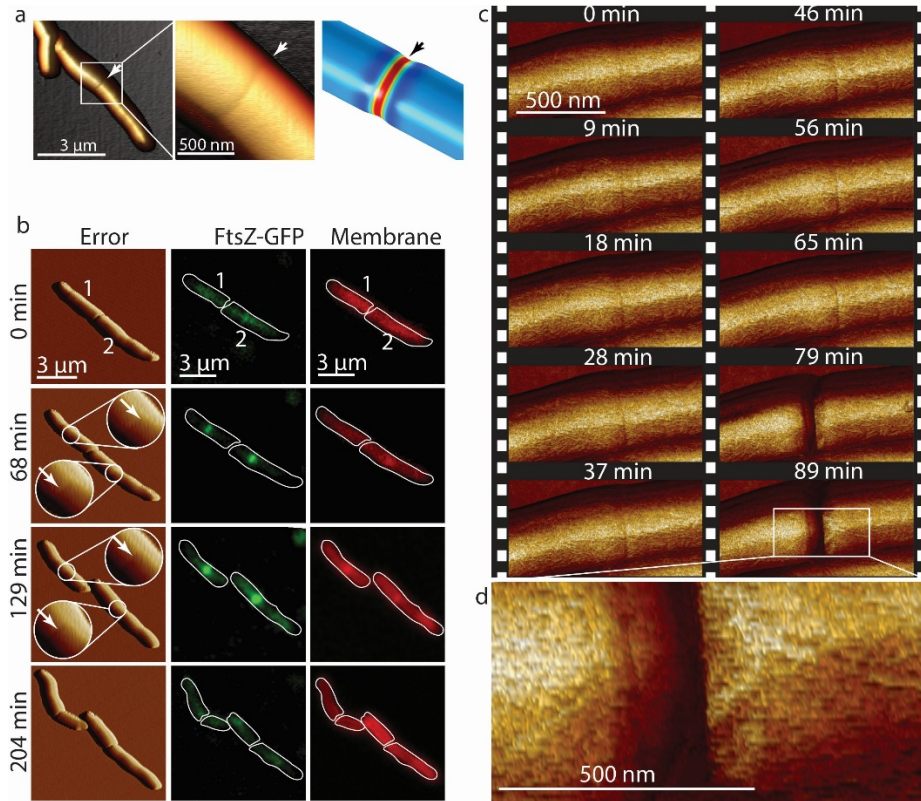


**Figure 25. The pre-cleavage furrow (PCF) is a nanoscale cell-surface feature that marks the future division site in *M. smegmatis*.**

(a) 3D AFM image and COMSOL finite element model of the deformation of a cell by the PCF. (b) Correlated AFM and fluorescence microscope imaging. The PCF co-localizes with the FtsZ-GFP (green) ring ( $n=12$ ) and the nascent septum stained with the membrane stain FM4-64 (red) at the future division site ( $n=5$ ). White arrows indicate the PCFs. The sequence shows two cells undergoing division, with the lower cell being slightly ahead (membrane at septum visible at 68 minutes) of the upper cell (membrane visible at septum at 129 minutes). (c) Time lapse AFM images of the appearance of the PCF and subsequent division. The PCF appears on the bacterial surface on average one hour before cleavage ( $n=15$ ). In the example shown, cleavage occurs between the images acquired at 65 and 79 minutes. Stiffness channel is shown. (d) Zoom-in image of the daughter cells' newly formed poles after cleavage. New cell poles and division scars ( $n>15$ ) on the cell wall envelope are separated by about 200 nm.

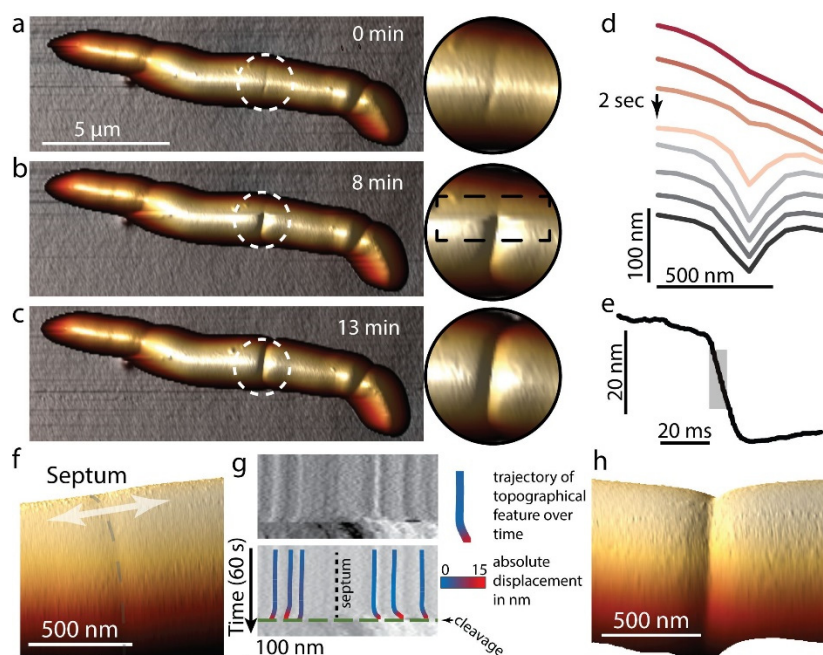


**Figure 26. Daughter cell cleavage occurs with millisecond kinetics by rupture around the PCF.**

(a-c) Consecutive 3D rendered AFM images of cleavage (b) and zoom-ins of the cleavage site. The AFM slow-axis scan direction in (b) is from top to bottom, revealing the transition from the PCF to cleavage. (d) Line sections through the AFM height data around the PCF during cleavage. In the example shown, the PCF progressed to the cleaved state within one scan line (2 seconds, arrow). (e) Constant point measurement of the height at the PCF with a repetition rate of 1 kHz reveals an abrupt drop in height, with 50% of the total decrease (grey area) occurring within 7 milliseconds. In all, similar rapid divisions have been observed >22 times. (f-h) Tracking topographical features (fiducial markers) on either side of the septum prior to cell cleavage reveals material stretching. (f) Zoom-in on center part of a cell with a septum (grey dashed line) prior to cell cleavage. (g) Kymograph of a continuous scan (1 line per second) over time perpendicular across the septum (arrow in (f)) revealing nanometer-sized movement of nanoscale structures on the cell surface (top). Immediately prior to cleavage (green dashed line (bottom)), the material stretches and surface features move apart in opposite directions on either side of the septum (black dotted line). Color-coding of the trajectory of surface features indicates the total lateral displacement away from the septum. (h) 3D height representation of a representative newly cleaved cell (same area as in (f)). See also Figure S 15.

We hypothesized that to initiate a mechanical fracture the ultimate material strength and/or tensile stress should be altered locally. As a proxy to quantify the in-plane tensile stress at the PCF we measured the out-of-plane stiffness, taking advantage of the fact that with increasing in-plane tensile stress a membrane becomes stiffer against out-of-plane deformation by AFM

in quantitative nanomechanical mode (QNM). In this mode, force-distance curves are recorded by sinusoidal oscillations of the cantilever at kHz rates in the z-direction<sup>112</sup>. QNM data can serve only as an indirect and qualitative proxy for cell wall tension, because QNM measures the stiffness of the sample rather than tension *per se*. Factors that contribute to the measured stiffness are the compound Young's modulus of the cell wall, the cell wall stress, and the turgor pressure. These factors are thought to affect different parts of the force curve<sup>110</sup> (see Figure S 16). For the small indentation depths used in QNM, the compound Young's modulus and the cell wall stress dominate the overall stiffness measurements. From the first appearance of the PCF (0 minutes in Figure 27a and Extended data Movie S2) until cleavage (44 minutes), we observed a significant and steady increase of the stiffness at the surface area surrounding the PCF, reaching a maximum about 10 minutes prior to cleavage followed by a slight decrease during the final phase before cleavage (Figure 27b, see also Figure S 17a-d). We hypothesize that the progressive stiffness increase is the result of increasing tensile stress at the PCF, while the measured stiffness decrease during the final phase before cleavage could result from the action of peptidoglycan hydrolytic enzymes<sup>111</sup>.

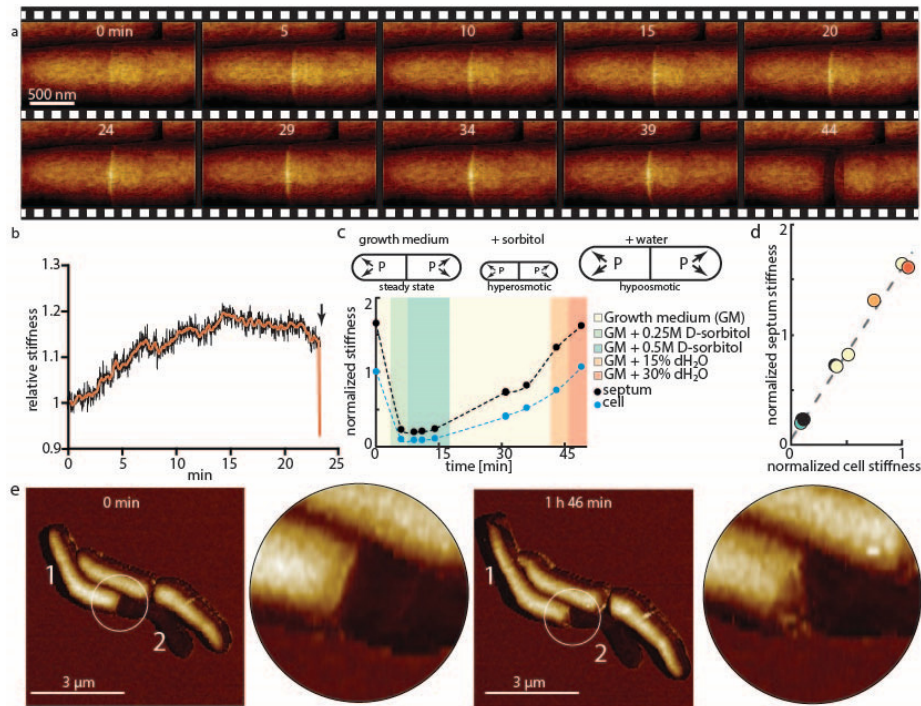


**Figure 27. Turgor pressure drives cell cleavage through stress concentration at the PCF.**

(a) Time sequence of measured stiffness map of the cell surface from appearance of the PCF until cleavage (n=22). (b) Changes in the local stiffness at the PCF leading up to cell cleavage (x-axis, time



in minutes; y-axis, PCF stiffness normalized to bulk stiffness of cell sidewalls). After an initial gradual increase of the stiffness at the septum, a small decrease occurs before cleavage (red line, average over 20 data points). **(c)** Measurement of apparent stiffness on top of the septum (black lines) and on top of the cell bodies (blue lines, average of the two nascent sibling cells) as turgor pressure is modulated by hyper-osmotic (green shading) and hypo-osmotic (orange shading) media. Measured stiffness on the PCF and cell bodies is affected by the turgor pressure to a different extent. Measured stiffness values on the cell and on the PCF are normalized to initial stiffness of the cell in normal growth medium. **(d)** When varying medium osmolarity, the measured PCF stiffness is linearly dependent with the measured cell stiffness with a slope of  $\sim 1.5$  ( $r^2=0.991$ ), suggesting a stress concentration of 50% on the PCF. Measured stiffness values on the cell and on the septum are normalized to the initial stiffness of the cell in normal growth medium. **(e)** If one nascent sibling cell is deflated after cytokinesis but before cleavage (0 minutes), rapid cleavage is replaced by gradual shedding of the deflated sibling cell, indicating that rapid cleavage requires turgor pressure in both sibling cells.

To assess the contribution of the turgor pressure to the cell wall tensile stress<sup>108,113</sup> as opposed to other mechanical effects due to septum formation, we quantified the local stiffness at the PCF and the nascent sibling cells as we modulated the turgor pressure. Following a hyperosmotic shock by addition of D-sorbitol (0.25 M or 0.5 M) to the medium, the measured stiffness at the PCF and the sister cells decreased to  $\sim 20\%$  of its initial values (Figure 27c). Conversely, the stiffness of the septum and the cells both increased upon hypoosmotic shocks by addition of water (15% and 30%). These measurements revealed a linear relationship between the average stiffness of the sibling cells and the stiffness at the PCF with a slope of  $\sim 1.5$  (Figure 27d). From these data we conclude that the measured increase in stiffness is indeed the result of the tensile stress in the cell wall exerted by the turgor pressure, and that turgor-induced tensile stress is disproportionately concentrated at the PCF compared to the stress on the sidewalls of the sibling cells. These results suggest that an increase in tensile stress, in conjunction with a decrease of mechanical strength, determines when and where the cell wall integrity catastrophically fails, resulting in abrupt cleavage.

We further explored how turgor pressure affects cell cleavage by piercing one nascent sibling cell after cytokinesis but before cleavage using a sharp AFM cantilever tip (Figure 27e and Figure S 19). Instead of a rapid cleavage event, the intact sibling (cell 1) gradually separated from its sibling as it shed the sacculus of the deflated sibling (cell 2) over the course of several hours (see also Extended data Movie S3). These results suggest that turgor pressure is necessary to provide the energy to drive rapid cell cleavage.

Based on these results, we hypothesize that cell cleavage occurs when tensile stress, driven by turgor pressure, exceeds the ultimate material strength of the cell wall peptidoglycan. In this view, artificially increasing tensile stress should cause premature cell cleavage and, conversely, preventing a decrease in material strength should delay the timing of cell cleavage. We tested this hypothesis by applying mechanical load on the PCF using the AFM cantilever. In cells undergoing normal cell division, the interval between PCF formation and cell cleavage lasts about one hour on average. We found that applying load on the PCF triggered immediate cell cleavage and formation of two viable, growing daughter cells up to 30 minutes earlier than normal (Figure 28a, Figure S 21, Figure S 22a and Figure S 23). Forced cleavage at earlier time points, often resulted in partial cleavage and formation of non-viable daughter cells (Figure 28b and Figure S 22b).

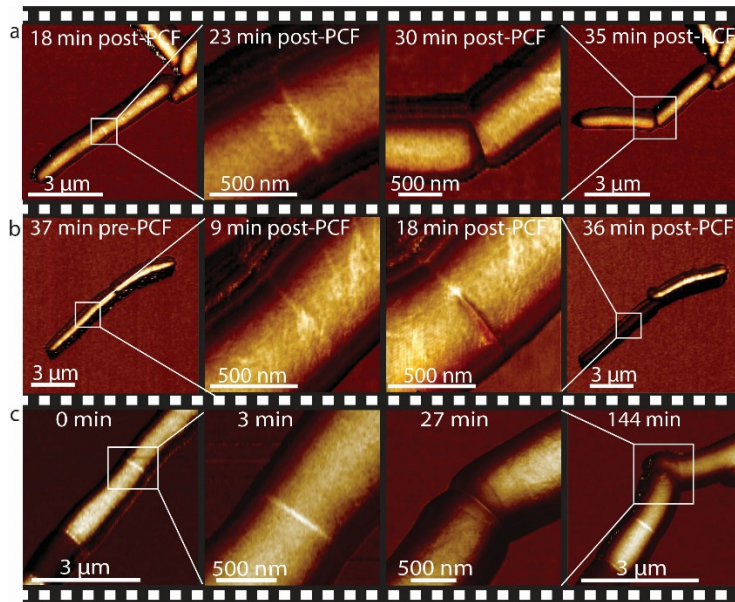


**Figure 28. AFM-applied local stress on the PCF can substitute for an essential cell division enzyme (RipA).**

(a) AFM stiffness images were recorded at low and high resolution at 18 and 23 minutes after first appearance of the PCF, respectively. Application of a force on the PCF with the AFM cantilever at 25 minutes (force curve, see Figure S 22a) triggers premature cell cleavage ( $n=11$ ). The forcibly cleaved daughter cells survive and initiate growth from the newly formed cell poles (30 and 35 minutes; see also Figure S 23). (b) Same experimental procedure as in (a) but the load was applied earlier, 18 minutes after first appearance of the PCF. Partial cleavage occurs (18 minutes; force curve, see Figure S 22b) and both cells subsequently deflate (image recorded at 36 minutes) ( $n=5$ ). (c) Cleavage of RipA-depleted cells can be induced by repeatedly scanning the same line over the PCF at elevated force, resulting in a sudden drop in height (27 minutes; see Figure S 22c). The previously

non-growing cells within the chain initiate growth from the newly liberated cell poles following forced cleavage (144 minutes) (n=4). See also Figure S 20 for corresponding height data.

The material strength of the cell wall is modulated by enzymes that add or remove crosslinks in the cell wall peptidoglycan<sup>45,114</sup>. In mycobacteria, cells depleted of the peptidoglycan hydrolase RipA<sup>115</sup>, which localizes to the septum and cell poles<sup>116</sup>, appear to septate normally but fail to undergo cleavage<sup>117</sup>. This defect results in the formation of long chains of attached cells in which only the two outermost cell poles at the ends of a chain continue to elongate, while cells interior to the chain, which lack free cell poles, cease growing after septation (Figure S 24). Loss of RipA peptidoglycan hydrolase activity likely prevents the decrease of the cell wall strength at the septum observed in wild-type cells just prior to division. Indeed, we observed that increased tensile stress in the sidewalls of cells within RipA-depleted chains (see Figure S 25) occasionally results in cell lysis (Figure S 26) but not cell cleavage at the septum. In contrast, local application of force on the PCF by the AFM cantilever was sufficient to trigger rapid cleavage of RipA-depleted cell chains (Figure 28c and Figure S 22c), although the force required was significantly higher (beyond the linear regime of our force measurements) compared to wild-type cells. We conclude that RipA-mediated local decrease of material strength of the cell wall at the septum is essential to allow cell cleavage driven by turgor pressure, yet cleavage can still occur if compensatory local stresses are applied externally. These results are consistent with our hypothesis that the timing of cell cleavage is determined by the balance of cell wall tensile stress and the ultimate material strength of the cell wall at the nascent division site.

We observed that the newly free cell poles generated by force-induced cleavage of chained RipA-depleted cells are able to initiate and maintain growth once the sibling cells separate (Figure 28c). This was true even of cells located in the center of long chains, which had persisted in a non-growing but evidently viable state for many hours. These results demonstrate that cleavage and physical separation of sibling cells are essential for initiation of new-pole growth, suggesting the existence of an unknown mechanism of contact-dependent growth inhibition.

Millisecond bacterial cell division, visualized as abrupt spatial reorientation of newborn daughter cells, has been observed by fast optical imaging of *Staphylococcus aureus*<sup>98</sup>. In their pioneering study, Zhou *et al.*<sup>98</sup> linked division of *S. aureus* to a fracture process and postulated that it might result from stress accumulation and mechanical failure of the cell wall, thereby laying the groundwork for viewing bacterial cell division from the perspective of physical

forces<sup>118</sup>. Their observations are reminiscent of the “V-snapping” model of cell division in *M. smegmatis*<sup>119</sup>; more recently, additional bacterial species have been identified that also undergo abrupt spatial reorientation during cell division<sup>99</sup> (see Figure 28a). This phenomenon (V-snapping) is consistent with a model in which rapid cleavage of sibling cells is due to progressive circumferential rupture of the connecting cell wall starting from the weakest section around the PCF. As the crack propagates from one side to the other (see Figure 28b), a bending moment occurs that will spatially displace the cells. The amount of V-snapping hence depends on the bending moment and the friction forces experienced by the bacterium, which are higher if the cells are adhered to a surface than when suspended in solution. These similarities suggest that mechanical forces might play an important role in evolutionarily diverse bacterial species during the final stage of cell division (cleavage of sibling cells).

#### D.4. Discussion

Using time-lapse AFM to study cell division in *M. smegmatis*, we observed progressive stiffening of the PCF over time, dependence of PCF stiffness on the internal turgor pressure, stress concentration at the PCF, and rapid (millisecond) physical cleavage of sibling cells. AFM force curves and QNM measurements have recently emerged as powerful tools for characterizing the relative stiffness of biological samples<sup>120</sup>. It is important to note, however, that the measured values for stiffness are very sensitive to factors such as cantilever tip geometry, sample topography, and other imaging parameters. Care should therefore be taken in the interpretation to evaluate *relative* rather than *absolute* values within a time series.

Our experimental demonstration that the PCF undergoes progressive stiffening prior to rapid cell cleavage, and that applied mechanical forces can induce premature cleavage, further strengthens the hypothesis that localized stress accumulation and mechanical fracture play a central role in mycobacterial cell division. The applied stress, however, is only one of the factors in fracture mechanics; the strength of the material is another important factor determining when and where fracture occurs. Thus, modulation of the ultimate tensile strength of the peptidoglycan by peptidoglycan synthesizing and hydrolytic enzymes is equally important to ensure that cell cleavage occurs at the appropriate time and place.

We propose a model in which increasing tensile stress on the PCF (due to stress concentration) and decreasing material strength at the PCF (due to the activity of the RipA peptidoglycan hydrolase) together create a positive feedback loop that culminates in rapid cell cleavage. Since molecular bonds under tensile stress require a lower activation energy for hydrolysis and are less likely to reform once broken<sup>104</sup>, tensile stress around the PCF will locally accelerate the

hydrolysis of peptidoglycan by RipA. As more chemical bonds are broken, the mechanical load on each remaining bond will increase, further facilitating hydrolysis. Following a similar reasoning, the vertical septal walls would, before cleavage, experience lower tensile stress compared to the peptidoglycan at the PCF. This, in turn, could act as a mechanical mechanism to protect the pre-cleavage septal walls from hydrolysis by RipA. The same mechanism could explain the observation that chained RipA-depleted cells do not grow, yet retain the ability to initiate growth if cleavage is induced. After cleavage, the previously flat septal wall is rapidly inflated by turgor pressure to form two hemispherical poles that experience the same longitudinal tension as the rest of the cell wall<sup>104</sup>, similar to observations in fission yeast<sup>121</sup>. Since hydrolysis of existing peptidoglycan bonds is necessary for insertion of new peptidoglycan chains, this might explain why cleavage is essential for initiation of new-pole growth. We conclude that localization of enzymes involved in cell wall biogenesis to subpolar growth zones determines *where* growth occurs<sup>10</sup>, while the balance between cell wall stress and material strength determines *when* growth occurs. The overlapping and essential contributions of RipA hydrolytic activity and mechanical forces in mycobacterial cell division illustrate the general importance of studying molecular mechanisms and physical factors in conjunction rather than either in isolation.

#### **D.5. Author contributions:**

P.D.O., G.E.F. and J.D.M conceptualized the study. P.D.O., M.T.M.H., A.H.E. developed imaging protocols. P.D.O., M.T.M.H. G.E.F and J.D.M. designed experiments. P.D.O. and M.T.M.H. performed the experiments and analyzed the data. A. P. N. participated in building the instrument and simulations. P.D.O., M.T.M.H., G.E.F and J.D.M. wrote the manuscript.

#### **D.6. Acknowledgements:**

We thank E.J. Rubin for generously providing the RipA conditional depletion strain of *M. smegmatis*. This research was supported in part by grants to G.E.F. from the Swiss National Science Foundation (205321\_134786 and 205320\_152675), from the European Union FP7/2007-2013/ERC under Grant Agreement No. 307338-NaMic, H2020 - UE Framework Programme for Research & Innovation (2014-2020); ERC-2017-CoG; InCell; Project number 773091, from the Commission for Technology and Innovation under CTI no. 18330.1 PFNM-NM, and by a grant to J.D.M. from the Swiss National Science Foundation (310030B\_176397). HAE was supported by an EMBO Long Term Fellowship (191-2014) and an EMBO Advanced Long Term Fellowship (750-2016).

## **D.7. Materials and methods**

### **Bacterial culture conditions**

*Mycobacterium smegmatis* mc2155 (wild-type) and derivative strains were grown in Middlebrook 7H9 liquid medium (Difco) supplemented with 0.5% albumin, 0.2% glucose, 0.085% NaCl, 0.5% glycerol, and 0.05% Tween-80. Cultures were grown at 37°C to an optical density at 600 nm (OD<sub>600</sub>) of ~ 0.5, corresponding to mid-exponential phase. Aliquots were stored in 15% glycerol at -80°C and thawed at room temperature before use; individual aliquots were used once and discarded.

### ***M. smegmatis* RipA depletion strain**

The RipA depletion strain was kindly provided by Eric Rubin and grown as described by Hett et al. 31. Briefly, the strain was initially grown in growth medium supplemented with hygromycin B (50 µg/ml), kanamycin (30 µg/ml), and anhydrotetracycline (50 ng/ml) for up to 5 days. The culture was then washed with PBS and grown in fresh 7H9 medium lacking anhydrotetracycline to deplete RipA expression.

### **Coverslips for AFM imaging**

For details, refer to Eskandarian et al.<sup>15</sup>. In short, polydimethylsiloxane (PDMS) (Sylgard 184, Dow Corning) was mixed in a ratio of 15:1 (elastomer : curing agent) and the coverslip (VWR) was spin-coated at 8,000 rpm (SUSS MicroTec LabSpin6) for 30 seconds on a 22 mm glass and baked at 80°C for 10 minutes before use.

### **Attachment of bacteria on coverslips**

An aliquot from an exponential-phase culture of *M. smegmatis* was pipetted onto a PDMS-coated glass coverslip, mounted in a custom-made coverslip holder with a built-in heating unit 37, and incubated at 37°C without agitation for ~15 minutes to allow attachment. Unattached bacteria were removed by rinsing the coverslip surface with 7H9 growth medium before imaging. The samples were maintained at 37°C in 7H9 liquid medium heated by a custom-made coverslip heating holder 37 controlled by a TC2-80-150 temperature controller (Bioscience Tools) during imaging. For details, refer to Eskandarian et al.<sup>16</sup>.

### **AFM imaging**

AFM images were recorded using a Fast Scan head (Bruker) at 0.5 Hz line rate using ScanAsyst Fluid cantilevers (Bruker) with a nominal spring constant of 0.7 N m<sup>-1</sup> in PeakForce

quantitative nanomechanical mode (QNM) at an oscillation rate of 1 kHz and a force setpoint  $< 2$  nN. Channels recorded include height sensor, peak force error, and DMT modulus. The abrupt height change during cell cleavage was measured by imaging in peak force tapping mode at the same spot (0 nm scan size) on the PCF and data were recorded at a rate of 1 kHz. AFM imaging of stiffness at the PCF was done by repeatedly scanning the same line across the PCF at 1 line per second, at a slightly elevated force setpoint (5 nN). The highest stiffness value from each scan line was plotted over time. Before force curves on the PCF were recorded, a small area on the PCF was scanned to determine its center. To force cell cleavage in RipA-depleted cells, the line along the septum was scanned repeatedly and the force setpoint was increased gradually in order to increase the applied pressure.

### **Correlated AFM and fluorescence imaging**

Correlated AFM and fluorescence images were acquired as described previously<sup>17</sup>. Briefly, fluorescence images were acquired with an EMCCD iXon Ultra 888 camera (Andor) mounted on an IX73 inverted optical microscope (Olympus) equipped with a 100X oil immersion objective (UAPON100XOTIRF, Olympus). Illumination was provided by an MLC monolithic laser combiner (Agilent) coupled to an optical fiber. For combined fluorescence imaging of FtsZ-GFP and FM4-64 the excitation filter and dichroic mirror of the EGFP filter cube F36-526 (AHF Analysetechnik, Germany) were used. The emission light was split by an optical system (DV2, Photometrics) equipped with a second dichroic mirror (T565lpxr) placed between the EMCCD camera and the microscope frame to separate the red and green channels each to one half of the EMCCD camera chip. Cleanup filters used were F37-528 (EGFP) for the green channel and F37-624 (TxRed) for the red channel. Additionally, a neutral density filter with OD 0.6 was placed on the red channel. Typically, 5 mW power of 488 nm laser light at the MLC400B output was used for illumination. Images were recorded with EM gain set to 300 and exposure time to 500 milliseconds. The AFM was mounted on top of the inverted microscope (IX73, Olympus) and the AFM laser was switched off before acquiring fluorescence images. Contrast and brightness were adjusted with ImageJ.

### **Membrane staining**

The bacterial cell membrane was stained with FM4-64 (Life Technologies) before fluorescence images were taken. The dye was diluted in 7H9 medium and used at a final concentration of 0.2  $\mu\text{g ml}^{-1}$ . After fluorescence images were taken the sample was washed with 2 ml 7H9 medium to remove unbound FM4-64 in order to minimize any potential effects on cell growth.

## AFM data processing

For processing AFM images, standard scanning probe software was used (Gwyddion, Nanoscope Analysis). For Figure 27b each line scanned across the PCF at 1 Hz was smoothed twice with a moving average at a 20-pixel window size and the peaks of each line were then centered with Matlab. The mean of the centermost eight pixels was extracted for each line using ImageJ. For each line, these values were then normalized to the mean of a feature far away from the center peak to correct for small temporal fluctuations during the measurement. Kymograph data in Figure 26g were smoothed two times with a moving average at a 3-pixel window size along the fast scan axis (x-direction).

## Finite-element model of a dividing cell

We made a model of a dividing cell building a septum (Figure S 27) with COMSOL Multiphysics® version 5.3, assuming a linear elastic structure with axial symmetry. The cell was inflated with a uniform internal turgor pressure.

### D.8. Supplementary figures

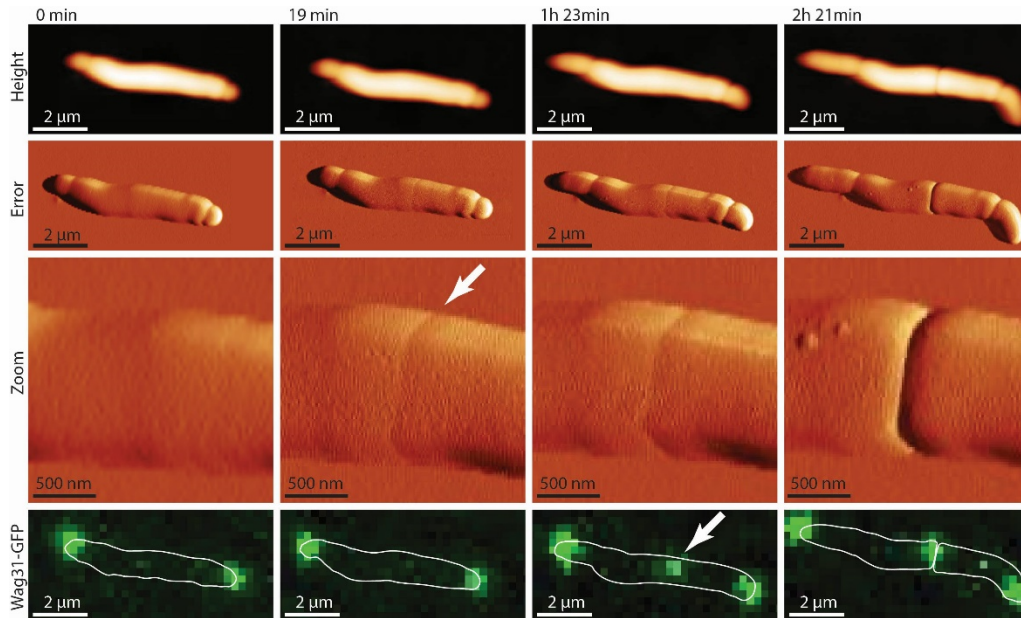


**Figure S 11. The pre-cleavage furrow (PCF) precedes the Wag31-GFP cytokinesis marker at the future cell division site.**

Time sequence of cells expressing Wag31-GFP imaged by correlated AFM and fluorescence microscopy. In this example, the PCF appears at 19 minutes (white arrow). Wag31-GFP, a marker of cytokinesis, appears much later and co-localizes with the PCF (arrow at 1 hour 23 minutes) (n=2).





**Figure S 12. AFM scan line across the PCF during cleavage.**

Cleavage of sibling cells was monitored by constantly scanning perpendicularly across the PCF with the AFM cantilever at 10 Hz. A representative example is shown. The cleavage event corresponds to an abrupt drop in the height profile (grey shading). Cleavage is completed within 10 milliseconds and no gradual constriction is observed leading up to this event (flat line).

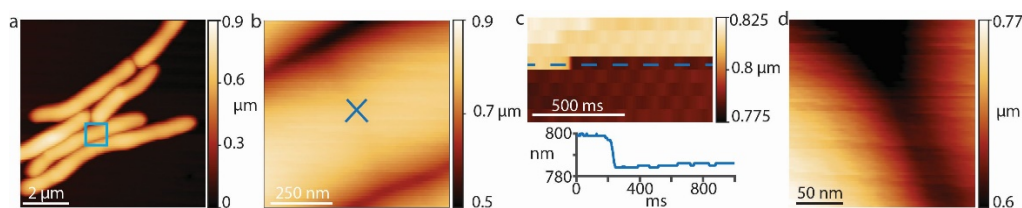


**Figure S 13. Height data of millisecond cell cleavage measured at 1 kHz rate (shown in Figure 26e).**

(a) Overview of a cell initiating septation. (b) Zoom-in (blue square) to the nascent PCF. The cantilever tip was positioned exactly on the center of the PCF (blue cross 'x') and the height was recorded without scanning the tip laterally at a rate of 1 kHz. (c) Height data (upper panel) and height profile (lower panel) at cleavage. (d) After the drop in height was observed an image was immediately recorded at the same position to confirm that the drop in height was due to cell cleavage and that the location of the AFM tip remained at the site of cell cleavage.

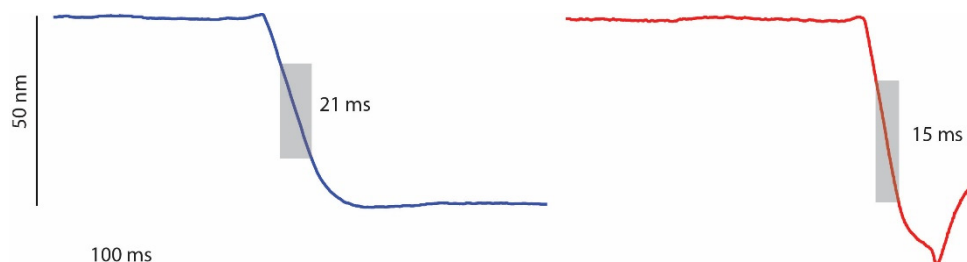


**Figure S 14. Cell cleavage measured at 1 millisecond time resolution.**

The time required for cell cleavage was measured at a 1 kHz rate by constantly measuring the height of a single point on top of the PCF. Two representative examples are shown. The cleavage event

corresponds to an abrupt drop in the height profile (grey shading). Cleavage is completed within 21 milliseconds (upper panel) or 15 milliseconds (lower panel) and no gradual constriction is observed leading up to this event (flat line).

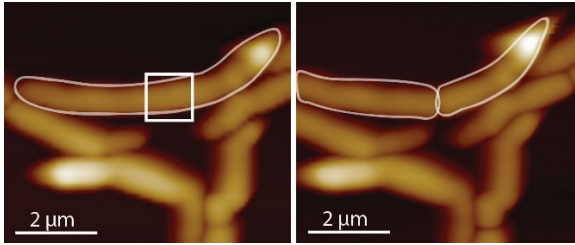


**Figure S 15. Overview height images of cell before (left) and after (right) cleavage shown in Figure 26f-h.**

The white square in the image on the left is the region corresponding to the 3D representation in Figure 26f.

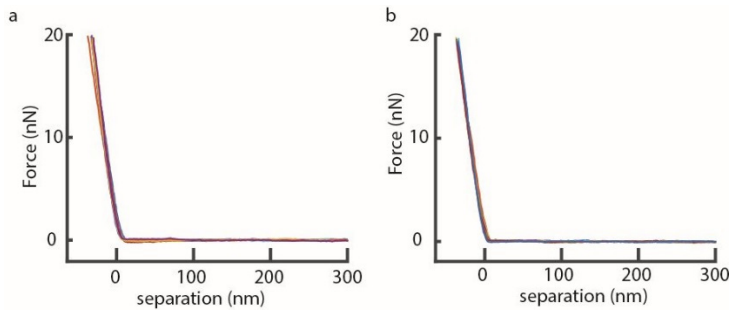


**Figure S 16. AFM force curves at the PCF of two representative cells over time.**

(a,b) Force curves on the PCF of two individual cells over time. Compared to measurements in QNM mode, the characteristics of acquiring force curve are significantly different: ~1,000 times lower ramp rate, ~200 times lower indentation velocity, ~20 times higher maximal force applied, and generally larger indentation depth.

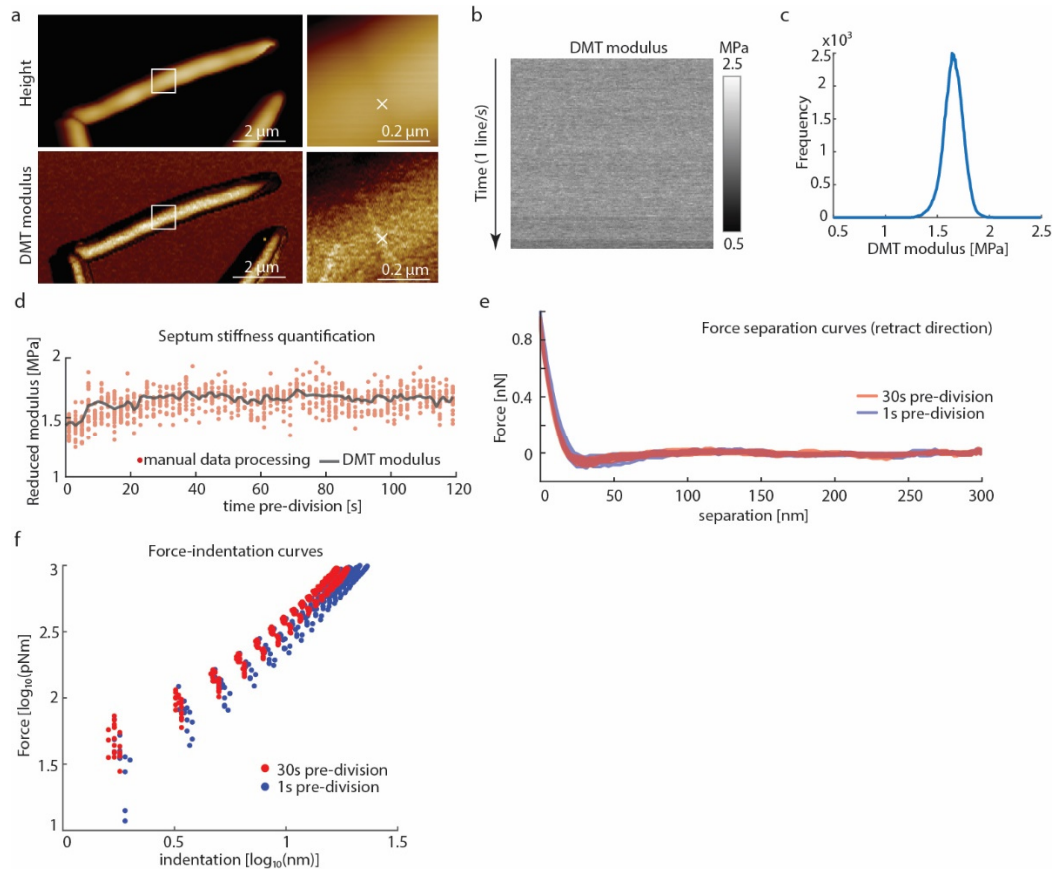


**Figure S 17. Comparison of stiffness values obtained from QNM DMT modulus imaging channel and analysis of the individual force-distance curves.**

To compare the stiffness given by the DMT modulus imaging channel with manual analysis of the recorded force curves, force curves were recorded leading up to a cell cleavage event using QNM mode in peak force capture to record the individual force-distance curves at a ramp rate of 1 kHz and a peak force of 1 nN. **(a)** The cantilever tip was positioned at the center of a PCF (white cross 'x'). **(b)** Force-distance curves were recorded at the same spot on top of the PCF without laterally moving the tip. **(c)** The mean value obtained from the DMT modulus channel was  $\sim 1.6$  MPa. **(d)** For each line in the DMT modulus image (corresponding to 128 data points in 0.5 seconds) the average stiffness value was calculated and plotted (black line). Every tenth force curve was then processed manually with Nanoscope Analysis software. Each retract direction of the force curve was corrected to set the baseline to 0 nN, then a moving average filter with a width of 5 units was applied. To extract mechanical property values, a Hertzian fit was used in the range between 4% to 98% of the maximal force (red dots), then 50% of the force curves with the highest  $r^2$  values were plotted. The DMT modulus values extracted from the QNM channel image are in good agreement with manual force-distance analysis. Decrease in stiffness at the septum during the last phase of cell division was observed in the DMT modulus channel and the force curve analysis alike (last  $\sim 20$  seconds). **(e)** Representative force-separation curves taken at either 30 seconds (red) or 1 second (blue) before cell

cleavage. **(f)** To unveil multiple slopes that could potentially derive from different cell wall layers, the same data as in **(e)** were used to plot the slope of the force-separation curves in a log-log plot as has been done by others to discriminate between the contribution of the cell wall and the turgor pressure. However, in these measurements there is no clear distinction that would account for two different linear slopes. The decrease in the stiffness at 1 second (blue) before cleavage compared to the stiffness at 30 seconds (red) before cleavage is clearly discernible in the log-log plot.

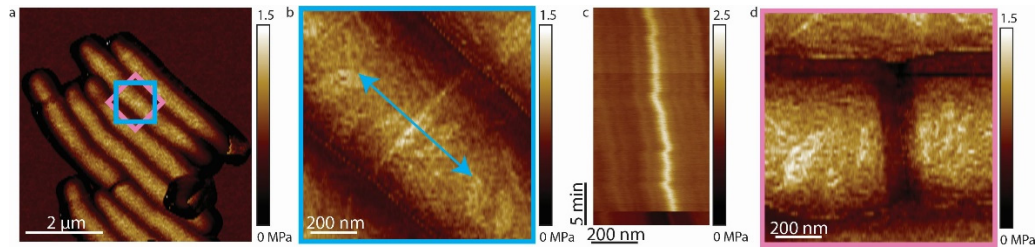


**Figure S 18. Stiffness at the PCF measured by repeatedly scanning across the PCF.** **(a)** Zoomed-out view of a cell initiating septation. **(b)** Zoom-in on the PCF (blue box in **(a)**). Stiffness evolution over time was measured by repeatedly scanning a line across the PCF at the same location (blue arrow) in QNM mode until a drop in height was observed. **(c)** Kymogram of PCF stiffness over time, proceeding from top to bottom. The abrupt decrease in stiffness at the bottom of the kymogram corresponds to cell cleavage. From these data the stiffness values were extracted as described in the Methods and plotted in Figure 27b. **(d)** Following the abrupt decrease in PCF stiffness recorded in **(c)**, zoom-in on the same region of the same cell (pink square in **(a)**) verified that cleavage had occurred.

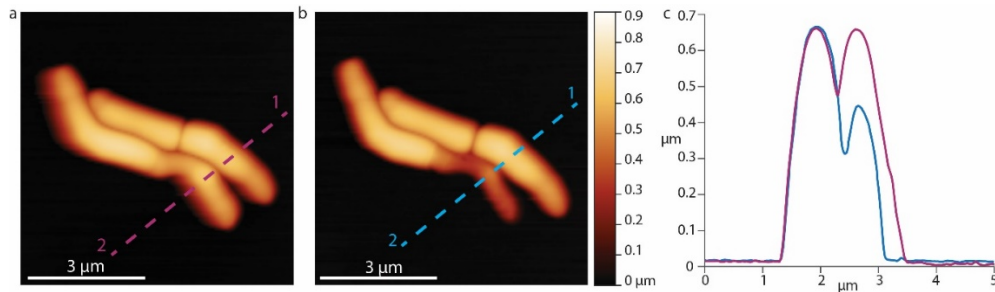


**Figure S 19. Height images of cells before and after deflation induced by piercing with a sharp AFM cantilever tip.**

(a,b) Height images of cells shown in Figure 3e at 0 minutes (a) and 1 hour 46 minutes (b). (c) Height profiles of cells before (red line) and after (blue line) AFM-mediated piercing show deflation of the cell pierced with the cantilever tip, confirming loss of turgor pressure.

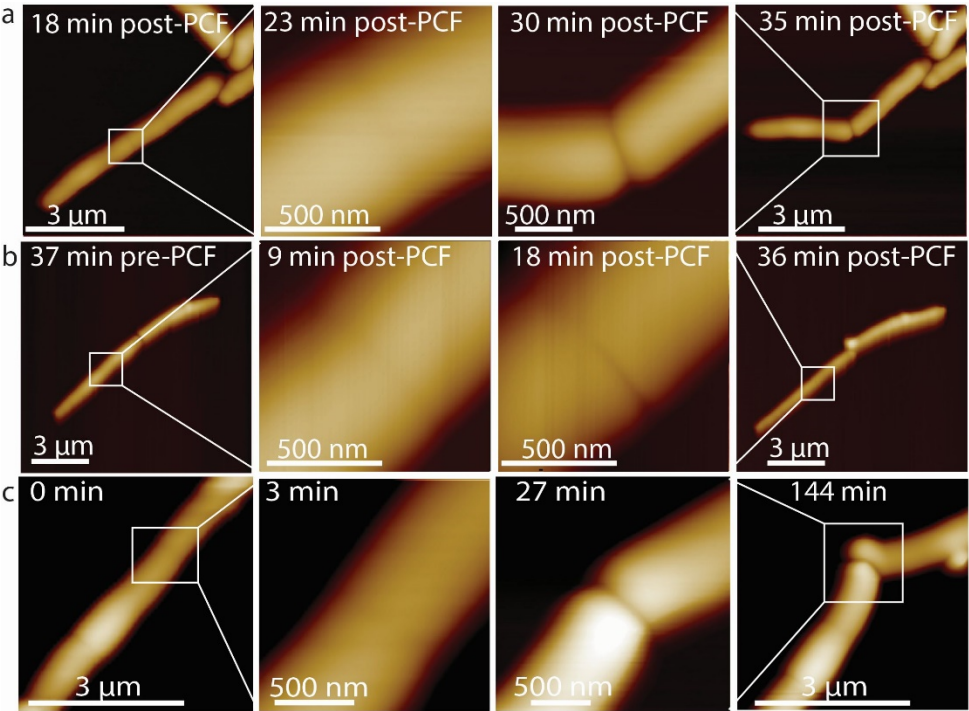


Figure S 20. Height images of cells corresponding to stiffness maps shown in Figure 28.

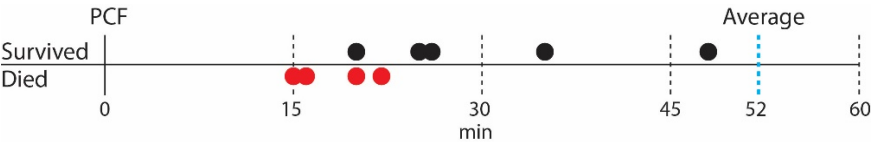
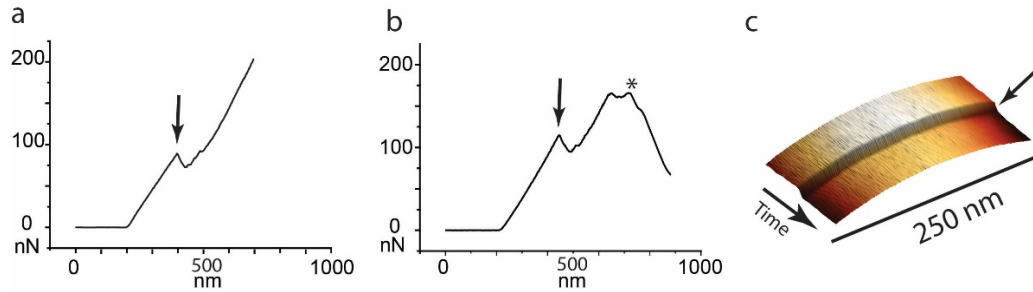


Figure S 21. Cell cleavage can be induced prematurely by increasing the mechanical stress on the PCF.

Cell cleavage was induced at different time points after the first appearance of the PCF (0 minutes) by applying a point force on the PCF with the AFM cantilever. In the majority of cases, forced cleavage at early time points resulted in two non-viable daughter cells (red dots), while forced cleavage at later time points resulted in two sibling cells that survived and continued to grow (black dots). The average time of natural cleavage of non-induced cells is indicated by the vertical blue dashed line at 52 minutes (n= 15).



**Figure S 22. Premature cleavage can be induced by AFM force curves or AFM scanning along the PCF.**

Cleavage of cells shown in Figure 4 was induced by applying force with the AFM cantilever, which was done either by recording a force curve (wild-type cells) or by scanning along the septum at an elevated force (RipA-depleted cells). **(a)** Force at the PCF was applied by recording a force curve on the center of the PCF. A sudden drop in the force (black arrow) indicates an induced cleavage event. Subsequent AFM images show newly cleaved poles (see Figure 28a). **(b)** As in **(a)** force was applied at the PCF by recording a force curve. A drop in the force (black arrow) indicates a rupture event of leading to premature partial cleavage as shown in Figure 28b. Subsequently, the increasing force on the forming septum leads to rupture (\*) and cell lysis. **(c)** Kymogram of the height while continuously scanning the same line (1 line/second) along the PCF of a RipA-depleted cell at high force. A sudden drop in the height (black arrow) indicates an induced cleavage event. AFM images prior and subsequent to induced cleavage events are shown in Figure 28.

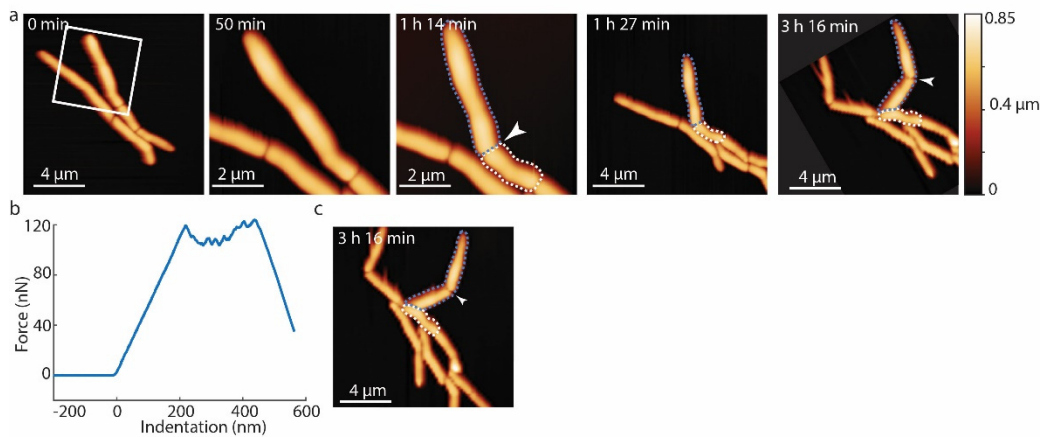


**Figure S 23. Cells forced to undergo premature cleavage continue to grow and divide.**

**(a)** Time lapse AFM height images of cells that continue to grow and divide after cleavage was prematurely induced by application of mechanical stress on the PCF using the AFM cantilever. At 50 minutes, a zoom-in shows the area outlined at 0 minutes (white box). At 1 hour 14 minutes, premature cell cleavage was induced by AFM-mediated application of force on the PCF (white



arrow). Between 1 hour 27 minutes and 3 hours 16 minutes, the prematurely cleaved new cell poles elongated and the corresponding sibling cells grew and divided (arrowhead at 3 hours 16 minutes, cropped and rotated to align with previous time points). **(b)** Force curve corresponding to forced cell cleavage at 1 hour 14 minutes. **(c)** Non-cropped and non-rotated image of time-lapse image shown in (a) at 3 hours 16 minutes.

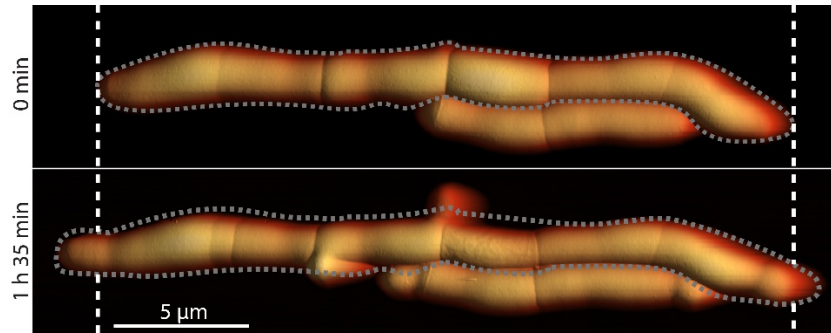


**Figure S 24. RipA-depleted cells form chains of cells that grow only at the free cell poles.** The two free (outermost) cell poles elongate and new septa continue to form, but failure of septated sibling cells to undergo cleavage, due to depletion of RipA, results in a cell-chaining phenotype. Growth occurs mainly at the free cell poles at the two extremities of a chain and occasionally at lateral budding locations (cf. 0 minutes and 1 hour 35 minutes). Grey dashed lines indicate the outline of the chain of cells. White dashed lines mark the positions of the free cell poles at 0 minutes.

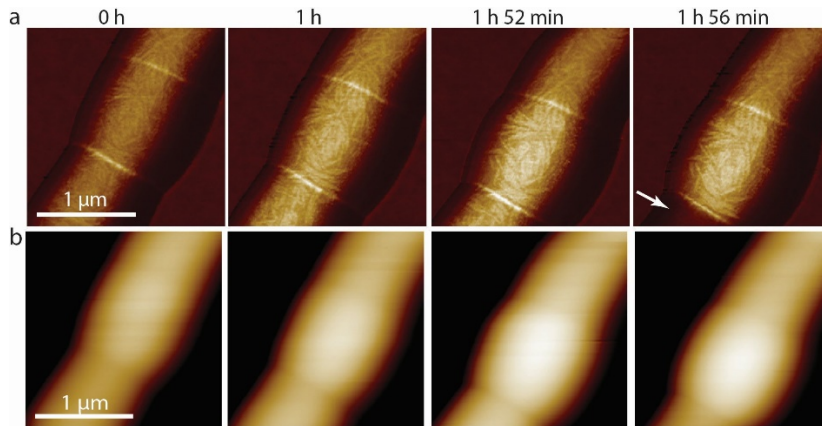


**Figure S 25. Height and stiffness changes of chained RipA-depleted cells.**

**(a)** Stiffness channel of a centrally located chained and non-elongating RipA-depleted cell over time. While the surface structural features do not change significantly, the measured stiffness at the PCF and the width of the non-elongating central cell increase over time, up to 1 hour 52 minutes (n=3). Upon loss of pressure of the neighboring sibling cell (1 hour 56 minutes, white arrow) the stiffness of the septum and the surviving sibling cell both decrease slightly. **(b)** Corresponding height images of (a). As the central chained cell becomes stiffer it also becomes higher over time.

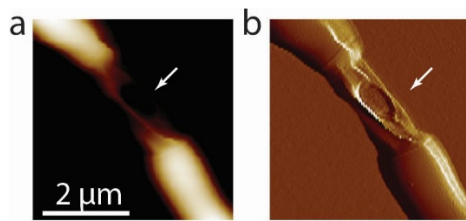


**Figure S 26. Cell wall failure of centrally located cells of RipA-depleted cell chains occurs in between the flanking PCFs.**

**(a)** AFM height image of a representative chained RipA-depleted cell that died (white arrow). **(b)** AFM error image showing a hole in the middle part of the cell that died.

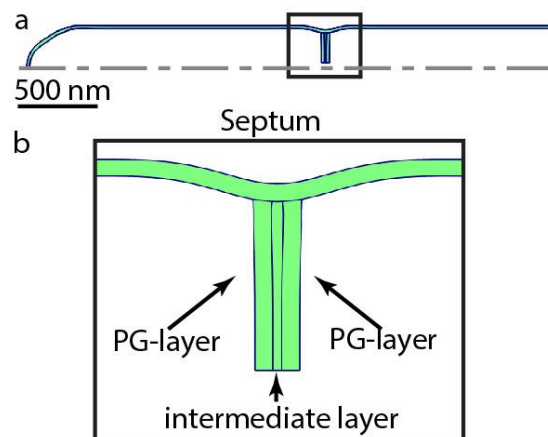


**Figure S 27. Finite element modeling of the PCF in a dividing cell.**

**(a)** Global cell geometry with a partially closed septum. The dotted line represents the axis of symmetry. **(b)** Zoom-in on the septum and PCF, showing the top part of the partially closed septum. The peptidoglycan (PG) layer on each side would become the new poles of the two respective daughter cells. These peptidoglycan layers are connected by a soft intermediate layer.



Similar data as represented in Figure	Experiment description	Total observations	Out of nr. of experiments
1a	PCF appearance before division	15	15
1b	PCF colocalizes with FtsZ	12*	12
1b	PCF site of septum formation	>20*	>20
S1	PCF site of localization of wag31	>10*	>10
1c	division scar at site of PCF	>15	>15
2	rapid (millisecond) division	>22	>22
3a-b	significant and steady increase of stiffness	22	22
3c-d	stiffness at PCF and sister cell with sorbitol/water	1	1
3e	pierce one sibling cell after cytokinesis	2	2
4a	induced cell division with viable cells	11	11
4b	induced cell division with dead cells	5	5
S15	center RipA-depleted cells become stiffer & wider	3	3
4c	Induced cleavage RipA-depleted cells	4	4
4c	free RipA-depleted cells grow out after induced cleavage	2	2

Supplementary Table 1



## **Part II**

Instrumentation developments for  
increasing resolution, speed or  
measurement modalities of combined  
AFM-optical microscopes



# ***Chapter E* openSIM: a 3D printed microscope add-on for structured illumination microscopy**

## **E.1. Preamble**

In Part I of this thesis, the resolution of the optical images was limited by the diffraction limit. Resolving the molecular mechanisms involved in pole growth and morphogenesis would greatly benefit from fluorescence microscopy techniques with higher resolution. In this chapter, we introduce an add-on for fluorescence microscopes to provide structured illumination and obtained SIM images with superresolution.

My contribution to this project is the design of the openSIM add-on (in collaboration with Theo Lasser) and its Labview interface, the data acquisition, in collaboration with Samuel Leitao (SIM-SICM image), Olivier Venzin and Andrew Oates (zebrafish embryo), Chiara Toniolo (infected macrophages), Antonius Chrisnandy (organoid) and Adrien Descloux (florescent beads). I reconstructed the SIM images using the SimToolbox<sup>32</sup>, with support from Jakub Popispil and Tomas Lukes.

I would like to thank David Nguyen for useful discussion and help with the CAD design of the openSIM 3D printed frame, and Guy Hagen for useful discussion about the optical design and hardware implementation for the openSIM.

## **E.2. Introduction**

Two main factors limit the performance of fluorescence microscopy: the diffraction limit<sup>12</sup> and the photon budget<sup>13</sup>. The resolution limit is due to the diffraction of light in the optical elements constituting a microscope. In practice, the resolution limit of conventional optical microscopes is limited to 200-300nm<sup>13</sup>. Superresolution imaging techniques, such as SMLM<sup>26,122</sup> (single molecule localization microscopy) or STED<sup>22</sup> (stimulated emission depletion), can overcome the diffraction limit by up to two orders of magnitude, and provide optical images with unprecedented resolution. However, increasing resolution comes at the cost of requiring a higher photon budget (i.e. a higher sample illumination intensity) to a level that is toxic and can induce cell death within seconds to minutes<sup>14,15,123,124</sup>. The photon budget

depends on the number and intensity of the fluorophores in the sample, the sensitivity of the sample to light, as well as in the goal of the experiment itself<sup>14,124</sup>: is sample damage acceptable? does it need to be a live cell? for how long do we need to image? is z-stacking required? Ultimately, the overall photon budget determines which technique can be used and which resolution can be obtained<sup>13</sup>. Structured illumination microscopy<sup>24</sup> (SIM) is a superresolution technique gaining interest for biological imaging, in particular for live cell imaging<sup>30,125–128</sup>. Although it provides only a moderate increase of resolution (two-fold maximum increase in lateral resolution for linear SIM<sup>24</sup>), it offers an increased resolution for a moderate cost in the photon budget<sup>13</sup>.

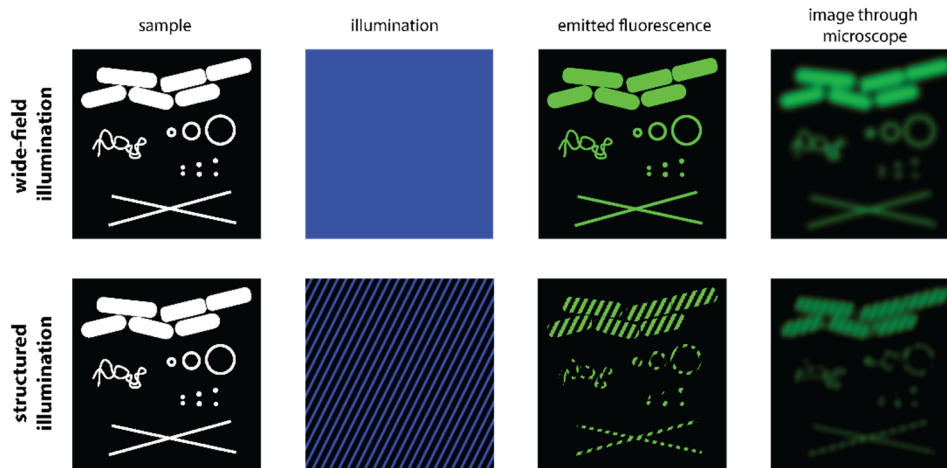
In addition to the two factors limiting the quality of the microscopy images – diffraction of light and limited photon budget, other factors have a large impact on the extent to which a microscopy technique will contribute to making scientific discoveries. The cost of the instrument and its complexity have a large impact on the number of scientific teams with access to the instrument for their own work<sup>13,129</sup>. Additionally, the versatility of the instrument directly determines the range of samples for which it will be useable<sup>13</sup>. Finally, accessible documentation of the instrument determines the extent to which other scientific teams will be able to build their own, tune the instrument for their own needs or improve it<sup>130</sup>. Several initiatives have introduced open-source microscopes, among which the light-sheet microscope openSPIM<sup>131,132</sup>, the wide field microscopes OpenFlexure<sup>133</sup> and Foldscope<sup>134</sup>, the 3D-printed optical toolbox UC2<sup>135</sup>, the AttoBright<sup>129</sup> for single-molecule detection, and the miCube<sup>136</sup> for single molecule localization microscopy. In addition to enabling fundamental discoveries as well as translational application for diagnosis<sup>137,138</sup>, these open-source microscopy initiative have a significant impact on the dissemination of optical design and instrument building techniques<sup>130,132</sup>.

Here we introduce the openSIM add-on, a structured illumination module to add SIM capability to conventional fluorescence microscopes. The openSIM integrates directly with the open-source SIMtoolbox<sup>32</sup> for SIM image reconstruction with a user-friendly interface. We demonstrate the versatility of the openSIM on a broad range of samples, from a whole pluricellular organism (zebrafish embryo) to the cytoskeleton of single cells. Additionally, we combined the openSIM with a scanning probe microscope, which demonstrate that the openSIM is a versatile system, and can be coupled to complex instruments without deteriorating their performance.

### **E.3. Results**

## Structured illumination microscopy: principle

A structured illumination microscope illuminates the sample with a predefined pattern (usually lines, Figure 29), instead of a constant illumination over the whole field of view (wide field illumination, Figure 29). In mathematical terms, the resulting image is the multiplication between the spatial distribution of fluorophores, and the excitation pattern.



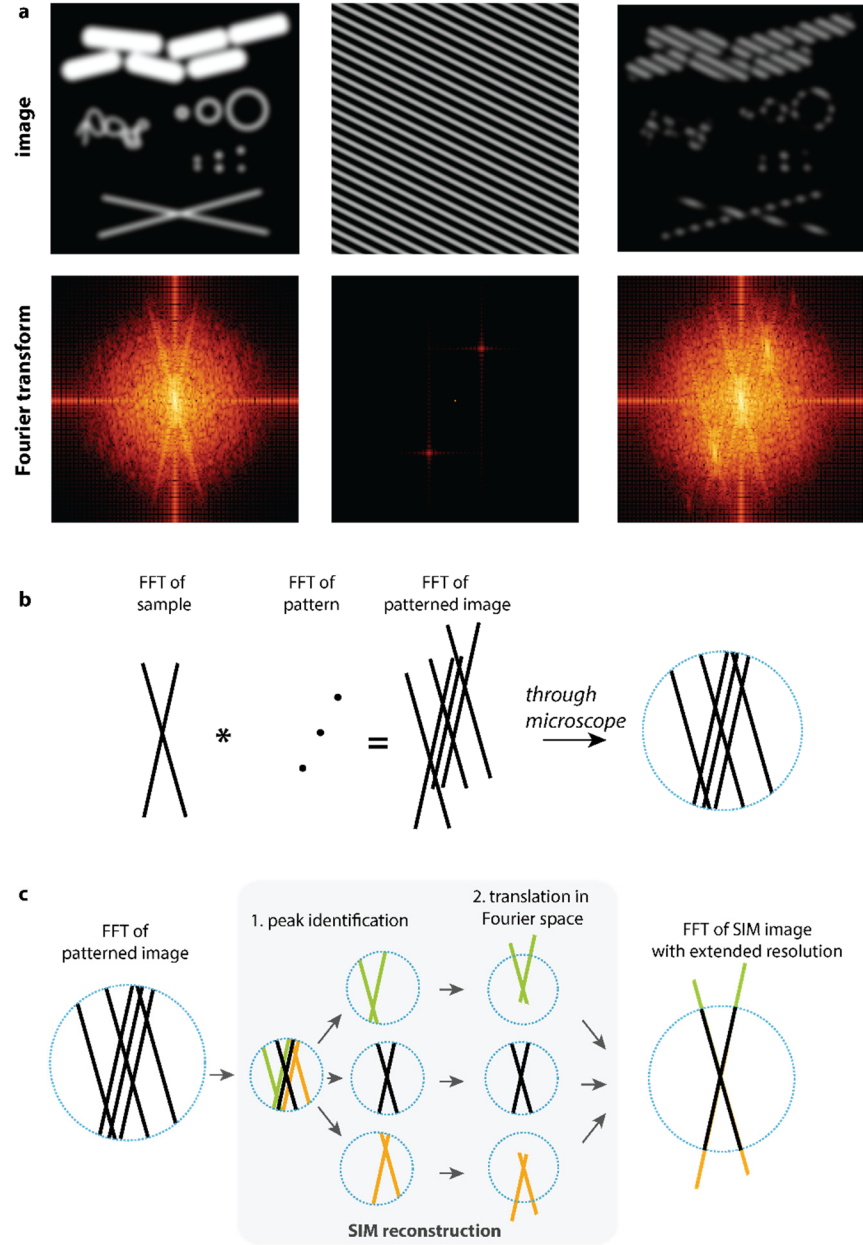
**Figure 29: Principle of structured illumination**

Illustration of the principle of wide field illumination compared to structured illumination. For wide field illumination, the whole field of view is illuminated with a constant excitation intensity, in response to which the fluorescent areas of the sample emit light. Due to the diffraction limit, a “blurred” version of the emitted fluorescence reaches the camera. For structured illumination, the excitation light is patterned, meaning that not all the areas of the sample are excited and emit light. In mathematical terms, the emitted fluorescence is the product of the fluorescent area of the sample and the excitation pattern. The emitted fluorescence image is “blurred” due to the diffraction limit in an identical manner as for wide field microscopy.

In the Fourier domain, multiplication becomes convolution, which means that the Fourier transform of the patterned image is the sum of the Fourier transform of the original image, plus two translated copies (Figure 30a,b). Because of the diffraction limit, the high spatial frequency information outside of the disk of radius  $R = \frac{1}{2\pi} \frac{2 \cdot NA}{\lambda}$  are blocked. (Figure 30b). High frequency information originally out of the disk have been translated within that disk and can now pass through the microscope (Figure 30b).

To reconstruct a superresolution image based on the patterned image, the three overlapping copies of the Fourier transform of the original image are identified (with a computer algorithm<sup>32,33</sup>). Each of the copies is translated back to the center in the Fourier domain (Figure

30c). We now have high spatial frequency information at a radius higher than  $R = \frac{1}{2\pi} \frac{2 \cdot NA}{\lambda}$ . This means that the reconstructed SIM image has a resolution higher than the diffraction limit (Figure 30c). Several images with different illumination patterns are combined to build an artificial superresolved image with a computational algorithm<sup>32,33</sup>.



**Figure 30: Principle of structured illumination microscopy reconstruction**

(a) Fourier transform of a simulated image, a pattern, and a simulated image with patterned excitation. (b) Illustration of the relationship between the Fourier transform (FFT) of the original image, the Fourier transform of the pattern and the Fourier transform of the image with patterned



excitation. The blue dotted circle represents the maximum spatial frequency that can be resolved by the microscope. The Fourier transform of the patterned image corresponds to the convolution of the Fourier transform of the original image with the Fourier transform of the pattern, i.e. the sum of three translated copies of the Fourier transform of the original image, since the Fourier transform of the pattern is three peaks. (c) Simplified representation of how structured illumination allows recovering information about higher spatial frequencies, outside of the blue circle. After peak identification, the copies of the image FFT are translated back to the center.

## **openSIM design**

The openSIM replaces the illumination source of a fluorescence microscope (being a lamp or laser based) and the associated shutter. Instead of providing homogenous illumination, the openSIM add-on projects the illumination patterns required to generate SIM images.

The openSIM add-on is based on optical designs using an LED (light emitting diode) illumination<sup>32,139,140</sup> instead of the lasers<sup>24</sup> used in most commercial SIM systems. It takes advantage of the recent developments of high-power LEDs and high resolution spatial light modulators, which are commercialized for the picoprojector<sup>141</sup> and virtual reality applications<sup>142</sup>. Three high-power LEDs provide 3-color excitation (blue, green, red) for the openSIM (Figure 31a). The light from the LEDs is collimated to illuminate a spatial light modulator. The spatial light modulator generates the pattern to be projected on the sample via the openSIM tube lens and the microscope objective (Figure 31a).

The tube lens is mounted on a linear translation stage to ensure that the spatial light modulator, the sample and the camera are in conjugated planes (Figure 31b). All other optical components are static and their position is imposed by a custom 3D printed frame (Figure 31b, c), which minimizes the complexity of the optical alignment procedures to assemble the openSIM. Additionally, 3D printed structures in plastic are lightweight, can be made for minimal cost and can be modified easily to customize or improve the microscope.

The assembled openSIM is a compact rectangular add-on that connects to the illumination port of a fluorescence microscope (Figure 31d, e). The openSIM connector to the microscope is interchangeable via a SM2 standard thread in order to be compatible with a large number of commercial microscopes, and connectors to Nikon, Olympus and Leica microscopes are commercially available.

## openSIM interface

For more automation, we have designed an instrument interface with Labview, which brings together on-the-fly pattern control, illumination color control, light intensity control, camera control (exposure time, camera gains, data saving...), and closed loop control of heat sink temperature. An interface box containing a DAQ and connectors allows for simple cabling between the elements of the system (openSIM add-on, camera, computer and optionally z-stage). Several analog and digital input and output lines of the DAQ remain available for customization by users.

The openSIM illuminates the sample with a chosen number of patterns, generally 9, 12 or 14, as illustrated in Figure 32a. The openSIM software allows the user to tune the pattern size optimal for the chosen microscope and sample. After acquisition of the images with patterned illumination, the data is saved in a format directly compatible with the open source SimToolbox<sup>32</sup> software for SIM image reconstruction.

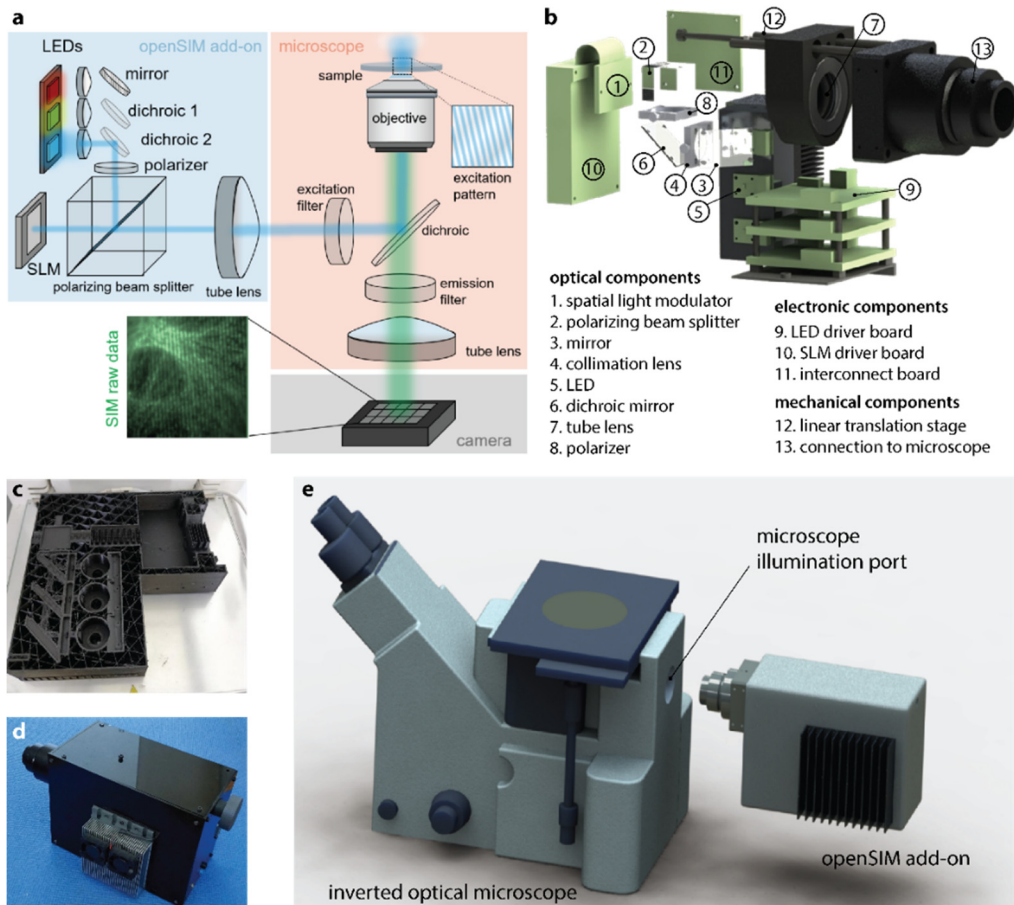


Figure 31: Design and assembly of the openSIM microscope add-on

(a) Schematic of the optical design of the openSIM add-on. LEDs are collimated to illuminate the spatial light modulator. The spatial light modulator generates a pattern by changing the polarity of the reflected light. The illumination pattern is transferred into the infinity space with a tube lens. (b) 3D rendering of the main optical, electrical and mechanical components of the openSIM. Only the components associated with the blue illumination channel are represented, for simplicity. (c) 3D printing of the openSIM body, which holds in position the components described in (b). (d) Photo of the openSIM. (e) 3D rendering illustrating the connection between the openSIM and an inverted optical microscope.

### **openSIM imaging**

To evaluate the performance of the openSIM, we imaged fluorescence beads (Figure 32b). After SIM reconstruction, the width of the point spread function was 169nm (average value on 20 beads), compared to 294nm for wide field illumination (Figure 32c). Some of the beads that were too close to each other to be resolved with wide field microscopy were resolved with the openSIM (Figure 32d): while one single large peak was visible on the wide field data, two distinct peaks were separated on the SIM image. In addition to increasing the resolution power of the microscope, SIM provides an optical sectioning effect (i.e. it reduces the contribution of out-of-focus light to the image). We show in Figure 32e a comparison between a wide field image and an openSIM image of an organoid. Only the cells in the focus plane are visible on the SIM image, while out-of-focus cells create a blurred background and lower the contrast of the wide field image.

We investigated the potential applications of the openSIM for a broad variety of biological samples. Actin and tubulin were imaged on a fixed pulmonary artery endothelial cell, using consecutively the blue and the green excitation channel of the openSIM (Figure 33a). With lower objective magnification, we imaged a mouse intestinal organoid (Figure 33b) and a whole zebrafish embryo (Figure 33c). We could also observe the distribution and organization of *Mycobacterium smegmatis* bacteria within macrophages during infection (Figure 33e). We also associated the openSIM to a scanning probe microscope system (SPM) for correlated imaging of the cell surface with SPM and the cytoskeleton with the openSIM (Figure 33e).

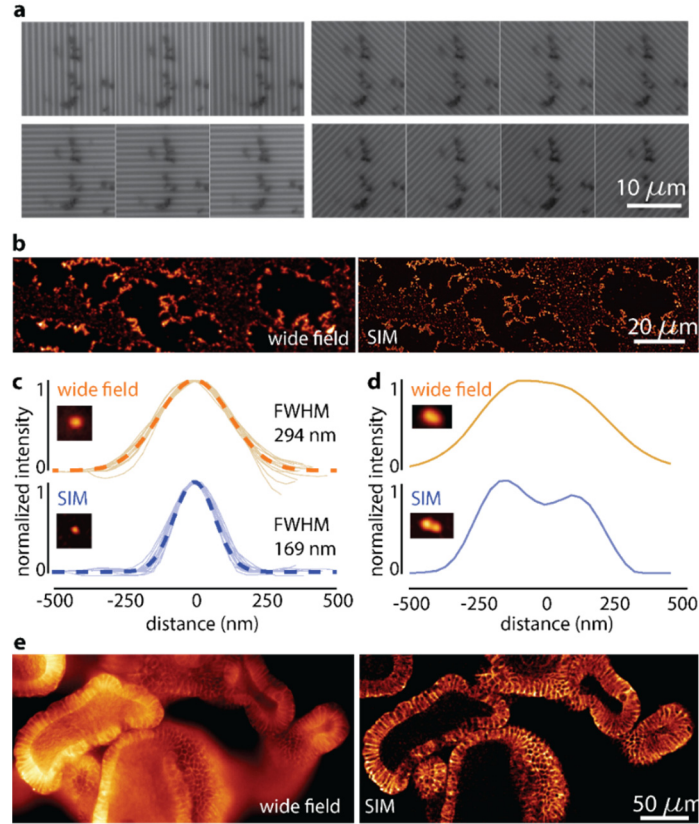


**Figure 32: Increase in resolution and optical sectioning when using the openSIM compared to wide field illumination**

(a) Patterned illumination with the openSIM on a thin fluorescent film. 4 angles are used and 14 different patterns. (b) Comparison between an image of 100nm beads with wide field blue illumination compared to the openSIM image. (c) Comparison between the point spread function of 20 isolated beads from (b), with wide field illumination (top) and with the openSIM (bottom). FWHM: full width at half maximum. Dotted line: average Gaussian fit. The picture inset is a representative point spread function. (d) Comparison between the openSIM and wide field illumination to resolve two individual beads placed close to each other. (e) Illustration of the optical sectioning effect when using the openSIM. On the wide field image, out of focus light is noticeable in the image; on the openSIM image, only the part of the sample directly in focus is visible. Sample: fixed mouse intestinal organoids labeled for E-cadherin.

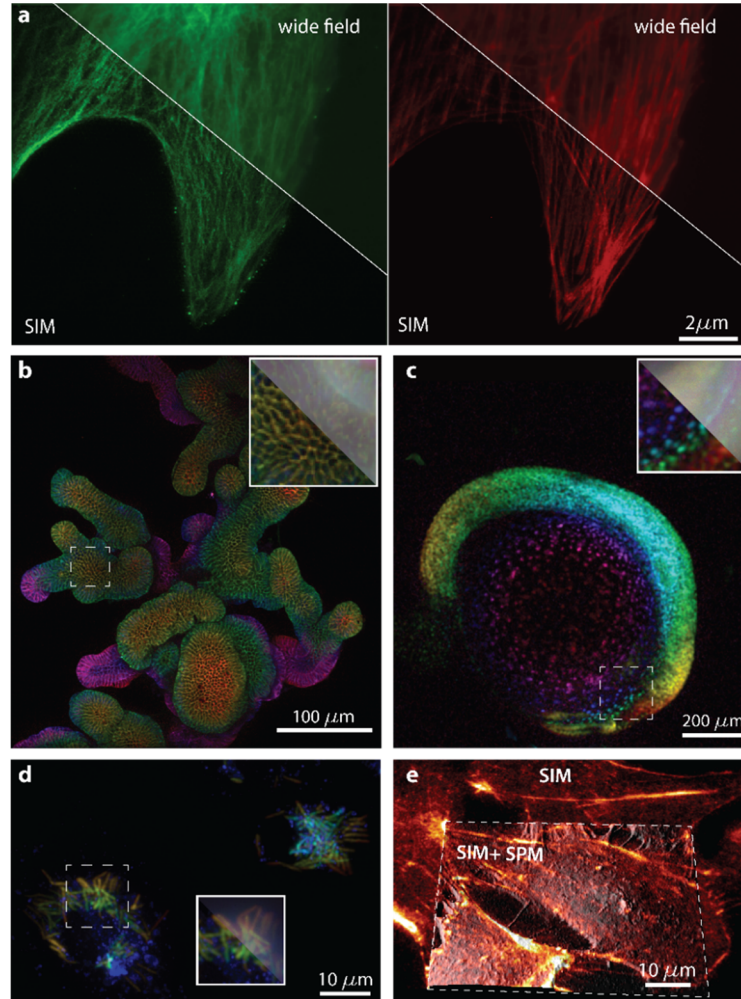


**Figure 33: openSIM images of fluorescent biological samples**

(a) Maximum intensity projection image of fixed bovine pulmonary artery endothelial cells. Left image:  $\alpha$ -tubulin labeled with BODIPY; right image: F-actin labeled with Texas Red-X phalloidin. Part of the image is not processed (equivalent wide field image, top right corner), while the bottom left corner is a SIM reconstruction. (b) Whole mount 3D color coded image of fixed mouse intestinal organoids labeled for E-cadherin (epithelial cell junctions). The inset represents a zoom in the area highlighted with a dotted square. Part of the image is not processed (equivalent wide field image, top right corner), while the bottom left corner is a SIM reconstruction. (c) 3D color coded image of a live zebrafish embryo with cell nucleus staining. (d) 3D color-coded image of fixed macrophages infected with *Mycobacterium smegmatis* bacteria. (e) Combined SIM and scanning probe microscopy (SPM) image of fixed actin-stained COS-7 cells. The SIM image is a maximum intensity projection, overlaid as a skin on the topography image obtained with a scanning ion conductance microscope.

#### E.4. Discussion

The openSIM add-on is a tool to upgrade conventional fluorescence microscopes with SIM capability, which increases resolution and optical sectioning.

Because it relies on incoherent LED light sources, the openSIM does not match the performance of the most advanced commercial or non-commercial SIM systems. The achievable projected pattern modulation depth is lower than what can be achieved with coherent laser light sources, because the pattern is projected through the diffraction-limited microscope, while it can be generated directly on the sample by interference of two coherent laser beams<sup>128</sup>. The excitation intensity is lower than what can be achieved with laser excitation because of the intensity losses associated with using a non-punctual, diverging light source<sup>143</sup>.

However, the openSIM requires minimal alignment procedures, and costs more than one order of magnitude less than a commercial SIM instrument. We show that replacing the wide-field microscope illumination with an openSIM add-on improves the quality of the obtained images (Figure 32), particularly in terms of optical sectioning (Figure 32e).

Studying biological organisms often requires dedicated equipment, which accommodate for the sample's requirements for its physiology (such as ambient temperature and CO<sub>2</sub> control, humidity control) and often combine several instrumentation modalities (patch clamp, electrode microarrays, microfluidic systems,...). We demonstrated the versatility of the openSIM by combining it with a scanning probe microscope, for correlated imaging with both SIM and SPM modalities (Figure 33e). Because it is an add-on to pre-existing fluorescence microscopes, the openSIM does not require acquiring a new microscope, but increases the performance of pre-existing resources.

## **E.5. Materials and methods**

### **Optical components for the openSIM**

Three high power PT54 LEDs (Luminous Devices) are used to generate the illumination light. The light emitted by the three LEDs is deflected by three mirrors (#43-875, Edmund optics), is collimated using 50mm lenses (#66-018, Edmund optics), and combined into one optical path with dichroic mirrors (#69-898, #69-900, Edmund optics). A polarizer selects for the specific polarization reflected by the polarizing beam splitter (#49-002, Edmund optics). Then, the light reaches the spatial light modulator (QXGA-3DM-STR, ForthDimension). A tube lens (ITL180-A, Thorlabs), of the same brand as the commercial microscope being used (IX71 and IX81, Olympus), is placed in such a way that the SLM is in the back focal place of

that tube lens. Commercially available connectors (SM2Y1, LCP11, Thorlabs) were used to connect the openSIM to the illumination port of the microscope.

### **Mechanical components for the openSIM**

The openSIM was designed with the Solidworks software. The openSIM was printed with the makerbot print software and the Makerbot Replicator 3D printer, as well as with the Cura software and the Ultimaker 3 Extended 3D printer. PLA was used as a printing material.

The position of the tube lens is adjusted using a linear translation stage. The translation stage was built with two linear shafts (SSFJ6-100, Misumi), a precision feed screw (XBRF6, Misumi) and two wire springs (WF8-40).

### **Electronic components for the openSIM**

The LEDs are powered and controlled using the boards and connectors supplied in the DK114N3 development kit (Luminous devices). A custom interconnect board was designed to facilitate the connection between the elements of the openSIM.

An interface box containing a DAQ (USB-6000, National Instruments) and connectors allow for simple cabling between the elements of the system (openSIM add-on, camera, computer and optionally z-stage). Several analog and digital input and output lines of the DAQ remain available for customization by users.

### **Labview interface and openSIM control**

We have designed a complete instrument interface with Labview, which brings together on-the-fly pattern control, illumination color control, light intensity control, camera control (exposure time, camera gains, data saving...), closed loop control of heat sink temperature. It also saves the detailed acquisition parameters and pre-formats the data to be compatible directly with the open source SimToolbox SIM processing algorithm.

### **Sample preparation**

The organoids were derived from Lgr5-eGFP-iRES-CreERT2 mouse intestinal crypts and grown in 3D Matrigel culture under expansion conditions (ENRCV)<sup>144</sup> which was adapted from Gjorevski *et al.*<sup>145</sup>. The preparation of imaging sample was adapted from Gjorevski *et al.*<sup>145</sup>. In short, the organoids were fixed with 4% paraformaldehyde (PFA) in PBS 1X. The fixed samples were permeabilized with 0.2% Triton X-100 in PBS 1X (1 h, room temperature)

and were blocked with 0.01% Triton X-100 in PBS 1X containing 10% goat serum (3 h, room temperature). The organoids were then stained using a monoclonal anti-E cadherin antibody (ab 11512; Abcam) followed by secondary antibody Goat- $\alpha$ -Rat Alexa Fluor 568 (A-11077; ThermoFisher Scientific). Extensive washing steps were performed subsequent to each antibody incubation step. The imaging slide was prepared by mounting the stained organoids on glass coverslips (#1) with addition of mounting medium Fluoromount-G® (0100-01; SouthernBiotech).

Bovine pulmonary artery endothelial (BPAE) cells with stained F-actin and tubulin were acquired from ThermoFisher (FluoCells prepared slide #2). F-Active is labeled with Texas RED-X phalloidid, and tubulin is labeled with anti-bovine  $\alpha$ -tubulin mouse monoclonal 236-10501 conjugated with BODIPY FL goat anti-mouse IgG antibody.

Bone marrow derived macrophages (BMDMs) were differentiated by seeding  $10^6$  bone marrow cells from C57BL/6 mice in petri dishes and maintaining them in DMEM supplemented with 10% heat-inactivated fetal bovine serum (HI-FBS), 1% sodium-pyruvate, 1% GlutaMax and 20% L929-cell-conditioned medium as a source of granulocyte/macrophage colony stimulating factor. After 1 week of cultivation at 37°C with 5% CO<sub>2</sub>, the adherent differentiated macrophages were gently detached from the plate using a cell lifter and resuspended in DMEM supplemented with 5% HI-FBS, 1% sodium-pyruvate, 1% GlutaMax and 5% L929-cell-conditioned medium.  $10^4$  cells were seeded in a 35 mm cell culture micro-dish with a coverslip bottom (IBIDI) and allowed to adhere for 24 h before infection. A GFP expressing *Mycobacterium smegmatis* (*Msm*) strain was cultured at 37°C in Middlebrook 7H9 (Difco) supplemented with 10% ABS, 0.5% glycerol, and 0.02% tyloxpol. 1 ml of culture at OD<sub>600</sub> 0.5 was pelleted, concentrated 5 times in the medium of the BMDMs and filtered with a 5  $\mu$ m filter to obtain a single cell suspension. BMDMs were infected with the single cell suspension with MOI 1:1 and incubated at 37°C with 5% CO<sub>2</sub>. After 4 h the cells were washed extensively with DMEM to eliminate extracellular bacteria and incubated at 37°C with 5% CO<sub>2</sub> for 48 h to allow the infection to proceed. Before imaging, the cells were stained with CellMask™ Orange (Invitrogen) according to the manufacturer's protocol and fixed with 4% formaldehyde in PBS for 30 minutes at room temperature.

African green monkey kidney fibroblast-like cells (COS-7), purchased from ATCC were grown in DMEM without phenol red medium (Sigma Aldrich), containing 10% fetal bovine serum. The #1.5 cover glass coverslips were cleaned with piranha solution and coated with fibronectin from bovine plasma (0.5 $\mu$ M/ml). Then the cells were fixed with 4% PFA in



1xPBS(pH=7.4) for 10min at room temperature and washed twice for 5min with PBS (pH=7.4). Prior to staining, the fixed cells were incubated with PBS containing 1% BSA for 30min to reduce nonspecific background. To visualize F-actin, the phalloidin staining solution (Fluor 488 phalloidin Thermofisher) was placed on the coverslip for 20 minutes at room temperature.

Zebrafish were maintained according to standard procedures and embryos were staged according to Kimmel et al<sup>146</sup>. Embryos were obtained from outcrosses of Tg(Xla.Eef1a1:H2B-mCherry) to WT fish by natural spawning and raised in fish water (pH  $7.8 \pm 0.1$ , conductivity  $500 \mu\text{S} \pm 50 \mu\text{S}$ ). For imaging, embryos were de-chorionated and laterally aligned in conical depressions in a pad of 2% low-melting agarose (Sigma) that was cast in a glass-bottom dish (Matek, 35 mm), as in Herrgen et al<sup>147</sup>.

### **Combined SIM/SICM microscopy**

Scanning probe microscopy was performed with a custom made scanning ion conductance microscope (SICM). The sample was actuated in X and Y by a piezo-stage (Piezosystemjena TRITOR102SG). The capillary was moved in Z by a home built actuator, operated in hopping mode. The hopping height was  $1\mu\text{m}$  at 100Hz rate. The current setpoint used in the hopping actuation was 99% of the normalized current recorded. Images with 256x256 pixels were generated.



# ***Chapter F* Photothermal Actuation for Tip-Scanning Atomic Force Microscopy**

## **F.1. Preamble**

Conventional optical microscopy techniques tend to have low resolution and high speed, while conventional AFM tends to have comparatively high resolution and low speed. In the previous chapter, we introduced the openSIM, as a mean to increase the optical resolution. In this chapter, we explore how photothermal actuation could increase the AFM imaging speed.

For this study, I designed and built a photothermal actuation module with input from Adrian Nievergelt and Jonathan Adams, integrated the photothermal actuation module in a commercial AFM setup, acquired the data and made the numerical simulation of PORT to quantify the impact of the tracking error.

## **F.2. Introduction**

Atomic force microscopy (AFM) is a unique tool for quantitative imaging at the micro- and nano- scale. AFM imaging can reach sub-nanometer resolution, but it is generally a slow process; acquiring a single image can take several minutes<sup>11,148</sup>, although several groups have proposed novel techniques to increase the AFM imaging speed<sup>47,48,149</sup>. Several imaging modes have been successively developed, such as contact mode<sup>150</sup>, tapping mode<sup>151–153</sup> and off-resonance tapping<sup>47</sup> (ORT, also called Pulsed Force mode<sup>20</sup>, PeakForce QNM<sup>21</sup>, HybriD mode, etc.) . Contact mode has been used to obtain high resolution images of proteins such as bacteriorhodopsin<sup>154</sup>. But contact mode often damages both the cantilever tip and the sample surface, due to the high normal and friction forces applied<sup>153</sup>. Tapping mode has been introduced to lower the forces applied to the sample, and minimize sample damage<sup>151–153</sup>. ORT lowers further the applied forces, and allows for direct measurement of the mechanical properties of the sample<sup>47,82,155</sup>. In both tapping mode and ORT, the cantilever is actuated in a sinusoidal fashion, generally using a piezoelectric actuator.<sup>148</sup> A feedback loop controls the vertical position of the cantilever in order to keep constant the cantilever deflection (for contact mode)<sup>150</sup>, the cantilever oscillation amplitude (for tapping mode)<sup>151–153</sup> or the applied maximum force (for ORT)<sup>47,82,155</sup>, while raster scanning the sample. Both in tapping mode and in ORT, high-speed AFM imaging requires a high actuation bandwidth to excite the cantilever.

Several techniques have been developed for high frequency actuation of AFM cantilevers<sup>150,156–159</sup>. In most systems, inertial piezoelectric actuation induces a motion of a cantilever holder, which in turn induces a motion of the cantilever<sup>152</sup>. The actuation bandwidth of a mechanical system is inversely proportional to the mass of the object in motion, and the sum of the masses of the cantilever holder, the cantilever body and the cantilever itself is significantly higher than the mass of the cantilever alone, which tends to lower the bandwidth. To move only the cantilever and therefore reduce the actuated mass, actuation systems have been directly integrated into so-called self-actuated cantilevers, using microfabrication techniques<sup>156,159–163</sup>. Additionally, self-actuation provides a stable actuation amplitude over a broad range of frequencies, whereas the amplitude response of inertial piezoelectric actuation is low at a low frequencies<sup>156,164</sup>, and, at higher frequencies, shows sharp peaks due to the resonances of the coupling between the inertial piezoelectric actuator and the cantilever itself (sometimes referred to as a “forest of peaks”)<sup>152</sup>.

Photothermal actuation is an alternative technique to self-actuation, and consists in focalizing a laser at the base of a bimorph cantilever to locally increase the temperature and induce a thermal bending moment<sup>157,165</sup>. Like self-actuation, photothermal actuation moves the cantilever only<sup>157,165</sup>; unlike self-actuation, photothermal actuation does not rely on specific cantilevers and is compatible with most commercially available cantilevers. Photothermal actuation has recently been combined with ORT (Photothermal Off-Resonance Tapping, PORT) for gentle high-speed imaging and was used to image the SAS-6 centriole protein assembly with unprecedented resolution and imaging speed<sup>47</sup>.

Until now, photothermal actuation has only been implemented in XY or XYZ sample scanning systems, in which the sample is attached to a scanner and translated with a raster motion under the cantilever tip. Sample-scanning AFM configuration is limited to low-weight samples to keep the actuated mass low, and the actuation bandwidth high. In contrast, in a tip-scanning AFM configuration, the sample is immobile and the cantilever is in motion during the scan. In addition to being compatible with higher-weight samples, the tip-scanning configuration allows for a high versatility: in-situ imaging of large samples is possible, biological samples can be placed in an incubation chamber to keep them in physiological conditions<sup>11,18</sup>, and tip-scanning AFMs can be combined with other microscopy techniques such as optical microscopy for simultaneous imaging in both modalities<sup>17,166</sup>, and scanning electron microscopy<sup>167,168</sup>. Here we investigate the design challenges for photothermal actuation in a XYZ tip-scanning AFM and propose a simple design modification to a widely used commercial tip scanning AFM.

### F.3. Results

Photothermal actuation consists in using a laser to heat locally at the base of a bimorph cantilever (Figure 34a, bottom panel). If the coefficient of thermal expansion of the two layers is different, a bending moment is induced<sup>157,165</sup>. The deflection of the cantilever is controlled in real time by varying the power of the laser<sup>157,165</sup>. With photothermal actuation, only the cantilever itself is in motion, contrary to piezoacoustic actuation (Figure 34a, top panel).

We modified a commercial tip-scanning AFM with built-in photoacoustic cantilever actuation (Dimension Icon AFM head, Bruker), and added a custom photothermal actuation module (Figure 34b). The photothermal actuation module was inserted in place of the original readout laser of the commercial tip-scanning AFM head (Figure 34b). The photothermal actuation module collimates the readout laser and the photothermal actuation laser and combines them using a dichroic mirror (Figure 34c). The ball joint placed under the photothermal actuation module controls the position on the cantilever of both the readout and the photothermal excitation laser (Figure 34b). The ball joint placed on the photothermal actuation module controls the position of the drive laser relative to the readout laser (Figure 34c). Two micrometer screws and a ball joint allow the user to position the readout laser at the free end of the cantilever. Two other micrometer screws and another ball joint allow the user to adjust the relative position of the photothermal laser compared to the readout laser, and place the photothermal actuation laser at the base of the cantilever.

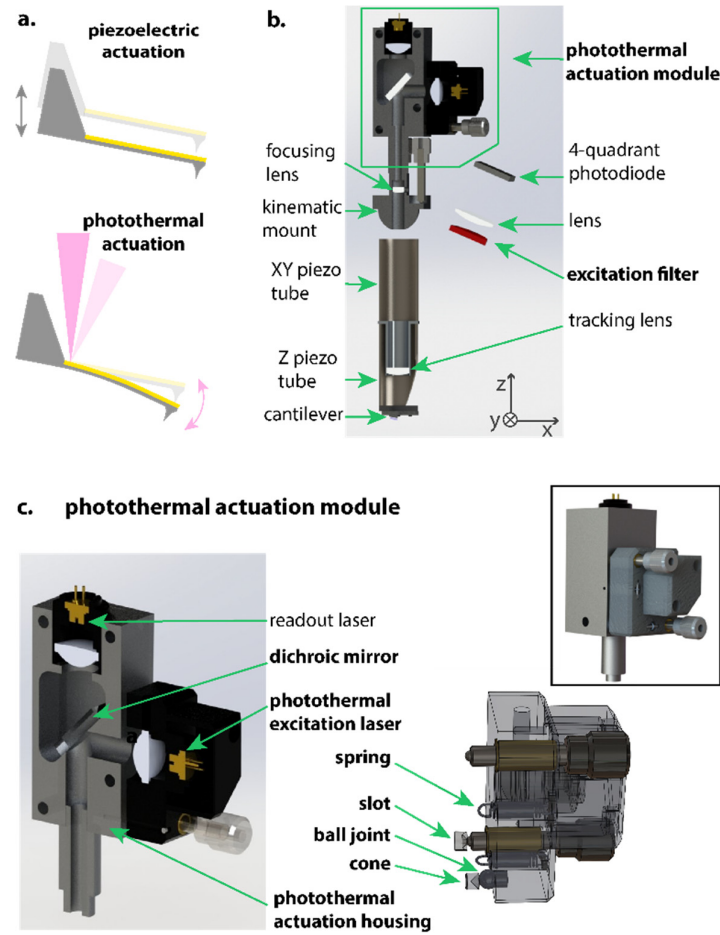


**Figure 34: Implementation of photothermal actuation in a tip-scanning AFM**

(a) Schematic representation of inertial piezoelectric and photothermal actuation. The readout laser is not represented for both cases. For photothermal actuation, a bending moment is induced by locally increasing the temperature of the cantilever using a focused laser beam (excitation laser, pink). (b) 3D representation of a commercial tip-scanning AFM, fitted with a custom photothermal excitation module. The elements added to the commercial AFM are indicated in bold letters. (c) 3D representation of the photothermal actuation module. Left: cutout view, highlighting the position of the optical components. Bottom right: ball-joint for adjusting the position of the photothermal laser with the two micrometer screws.

In a tip-scanning AFM, the cantilever is translated in the three dimensions to track the surface of a static sample. The readout laser and the photothermal excitation laser have to remain positioned on the cantilever during the scan motion; this constitutes the main challenge for implementing laser readout or excitation in a tip-scanning AFM. In the original Dimension Icon AFM scanner, the laser tracking is achieved using two lenses (number 4 and 5 in Figure 35a). The focusing lens creates an image of the readout laser

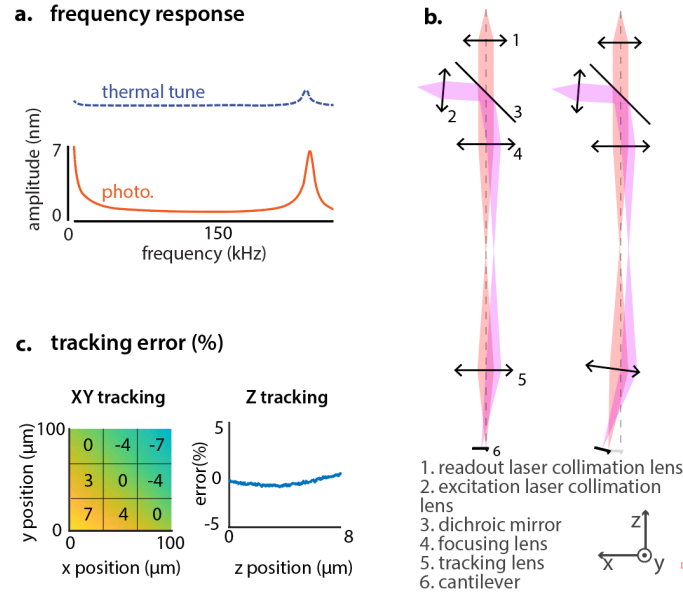


**Figure 35: Photothermal cantilever actuation**

(a) Optical path of the readout (orange) and excitation (pink) lasers through the AFM tip-scanning head fitted with a photothermal actuation module. Left: the cantilever is in the center of the scan. Right: cantilever is away from the center. (b) Variation (in %) of the measured deflection amplitude, while using a constant photothermal amplitude and far away from the sample surface. Left: XY scan area of  $100 \times 100 \mu\text{m}$  and constant Z position. Right: Vertical scan of  $12 \mu\text{m}$  and constant XY position. (c) Evolution of the measured deflection amplitude as a function of the actuation frequency, with no actuation (thermal tune, blue) and photothermal actuation (orange). Cantilever: Fastscan C, in air.

light source and the excitation laser light source at the junction between the XY piezo tube and the Z piezo tube (Figure 34b, Figure 35a). The tracking lens generates an image of this virtual point source on the cantilever. The tracking lens is rigidly connected to the XY piezo tube (Figure 34b), which ensures that the optical axis of the tracking lens remains aligned with the cantilever during the scan motion (Figure 35b). We made use of the same two lenses for cantilever tracking with both the readout laser and the excitation laser (Figure 35b).

We quantified how well the two-lens tracking system keeps the readout laser and the excitation laser positioned on the cantilever during the scan motion. In photothermal tapping mode, two effects will change the measured deflection amplitude. One is the change in measured deflection amplitude due to non-perfect readout laser tracking. The second is the change in actual deflection amplitude due to less effective photothermal actuation when the drive laser does not perfectly track the cantilever. In order to quantify these two effects individually, we compared the frequency response of a Fastscan C cantilever in air actuated with the inertial piezoelectric and the photothermal method (Figure 35c) at different XY positions.

To do so, we modulated the current of the drive laser with a sine wave of constant amplitude, and read the corresponding deflection amplitude of the cantilever using the readout laser. We subsequently measured the variations of the measured deflection amplitude, while translating the cantilever over the whole range of the piezo tube actuator. The cantilever tracking error of the deflection amplitude was less than  $\pm 7\%$  of the nominal value over the horizontal XY range of our AFM head ( $100\mu\text{m}$ ), and less than  $\pm 0.8\%$  over the vertical Z range ( $8\mu\text{m}$ ) (Figure 35b).

We imaged a calibration grating with our modified AFM head, with photothermal actuation both in tapping mode (Figure 36).

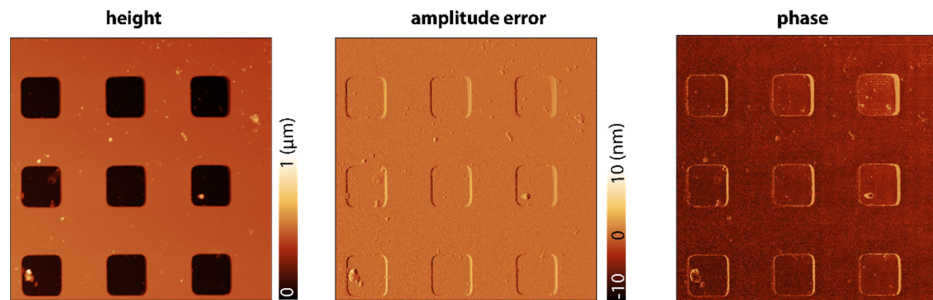


**Figure 36: Imaging in air with photothermal actuation in tapping mode**

AFM height, amplitude error and phase images of a calibration grating. Tapping mode with photothermal actuation. Image size:  $34 \times 34 \mu\text{m}$

For PORT, the local interaction curve is calculated at every point of the sample surface by subtracting the cantilever dynamics (free deflection). The applied peak force is deduced (Figure 37c), as well as the local mechanical properties. The applied force is compared to the force setpoint. The difference is the input of a proportional integral controller (PI controller), and the controller calculates the voltage to be sent to the piezoelectric actuator to reduce the error. This feedback loop ensures that the applied force remains close to the setpoint while scanning (Figure 37d).



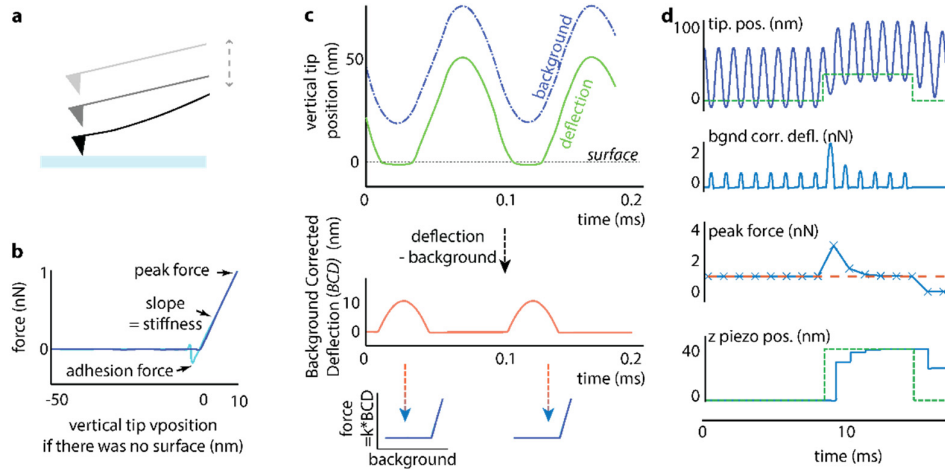


**Figure 37: Measuring topography and mechanical properties with AFM in off-resonance tapping (PORT) mode**

(a) Illustration of the cantilever (black) being deflected when it is in contact with the sample surface (light blue). (b-d) are numerical simulations made with a custom Matlab script, based on Newton's law, assuming linear interaction forces, and transferred in the discrete temporal domain with Euler approximation. (b) Simulated force curve, from which sample mechanical properties (stiffness, adhesion) are deduced. In PORT, interaction curves are obtained by plotting the cantilever deflection (multiplied by the cantilever spring constant) as a function of the background (i.e. free deflection). As long as the cantilever is away from the surface, no force is applied. When the cantilever touches the surface, the force applied increases with the indentation, proportionally to the sample stiffness. (c) Simulated PORT measurement of the sample mechanical properties without scanning. During PORT, the cantilever is actuated with a sine wave signal. When the cantilever is away from the surface, the cantilever motion is therefore a sine wave (dotted blue line, background). When the cantilever is brought closer to the surface, the cantilever motion deviates from a sine wave (green line). The difference between the free deflection and the deflection signal in contact gives the background corrected deflection signal (orange), from which interaction curves are calculated (blue).  $k$ : cantilever stiffness. (d) Simulated PORT measurement of the sample topography and mechanical properties while scanning a line of a sample. The topography of the simulated sample is a step represented by a green dotted line. The background corrected deflection is calculated in real time to determine the peak force applied. The peak force is compared to the force setpoint (1 nN here, indicated by the red dotted line). The controller adapts the voltage sent to the piezoelectric actuator to keep applying a constant force. The position of the piezoelectric actuator ("z piezo pos.") reflects the topography of the sample and is our output, i.e. one line of the AFM image.

We sought to quantify the effect of the cantilever tracking error on the measurement of the peak force applied. Because of the tracking error, the measured free amplitude is not constant in XY (Figure 35c). In PORT, the free amplitude is measured only once, at the center position of the scan. This is

equivalent to doing the background subtraction with a sine wave of amplitude too low or too high for points that are away from the center of the scan. With a numeric simulation, we show that the tracking error has a significant impact on the measured peak force (Figure 38, about 20% error on the peak force for an amplitude error of 7%, while imaging an infinitely stiff sample with PORT at 1kHz, 50nm amplitude, and 1nN setpoint). While the error is large for large scans, it will be much smaller for smaller scans (tracking error of less than 1% for scans of less than 10 $\mu$ m, which corresponds to an error on the measured peak force of 1.8% with the same simulation parameters as for Figure 38).

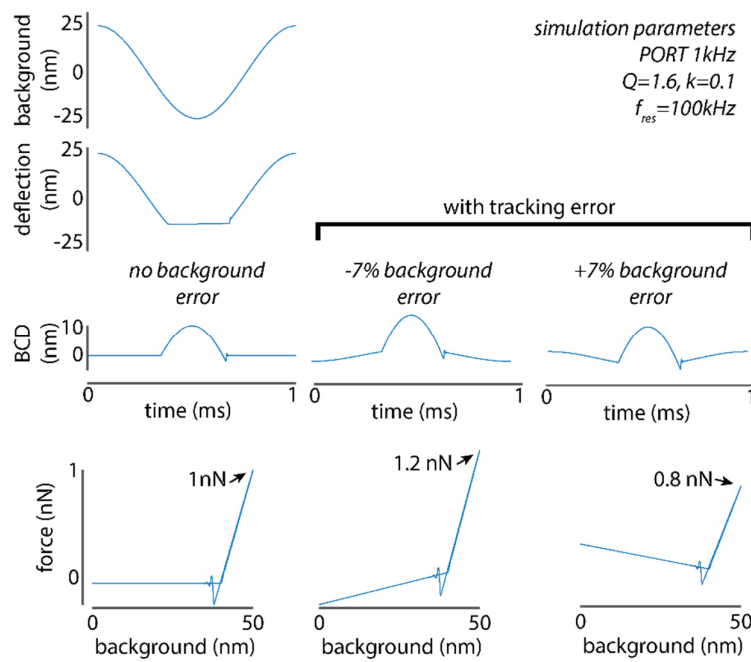


**Figure 38: Impact of the tracking error for PORT**

When there is a mismatch between the recorded background and the real background (for example because of the tracking error), the background corrected deflection (BCD) is no longer a flat line when the cantilever is away from the surface. Additionally, there is an error in the measured peak force (1nN setpoint here). Numerical simulations made with a custom Matlab script, based on Newton's law, assuming linear interaction forces.

We imaged a calibration grating with our modified AFM head, with photothermal actuation in PORT mode (Figure 39a). Collagen fibers were also imaged in PORT mode, and the collagen sub-structures (fibrils) were resolved (Figure 39c). We compared inertial piezoelectric actuation in ORT with photothermal actuation in PORT for high-speed imaging. In both ORT (inertial piezoelectric actuation) and in PORT (photothermal actuation) modes, an interaction curve is recorded at each point of the sample (Figure

39b). The sample is tracked accurately for a scan speed of 2 Hz, in both ORT (2 kHz excitation, maximum value set by the manufacturer; Figure 39d, top-left panel) and PORT (16 kHz excitation; Figure 39d, top-right panel). When the scan speed is increased from 2 Hz to 10 Hz, the quality of the sample tracking is low in ORT, and a significant amount of parachuting is visible compared to the image acquired in PORT mode.

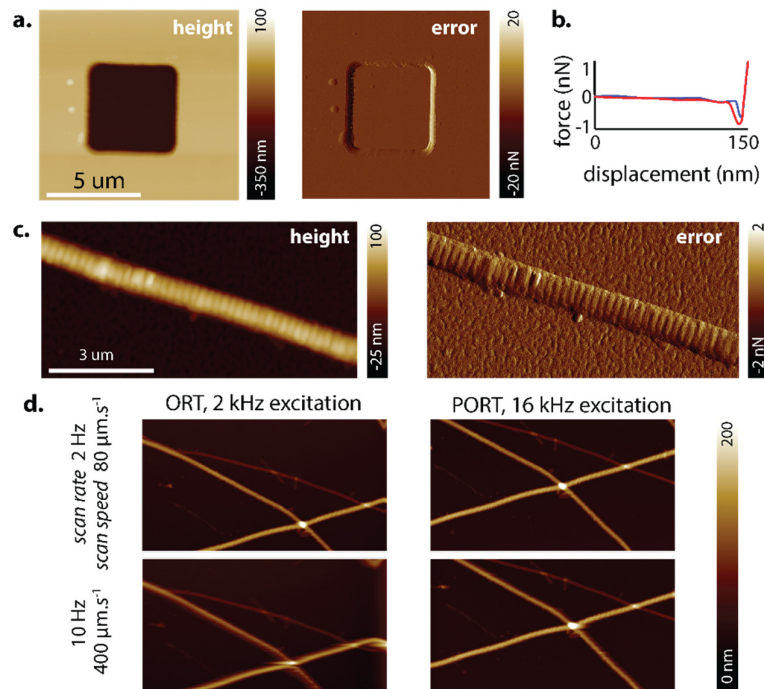


**Figure 39: Imaging in air in photothermal off-resonance tapping (PORT) mode**  
 (a) AFM height and peak force error images of a calibration grating. Photothermal off-resonance tapping. Image size: 11.1x11.1 μm (b) Example of an interaction curve obtained while scanning in PORT. (c) PORT height and error image of a mouse collagen fiber. Excitation frequency: 8 kHz. Scan rate: 1 Hz. Image size: 3x1.5 μm. (d) AFM height images of a mouse collagen fiber in ORT with inertial piezoelectric actuation at 2 kHz (left) and in PORT with photothermal actuation at 16 kHz (right). Image size: 20x10 μm

#### F.4. Discussion

Several groups, including ourselves, have shared designs to add photothermal actuation to sample-scanning AFM microscopes<sup>169–171</sup>, because photothermal actuation generates a clean cantilever response in low-Q environments<sup>170</sup>, and can actuate cantilevers at high speed<sup>171</sup>. Here, we report the first implementation of photothermal actuation in a XYZ tip-scanning AFM. We modified a commercial tip-scanning AFM head with inertial piezoelectric actuation (Dimension Icon head, Bruker), and added to it a custom photothermal actuation module. Our design therefore does not require major modification

to add photothermal actuation to an AFM head with optical readout<sup>172</sup>, and photothermal actuation could be added to other commercial or non-commercial AFM microscopes using our method.

The tracking error of the readout and drive lasers affects significantly the peak force measurement in PORT. This is particularly true for large scan sizes ( $>10\mu\text{m}$ ). The error on the peak force measurement could be reduced either by adjusting the position of the focusing lens and the tracking lens to minimize the tracking error. We could also compensate for the tracking error via a simple calibration step. One would record the amplitude of the measured free deflection of the cantilever covering the XY scan area, for a constant photothermal excitation amplitude. The inverse of the ratio between the measured amplitude and the amplitude setpoint would be used as a multiplication factor to correct for the tracking error for each XY position. Ideally, these two methods would be combined to minimize the peak force measurement error.

Thanks to photothermal actuation, the actuation bandwidth for PORT is decoupled from the bandwidth of the piezoelectric Z actuator used for tracking the sample topography. We therefore benefit from an extra degree of freedom to improve the AFM imaging speed. During PORT (and ORT in general), the applied force is measured every period of the excitation. If the excitation frequency is  $f$ , the delay between each measurement of the applied force is  $T=1/f$ . A delay in a feedback loop (or a phase lag) is known to cause instability, therefore limiting the achievable scan speed<sup>173</sup>. Increasing the excitation frequency with PORT reduces the delay in the feedback loop, which results in an improvement in the scanning speed (Figure 39).

The efficiency of photothermal excitation depends on several main factors<sup>174</sup>: the cantilever bimorph effect, the value of the excitation frequency compared to the photothermal actuation cutoff frequency, and the width of the cantilever compared to the size of the photothermal laser spot.

As shown in Figure 35a, the efficiency of photothermal actuation efficiency drops as the excitation frequency increases. More precisely, the photothermal actuation efficiency stays relatively constant up to the photothermal cutoff frequency, and drop for higher frequencies. We calculated the cutoff frequency for several commercial cantilevers (Figure 40). It shows that it will be possible to have high photothermal excitation frequencies for cantilever with a small length ( $9\mu\text{m}$  length for an AC10) and made out of a material high thermal conductivity (such as silicon). Such cantilever should therefore be preferred for high-speed photothermal actuation.

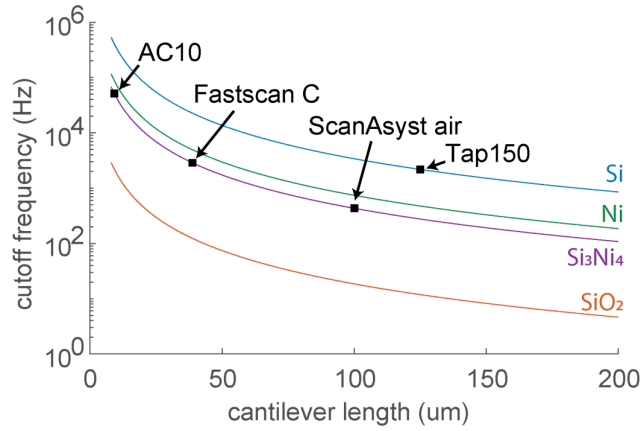


**Figure 40: Estimated photothermal actuation bandwidth for several commercial cantilevers**

The cutoff frequency of cantilevers depends mainly on the cantilever length and the cantilever material. The cutoff frequency was calculated using the following equations and assuming that the cutoff frequency is mainly limited by thermal diffusivity:  $D_{th} = \frac{k_{th}}{\rho \cdot c_p}$ ,  $\tau = \frac{l^2}{2 \cdot D_{th}}$ ,  $f_{cutoff} = \frac{1}{2\pi\tau}$  where  $D_{th}$  is the thermal diffusivity,  $\rho$  is the cantilever material density,  $c_p$  is the specific heat capacity of the cantilever material, and  $l$  is the cantilever length.

However, if the cantilever is smaller than the focus spot of the photothermal actuation laser, the efficiency will drop. It is therefore important to focus the photothermal laser with a high numerical aperture optical system, which minimizes the size of the laser spot. For an AC10 cantilever, the cantilever width is 2  $\mu\text{m}$ , which means that a spot size lower than 2  $\mu\text{m}$  is needed. This can be achieved for a numerical aperture of  $NA = \frac{\lambda}{2 \cdot w} = \frac{0.6 \mu\text{m}}{2 \cdot 2 \mu\text{m}} = 0.15$ , where  $\lambda$  is the wavelength of the light used,  $w$  is the width of the cantilever, and  $NA$  is the numerical aperture of the system constituted by the focusing lens and the tracking lens.

Overall, this means that photothermal actuation will be most beneficial for high excitation frequencies, which requires small cantilevers made out of a thermally conductive material. This will required optimizing the optical design of the AFM head to increase the numerical aperture and reduce the spot size.

High-speed PORT AFM microscopy is a powerful tool to image the molecular dynamics of protein assembly<sup>47</sup>. However, it is sometimes challenging to link the AFM topography data to biological function. Because the sample remains static during tip scanning PORT imaging (TS-PORT), it is possible to combine high-speed TS-PORT AFM and optical superresolution microscopy. Optical fluorescence microscopy can be used to determine the biological function using fluorescence labels to tag specific proteins, and optical

superresolution techniques can now reach a precision in the nanometer range<sup>17,26,175</sup>. Combining high-speed TS-PORT and superresolution optical microscopy will enable the observation of protein assembly in real time, with both high spatiotemporal resolution (AFM) and high specificity (fluorescence microscopy).

## F.5. Materials and methods

### AFM

We used a Bioscope head with a Nanoscope III controller (Bruker) as well as an Icon head with a Nanoscope V controller (Bruker for this study). The signal access module (Bruker) was used to access the photothermal excitation signal and send it to a laser driver (Newport 505B) controlling the photothermal excitation laser diode. The wavelength of the readout laser diode was 645nm, and the wavelength of the excitation laser 686nm. Each laser diode was collimated with a 4.6mm aspheric lens (A390-A). The lasers were combined using a short-pass dichroic mirror (HL6750MG, Thorlabs). A bandpass filter prevents the excitation light from reaching the photodiode (86-941, Edmund Optics).

AFM data was processed using Gwyddion<sup>68</sup> and Nanoscope Analysis (Bruker).

### Collagen sample

A freshly cleaved mica disk was glued on a metal disk. Collagen fibers were extracted from a rat tail tendon. The tendon was gently pulled apart using sharp tweezers to expose the individual collagen fibers, and the collagen fibers were spread on the mica disk. The sample was then carefully dried with compressed air.

### PORT simulation

The PORT simulation was done with a custom MATLAB program. The model relied on the application of Newton's law and the assumption of linear interaction between the cantilever tip and the sample surface. Given that the system is approximated as being linear, the superposition principle applies:  $X_{tot}(t) = X_0 \cdot \sin(2\pi ft) + X(t)$  where  $X_{tot}(t)$  is the position of the tip of the cantilever over time,  $X_0 \cdot \sin(2\pi ft)$  is the sinusoidal motion of the tip imposed by photothermal actuation alone, and  $X(t)$  is the contribution of the surface interaction to the cantilever tip position. The cantilever is modeled as a simple resonant system:  $m\ddot{X} + \alpha\dot{X} + kX + u(X_s - X) \cdot k_s(X - X_s) = 0$  where  $m$  is the equivalent mass of the cantilever,  $\alpha$  is the damping coefficient,  $k$  is the spring constant of the cantilever,  $X_s$  is the position of the surface,  $k_s$  is the stiffness of the surface and  $u(X_s - X)$  is a step function, equal to 1 when  $X_s - X > 0$  and else equal to 0.

0. These differential equations are resolved iteratively after being transferred in the discrete time domain using Euler approximation:  $\dot{X} \rightarrow \frac{X_i - X_{i-1}}{dt}$  and  $\ddot{X} \rightarrow \frac{X_i - 2X_{i-1} + X_{i-2}}{dt^2}$ .





# ***Chapter G* Volcano-shaped SPM probe for combined force-electrogram recordings from excitable cells**

## **G.1. Preamble**

AFM is most often used to scan and acquire images of a sample. Its nanometer precision make is a convenient tool for other applications, such as single cell micromanipulation or killing (Chapter B). Here, we combine an AFM head with a volcano-shaped probe for electrogram measurements.

This is a verbatim copy of an article that has been published in a peer reviewed journal<sup>176</sup>. Permission was granted by the publisher to reproduce the article in this thesis dissertation. Further permissions related to the material excerpted should be directed to the ACS.

Desbiolles, B. X. E., Hannebelle, M. T. M., Coulon, E. De, Bertsch, A., Rohr, S., Fantner, G. E. & Renaud, P. Volcano-Shaped Scanning Probe Microscopy Probe for Combined Force-Electrogram Recordings from Excitable Cells. (2020).  
<https://pubs.acs.org/doi/10.1021/acs.nanolett.0c01319>

For this study, I participated in the design of the cantilever and cantilever holder for electronic interfacing. I also used the cantilevers with nanovolcanoes fabricated by Benoit Desbiolles to measure the displacement of beating cardiomyocytes, while Benoit Desbiolles was recording simultaneous extracellular electrograms. Both of us analyzed the data.

## **G.2. Abstract**

AFM based approaches have led to remarkable advances in the field of mechanobiology. However, linking the mechanical cues to biological responses requires complementary techniques capable of recording these physiological characteristics. In this study, we present an instrument for combined optical, force, and electrical measurements based on a novel type of scanning probe microscopy cantilever composed of a protruding volcano-shaped nanopatterned microelectrode (nanovolcano probe) at the tip of a suspended microcantilever. This probe enables simultaneous force and electrical recordings from single cells. The complex three-dimensional microelectrode was manufactured at the wafer-scale following a straightforward non-conventional nanofabrication process based

on ion beam etching redeposition. Successful impedance measurements on mechanically stimulated neonatal rat cardiomyocytes in-situ were achieved using these nanovolcano probes. Furthermore, proof of concept experiments demonstrated that extracellular field potentials (electrogram) together with contraction displacement curves could simultaneously be recorded. These features render the nanovolcano probe especially suited for mechanobiological studies aiming at linking mechanical stimuli to electrophysiological responses of single cells.

### **G.3. Introduction**

Mechanobiology is an emerging field at the frontiers between biology and engineering that focuses on studying the role of mechanical properties of biological specimens and the effect of forces acting on those specimens in physiology.<sup>177–180</sup> Over the last three decades, atomic force microscopy (AFM)<sup>181</sup> has been widely used to map mechanical properties and responses of biological systems to mechanical cues.<sup>83,182–185</sup> AFM exhibits force sensitivities in the piconewton range<sup>186</sup> with nanometer-scale lateral resolutions.<sup>187</sup> It is compatible with a broad range of biological samples ranging from single molecules to cells and tissues. The mechanical properties of mammalian cells were extensively studied using AFM based approaches<sup>188–195</sup>. For instance, cell differentiation<sup>196,197</sup> or fibrosis<sup>198</sup> was shown to be dependent of the substrate stiffness. AFM was also used to study mechanical stresses during bacterial division<sup>18</sup>, turgor pressure<sup>108</sup> and adhesion<sup>199</sup>.

The key challenge in mechanobiology consists of linking functional responses of complex biological systems to mechanical stimuli.<sup>200</sup> AFM based approaches alone are essentially blind to mechanically triggered biological responses such as changes in cellular electrophysiology and, accordingly, complementary techniques need to be developed to convey multimodal capabilities to the AFM. Presently, this is achieved by combining AFM with optical microscopy of cells expressing or being loaded with fluorescent indicators of physiological parameters like transmembrane potentials<sup>201</sup> (e.g., voltage-sensitive dye, voltage-sensitive fluorescent proteins) or ion concentrations<sup>202</sup> (e.g., calcium indicators). As an example, cells expressing mechanosensitive ion channels can be mechanically stimulated by AFM and their electrophysiological response be monitored in real time using fluorescent calcium imaging.<sup>203</sup> Disadvantages of optical techniques include, apart from the requirement of cell manipulation and the introduction of indicators that themselves may adversely affect cellular function, phototoxicity that limits the duration of experiments.<sup>204</sup> Other studies combined AFM recordings of contraction displacement of cardiomyocytes with extracellular field potential (electrograms) measurements provided by multielectrode arrays (MEA).<sup>205,206</sup> Similarly, planar patch-clamp devices were used to record transmembrane potentials of mechanically stimulated cells.<sup>207,208</sup> Even though

direct recordings of electrical activities were achieved, the limitation of these techniques mainly consist in their complexity and the lack of freedom when selecting a specific cell, because that cell has to be located exactly on top of a given microelectrode. To overcome these challenges, Ossola *et al.* used the FluidFM probe<sup>209,210</sup> as a force-controlled nanopipette to simultaneously record force and ion channel activities in a whole-cell configuration, therefore pioneering the field of AFM-based force-controlled electrophysiology.<sup>211</sup> In this study, the electrical access to the cell was granted via an embedded microfluidic channel filled with saline solution that connected the tip opening to the recording system. Depending on the experimental question asked, this methodology has the disadvantage of wash-out of intracellular small molecules thereby compromising, e.g., the integrity of the second messenger signaling cascade.<sup>212</sup> Moreover, a fluidic access to the cell significantly complicates the experimental setup as fluidic connections and pressure controllers are needed. Additionally, the embedded microchannel significantly limits the minimal cantilever thickness achievable; therefore limiting the bandwidth and the sensitivity during force measurements.

Cells are constantly interacting with each other and with their environment through chemical, mechanical, and electrical factors. The latter include mechanical forces, cellular stiffness, electrical potentials, and ion currents that determine the cell behavior. Here we propose a new fluidic-free instrument that combines, within a single probe, measurement capabilities for optical, electrical, and mechanical factors determining cell functions. Central to the device is a novel type of probe for scanning probe microscopy (SPM) consisting of a protruding three-dimensional (3D) volcano-shaped microelectrode at its apex that enables fluidic-free combined force and electrophysiological recordings from single cells or tissues. The device is termed ‘nanovolcano probe’ as it integrates our recently developed nanovolcano electrode<sup>34,213</sup> at the tip of an AFM cantilever.

Force and impedance were concurrently measured when engaging onto neonatal rat cardiomyocytes to confirm the proper functioning of the probe in a conventional AFM setup. Thereafter, the nanovolcano probe was used to investigate whether it could be used to record simultaneously mechanical and electrophysiological activity from single cells. Successful recording of electrograms together with cardiomyocyte contraction displacements demonstrated that the nanovolcano probe enables combined force-electrogram recordings. These findings render the nanovolcano probe particularly suitable for mechanobiological studies aiming at linking electrophysiological responses with mechanical stimuli at the single-cell level.

#### **G.4. Results**

## Microfabrication

The nanovolcano probe concept and design are summarized in Figure 41-A. The inner surface of the 8  $\mu\text{m}$ -wide nanovolcano consists of a large electrodeposited platinum-black electrode that minimizes the access impedance to the cell. The outside of the 6  $\mu\text{m}$ -high structure is covered with a 20 nm-thick insulating  $\text{SiO}_2$  layer that prevents current leaks from the electrode. Furthermore, a 5 to 10 nm-thick gold nanoring stacked in-between two Ti layers and functionalized with self-assembled monolayers of alkanethiols forms the site of contact with the cell membrane and is thought to optimize the cell-electrode interface<sup>214–218</sup>. The microelectrode is attached to a 2.2  $\mu\text{m}$  thick  $\text{SiO}_2$  cantilever, that is coated on the backside with a 50 nm-thick Cr-Au reflective layer allowing for conventional optical beam deflection measurement in an AFM.<sup>219</sup>

As illustrated in Figure 41-B, conventional ion beam etching was used to pattern 3  $\mu\text{m}$ -wide conductive tracks on a Si substrate covered with a 2  $\mu\text{m}$  thick layer of thermally grown  $\text{SiO}_2$  that was subsequently insulated with 200 nm of sputtered  $\text{SiO}_2$ . The nanovolcano was then manufactured at the tip of the Ti-Pt-Ti-Au-Ti- $\text{SiO}_2$  pattern by ion beam etching redeposition<sup>34,220</sup>. To this end, openings with a diameter of 8  $\mu\text{m}$  were patterned into a 6  $\mu\text{m}$ -thick negative photoresist layer. During ion beam etching, a part of the etched material from the substrate was redeposited onto the photoresist sidewalls, thereby creating the multilayered nanovolcano wall after resist stripping by  $\text{O}_2$  plasma. The  $\text{SiO}_2$  cantilever was then defined, with a wider circular shape close to the tip to maximize the laser reflection, and released by reactive ion etching (RIE). Due to the compressive stress accumulated in the  $\text{SiO}_2$  layer during thermal growth, the released cantilever bent in the opposite direction from the substrate. In a final fabrication step, stressed layers of Cr-Au (50-50 nm) were evaporated onto the backside of the cantilever to compensate for their bending and to render them reflective.

Scanning electron microscope (SEM) images of the finalized nanovolcano probe are shown in Figure 41-C-E. As illustrated by Figure 41-C and D, the  $\text{SiO}_2$  cantilever dimensions were chosen such as to ensure a stiffness comparable to cells (for the nanovolcano probe: 0.45 N/m). The nanovolcano electrode placed at the tip of the cantilever was fabricated with a relatively large diameter to ensure a low electrode-electrolyte impedance while permitting a sufficient lateral resolution to perform experiments at the single-cell level. The height of the nanovolcano guaranteed that the nanovolcano touched the sample first during AFM manipulation. The inset in Figure 41-E shows the 7 nm-thick gold nanoring flanked by two titanium layers in the middle of the 70 nm-thick multilayered nanovolcano wall. A complete characterization of the

nanovolcano wall cross-section by transmission electron microscopy combined with energy dispersive X-ray spectroscopy can be found in our previous work.<sup>34</sup>

The nanovolcano probe was interfaced to a custom-made AFM holder (see Supplementary Information, section 1) and platinum-black was locally electrodeposited into the nanovolcano to decrease its electrode-electrolyte impedance. A complete electrochemical characterization of the nanovolcano probe is provided in Supplementary Information, section 2.

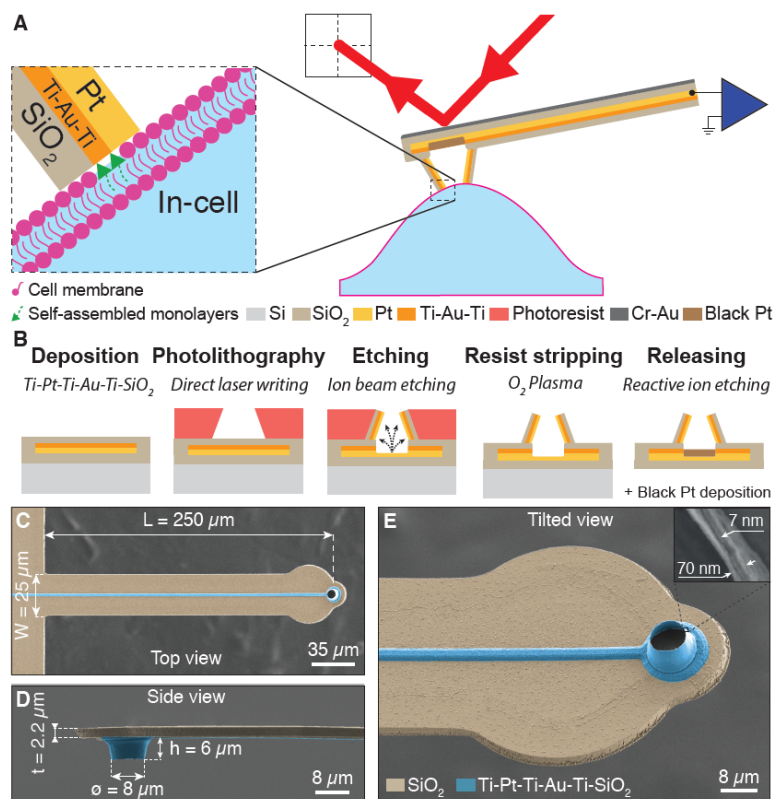


**Figure 41: Concept and microfabrication of the nanovolcano probe.**

A) Schematic drawing showing the nanovolcano probe in contact with a cell. The cantilever deflection as well as the electrical signal from the nanovolcano are measured simultaneously. The insert shows the cell-electrode interface in detail. B) Microfabrication process used to manufacture the nanovolcano probe. Insulated metallic tracks are patterned onto a 2  $\mu$ m thick SiO<sub>2</sub> layer covering the Si substrate. During ion beam etching, the material etched from the substrate is redeposited on the photoresist sidewalls therefore forming the nanovolcano after resist stripping. The SiO<sub>2</sub> cantilever is subsequently defined and released by reactive ion etching. C-E) SEM images showing top view, side view, and tilted view (angle of 30°) of the nanovolcano probe. The volcano electrode structure and the conductive tracks are colored in blue.

## Force and electrical measurements on neonatal rat cardiomyocytes

The nanovolcano probe was mounted on a custom-made setup composed of a tip-scanning AFM mounted above an optical inverted microscope and a custom sample holder to keep the biological sample in physiological conditions (see Materials and Methods section). Experiments with neonatal rat cardiomyocytes were performed to validate that both force and impedance signals can be recorded simultaneously by the nanovolcano probe.

Cardiomyocytes were cultured at low density for 48 hours prior to the experiment. During experiments, the cantilever position and deflection were recorded while the nanovolcano probe was repeatedly brought in contact with a cell of interest followed by pulling away using the AFM piezoelectric actuator. A typical result of such an experiment is shown in Figure 42-A: the probe was initially lowered towards the cell by  $\sim 11\ \mu\text{m}$  while applying a maximal force of 772 nN before being withdrawn again at  $t = 0.25\ \text{s}$ . The maximally applied force is three orders of magnitude larger than the force usually used as a setpoint for non-destructive AFM imaging (a few hundred pN). However, because the contact area between the nanovolcano rim and the cell under investigation is about three orders of magnitude larger than the contact area of a pyramidal cantilever tip, local strain and stress applied to the cell are below the cell damage threshold for the nanovolcano measurements as well. The ramp curve depicting the force-position relation (Figure 42-B) shows a typical smooth increase of the force between  $7\ \mu\text{m}$  and  $11\ \mu\text{m}$  indicating indentation of the cell by the nanovolcano. The hysteresis visible in the force curve is due to mechanical energy dissipated by the cell, whereas the step during withdrawing highlights the detachment of the cantilever from the cell.

Simultaneous with the force measurements, square wave amperometry was performed through the nanovolcano probe to observe the impedance variation when engaging onto a cell. A 5 mV square wave oscillating at 20 Hz was applied between the nanovolcano and a counter electrode located in the bath while measuring the resulting current. Capacitive current peak amplitudes and current pulse time constants were extracted and plotted in Figure 42-C as the tip approached the cell and then was withdrawn again. Both the 'high frequency impedance' and the time constants significantly increased when the probe came close to the cell. Impedance increased to 189 % and time constants to 160 %. No variations of the resistive current at low frequency was observed. In Supplementary Information, section 2, an electrical equivalent circuit of the cell-electrode interface is presented that illustrates the increase of the impedance and time constant as the probe approached the cell. Figure 42-D shows the variation of impedance with respect to the cantilever position.

A significant increase of high frequency impedance can be noted for cantilever displacements larger than 3  $\mu\text{m}$  that saturates at 10.5  $\mu\text{m}$ . Force-controlled impedance measurements conducted on non-beating human embryonic kidney (HEK) cells showed similar behaviors compared to cardiomyocytes, therefore suggesting that spontaneous contractions did not significantly influence the impedance measurements. Amperometric measurements allow for an earlier cell detection compared to force recording. Forces in the nN range were applied and currents with <10 pA amplitude were measured. This experiment was successfully repeated on seven different HEK cells and seven primary rat cardiomyocytes with two different cantilevers. Experimental results are summarized in Supplementary Information, sub-section 3.1.

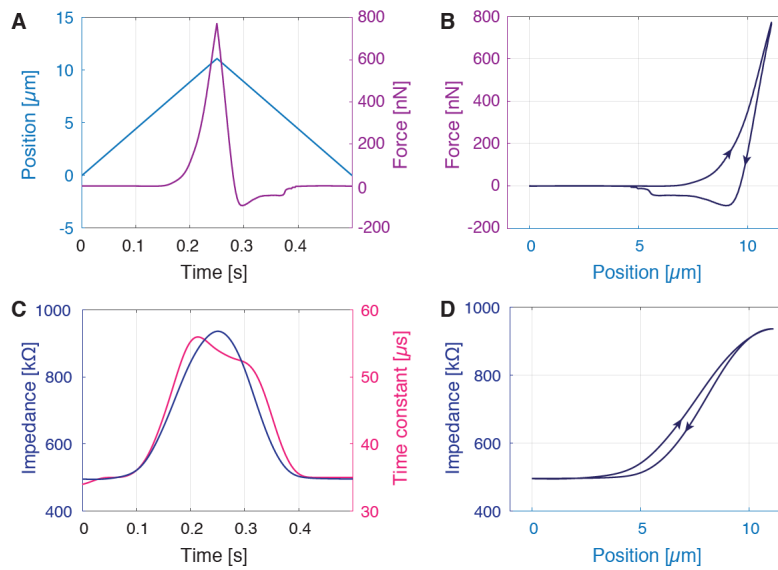


**Figure 42: Force and electrical measurements on neonatal rat cardiomyocytes.**

A) Evolution of the nanovolcano cantilever position along the z-axis (left axis, light blue) and the resulting force applied to the cell (right axis, purple) with time. The first contact with the cell was initiated at  $t \approx 0.15$  s and position  $\sim 7 \mu\text{m}$  (maximum force = 772 nN). B) Ramp curve showing the force – position relationship. C) Evolution of the nanovolcano probe impedance (left axis, dark blue) and time constant (right axis, magenta) with time, measured by pulsed amperometry. D) Ramp curve showing the impedance – position relationship.

### Recording of cardiomyocyte contraction displacements using the nanovolcano probe.

Following the basic characterization of the nanovolcano probe, we tested its suitability for performing measurements of contraction displacements from spontaneously active primary neonatal rat ventricular cardiomyocytes. Cardiomyocytes were cultured at low

density for 48 to 72 hours prior to the electrophysiological recordings. The time-lapse images in Figure 43-A show one contraction of a spontaneously active cell studied with the nanovolcano probe maintained at a constant height. The blue pixels illustrate variation of intensity compared to the previous frame and therefore highlight the contraction-related movement of the cell. At  $t_0$ , the cardiomyocyte is quiescent. It initiates its contraction at  $t_{1,2}$ , stays contracted during  $t_{3,4}$  before relaxing again at  $t_{5-9}$ . The bottom panel in Figure 43-A represents the sum of the derivative for every pixels from the video in the region of interest presented in the top panel. This measure is conventionally used to quantify cardiomyocyte contractions<sup>221,222</sup> and serves as visual control for the nanovolcano measurements.

Cantilever displacements recorded in parallel are shown in Figure 43-B (top panel). The first contraction (corresponding to the time-lapse data) has an amplitude of 367 nm and a duration (at 10 % of the amplitude) of 646 ms. Similarly, the second contraction had an amplitude of 422 nm and displayed a duration of 614 ms. The panel below depicts the corresponding derivatives (absolute values). For both activations, contraction rates amounted to  $2.9 \mu\text{m/s}$  and  $3.5 \mu\text{m/s}$ , respectively. Relaxation was slower and amounted to  $1.5 \mu\text{m/s}$  and  $1.7 \mu\text{m/s}$ , respectively. The absolute derivatives of the cantilever displacement and those derived from the video data reliably matched. Additional contraction displacement characteristics measured from five different primary rat cardiomyocytes using the nanovolcano probe are presented in Supplementary Information, sub-section 3.2.

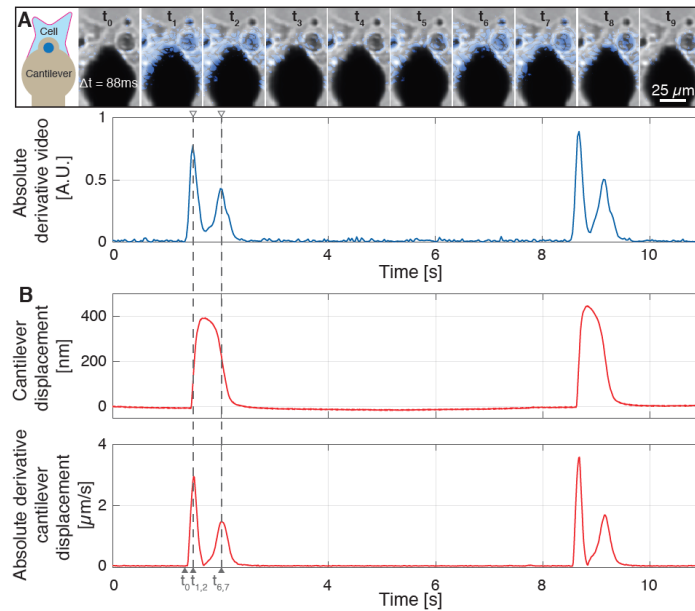


Figure 43: Recording of contraction displacements from primary rat cardiomyocytes.



A) Upper panel: Schematic drawing (left) and series of time lapse images showing the nanovolcano probe engaged on a beating cardiomyocyte (right). Pixels showing intensity variations compared to the previous frame are highlighted in blue and indicate cardiomyocyte contraction.<sup>221,222</sup> Lower panel: Temporal evolution of the sum of the derivatives of every pixels for the entire area depicted in the upper panel. B) Cantilever displacement (top panel) and its absolute derivative (bottom panel) from the same cardiomyocyte. The first contraction starts at  $t_0$  and corresponds to the time-lapse images presented in A). The cantilever displacement absolute derivative matches the absolute derivative of the video signal.

### Simultaneous recording of contraction displacements and electrogram from cardiomyocytes using the nanovolcano probe.

Neonatal rat ventricular cardiomyocytes were also used to investigate the possibility of recording contraction displacement together with electrophysiological activity using the nanovolcano probe. As demonstrated in Figure 44, both contraction displacements (cf. Figure 44-A) and electrograms (cf. Figure 44-B) could simultaneously be recorded by the nanovolcano probe. Electrograms showed typical biphasic shapes and displayed amplitudes ranging from  $-38 \mu\text{V}$  to  $-75 \mu\text{V}$  that slightly preceded contraction. During a 25 s long recording session, contraction amplitudes of  $250 \pm 35 \text{ nm}$  with a duration at 50 % amplitudes of  $225 \pm 35 \text{ ms}$  (average  $\pm$  standard deviation) were observed together with electrograms showing downstroke amplitudes of  $47 \pm 9 \mu\text{V}$  ( $N = 49$ ). Electrograms recorded from a second cell with the same probe produced similar results (cf. Supplementary Information, sub-section 3.3). This demonstrates the possibility to perform successive electrogram recordings at different location using a single probe.

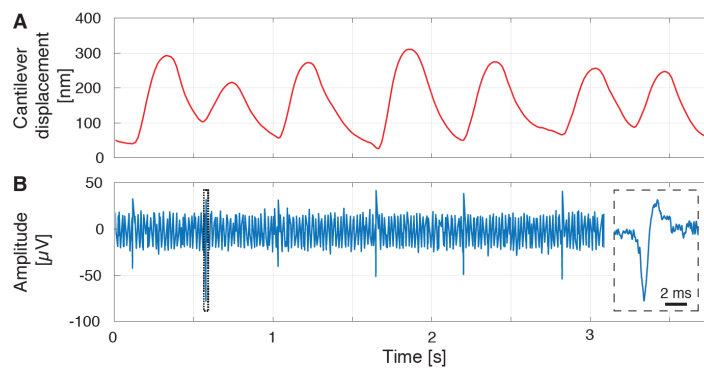


Figure 44: Simultaneous recording of cardiomyocyte contraction displacements electrograms.

A) Cantilever displacement simultaneously recorded with B) electrograms from a spontaneously active cardiomyocyte using the nanovolcano probe. The insert presents an expanded view of the region of the electrogram framed with dashed lines.

### G.5. Discussion

The novel SPM probe presented in this study enables direct combined force and electrical signal recordings by placing a 3D microelectrode at the tip of an AFM cantilever. The protruding electrode at the cantilever tip combines several technological advances in a single structure: (1) the platinum-black coated nanovolcano interior ensures a relatively low electrode impedance and, hence, optimizes signal-to-noise ratios (see Supplementary Information, section 2.1); (2) the electrically insulating nanovolcano walls prevent current leakage from the electrode which contribute to the robustness of the cell-electrode interface robustness.

The 3D multimaterial nanopatterned microelectrode was manufactured following a reliable and scalable non-conventional four-step fabrication process based on ion beam etching redeposition that was completed with the patterning and release of the cantilever by conventional reactive ion etching techniques. All manufacturing steps used to produce both the nanopatterned electrode and the cantilever are compatible with complementary metal oxide semiconductor (CMOS) technologies. Accordingly, it is feasible to integrate CMOS amplifiers on the nanovolcano probes in the future to minimize electrical signal attenuation and noise. In contrast to previous technologies using FIB milling,<sup>211,223</sup> the fabrication process is simple, scalable, and leads to homogeneous structures at the wafer scale (> 250 chips per wafer). Compared to regular nanovolcano arrays,<sup>34</sup> the photoresist layer used to manufacture the 3D microelectrode presented in this study is thicker which results in a wider undercut after development. As a consequence, the redeposited materials composing the nanovolcano wall are electrically insulated from the electrode area (cf. Figure 41-B) thereby preventing the gold nanoring to be coated during platinum-black electrodeposition.

Compared to conventional conductive AFM tips, nanovolcano probes show the distinct advantage of being insulated up to the very end of the tip, allowing for a confined measurement with minimal current leaks. Furthermore, the volcano geometry enables low access impedance in physiological saline solutions compared to conductive AFM tips and therefore permits electrophysiological recordings.

Simultaneous force and impedance recordings on neonatal rat cardiomyocytes confirmed that pulsed amperometry could be used to gauge the engaging process and allows for

gentle engaging on soft biological samples. As already reported in the literature, the probing depth of a microelectrode is mainly influenced by its spreading resistance and proportional to its radius.<sup>224</sup> For this reason, cells were detected by impedance measurements  $\sim 4\text{ }\mu\text{m}$  ( $\sim$  microelectrode radius) prior to mechanical contact. Presently, the lateral resolution achievable with the nanovolcano probe is limited by the  $8\text{ }\mu\text{m}$  in diameter protruding electrode. The relatively large electrode area is necessary to decrease the electrode impedance at the electrode-electrolyte interface and therefore to permit electrical measurements. Prospectively, platinum black could be substituted by lower impedance materials (e.g., PEDOT:PSS) to potentially achieve similar access resistances for smaller electrode diameters, thus improving the lateral resolution.

These experiments demonstrated that the nanovolcano probe was suited to map the impedance properties of mechanically stimulated cells at the single-cell level, hence providing opportunities in the field of mechanobiology.

When performing experiments with primary neonatal rat ventricular cardiomyocytes, their morphology and contractility did not change during the duration of the experiments. For the first time, electrograms together with contraction displacements were successfully recorded using a single probe and were confirmed by simultaneous optical recordings. Positive monophasic cantilever displacements with an amplitude and duration similar to the ones observed with conventional probes were reported.<sup>205</sup> Simultaneously, biphasic voltage pulses corresponding to electrograms showed shapes, durations, and amplitudes consistent with extracellular activities recorded with standard MEAs.<sup>225</sup> Even though, amplitudes close to  $1\text{ mV}$  are commonly reported in the literature for cardiomyocyte monolayers, recording performed on single cardiomyocyte with conventional MEAs showed similarly low amplitudes ( $< 100\text{ }\mu\text{V}$ ).<sup>226</sup>

The nanovolcano probe permits combined force-electrogram measurements within a single probe and therefore is an alternative to the AFM-MEA system that has, besides a reduction of system complexity, the added advantage of permitting the free selection of cells of interest. In comparison to FluidFM technology, no microfluidic channels were needed to transmit the electrical signal from the tip to the recording system, therefore bypassing the high fluid resistance and simplifying the experimental system.<sup>211</sup> Compared to the recently developed ultrasmall nanowire transistor probes (U-NWFET) enabling intracellular recording of action potentials from individual cells,<sup>227</sup> the nanovolcano system is limited to recording electrograms only but has the advantage of permitting simultaneous force recording.

Future developments of the nanovolcano probe should focus on permitting combined force and intracellular electrophysiological recordings such as action potentials or ion-channel activity. This might be challenging as, compared to extracellular recording, a high seal resistance is essential in intracellular electrophysiology to maintain the punctured cell activity and enable high quality recordings. In this study, the seal resistance was estimated to be much lower than the nanovolcano probe access resistance ( $R_{\text{seal}} < 309 \text{ M}\Omega$ , see Supplementary Information, section 2.2). The nanometer-wide alkanethiols nanopattern hypothesized to strengthen the cell-electrode interface was seemingly not sufficient to provide the gigaseal required to perform decent intracellular electrophysiology. Nevertheless, a systematic investigation of the nanopattern contribution to the seal formation could be performed with diverse types of self-assembled monolayers, not only based on alkane chains but also on positively charged molecules (e.g., poly-amine) or proteins (glutaraldehyde). On the other hand, a chemical-mechanical polishing step of the nanovolcano tip could be added in the microfabrication process to significantly reduce its roughness; therefore potentially improving the interface strength. In this context, the nanovolcano probe is certainly of interest to characterize the cell-electrode interface electrical properties by in-situ impedance spectroscopy.

## G.6. Conclusion

In this work, we present an instrument for combined optical, force and electrical measurements using a novel type of SPM probe composed of a nanopatterned volcano-shaped protruding electrode. Parallel mechanical, optical and electrical measurements of single cells were acquired thereby presenting a new approach for integrated mechano-electrical investigations.

The protruding microelectrode is electrically insulated to prevent current leaks at the cell-electrode interface. Additionally, a platinum-black coating of the large electrode area results in a relatively low impedance at the electrode-electrolyte interface. The complex 3D multimaterial microstructure was successfully manufactured at the tip of a suspended cantilever, exploiting a straightforward process that is reliable at the wafer scale. It combines a non-conventional redeposition processes occurring during ion beam etching with standard microfabrication techniques.

Experiments with neonatal rat cardiomyocytes demonstrate that the nanovolcano probe enables *in-situ* impedance recordings of mechanically stimulated cells with conventional liquid AFM setups. Proof of principle experiments confirm that combined measurement of force and electrical signals can be achieved with the presented probe. Electrograms and

contraction displacements from spontaneously active cardiomyocyte were simultaneously recorded with similar characteristics to the one measured with conventional methods.

These features render the nanovolcano probe particularly suitable for mechanobiological studies aimed at linking functional electrophysiological single-cell responses with mechanical stimuli.

## **G.7. Materials and methods**

### **Microfabrication**

A 380  $\mu\text{m}$ -thick double-side polished silicon wafer (100 mm in diameter) coated with 2  $\mu\text{m}$  of  $\text{SiO}_2$  obtained by wet thermal oxidation was covered by successive evaporations of Ti-Pt-Ti-Au-Ti (10-250-100-100-100 nm) using an EVA 760 e-beam evaporator (Alliance Concept, France). Electrically conductive tracks were patterned in a 750 nm-thick layer of AZ ECI 3007 positive photoresist layer (MicroChemicals, Germany) spin coated with a Rite Track 88 series automatic coater (Rite Track, USA), exposed with an i-line VPG 200 direct laser writer (Heidelberg, Germany) at a dose of 93 mJ/cm<sup>2</sup> and developed for 36 s in an AZ 726 MIF commercial developer (MicroChemicals) using a Rite Track 88 series automatic developer (Rite Track). Thereafter, a 2 min reflow at 120°C was performed on a Sawatec HP200 hotplate (Sawatec, Switzerland) prior to etching the substrate positioned at an angle of incidence of -35° with respect to the ion beam generated in an IBE 350 ion beam etcher (Veeco, USA) for 9 min 30 s. The photoresist was stripped in a 500 W  $\text{O}_2$  plasma ( $\text{O}_2$  flow 400 mL/min) for 7 min created by a TePla 300 microwave plasma system (PVA TePla, Germany). The conductive tracks were subsequently insulated by 200 nm of  $\text{SiO}_2$  sputtered with a Spider 600 sputter-coater (Pfeiffer Vacuum, France).

A monolayer of hexamethyldisilazane (HMDS) was deposited on the top-most  $\text{SiO}_2$  layer using a primer hotplate VB20 (ATMsse, Germany) before spin coating a 6  $\mu\text{m}$ -thick layer of negative photoresist AZ nLoF 2070 (MicroChemicals) using an OPTIspin SB20 manual coater (ATMsse) rotating at 3500 rpm. 8  $\mu\text{m}$ -diameter openings were patterned in the photoresist layer using an i-line VPG200 direct laser writer (Heidelberg) operating at a dose of 105 mJ/cm<sup>2</sup>. After a postexposure bake at 110°C with a 50  $\mu\text{m}$  proximity gap for 75 s, the wafer was developed for 91 s using an AZ 726 MIF developer (MicroChemicals) dispensed using an EVG150 automatic coater/developer (EVG, Austria). The sample was then bombarded with  $\text{Ar}^+$  ions for 15 min at an angle of incidence of 0° using an IBE350 ion beam etcher (Veeco). During this step, materials from the substrate were etched and redeposited on the photoresist sidewalls. The photoresist was finally stripped by  $\text{O}_2$  plasma

(10 min, 500 W, O<sub>2</sub> flow 400 mL/min) in a Tepla 300 microwave plasma system (PVA TePla), letting the nanovolcanoes protrude from the insulated tracks.

Both the cantilever and chip body were then patterned into a 15 µm-thick AZ 40xT photoresist layer (MicroChemicals) coated with an ACS200 gen 3 automatic coater-developer (Süss, Germany), exposed with an i-line VPG200 direct laser writer (Heidelberg) at a dose of 93mJ/cm<sup>2</sup>, and developed in an AZ 726 MIF developer (MicroChemicals) for 80 s using an ACS200 gen 3 automatic coater-developer (Süss). Following an overnight bake at 85°C in a Heraeus T6060 oven (Heraeus, Germany), the cantilever shape was transferred into the 2.2 µm-thick SiO<sub>2</sub> layer by a 7 min long reactive ion etching process (He/H<sub>2</sub>/C<sub>4</sub>F<sub>8</sub> based chemistry) performed using a SPTS APS dielectric etcher (SPTS, United Kingdom). The cantilever and chip body outlines were subsequently etched throughout the 380 µm-thick Si wafer by Bosch processing in an AMS 200 dry etcher (AMS, Austria), until reaching the 2 µm-thick backside Al etching stop layer deposited beforehand with an EVA760 e-beam evaporator (Alliance Concept). Finally, the SiO<sub>2</sub> cantilever was released by Si isotropic dry etching performed in an AMS 200 reactive ion etcher (AMS). The photoresist was then removed by O<sub>2</sub> plasma (10 min, 500 W, O<sub>2</sub> flow 400 mL/min) performed in a TePla 300 microwave plasma system (TePla), followed by a 15 min long piranha etch (H<sub>2</sub>SO<sub>4</sub>:H<sub>2</sub>O<sub>2</sub>, 3:1) to remove both dry etching residues as well as the backside Al membrane.

The 2.2 µm-thick SiO<sub>2</sub> handlers connecting the chips to the substrate were manually removed to place the cantilevers upside down in an EVA760 e-beam evaporator (Alliance Concept) and coat their backside with 50 nm-thick layers of Cr and Au.

### **Interfacing**

The nanovolcano probe was mechanically assembled on a custom-made PCB using a H20E epoxy cured for 3 hours at 80°C (Epoxy Technology, USA). The PCB was then mounted onto a custom-made AFM holder prior to wire-bonding the chip contact pad (electrically connected to the nanovolcano) with the PCB gold coated pad (linked to a standard U. FL coaxial cable) using a HB05 wedge and ball bonder (TPT, Germany). The chip-PCB interface was electrically insulated using a H70E-2 glob top epoxy (Epoxy Technology) that was dispensed manually and cured at 80°C for 1 h 30 min. Optical images of the interface are presented in Supplementary Information, section 1.

### **Electrodeposition of platinum-black**

Platinum-black was locally deposited into nanovolcanoes by pulsed potentiostatic deposition as described before.<sup>228</sup> Briefly, the nanovolcanoes were electrochemically treated by varying the electrode potential from -0.2 V to +1.2 V vs. Ag/AgCl (scan rate of 100 mV/s) for 20 cycles in a 0.5 M H<sub>2</sub>SO<sub>4</sub> solution. Subsequently, the microelectrodes were immersed into a solution of hexachloroplatinic acid (17.5 mmol/L, 262587, Sigma) and lead(II) acetate trihydrate (0.03 mmol/L, 467863-50G, Sigma) prior to applying -700 mV voltage pulses with respect to the open circuit potential ( $V_{\text{OCP}}$ ) for an overall duration of 45 s ( $t_{\text{on}} = 0.2$  s,  $t_{\text{off}} = 0.4$  s, number of pulses = 225).

### **Isolation and culture of primary rat cardiomyocytes**

Primary neonatal rat (Wistar, 1 day old) ventricular cardiomyocytes were isolated using established procedures in compliance with federal guidelines for animal experimentation under license BE27/17 of the Bernese Veterinary Department. The resulting cell suspension was centrifuged at 1000 rpm for 5 min, resuspended in DMEM (41965-039, Gibco) containing 10% fetal bovine serum (16140071, ThermoFisher Scientific) and 1% penicillin/streptomycin and seeded in 6 cm diameter petri dishes at a density of  $\sim 350$  cells/mm<sup>2</sup>. Cells were incubated at 37 °C in an atmosphere containing 5% CO<sub>2</sub>. The cell medium was renewed every 24 hours. Experiments were conducted 48 to 72 h post-seeding. At this time, the cellular electrophysiology of cardiomyocytes has recovered from the isolation process and overgrowth with non-cardiomyocytes such as myofibroblasts is still moderate.

### **Device functionalization**

The nanovolcano probes were sterilized for 30 s with O<sub>2</sub> plasma (100 W, 650 mTorr; Diener Electronic, Germany) prior to being immersed for 1 hour in a 20 mM hexanethiol solution in pure ethanol for self-assembled monolayer formation. After ethanol rinsing, the probes were thoroughly rinsed in sterile deionized water.

### **Combined AFM-optical-electrical setup and recordings**

A detailed description of the system combining AFM, optical and electrical recordings is presented in Supplementary Information, section 1.

In short, the combined AFM-optical setup is a custom system<sup>17</sup> associating a tip-scanning AFM (Dimension Icon, Bruker, Germany) and an optical microscope (IX73 or IX81, Olympus, Japan) equipped with a 20x objective and a camera (ixon Ultra 897, Oxford Instruments, United Kingdom). The camera was used in frame transfer mode with a 20Hz

acquisition rate. The AFM was used in contact mode without (constant height mode) or with feedback enabled (constant deflection mode). Contraction displacement curves were established by converting image data into height and deflection as a function of time. Data were recorded while imaging with a scan size of 0 nm, a scan rate of about 40 Hz and 1024 samples per line, which corresponds to a sampling rate of about 80 kHz. The images were pre-processed using gwyddion,<sup>68</sup> before further processing with a custom Matlab script to convert the “trace” and “retrace” AFM images into height and deflection as a function of time.

Two different nanovolcano probes were used to collect the data presented in this study. Impedance measurements were performed with probes 1 and 2. Probe 2 was subsequently cleaned by O<sub>2</sub> plasma (100W, 650 mTorr, 30 s; Diener Electronic), inspected by SEM, functionalized, and re-used to record electrophysiological signals from cardiomyocytes.

### **Electrophysiology**

Electrophysiological recordings were performed at room temperature on preparations kept in Hank's balanced salt solution supplemented with 10 mmol/L Hepes (pH 7.2). An Axopatch 200B microelectrode amplifier together with a CV 203 BU headstage (Molecular Devices, USA) were used to perform pulsed amperometry and to record electrograms from cardiomyocytes (bandwidth: 0 – 100 kHz). The analog to digital conversion was performed by a Powerlab 4/25 acquisition card (AD Instruments, Australia) at a sampling frequency of 200 kS/s. Extracellular signals were post processed with a Butterworth bandpass filter (100 Hz - 500 Hz).

### **G.8. Acknowledgments**

This work was partially funded by the Swiss National Science Foundation (grant numbers 200021-175943 to P.R. and 310030\_169234 to S.R.), and the H2020 - UE Framework Programme for Research & Innovation (2014-2020); ERC-2017-CoG; InCell; Project number 773091. The authors thank the EPFL Center of Micronanotechnology (CMi) staff for their outstanding support and availability. Special thanks to Dominik Ziegler (Scuba Probe Technologies LLC) for his help with the long-term electrochemical characterization, Rodrigo de Campos Perin (EPFL) for kindly lending us the Axon Axopatch 200B amplifier, Mathieu Aberle (EPFL) for his preliminary contribution, and Regula Flückiger Labrada (UNIBE) for her cell culture work.

### **G.9. Authors contribution**

P.R. and B.X.E.D. conceived the project, B.X.E.D. manufactured the nanovolcano probe in a clean room, B.X.E.D. and M.T.M.H developed the interface, G.E.F. and M.T.M.H



provided the combined AFM-optical setup, E.d.C. and S.R. handled the cardiomyocyte isolation and B.X.E.D. the culture, M.T.M.H and B.X.E.D. conducted the electrophysiological experiments, B.X.E.D, M.T.M.H., E.d.C., and S.R. interpreted the results, P.R., G.E.F., and A.B. supervised the technological part of the project and S.R. the biological part. All authors discussed the results and contributed to the final manuscript.

## G.10. Supplementary information

### Custom cantilever holder

A custom interface was necessary to connect the nanovolcano probe to both the AFM and the electronic measurement system. A custom-made shielded PCB connected to a 800  $\mu\text{m}$ -diameter U. FL coaxial cable was screwed to a custom-made AFM cantilever holder as illustrated in Figure S 28-A. Figure S 28-B shows the nanovolcano probe glued to the PCB and wire-bonded to the gold coated pad of the PCB. The PCB directly connects the gold coated pad to the inner wire of the coaxial output, therefore guaranteeing an standard electrical connection to the nanovolcano. A glob top was used to electrically insulate the chip-PCB interface when the system is immersed in liquid (cf. Figure S 28-C). Overall, this interface prevents any electrical shortcut when working in a liquid environment, and shields the recorded electrical signals from external electromagnetic noises, therefore allowing for low-noise recordings.

The cantilever holder keeps the nanovolcano probe tilted at an angle of  $11^\circ$  with respect to the horizontal, as required for the optical deflection measurement with AFM.

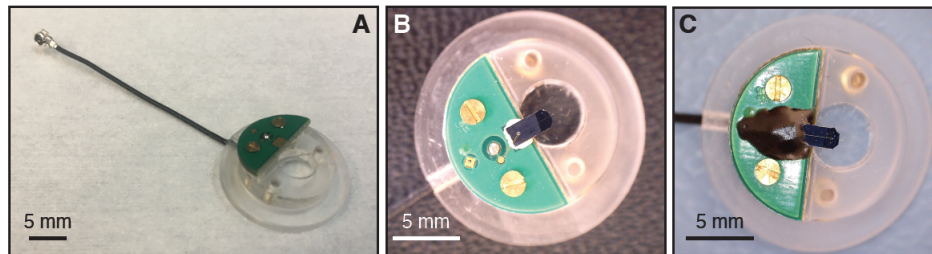


**Figure S 28: Mechanical and electrical interfacing of the nanovolcano probe.**

A) Picture of the custom-made AFM holder without the nanovolcano probe assembled. B) Top-view image of the nanovolcano probe mechanically assembled and wire-bonded to the custom-made holder. C) Top-view image of the interface with the glob top used to insulate the chip-PCB electrical contact.

### Setup for simultaneous optical imaging, force, and electrical recordings

A custom setup was necessary to obtain simultaneously optical images as well as mechanical forces and electrical recordings (Figure S 29-A). The cells were seeded to 6 cm

in diameter petri dish, which was mounted in a custom sample holder. The cells were then covered with liquid medium (Figure S 29-A). The sample holder rests on a large aluminum structure placed on a noise cancelling table (not represented in the figure) to ensure minimal mechanical noise. The nanovolcano probe was placed on top of the sample using the custom cantilever holder described above (Figure S 28), connected to a commercial tip-scanning AFM head (Figure S 29). The cantilever deflection is measured using an optical laser readout. The force applied by the cell to the cantilever is calculated based the cantilever deflection signal, knowing the cantilever stiffness and deflection sensitivity. The nanovolcano cantilever electrode is connected through a coaxial cable to a microelectrode amplifier and a digital acquisition system to record the electrical signal. An inverted microscope was placed under the sample holder to allow for simultaneous optical imaging.

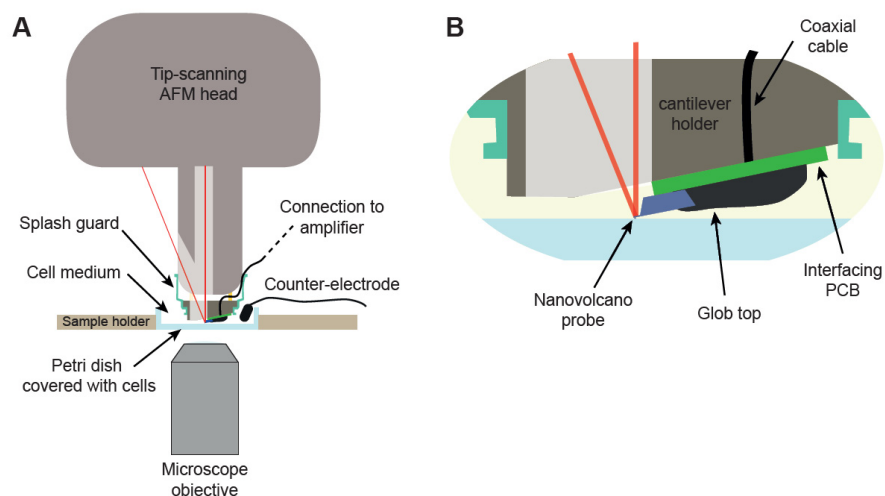


**Figure S 29: Description of the custom AFM-optical system.**

A) Schematic drawing showing a cross-section view of the custom-made AFM-optical system. B) Expanded cross-section view of the custom-made cantilever holder mounted on the AFM head.

### Electrode-electrolyte interface

Figure S 30-A shows the electrical equivalent model of the electrode-electrolyte interface. As previously described in the literature,<sup>34</sup> it is composed of a non-linear resistance,  $R_{CT}$ , that represents faradaic charge transfer secondary to redox reactions, in parallel with a constant phase element  $Z_{CPE,DL}$  representing the double layer capacitance underlying the capacitive charge transfer.  $R_{spread}$  represents the resistance induced the confinement of the electric field lines near the microelectrode. The stray capacitance,  $C_{stray}$ , denotes the capacitive current leaks along the insulated tracks.

The electrode-electrolyte interface properties have been experimentally measured using electrochemical impedance spectroscopy (EIS) based on a 100 mV sinusoidal signal

applied to the nanovolcano probe in presence of phosphate buffer saline (PBS) at room temperature. The EIS data are shown in Figure S 30-B and show a typical electrode-electrolyte behavior.<sup>224</sup> Values for each element composing the electrical equivalent circuit have been extracted and are summarized in Table S1.

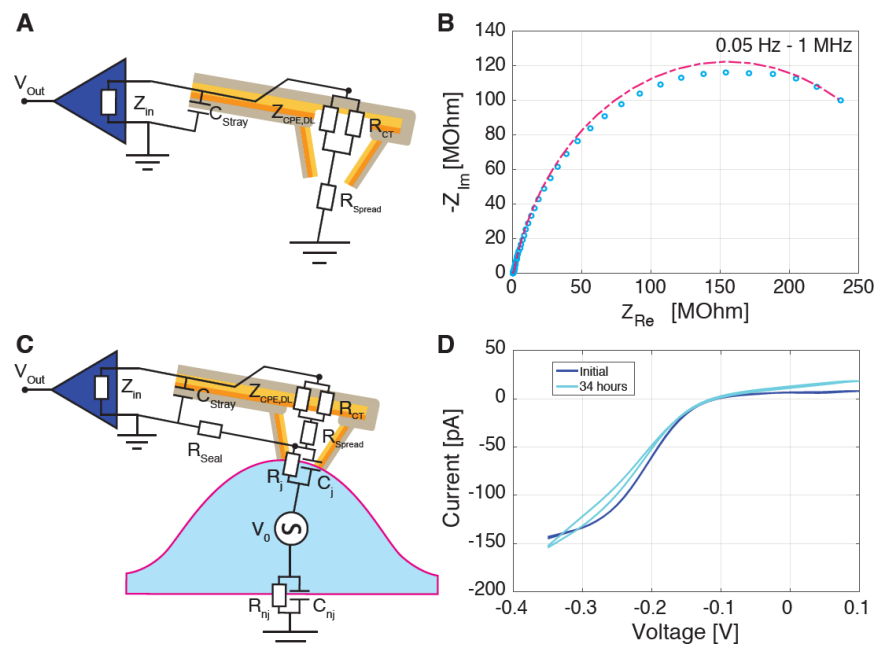


**Figure S 30: Electrochemical characterization of the nanovolcano probe.**

A) Equivalent electrical model of the electrode-electrolyte interface. B) Electrochemical impedance spectroscopy of a single nanovolcano probe in PBS. C) Equivalent electrical model of the cell-electrode interface. D) Cyclic voltammogram of the nanovolcano probe right after immersion in a solution of 5 mM hexamine ruthenium chloride and 100 mM potassium nitrate in deionized water (dark blue) and after 34 hours of continuous chronoamperometry at a fixed potential of -0.35 V (light blue).

Element	Value
$R_{CT}$	315 M $\Omega$
$C_{DL}$	4.15 nF, 0.82
$R_{spread}$	74.4 k $\Omega$
$C_{stray}$	30 pF

**Table S1: Experimental values of every element composing the electrical equivalent circuit of the electrode-electrolyte interface.**

### Cell-electrode interface

Figure S 30-C represents the electrical equivalent circuit once the nanovolcano probe is engaged onto a cell. In this situation, the junctional membrane resistance  $R_j$  and capacitance  $C_j$  are added in parallel with the seal resistance  $R_{\text{seal}}$ , representing the leaks at the cell-electrode interface, at the tip of the nanovolcano probe.  $V_0$  is the cell transmembrane potential whereas  $R_{\text{nj}}$  and  $C_{\text{nj}}$  respectively represent the non-junctional cell membrane resistance and capacitance.

During engaging, no variation of the resistance is observed at low frequency; therefore suggesting that the seal resistance  $R_{\text{seal}}$  is much lower compared to the charge transfer resistance  $R_{\text{CT}}$ . However, at higher frequency, the impedance of the electrode-electrolyte interface ( $Z_{\text{CPE,DL}} \parallel R_{\text{CT}}$ ) becomes negligible as most of the current passes through the low double layer impedance. At this frequency, impedance measurements (as reported in Figure 42, main manuscript) directly represent the spreading resistance in serial with the other components of the cell-electrode interface ( $R_{\text{seal}} \parallel R_j \parallel C_j$ ). For this reason, the impedance and time constant seen by the nanovolcano probe increases when approaching the cell surface.

### Long-term characterization

The long-term stability of the nanovolcano probe was characterized by Scuba Probe Technologies LLC. The nanovolcano probe was immersed into a solution of 5 mM hexamine ruthenium chloride and 100 mM potassium nitrate in deionized water. As shown in Figure S 30-D, a first cyclic voltammogram was acquired between -0.35 V to 0.1 V vs. Ag/AgCl at a scan rate of 50 mV/s using a 3 electrodes setup (dark blue curve). For the next 34 hours, the nanovolcano potential was hold at -0.35 V while similar cyclic voltammograms were registered every 20 minutes as control. The light blue cyclic voltammogram in Figure S 30-D shows nearly no significant differences compared to the initial one, thereby demonstrating that the nanovolcano probe was functional for 34 hours.

### Force-controlled impedance measurements

Overall, force-controlled impedance measurements were performed on seven human embryonic kidney (HEK) cells and seven primary rat cardiomyocytes (CMCs) using two different nanovolcano probes. Experimental results are summarized in Table S2.

Cell ID	Cell type	Probe	Impedance Z [kΩ]			Time constant [μs]			Peak force [nN]	Ramp rate [Hz]
			Off cell	On cell	$\Delta Z$ [%]	Off cell	On cell	$\Delta$ [%]		
1	HEK	1	458	502	109	30	40	133	15	0.25
2	HEK	2	361	485	131	25	35	140	400	0.1

3	HEK	2	358	640	178	25	45	180	22.1	0.1
4	HEK	2	400	850	212	25	40	160	60	0.1
5	HEK	2	426	594	139	25	30	120	12	1
6	HEK	2	440	820	186	25	35	140	115	1
7	HEK	2	441	718	163	25	35	140	19.5	0.1
8	CMC	2	493	993	201	35	65	186	470	2
9	CMC	2	458	601	131	30	45	150	36	3
10	CMC	2	467	496	106	30	35	117	15.5	3
11	CMC	2	498	941	195	35	56	160	772	2
12	CMC	2	507	561	111	35	40	114	46	3
13	CMC	2	494	560	113	30	35	117	12.5	3
14	CMC	2	432	625	145	30	40	133	43	3

Table S2: Summary of the force-controlled impedance measurements performed on human embryonic kidney cells and primary rat cardiomyocytes.

### Contraction displacement measurements

Contraction characteristics recorded from five different primary rat cardiomyocytes are summarized in Table S3. Parameters include the contraction amplitude, duration at 50% of the amplitude, contraction number, as well as the overall recording duration for each cell tested.

Cell ID	Contraction amplitude [nm]	Contraction duration [s]	Number of contractions	Recording duration [s]
1	382 ± 95	415 ± 117	11	50
2	262 ± 88	436 ± 26	12	25
3	207 ± 28	545 ± 78	6	7
4	26 ± 3	231 ± 124	3	3
5	121 ± 44	297 ± 18.1	19	50

Table S3: Summary of the primary rat cardiomyocyte contraction characteristics recorded from different cells with a single nanovolcano probe (mean ± SD).

### Electrogram measurements

Overall, two electrograms were successively recorded from two different cells using a single nanovolcano probe, therefore demonstrating the capability of successive recordings at different location with a single probe. The signals of the first recording are presented in main manuscript Figure 44, those of the second recording are shown in Figure S 31. Electrograms displayed downstroke amplitudes of  $64 \pm 17 \mu\text{V}$  (N = 42) for an overall recording duration of 25 s.

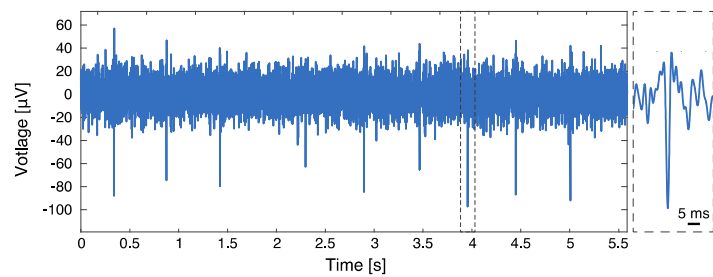


**Figure S 31: Recording of a cardiomyocyte electrogram using the nanovolcano probe.**  
The insert presents an expanded view of the region of the electrogram framed with dashed lines.

# Chapter H Conclusion

## H.1. Main contributions of the thesis

### How do mycobacteria grow?

I proposed a new biphasic model for the growth dynamics of mycobacteria<sup>11</sup>, which has resolved a controversy in the field regarding mycobacterial growth modes being either unipolar or bipolar<sup>6,7</sup>. This work uncovered that mycobacteria growth is not unipolar or bipolar. Instead, mycobacteria adopt a biphasic growth dynamics, similar to the “new end take off” (NETO) dynamics of fission yeast, which is very surprising considering the billion years of evolutionary distance between them<sup>11</sup>. This work constitutes the Chapter B of this document.

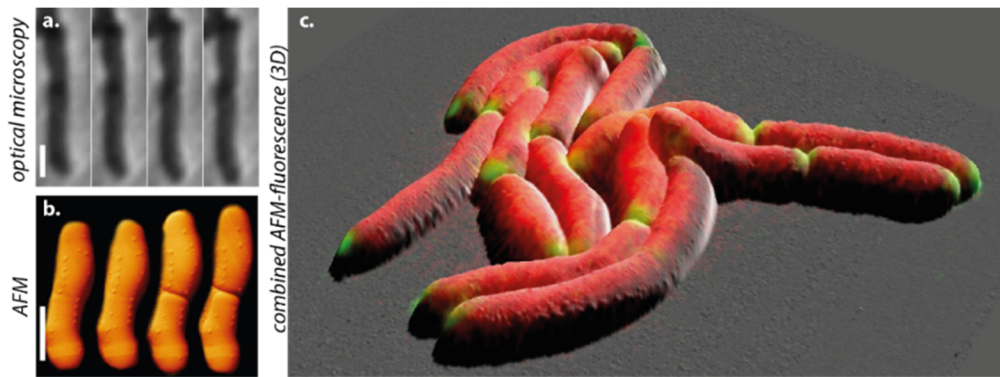


**Figure 45: Combined AFM-fluorescence imaging of live *M. smegmatis* bacteria**  
(a,b) Comparison between time-lapse phase contrast and AFM images of a live bacterium (division happens between the second and the third image). Time between two consecutive images is about 10 minutes. Scale bar, 1  $\mu$ m. (c) Combined 3D AFM (grey) and fluorescence (red: cytoplasm, green: Wag31 protein) images.

### Measuring the topography and local mechanical properties of a growing pole with atomic force microscopy

Because of this intriguing analogous dynamics of pole growth between yeast and mycobacteria, I then chose to study the pole growth and morphogenesis of fission yeast cells. To do so, I developed a protocol to hold fission yeast cells vertically in order to image the pole of the growing cell. We observed the formation of a stiff fibril mesh on the pole of fission yeast cell and showed that this mesh is stretched as it translates radially away from the top of the cell. This work constitutes the Chapter C of this document.

### **How do mycobacteria divide?**

Willing to elucidate the physical route of mycobacterial division, I showed that there is a concentration of mechanical stress at the future division site, using a combination of COMSOL finite element modeling and AFM measurements while controlling the cell turgor pressure<sup>18</sup>. This work was integrated into a broader study led by Pascal Odermatt, showing that the accumulation of mechanical stress, in combination of enzymatic activity, ultimately leads to mechanical fracture and separation of the sibling bacteria<sup>18</sup>. This work is the Chapter D of this document.

### **Designing a SIM add-on for fluorescence microscopes**

I also sought to improve the performance of the instruments available for live-cell imaging. To improve the resolution of fluorescence microscopes, I designed and built a 3D-printed structured illumination (SIM) module that can be easily added to commercial fluorescence microscopes, which enables a larger community of scientists to access such imaging performances with their already existing microscopes. The openSIM module has been used to image a broad range of biological samples (zebrafish embryo, host-pathogen interaction, organoid), in collaboration with four other EPFL laboratories. This work constitutes the Chapter E of this document.

### **Adding photothermal actuation capability to a tip-scanning AFM head**

Opposite to conventional fluorescence microscopy, for which spatial resolution is above 200 nm but temporal resolution can often be below a few tens of milliseconds per image, AFM reaches nanometer resolution but is a relatively slow technique to image bacteria (typically 10 minutes per image). AFM reaches nanometer resolution, but it is a relatively slow technique to image bacteria (typically 10 minutes per image). Thus, I sought to explore the potential benefit of photothermal actuation for increasing the AFM imaging speed. After building a photothermal actuation module, I obtained the first XYZ tip-scanning head with photothermal actuation, and demonstrated its use for imaging collagen fibers at high speed in PORT mode. Additionally, I determined which factors affects the imaging performance of and XYZ tip-scanning photothermal AFM head for high-speed PORT, such as the impact of cantilever tracking error, the importance of the cantilever size and material, and the numerical aperture of the AFM head. This work constitutes the Chapter F of this document.



## **Adding live-cell electrical measurement capability to an AFM**

In collaboration with Benoit Desbiolles, we developed a new kind of AFM cantilever and demonstrated the simultaneous measurement of the electric potential and contraction of live cardiac cells. This work constitutes the Chapter G of this document.

## **H.2. Possibilities for future development of the work presented in the thesis**

### **Is there a link between NETO and the other events of the cell cycles in mycobacteria?**

In fission yeast, two main factors control when NETO occurs: the cell needs to have reached the G2 phase of DNA replication, and the cell must have reached a size of at least  $9\text{-}9.5\mu\text{m}$ <sup>51,60</sup>. Several proteins have been identified and form a complex acting at the fission yeast cell poles to promote growth<sup>229</sup> (Mod5, Tea1-4, Tip1, Pom1, Bud6). It remains unclear how these molecular players are regulated as a function of the events of the cell cycle (such as reaching the G2 phase or a minimal cell size), with the exception of the existing link between DNA replication and NETO mediated by calcineurin<sup>230</sup>. If DNA replication is perturbed, calcineurin dephosphorylates Tip1, which in turn prevents NETO from occurring<sup>230</sup>.

In Chapter B, we showed that the pole growth dynamics of mycobacteria follows a biphasic pattern, like fission yeast cells. This work therefore introduces a new event in the mycobacterial cell cycle, the initiation of new pole growth (NETO). Is NETO linked to other cell cycle events? NETO corresponds to a rapid two-fold increase of the cell growth rate, which requires rapid doubling of the amount of proteins and enzymes. Cells need to precisely coordinate DNA replication, growth and division to ensure viability of the cells. An extra copy of the genes involved in growth could be the template used to double the production of the proteins and enzymes involved in growth. Thus, it is not unlikely that NETO is linked to DNA replication, similarly to the observations for fission yeast cells. In the future, it would be interesting to determine if there is a correlation between the initiation of DNA replication (C-period, visible using a fluorescently tagged the DnaN protein<sup>6</sup>) and NETO: does NETO always occur after the initiation of DNA replication?

### **Tip-growth morphogenesis: surprising similarities between evolutionarily distant organisms and potential insights on mycobacteria to be gained from analogous tip-growing organisms**

Beside Mycobacteria, numerous living organisms form elongated structures by growing from their tip, such as root hairs and pollen tubes in plants, axons of neuron in animals, fission yeast

cells. Some of the tip-growing genus are highly medically relevant, such as *Mycobacteria* or *Streptomyces*, from which a large portion of the current antibiotics comes<sup>75</sup>.

It is striking to see the similarity of the morphogenesis in such a broad variety of species, including unicellular and multicellular organisms, eukaryotes and prokaryotes. Pollen tubes and root hairs both show maximum cell wall extension in the subpolar region, in an annular ring centered at the tip<sup>231,232</sup>. Similarly, it has been discovered independently that addition of new cell wall material is concentrated in the sub-polar region in mycobacteria<sup>10</sup>. We have shown that *Mycobacteria* (a prokaryote) and the fission yeast *Schizosaccharomyces pombe* (an eukaryote) share the same biphasic pole growth dynamics, called “new end take off” (NETO)<sup>11,51</sup>. This hints at a convergent evolution, during which the physical constraints associated with tip growth morphogenesis selected for analogous mechanisms (Figure 46), in a similar manner as birds, bats, butterflies evolved wings independently as an answer to the biophysical constraints of flight.

But tip growth is referred to by various names, depending on the fields: the terms “apical growth”, “hyphal growth”, “pole growth”, “tip growth” all refer to the morphogenesis of an elongated cylindrical structure from a growing tip and driven by turgor pressure. Because of the diversity of appellations, it seems that the observations and physical modeling of pole growth in some species are sometimes not mentioned in the literature about other organisms.

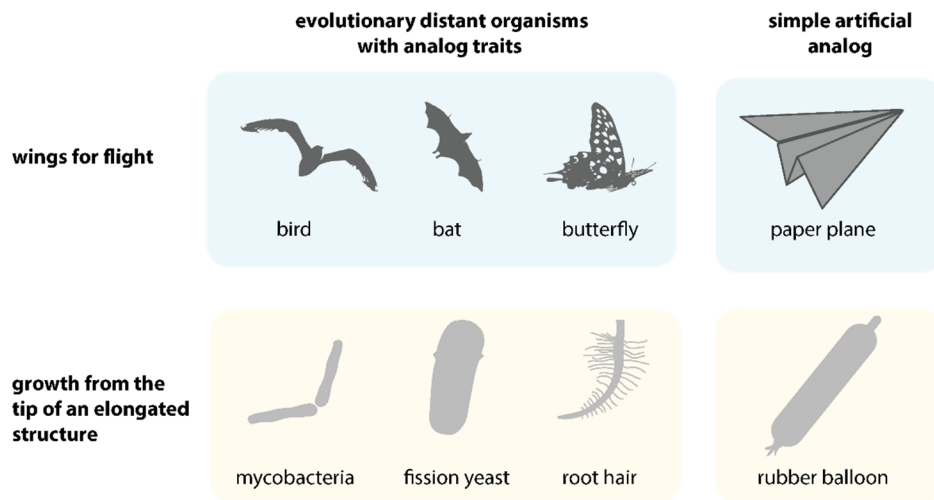


**Figure 46: Convergent evolution of analog traits between evolutionary distant organisms**  
**(top)** Example of convergent evolution between evolutionary distant organisms: birds, bats and butterflies evolved wings separately, to address the environmental and physical constraints associated with flight. A simple paper plane could potentially be also a good

model to gain some insights into the biophysics of flight. **(bottom)** Proposed analogy between mycobacteria, fission yeast, root hairs and other tip-growing organisms. Rubber balloons have been proposed as a model for tip growth morphogenesis<sup>233</sup>

Many questions remain for tip growing microorganisms, because of the challenges associated with microscopy at sub-micron scale. How do the organisms regulate the time and place for insertion of new material while preserving cell integrity? What controls the NETO transition from slow to fast pole growth in mycobacteria? Fission yeast cells, pollen tubes or root hairs might bring more insight about pole growth of mycobacteria than the traditional bacterial model *E. coli*, which is not pole growing. Additionally, larger pole-growing organisms such as fission yeast cells are easier to observe, resulting in a broad range of experimental results<sup>57,88,232,234–236</sup> and detailed biophysical models<sup>233,237</sup>.

Building on Chapter C and on the large amount of experimental and theoretical results obtained on non-mycobacteria pole growing organisms, it could be highly beneficial to explore which of the observations on pole-growing organisms also apply to *M. tuberculosis*. A first step in this direction could be the adaptation of the vertical traps proposed in Chapter C for mycobacteria, and observing mycobacterial pole growth over time with AFM, while changing the turgor pressure inside the cells by changing the osmolarity of the growth medium.

### **What is the relationship between tip-growth and infection?**

Several examples indicate that tip growing species share the property of applying forces to invade their environment<sup>231,238</sup>. For instance, *Candida* species can pierce through keratinized skin to infect a host, and root hairs make their way into the ground using turgor pressure as a driving force<sup>231</sup>. Overall, restricting growth to the tip may make the cells able to apply high forces to pierce through an obstacle<sup>239</sup>, or reorient their direction<sup>231</sup>, and reduce friction during growth<sup>231</sup>.

Our group has been studying *M. tuberculosis* infection of a lung-on-a-chip<sup>240</sup>. The *M. tuberculosis* bacteria form complex cord structures and grow at the junction between neighboring epithelial cells (Figure 47 a-c). This behavior may potentially hide them from the macrophages patrolling at the surface of the alveoli. Coherently with the idea of tip-growing cells applying forces, we found that *M. tuberculosis* bacteria could deform lung alveolar cells significantly during infection (Figure 47 d,e).

Studying how the cord structure formed by the mycobacteria might allow them to apply forces and infect lung tissue more efficiently could give us a better understanding of the biophysics involved in tuberculosis infection. An assay measuring the forces that cord structures apply could be the basis for a biophysical screening for new drugs inhibiting the mechanical mechanisms through which tuberculosis bacteria infect their host. The openSIM could be used to resolve the bacteria within a cord structure (Figure 47 c) grown in a soft agarose trap with the drugs to be screened. This would allow us to determine which compounds perturb the cord morphology and its ability to apply forces and deform the agarose trap. The compounds preventing cords to form or deform their environment could have interesting therapeutic applications against tuberculosis.

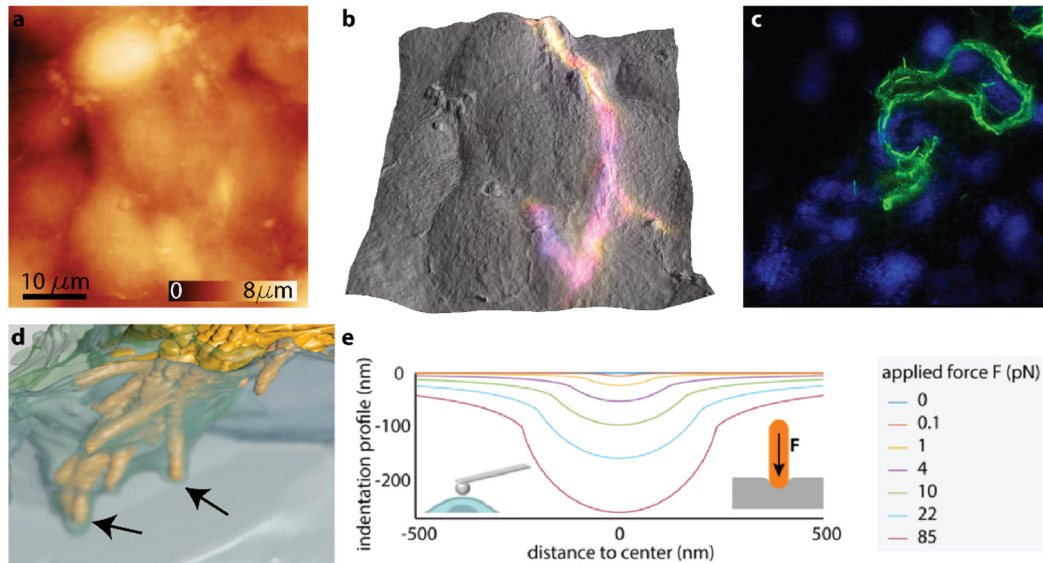


**Figure 47: *M. tuberculosis* bacteria form intercellular cord structures and deform their environment during infection**

(a) AFM image of fixed alveolar epithelial cells, cultured on a lung on a chip<sup>240</sup>, and infected with *M. tuberculosis* bacteria. (b) Correlated AFM and fluorescence image of infected cell. The image is an overlay of the 3D rendering of the AFM image from (a), in grey, and the color-coded z-projection of the fluorescence image of green-fluorescent *M. tuberculosis* bacteria (in color). The bacteria are visible in the fluorescence channel, but not on the AFM image of the surface of the epithelial cells, indicating that the bacterial cord sits in the junction between epithelial cells. (c) Maximum intensity projection of a *M. tuberculosis* cord (green) imaged with the openSIM (see Chapter E). The nucleus of the infected cells is stained with DAPI (blue). (d) 3D rendering of an electron microscopy tomography dataset, showing indentation (black arrows) of a bacterial cord (yellow) in alveolar epithelial cells (light green). (e) Mechanical model linking force and indentation profile for a rod-shaped indenter<sup>241</sup>, applied to a *M. tuberculosis* bacterium indenting an alveolar epithelial cell (stiffness

of the alveolar cell: 0.32 kPa<sup>242</sup>). This kind of model is usually used to calculate the stiffness of a sample based on the force applied by AFM cantilever while indenting into the sample, but we use it here to calculate the force applied by bacterium based on its indentation into a tissue of known stiffness. (a-c) *Sample from V. Thacker.* (d) *Sample and image from V. Thacker.*

## **Future developments for the openSIM**

In Chapter E, we have introduced a new design for an add-on to upgrade conventional fluorescence microscopes with structured illumination. We have also shown, in collaboration with other EPFL laboratories, that the openSIM is suitable for a broad range of biological samples, from single cells to whole organisms. How are we going to share the openSIM in such a way that it benefits a larger number of laboratories?

The traditional approach would consist in patenting our design and collaborating with a company to produce and distribute the instrument. The company would take charge of doing further development to minimize the manufacturing costs, ensure that there is a sufficient supply of the parts needed, and ensure compliance with the norms. It would also organize the production, distribution and sales of the SIM microscopes, as well as offer a warranty and customer support.

Inspired by pioneering work in open instrumentation<sup>130,132–136,243</sup>, we chose to adopt a different approach and share openly the openSIM design. This approach has been shown to shorten the time for other labs to get access to the instrument, compared to a traditional commercial approach, increase the accessibility, as well as act as a strong vector for education and knowledge transfer<sup>130</sup>. Based on our own past experience in LBNI with sharing an open AFM head<sup>173</sup> and the experience of other actors in open hardware<sup>130,132–136,243</sup>, we have identified two key steps for the future of the openSIM: providing a detailed documentation for the instrument assembly (for example, on a public website as well as in person, through workshops), and establishing a community of long term builders and users of the openSIM.



# References

1. World Health Organization (WHO). *Global tuberculosis report 2019*. (WHO, 2019).
2. Hett, E. C. & Rubin, E. J. Bacterial Growth and Cell Division: a Mycobacterial Perspective. *Microbiol. Mol. Biol. Rev.* **72**, 126–156 (2008).
3. Zumla, A., Atun, R., Maeurer, M., Mwaba, P., Ma, Z., O’Grady, J., Bates, M., Dheda, K., Hoelscher, M. & Grange, J. Viewpoint: Scientific dogmas, paradoxes and mysteries of latent *Mycobacterium tuberculosis* infection. *Trop. Med. Int. Heal.* **16**, 79–83 (2011).
4. Dhar, N. & McKinney, J. D. Microbial phenotypic heterogeneity and antibiotic tolerance. *Curr. Opin. Microbiol.* **10**, 30–38 (2007).
5. Wakamoto, Y., Dhar, N., Chait, R., Schneider, K., Signorino-Gelo, F., Leibler, S. & McKinney, J. D. Dynamic persistence of antibiotic-stressed mycobacteria. *Science (80-. ).* **339**, 91–95 (2013).
6. Santi, I., Dhar, N., Bousbaine, D., Wakamoto, Y. & McKinney, J. D. Single-cell dynamics of the chromosome replication and cell division cycles in mycobacteria. *Nat. Commun.* **4**, 2470 (2013).
7. Aldridge, B. B., Fernandez-Suarez, M., Heller, D., Ambravaneswaran, V., Irimia, D., Toner, M. & Fortune, S. M. Asymmetry and aging of mycobacterial cells lead to variable growth and antibiotic susceptibility. *Science (80-. ).* **335**, 100–104 (2012).
8. Kieser, K. J. & Rubin, E. J. How sisters grow apart: mycobacterial growth and division. *Nat. Rev. Microbiol.* **12**, 550–562 (2014).
9. Rego, E. H., Audette, R. E. & Rubin, E. J. Deletion of a mycobacterial divisome factor collapses single-cell phenotypic heterogeneity. *Nature* **546**, 153–157 (2017).
10. Meniche, X., Otten, R., Siegrist, M. S., Baer, C. E., Murphy, K. C., Bertozzi, C. R. &

- Sasseti, C. M. Subpolar addition of new cell wall is directed by DivIVA in mycobacteria. *Proc. Natl. Acad. Sci.* **111**, E3243–E3251 (2014).
11. Hannebelle, M. T. M., Ven, J. X. Y. Y., Toniolo, C., Eskandarian, H. A., Vuaridel-Thurre, G., McKinney, J. D. & Fantner, G. E. A biphasic growth model for cell pole elongation in mycobacteria. *Nat. Commun.* **11**, (2020).
  12. Abbe, E. Beiträge zur Theorie des Mikroskops und der mikroskopischen Wahrnehmung: I. Die Construction von Mikroskopen auf Grund der Theorie. *Arch. für mikroskopische Anat.* **9**, 413–418 (1873).
  13. Schermelleh, L., Ferrand, A., Huser, T., Eggeling, C., Sauer, M., Biehlmaier, O. & Drummen, G. P. C. Super-resolution microscopy demystified. *Nat. Cell Biol.* **21**, 72–84 (2019).
  14. Waldchen, S., Lehmann, J., Klein, T., Van De Linde, S. & Sauer, M. Light-induced cell damage in live-cell super-resolution microscopy. *Sci. Rep.* **5**, 1–12 (2015).
  15. Marx, V. Is super-resolution microscopy right for you? *Nat. Methods* **10**, 1157–1163 (2013).
  16. Eskandarian, H. A., Odermatt, P. D., Ven, J. X. Y., Hannebelle, M. T. M., Nievergelt, A. P., Dhar, N., McKinney, J. D. & Fantner, G. E. Division site selection linked to inherited cell surface wave troughs in mycobacteria. *Nat. Microbiol.* **2**, 17094 (2017).
  17. Odermatt, P. D., Shivanandan, A., Deschout, H., Jankele, R., Nievergelt, A. P., Feletti, L., Davidson, M. W., Radenovic, A. & Fantner, G. E. High-Resolution Correlative Microscopy: Bridging the Gap between Single Molecule Localization Microscopy and Atomic Force Microscopy. *Nano Lett.* **15**, 4896–4904 (2015).
  18. Odermatt, P. D., Hannebelle, M. T. M., Eskandarian, H. A., Nievergelt, A. P., McKinney, J. D. & Fantner, G. E. Overlapping and essential roles for molecular and mechanical mechanisms in mycobacterial cell division. *Nat. Phys.* **16**, 57–62 (2019).
  19. Nievergelt, A. P., Brillard, C., Eskandarian, H. A., McKinney, J. D. & Fantner, G. E. Photothermal off-resonance tapping for rapid and gentle atomic force imaging of live cells. *Int. J. Mol. Sci.* **19**, 1–11 (2018).



20. Butt, H.-J., Cappella, B. & Kappl, M. Force measurements with the atomic force microscope: Technique, interpretation and applications. *Surf. Sci. Rep.* **59**, 1–152 (2005).
21. Hu, Y., Hu, S. & Su, C. Method and Apparatus of Operating a Scanning Probe Microscope. (2016).
22. Hell, S. W. & Wichmann, J. Breaking the diffraction resolution limit by stimulated emission: stimulated-emission-depletion fluorescence microscopy. *Opt. Lett.* **19**, 780 (1994).
23. V.A. Okhonin. A method of examination of sample microstructure. 4–6 (1986).
24. Gustafsson, M. G. L. Surpassing the lateral resolution limit by a factor of two using structured illumination microscopy. *J. Microsc.* **198**, 82–87 (2000).
25. Balzarotti, F., Eilers, Y., Gwosch, K. C., Gynnå, A. H., Westphal, V., Stefani, F. D., Elf, J. & Hell, S. W. With Minimal Photon Fluxes. *Science (80-. ).* **355**, 606–612 (2017).
26. Betzig, E., Patterson, G. H., Sougrat, R., Lindwasser, O. W., Olenych, S., Bonifacino, J. S., Davidson, M. W., Lippincott-Schwartz, J. & Hess, H. F. Imaging intracellular fluorescent proteins at nanometer resolution. *Science (80-. ).* **313**, 1642–1645 (2006).
27. Moerner, W. E. Single-molecule mountains yield nanoscale cell images. *Nat. Methods* **3**, 781–782 (2006).
28. Dertinger, T., Colyer, R., Iyer, G., Weiss, S. & Enderlein, J. Fast, background-free, 3D super-resolution optical fluctuation imaging (SOFI). *Proc. Natl. Acad. Sci. U. S. A.* **106**, 22287–22292 (2009).
29. Gustafsson, N., Culley, S., Ashdown, G., Owen, D. M., Pereira, P. M. & Henriques, R. Fast live-cell conventional fluorophore nanoscopy with ImageJ through super-resolution radial fluctuations. *Nat. Commun.* **7**, 12471 (2016).
30. Markwirth, A., Lachetta, M., Mönkemöller, V., Heintzmann, R., Hübner, W., Huser, T. & Müller, M. Video-rate multi-color structured illumination microscopy with simultaneous real-time reconstruction. *Nat. Commun.* **10**, 1–11 (2019).
31. Descloux, A., Müller, M., Navikas, V., Markwirth, A., Van Den Eynde, R., Lukes, T., Hübner, W., Lasser, T., Radenovic, A., Dedecker, P. & Huser, T. High-speed

- multiplane structured illumination microscopy of living cells using an image-splitting prism. *Nanophotonics* **9**, 143–148 (2020).
32. Krizek, P., Lukeš, T., Ovesný, M., Fliegel, K. & Hagen, G. M. SIMToolbox: a MATLAB toolbox for structured illumination fluorescence microscopy OS-SIM e SR-SIM g MAP-SIM. 2–3 (2015).
  33. Müller, M., Mönkemöller, V., Hennig, S., Hübner, W. & Huser, T. Open-source image reconstruction of super-resolution structured illumination microscopy data in ImageJ. *Nat. Commun.* **7**, 1–6 (2016).
  34. Desbiolles, B. X. E., De Coulon, E., Bertsch, A., Rohr, S. & Renaud, P. Intracellular Recording of Cardiomyocyte Action Potentials with Nanopatterned Volcano-Shaped Microelectrode Arrays. *Nano Lett.* **19**, 6173–6181 (2019).
  35. Eswara, P. J. & Ramamurthi, K. S. Bacterial cell division: nonmodels poised to take the spotlight. *Annu. Rev. Microbiol.* **71**, 393–411 (2017).
  36. Kubitschek, H. E. Increase in cell mass during the division cycle of *Escherichia coli* B/rA. *J. Bacteriol.* **168**, 613–618 (1986).
  37. Schaechter, M., Williamson, J. P., Hood, J. R. & Koch, A. L. Growth, Cell and Nuclear Divisions in some Bacteria. *J. Gen. Microbiol.* **29**, 421–434 (1962).
  38. Godin, M., Delgado, F. F., Son, S., Grover, W. H., Bryan, A. K., Tzur, A., Jorgensen, P., Payer, K., Grossman, A. D., Kirschner, M. W. & Manalis, S. R. Using buoyant mass to measure the growth of single cells. *Nat. Methods* **7**, 387–390 (2010).
  39. Botella, H., Yang, G., Ouerfelli, O., Ehrt, S., Nathan, C. F. & Vaubourgeix, J. Distinct spatiotemporal dynamics of peptidoglycan synthesis between *Mycobacterium smegmatis* and *Mycobacterium tuberculosis*. *MBio* **8**, e01183-17 (2017).
  40. Dufrêne, Y. F. Using nanotechniques to explore microbial surfaces. *Nat. Rev. Microbiol.* **2**, 451–460 (2004).
  41. Dufrêne, Y. F. Atomic Force Microscopy in Microbiology: New Structural and Functional Insights into the Microbial Cell Surface. *MBio* **5**, 1–14 (2014).
  42. Touhami, A., Jericho, M. H. M. & Beveridge, T. T. J. T. Atomic Force Microscopy of

Cell Growth and Division in. *J. Bacteriol.* **186**, 3286–3295 (2004).

43. Andre, G., Kulakauskas, S., Chapot-Chartier, M.-P., Navet, B., Deghorain, M., Bernard, E., Hols, P. & Dufrêne, Y. F. Imaging the nanoscale organization of peptidoglycan in living *Lactococcus lactis* cells. *Nat. Commun.* **1**, 27 (2010).
44. Alsteens, D., Verbelen, C., Dague, E., Raze, D., Baulard, A. R. & Dufrêne, Y. F. Organization of the mycobacterial cell wall: A nanoscale view. *Pflügers Arch. Eur. J. Physiol.* **456**, 117–125 (2008).
45. Francius, G., Domenech, O., Mingeot-Leclercq, M. P. & Dufrêne, Y. F. Direct observation of *Staphylococcus aureus* cell wall digestion by lysostaphin. *J. Bacteriol.* **190**, 7904–7909 (2008).
46. Fantner, G. E., Barbero, R. J., Gray, D. S. & Belcher, A. M. Kinetics of antimicrobial peptide activity measured on individual bacterial cells using high-speed atomic force microscopy. *Nat. Nanotechnol.* **5**, 280–285 (2010).
47. Nievergelt, A. P., Banterle, N., Andany, S. H., Gönczy, P. & Fantner, G. E. High-speed photothermal off-resonance atomic force microscopy reveals assembly routes of centriolar scaffold protein SAS-6. *Nat. Nanotechnol.* **13**, 696–701 (2018).
48. Kodera, N., Yamamoto, D., Ishikawa, R. & Ando, T. Video imaging of walking myosin V by high-speed atomic force microscopy. *Nature* **468**, 72–76 (2010).
49. Takade, A., Umeda, A., Matsuoka, M., Yoshida, S., Nakamura, M. & Amako, K. Comparative studies of the cell structures of *Mycobacterium leprae* and *M. tuberculosis* using the electron microscopy freeze-substitution technique. *Microbiol. Immunol.* **47**, 265–270 (2003).
50. Prados-Rosales, R., Weinrick, B. C., Pique, D. G., Jacobs, W. R., Casadevall, A., Rodriguez, G. M., Pique, D. G., Weinrick, B. C., Jacobs, W. R. & Prados-Rosales, R. Role for *Mycobacterium tuberculosis* membrane vesicles in iron acquisition. *J. Bacteriol.* **196**, 1250–1256 (2014).
51. Mitchison, J. M. & Nurse, P. Growth in cell length in the fission yeast *Schizosaccharomyces pombe*. *J. Cell Sci.* **75**, 357–76 (1985).

52. Lenarcic, R., Halbedel, S., Visser, L., Shaw, M., Wu, L. J., Errington, J., Marenduzzo, D. & Hamoen, L. W. Localisation of DivIVA by targeting to negatively curved membranes. *EMBO J.* **28**, 2272–2282 (2009).
53. Ramamurthi, K. S. & Losick, R. Negative membrane curvature as a cue for subcellular localization of a bacterial protein. *Proc. Natl. Acad. Sci.* **106**, 13541–13545 (2009).
54. Gurskaya, N. G., Verkhusha, V. V., Shcheglov, A. S., Staroverov, D. B., Chepurnykh, T. V., Fradkov, A. F., Lukyanov, S. & Lukyanov, K. A. Engineering of a monomeric green-to-red photoactivatable fluorescent protein induced by blue light. *Nat. Biotechnol.* **24**, 461–465 (2006).
55. Manina, G., Dhar, N. & McKinney, J. D. Stress and host immunity amplify mycobacterium tuberculosis phenotypic heterogeneity and induce nongrowing metabolically active forms. *Cell Host Microbe* **17**, 32–46 (2015).
56. Kysela, D. T., Brown, P. J. B., Huang, K. C. & Brun, Y. V. Biological consequences and advantages of asymmetric bacterial growth. *Annu. Rev. Microbiol.* **67**, 417–435 (2013).
57. Minc, N., Boudaoud, A. & Chang, F. Mechanical forces of fission yeast growth. *Curr. Biol.* **19**, 1096–1101 (2009).
58. Das, M., Drake, T., Wiley, D. J., Buchwald, P., Vavylonis, D. & Verde, F. Oscillatory dynamics of Cdc42 GTPase in the control of polarized growth. *Science (80-. )*. **337**, 239–243 (2012).
59. Chang, F. & Martin, S. G. Shaping fission yeast with microtubules. *Cold Spring Harb. Perspect. Biol.* **1**, a001347–a001347 (2009).
60. Navarro, F. J., Weston, L. & Nurse, P. Global control of cell growth in fission yeast and its coordination with the cell cycle. *Curr. Opin. Cell Biol.* **24**, 833–837 (2012).
61. Jani, C., Eoh, H., Lee, J., Hamasha, K., Sahana, M., Han, J.-S., Nyayapathy, S., Lee, J.-Y., Suh, J.-W., Lee, S., Rehse, S. J., Crick, D. C. & Kang, C.-M. Regulation of polar peptidoglycan biosynthesis by Wag31 phosphorylation in mycobacteria. *BMC Microbiol.* **10**, 327 (2010).

62. Kang, C.-M., Nyayapathy, S., Lee, J.-Y., Suh, J.-W. & Husson, R. N. Wag31, a homologue of the cell division protein DivIVA, regulates growth, morphology and polar cell wall synthesis in mycobacteria. *Microbiology* **154**, 725–735 (2008).
63. Hu, Z. & Lutkenhaus, J. Topological regulation of cell division in *Escherichia coli* involves rapid pole to pole oscillation of the division inhibitor MinC under the control of MinD and MinE. *Mol. Microbiol.* **34**, 82–90 (1999).
64. Bach, J. N., Albrecht, N. & Bramkamp, M. Imaging DivIVA dynamics using photo-convertible and activatable fluorophores in *Bacillus subtilis*. *Front. Microbiol.* **5**, 1–9 (2014).
65. Kieser, K. J., Boutte, C. C., Kester, J. C., Baer, C. E., Barczak, A. K., Meniche, X., Chao, M. C., Rego, E. H., Sassetti, C. M., Fortune, S. M. & Rubin, E. J. Phosphorylation of the peptidoglycan synthase PonA1 governs the rate of polar elongation in mycobacteria. *PLOS Pathog.* **11**, e1005010 (2015).
66. Marin, J., Battistuzzi, F. U., Brown, A. C. & Hedges, S. B. The timetree of prokaryotes: new insights into their evolution and speciation. *Mol. Biol. Evol.* **34**, msw245 (2016).
67. Mohr, M. A., Argast, P. & Pantazis, P. Labeling cellular structures in vivo using confined primed conversion of photoconvertible fluorescent proteins. *Nat. Protoc.* **11**, 2419–2431 (2016).
68. Nečas, D. & Klapetek, P. Gwyddion: An open-source software for SPM data analysis. *Cent. Eur. J. Phys.* **10**, 181–188 (2012).
69. Schindelin, J., Arganda-Carreras, I., Frise, E., Kaynig, V., Longair, M., Pietzsch, T., Preibisch, S., Rueden, C., Saalfeld, S., Schmid, B., Tinevez, J.-Y., White, D. J., Hartenstein, V., Eliceiri, K., Tomancak, P. & Cardona, A. Fiji: an open-source platform for biological-image analysis. *Nat. Methods* **9**, 676–682 (2012).
70. Thevenaz, P., Ruttimann, U. E. & Unser, M. A pyramid approach to subpixel registration based on intensity. *IEEE Trans. Image Process.* **7**, 27–41 (1998).
71. Straume, M. & Johnson, M. L. in *Technometrics* **6**, 87–105 (1992).
72. Wang, L. & Tran, P. T. *Visualizing Single Rod-Shaped Fission Yeast Vertically in Micro-Sized*

*Holes on Agarose Pad Made by Soft Lithography. Methods Cell Biol.* **120**, (Elsevier Inc., 2014).

73. Bisson-Filho, A. W., Hsu, Y.-P., Squyres, G. R., Kuru, E., Wu, F., Jukes, C., Sun, Y., Dekker, C., Holden, S., VanNieuwenhze, M. S., Brun, Y. V & Garner, E. C. Treadmilling by FtsZ filaments drives peptidoglycan synthesis and bacterial cell division. *Science* **355**, 739–743 (2017).
74. Vinet, L. & Zhedanov, A. A ‘missing’ family of classical orthogonal polynomials. *J. Phys. A Math. Theor.* **44**, 085201 (2011).
75. Bhole, B. D. How many antibiotics are produced by the genus *Streptomyces*? 386–390 (2001). doi:10.1007/s002030100345
76. Mata, J. & Nurse, P. Discovering the poles in yeast. *Trends Cell Biol.* **8**, 163–167 (1998).
77. Verveer, P. *Advanced fluorescence microscopy. Springer Protoc.* **1251**, (2014).
78. Osumi, M. Visualization of yeast cells by electron microscopy. *J. Electron Microsc.* (Tokyo). **61**, 343–365 (2012).
79. Beveridge, T. J. & Graham, L. L. Surface layers of bacteria. *Microbiol. Rev.* **55**, 684–705 (1991).
80. Dufrêne, Y. F. Towards nanomicrobiology using atomic force microscopy. *Nat. Rev. Microbiol.* **6**, 674–680 (2008).
81. Krieg, M., Fläschner, G., Alsteens, D., Gaub, B. M., Roos, W. H., Wuite, G. J. L., Gaub, H. E., Gerber, C., Dufrêne, Y. F. & Müller, D. J. Atomic force microscopy-based mechanobiology. *Nat. Rev. Phys.* **1**, 41–57 (2019).
82. Ortega-Esteban, A., Horcas, I., Hernando-Pérez, M., Ares, P., Pérez-Berná, A. J., San Martín, C., Carrascosa, J. L., De Pablo, P. J. & Gómez-Herrero, J. Minimizing tip-sample forces in jumping mode atomic force microscopy in liquid. *Ultramicroscopy* **114**, 56–61 (2012).
83. Radmacher, M., Tillamnn, R. W., Fritz, M. & Gaub, H. E. From molecules to cells: imaging soft samples with the atomic force microscope. *Science* **257**, 1900–5 (1992).
84. Kunio, K., Takeyasu, T. & Takeyasu, K. *Atomic force microscopy in nanobiology.*

85. Dufrêne, Y. . Application of atomic force microscopy to microbial surfaces: from reconstituted cell surface layers to living cells. *Micron* **32**, 153–165 (2001).
86. Peric, O., Hannebelle, M., Adams, J. D. & Fantner, G. E. Microfluidic bacterial traps for simultaneous fluorescence and atomic force microscopy. *Nano Res.* **10**file:/// , 3896–3908 (2017).
87. Tran, P. T., Paoletti, A. & Chang, F. Imaging green fluorescent protein fusions in living fission yeast cells. *Methods* **33**, 220–225 (2004).
88. Abenza, J. F., Couturier, E., Dodgson, J., Dickmann, J., Chessel, A., Dumais, J. & Carazo Salas, R. E. Wall mechanics and exocytosis define the shape of growth domains in fission yeast. *Nat. Commun.* **6**, 1–13 (2015).
89. Osumi, M., Sato, M., Ishijima, S. A., Konomi, M., Takagi, T. & Yaguchi, H. Dynamics of cell wall formation in fission yeast, *Schizosaccharomyces pombe*. *Fungal Genet. Biol.* **24**, 178–206 (1998).
90. Viljoen, A., Foster, S. J., Fantner, G. E., Hobbs, J. K. & Dufrêne, Y. F. Scratching the surface: bacterial cell envelopes at the nanoscale. *MBio* **11**, 1–12 (2020).
91. Hayhurst, E. J., Kailas, L., Hobbs, J. K. & Foster, S. J. Cell wall peptidoglycan architecture in *Bacillus subtilis*. *Proc. Natl. Acad. Sci. U. S. A.* **105**, 14603–14608 (2008).
92. Turner, R. D., Mesnage, S., Hobbs, J. K. & Foster, S. J. Molecular imaging of glycan chains couples cell-wall polysaccharide architecture to bacterial cell morphology. *Nat. Commun.* **9**, (2018).
93. Cabeen, M. T. & Jacobs-Wagner, C. Bacterial cell shape. *Nat. Rev. Microbiol.* **3**, 601–610 (2005).
94. Egan, A. J. F. & Vollmer, W. The physiology of bacterial cell division. *Ann. N. Y. Acad. Sci.* **1277**, 8–28 (2013).
95. Gray, A. N., Egan, A. J. F., van't Veer, I. L., Verheul, J., Colavin, A., Koumoutsis, A., Biboy, J., Altelaar, A. F. M., Damen, M. J., Huang, K. C., Simorre, J.-P., Breukink, E., den Blaauwen, T., Typas, A., Gross, C. A. & Vollmer, W. Coordination of peptidoglycan synthesis and outer membrane constriction during *Escherichia coli* cell

- division. *Elife* **4**, (2015).
96. Van Der Hofstadt, M., Hüttener, M., Juárez, A. & Gomila, G. Nanoscale imaging of the growth and division of bacterial cells on planar substrates with the atomic force microscope. *Ultramicroscopy* **154**, 29–36 (2015).
  97. Chao, M. C., Kieser, K. J., Minami, S., Mavrici, D., Aldridge, B. B., Fortune, S. M., Alber, T. & Rubin, E. J. Protein Complexes and Proteolytic Activation of the Cell Wall Hydrolase RipA Regulate Septal Resolution in Mycobacteria. *PLoS Pathog* **9**, e1003197 (2013).
  98. Zhou, X., Halladin, D. K., Rojas, E. R., Koslover, E. F., Lee, T. K., Huang, K. C. & Theriot, J. A. Mechanical crack propagation drives millisecond daughter cell separation in *Staphylococcus aureus*. *Science (80-. )*. **348**, 574–578 (2015).
  99. Zhou, X., Halladin, D. K. & Theriot, J. A. Fast Mechanically Driven Daughter Cell Separation Is Widespread in. *MBio* **7**, 1–6 (2016).
  100. Monteiro, J. M., Fernandes, P. B., Vaz, F., Pereira, A. R., Tavares, A. C., Ferreira, M. T., Pereira, P. M., Veiga, H., Kuru, E., Vannieuwenhze, M. S., Brun, Y. V., Filipe, S. R. & Pinho, M. G. Cell shape dynamics during the staphylococcal cell cycle. *Nat. Commun.* **6**, 1–12 (2015).
  101. Vijay, S., Anand, D. & Ajitkumar, P. Unveiling unusual features of formation of septal partition and constriction in mycobacteria-an ultrastructural study. *J. Bacteriol.* **194**, 702–707 (2012).
  102. Akemi Takade , Kenji Takeya , Hatsumi Taniguchi, Y. M. Electron Microscopic Observations of Cell Division in *Mycobacterium vaccae* V1. *J. Gen. Microbiol.* 0–5 (1983).
  103. Dahl, J. L. Electron microscopy analysis of *Mycobacterium tuberculosis* cell division. *FEMS Microbiol. Lett.* **240**, 15–20 (2004).
  104. Koch, A. L. Biophysics of bacterial walls viewed as stress-bearing fabric. *Microbiol. Rev.* **52**, 337–53 (1988).
  105. Herman-Bausier, P., Valotteau, C., Pietrocola, G., Rindi, S., Alsteens, D., Foster, T. J.,



- Speziale, P. & Dufrêne, Y. F. Mechanical strength and inhibition of the *Staphylococcus aureus* collagen-binding protein Cna. *MBio* **7**, (2016).
106. Oh, Y. J., Hubauer-Brenner, M., Gruber, H. J., Cui, Y., Traxler, L., Siligan, C., Park, S. & Hinterdorfer, P. Curli mediate bacterial adhesion to fibronectin via tensile multiple bonds. *Sci. Rep.* **6**, (2016).
  107. Deng, Y., Sun, M. & Shaevitz, J. W. Direct measurement of cell wall stress stiffening and turgor pressure in live bacterial cells. *Phys. Rev. Lett.* **107**, (2011).
  108. Saar Dover, R., Bitler, A., Shimoni, E., Trieu-Cuot, P. & Shai, Y. Multiparametric AFM reveals turgor-responsive net-like peptidoglycan architecture in live streptococci. *Nat. Commun.* **6**, 1–10 (2015).
  109. Turner, R. D., Hurd, A. F., Cadby, A., Hobbs, J. K. & Foster, S. J. Cell wall elongation mode in Gram-negative bacteria is determined by peptidoglycan architecture. *Nat. Commun.* **4**, (2013).
  110. Bailey, R. G., Turner, R. D., Mullin, N., Clarke, N., Foster, S. J. & Hobbs, J. K. The interplay between cell wall mechanical properties and the cell cycle in *staphylococcus aureus*. *Biophys. J.* **107**, 2538–2545 (2014).
  111. Loskill, P., Pereira, P. M., Jung, P., Bischoff, M., Herrmann, M., Pinho, M. G. & Jacobs, K. Reduction of the peptidoglycan crosslinking causes a decrease in stiffness of the *staphylococcus aureus* cell envelope. *Biophys. J.* **107**, 1082–1089 (2014).
  112. Dufrêne, Y. F., Martínez-Martín, D., Medalsy, I., Alsteens, D. & Müller, D. J. Multiparametric imaging of biological systems by force-distance curve-based AFM. *Nat. Methods* **10**, 847–854 (2013).
  113. Sun, S. X. & Jiang, H. Physics of Bacterial Morphogenesis. *Microbiol. Mol. Biol. Rev.* **76**, 113–113 (2012).
  114. Wheeler, R., Turner, R. D., Bailey, R. G., Salamaga, B., Mesnage, S., Mohamad, S. A. S., Hayhurst, E. J., Horsburgh, M., Hobbs, J. K. & Foster, S. J. Bacterial cell enlargement requires control of cell wall stiffness mediated by peptidoglycan hydrolases. *MBio* **6**, (2015).

115. Ruggiero, A., Marasco, D., Squeglia, F., Soldini, S., Pedone, E., Pedone, C. & Berisio, R. Structure and functional regulation of RipA, a mycobacterial enzyme essential for daughter cell separation. *Structure* **18**, 1184–1190 (2010).
116. Hett, E. C., Chao, M. C., Steyn, A. J., Fortune, S. M., Deng, L. L. & Rubin, E. J. A partner for the resuscitation-promoting factors of Mycobacterium tuberculosis. *Mol. Microbiol.* **66**, 658–668 (2007).
117. Hett, E. C., Chao, M. C., Deng, L. L. & Rubin, E. J. A mycobacterial enzyme essential for cell division synergizes with resuscitation-promoting factor. *PLoS Pathog.* **4**, (2008).
118. Jiang, Y., Liang, X., Guo, M., Cao, Y. & Cai, S. Fracture mechanics modeling of popping event during daughter cell separation. *Biomech. Model. Mechanobiol.* **17**, 1131–1137 (2018).
119. Thanky, N. R., Young, D. B. & Robertson, B. D. Unusual features of the cell cycle in mycobacteria: Polar-restricted growth and the snapping-model of cell division. *Tuberculosis* **87**, 231–236 (2007).
120. Smolyakov, G., Formosa-Dague, C., Severac, C., Duval, R. E. & Dague, E. High speed indentation measures by FV, QI and QNM introduce a new understanding of bionanomechanical experiments. *Micron* **85**, 8–14 (2016).
121. Atilgan, E., Magidson, V., Khodjakov, A. & Chang, F. Morphogenesis of the fission yeast cell through cell wall expansion. *Curr. Biol.* **25**, 2150–2157 (2015).
122. Rust, M. J., Bates, M. & Zhuang, X. Sub-diffraction-limit imaging by stochastic optical reconstruction microscopy (STORM). *Nat. Methods* **3**, 793–796 (2006).
123. Laissue, P. P., Alghamdi, R. A., Tomancak, P., Reynaud, E. G. & Shroff, H. Assessing phototoxicity in live fluorescence imaging. *Nat. Publ. Gr.* **14**, 657–661 (2017).
124. Magidson, V. & Khodjakov, A. *Circumventing photodamage in live-cell microscopy. Methods Cell Biol.* **114**, (Elsevier Inc., 2013).
125. Eswaramoorthy, P., Winter, P. W., Wawrzusin, P., York, A. G., Shroff, H. & Ramamurthi, K. S. Asymmetric Division and Differential Gene Expression during a Bacterial Developmental Program Requires DivIVA. *PLoS Genet.* **10**, e1004526 (2014).

126. Coltharp, C. & Xiao, J. Superresolution microscopy for microbiology. *Cell. Microbiol.* **14**, 1808–1818 (2012).
127. Shao, L., Kner, P., Rego, E. H. & Gustafsson, M. G. L. Super-resolution 3D microscopy of live whole cells using structured illumination. *Nat. Methods* **8**, 1044–1046 (2011).
128. Demmerle, J., Innocent, C., North, A. J., Ball, G., Müller, M., Miron, E., Matsuda, A., Dobbie, I. M., Markaki, Y. & Schermelleh, L. Strategic and practical guidelines for successful structured illumination microscopy. *Nat. Protoc.* **12**, (2017).
129. Brown, J. W. P., Bauer, A., Polinkovsky, M. E., Bhumkar, A., Hunter, D. J. B., Gaus, K., Sierrecki, E. & Gambin, Y. Single-molecule detection on a portable 3D-printed microscope. *Nat. Commun.* **10**, 1–7 (2019).
130. Girstmair, J., Zakrzewski, A., Lapraz, F., Handberg-Thorsager, M., Tomancak, P., Pitrone, P. G., Simpson, F. & Telford, M. J. Light-sheet microscopy for everyone? Experience of building an OpenSPIM to study flatworm development. *BMC Dev. Biol.* **16**, 1–16 (2016).
131. Pitrone, P. G., Schindelin, J., Stuyvenberg, L., Preibisch, S., Weber, M., Eliceiri, K. W., Huiskens, J. & Tomancak, P. OpenSPIM: An open-access light-sheet microscopy platform. *Nat. Methods* **10**, 598–599 (2013).
132. Marx, V. Microscopy: OpenSPIM 2.0. *Nat. Methods* **13**, 979–982 (2016).
133. Sharkey, J. P., Foo, D. C. W., Kabla, A., Baumberg, J. J. & Bowman, R. W. A one-piece 3D printed flexure translation stage for open-source microscopy. *Rev. Sci. Instrum.* **87**, (2016).
134. Cybulski, J. S., Clements, J. & Prakash, M. Foldscope: Origami-based paper microscope. *PLoS One* **9**, (2014).
135. Diederich, B., Richter, R., Carlstedt, S., Uwurukundo, X., Wang, H., Mosig, A. & Heintzmann, R. UC2 - A 3D-printed general-purpose optical toolbox for microscopic imaging. *Opt. InfoBase Conf. Pap. Part F157-*, 3–4 (2019).
136. Martens, K. J. A., van Beljouw, S. P. B., van der Els, S., Vink, J. N. A., Baas, S.,

- Vogelaar, G. A., Brouns, S. J. J., van Baarlen, P., Kleerebezem, M. & Hohlbein, J. Visualisation of dCas9 target search in vivo using an open-microscopy framework. *Nat. Commun.* **10**, 1–11 (2019).
137. Patel, T. P., Kim, T. N., Yu, G., Dedania, V. S., Lieu, P., Qian, C. X., Besirli, C. G., Demirci, H., Margolis, T., Fletcher, D. A. & Paulus, Y. M. Smartphone-based, rapid, wide-field fundus photography for diagnosis of pediatric retinal diseases. *Transl. Vis. Sci. Technol.* **8**, (2019).
  138. Li, H., Soto-Montoya, H., Voisin, M., Valenzuela, L. F. & Prakash, M. Octopi: Open configurable high-throughput imaging platform for infectious disease diagnosis in the field. *bioRxiv* 684423 (2019). doi:10.1101/684423
  139. Poher, V., Zhang, H. X., Kennedy, G. T., Griffin, C., Oddos, S., Gu, E., Elson, D. S., Girkin, J. M., French, P. M. W., Dawson, M. D. & Neil, M. A. A. Optical sectioning microscopes with no moving parts using a micro-stripe array light emitting diode. *Opt. Express* **15**, 11196 (2007).
  140. Xu, D., Jiang, T., Li, A., Hu, B., Feng, Z., Gong, H., Zeng, S. & Luo, Q. Fast optical sectioning obtained by structured illumination microscopy using a digital mirror device. *J. Biomed. Opt.* **18**, 060503 (2013).
  141. Darmon, D., McNeil, J. R. & Handschy, M. A. 70.1: LED-Illuminated Pico Projector Architectures. *SID Symp. Dig. Tech. Pap.* **39**, 1070 (2008).
  142. He, Z., Sui, X., Jin, G. & Cao, L. Progress in virtual reality and augmented reality based on holographic display. *Appl. Opt.* **58**, A74 (2019).
  143. Bosse, J. B., Tanneti, N. S., Hogue, I. B. & Enquist, L. W. Open LED illuminator: A simple and inexpensive LED illuminator for fast multicolor particle tracking in neurons. *PLoS One* **10**, 1–21 (2015).
  144. Yin, X., Farin, H. F., Van Es, J. H., Clevers, H., Langer, R. & Karp, J. M. Niche-independent high-purity cultures of Lgr5 + intestinal stem cells and their progeny. *Nat. Methods* **11**, 106–112 (2014).
  145. Gjorevski, N., Sachs, N., Manfrin, A., Giger, S., Bragina, M. E., Ordóñez-Morán, P., Clevers, H. & Lutolf, M. P. Designer matrices for intestinal stem cell and organoid

- culture. *Nature* **539**, 560–564 (2016).
146. Kimmel, C. B., Ballard, W. W., Kimmel, S. R., Ullmann, B. & Schilling, T. F. Stages of embryonic development of the zebrafish. *Dev. Dyn.* **203**, 253–310 (1995).
  147. Herrgen, L., Schröter, C., Bajard, L. & Oates, A. C. Multiple embryo time-lapse imaging of zebrafish development. *Methods Mol. Biol.* **546**, 243–254 (2009).
  148. Dufrêne, Y. F., Ando, T., Garcia, R., Alsteens, D., Martinez-Martin, D., Engel, A., Gerber, C. & Müller, D. J. Imaging modes of atomic force microscopy for application in molecular and cell biology. *Nat. Nanotechnol.* **12**, 295–307 (2017).
  149. Humphris, A. D. L., Hobbs, J. K. & Miles, M. J. Ultrahigh-speed scanning near-field optical microscopy capable of over 100 frames per second. *Appl. Phys. Lett.* **83**, 6–8 (2003).
  150. Binnig, G., Quate, C. F. & Gerber, C. Atomic Force Microscope. *Phys. Rev. Lett.* **56**, 930–933 (1986).
  151. Anselmetti, D., Luthi, R., Meyer, E., Richmond, T., Dreier, M., Frommer, J. E. & Guntherodt, H. J. Attractive-mode imaging of biological materials with dynamic force microscopy. *Nanotechnology* **5**, 87–94 (1994).
  152. Schäffer, T. E., Cleveland, J. P., Ohnesorge, F., Walters, D. A. & Hansma, P. K. Studies of vibrating atomic force microscope cantilevers in liquid. *J. Appl. Phys.* **80**, 3622–3627 (1996).
  153. Hansma, P. K., Cleveland, J. P., Radmacher, M., Walters, D. A., Hillner, P. E., Bezanilla, M., Fritz, M., Vie, D., Hansma, H. G., Prater, C. B., Massie, J., Fukunaga, L., Gurley, J. & Elings, V. Tapping mode atomic force microscopy in liquids. *Appl. Phys. Lett.* **64**, 1738–1740 (1994).
  154. Müller, D. J., Büldt, G. & Engel, A. Force-induced conformational change of bacteriorhodopsin. *J. Mol. Biol.* **249**, 239–243 (1995).
  155. Rosa-Zeiser, A., Weilandt, E., Hild, S. & Marti, O. Simultaneous measurement of elastic, electrostatic and adhesive properties by scanning force microscopy: Pulsed-force mode operation. *Meas. Sci. Technol.* **8**, 1333–1338 (1997).

156. Han, W., Lindsay, S. M. & Jing, T. A magnetically driven oscillating probe microscope for operation in liquids. *Appl. Phys. Lett.* **69**, 4111–4113 (1996).
157. Umeda, N., Ishizaki, S. & Uwai, H. Scanning attractive force microscope using photothermal vibration. *J. Vac. Sci. Technol. B Microelectron. Nanom. Struct.* **9**, 1318 (1991).
158. Indermühle, P. F., Schürmann, G., Racine, G. A. & De Rooij, N. F. Fabrication and characterization of cantilevers with integrated sharp tips and piezoelectric elements for actuation and detection for parallel AFM applications. *Sensors Actuators, A Phys.* **60**, 186–190 (1997).
159. Rogers, B., Manning, L., Sulchek, T. & Adams, J. D. Improving tapping mode atomic force microscopy with piezoelectric cantilevers. *Ultramicroscopy* **100**, 267–276 (2004).
160. Tortonese, M., Barrett, R. C. & Quate, C. F. Atomic resolution with an atomic force microscope using piezoresistive detection. *Appl. Phys. Lett.* **62**, 834–836 (1993).
161. Fantner, G. E., Schumann, W., Barbero, R. J., Deutschinger, A., Todorov, V., Gray, D. S., Belcher, A. M., Rangelow, I. W. & Youcef-Toumi, K. Use of self-actuating and self-sensing cantilevers for imaging biological samples in fluid. *Nanotechnology* **20**, (2009).
162. Fantner, G. E., Burns, D. J., Belcher, A. M., Rangelow, I. W. & Youcef-Toumi, K. DMCMN: In depth characterization and control of AFM cantilevers with integrated sensing and actuation. *J. Dyn. Syst. Meas. Control. Trans. ASME* **131**, 1–13 (2009).
163. Rangelow, I. W., Ivanov, T., Ivanova, K., Volland, B. E., Grabiec, P. & Sarov, Y. Piezoresistive and self-actuated 128-cantilever arrays for nanotechnology applications. **84**, 1260–1264 (2007).
164. Herruzo, E. T. & Garcia, R. Frequency response of an atomic force microscope in liquids and air: Magnetic versus acoustic excitation. *Appl. Phys. Lett.* **91**, 22–25 (2007).
165. Ratcliff, G. C., Erie, D. A. & Superfine, R. Photothermal modulation for oscillating mode atomic force microscopy in solution. *Appl. Phys. Lett.* **72**, 1911–1913 (1998).
166. Suzuki, Y., Sakai, N., Yoshida, A., Uekusa, Y., Yagi, A., Imaoka, Y., Ito, S., Karaki, K. & Takeyasu, K. High-speed atomic force microscopy combined with inverted optical

- microscopy for studying cellular events. *Sci. Rep.* **3**, 1–7 (2013).
167. Kreith, J., Strunz, T., Fantner, E. J., Fantner, G. E. & Cordill, M. J. A versatile atomic force microscope integrated with a scanning electron microscope. *Rev. Sci. Instrum.* **88**, (2017).
  168. Bauerdick, S., Burkhardt, C., Rudolf, R., Barth, W., Bucher, V. & Nisch, W. In-situ monitoring of electron beam induced deposition by atomic force microscopy in a scanning electron microscope. *Microelectron. Eng.* **67–68**, 963–969 (2003).
  169. Adam, H., Rode, S., Schreiber, M., Kobayashi, K., Yamada, H. & Kühnle, A. Photothermal excitation setup for a modified commercial atomic force microscope. *Rev. Sci. Instrum.* **85**, (2014).
  170. Labuda, A., Kobayashi, K., Miyahara, Y. & Grütter, P. Retrofitting an atomic force microscope with photothermal excitation for a clean cantilever response in low Q environments. *Rev. Sci. Instrum.* **83**, (2012).
  171. Nievergelt, A. P., Adams, J. D., Odermatt, P. D. & Fantner, G. E. High-frequency multimodal atomic force microscopy. *Beilstein J. Nanotechnol.* **5**, 2459–2467 (2014).
  172. Prater, C. B., Massie, J., Grigg, D. A., Elings, V. B., Hansma, P. K., Drake, B. & Barbara, S. Scanning stylus atomic force microscope with cantilever tracking and optical access. *Processing* (1991).
  173. Nievergelt, A. P., Andany, S. H., Adams, J. D., Hannebelle, M. T. & Fantner, G. E. Components for high-speed atomic force microscopy optimized for low phase-lag. in *2017 IEEE Int. Conf. Adv. Intell. Mechatronics* 731–736 (IEEE, 2017). doi:10.1109/AIM.2017.8014104
  174. Michler, G. H. in *Electron Microsc. Polym.* 121–143 (Springer Berlin Heidelberg, 2008). doi:10.1007/978-3-540-36352-1\_6
  175. Henriques, R., Griffiths, C., Rego, E. H. & Mhlanga, M. M. PALM and STORM: Unlocking Live-Cell Super-Resolution.
  176. Desbiolles, B. X. E., Hannebelle, M. T. M., de Coulon, E., Bertsch, A., Rohr, S., Fantner, G. E. & Renaud, P. Volcano-Shaped Scanning Probe Microscopy Probe for

- Combined Force-Electrogram Recordings from Excitable Cells. *Nano Lett.* **20**, 4520–4529 (2020).
177. Hoffman, B. D., Grashoff, C. & Schwartz, M. A. Dynamic molecular processes mediate cellular mechanotransduction. *Nature* **475**, 316–323 (2011).
  178. Howard, J., Grill, S. W. & Bois, J. S. Turing’s next steps: The mechanochemical basis of morphogenesis. *Nat. Rev. Mol. Cell Biol.* **12**, 400–406 (2011).
  179. Brugués, A., Anon, E., Conte, V., Veldhuis, J. H., Gupta, M., Colombelli, J., Muñoz, J. J., Brodland, G. W., Ladoux, B. & Trepát, X. Forces driving epithelial wound healing. *Nat. Phys.* **10**, 683–690 (2014).
  180. Petridou, N. I., Spiró, Z. & Heisenberg, C. P. Multiscale force sensing in development. *Nat. Cell Biol.* **19**, 581–588 (2017).
  181. Binnig, G., Quate, C. F. & Gerber, C. Atomic force microscope. *Phys. Rev. Lett.* **56**, 930–933 (1986).
  182. Radmacher, M., Tillmann, R. W. & Gaub, H. E. Imaging viscoelasticity by force modulation with the atomic force microscope. *Biophys. J.* **64**, 735–742 (1993).
  183. Matzke, R., Jacobson, K. & Radmacher, M. Direct, high-resolution measurement of furrow stiffening during division of adherent cells. *Nat. Cell Biol.* **3**, 607–610 (2001).
  184. Iyer, S., Gaikwad, R. M., Subba-Rao, V., Woodworth, C. D., Sokolov, I., Subba-Rao, V., Woodworth, C. D. & Sokolov, I. Atomic force microscopy detects differences in the surface brush of normal and cancerous cells. *Nat. Nanotechnol.* **4**, 389–393 (2009).
  185. Cross, S. E., Jin, Y.-S., Rao, J. & Gimzewski, J. K. Nanomechanical analysis of cells from cancer patients. *Nat. Nanotechnol.* **2**, 780–783 (2007).
  186. Viani, M. B., Schäffer, T. E., Chand, A., Rief, M., Gaub, H. E. & Hansma, P. K. Small cantilevers for force spectroscopy of single molecules. *J. Appl. Phys.* **86**, 2258–2262 (1999).
  187. Laskowski, P. R., Pfreundschuh, M., Stauffer, M., Ucurum, Z., Fotiadis, D. & Müller, D. J. High-Resolution Imaging and Multiparametric Characterization of Native Membranes by Combining Confocal Microscopy and an Atomic Force Microscopy-



Based Toolbox. *ACS Nano* **11**, 8292–8301 (2017).

188. Moeendarbary, E., Valon, L., Fritzsche, M., Harris, A. R., Moulding, D. A., Thrasher, A. J., Stride, E., Mahadevan, L. & Charras, G. T. The cytoplasm of living cells behaves as a poroelastic material. *Nat. Mater.* **12**, 253–261 (2013).
189. Hoh, J. H. & Schoenenberger, C. A. Surface morphology and mechanical properties of MDCK monolayers by atomic force microscopy. *J. Cell Sci.* **107**, 1105–1114 (1994).
190. Rotsch, C., Braet, F., Wisse, E. & Radmacher, M. AFM imaging and elasticity measurements on living rat liver macrophages. *Cell Biol. Int.* **21**, 685–696 (1997).
191. Rotsch, C., Jacobson, K. & Radmacher, M. Dimensional and mechanical dynamics of active and stable edges in motile fibroblasts investigated by using atomic force microscopy. *Proc. Natl. Acad. Sci. U. S. A.* **96**, 921–926 (1999).
192. Rotsch, C. & Radmacher, M. Drug-induced changes of cytoskeletal structure and mechanics in fibroblasts: An atomic force microscopy study. *Biophys. J.* **78**, 520–535 (2000).
193. Blaue, C., Kashef, J. & Franz, C. M. Cadherin-11 promotes neural crest cell spreading by reducing intracellular tension—Mapping adhesion and mechanics in neural crest explants by atomic force microscopy. *Semin. Cell Dev. Biol.* **73**, 95–106 (2018).
194. Domke, J., Parak, W. J., George, M., Gaub, H. E. & Radmacher, M. Mapping the mechanical pulse of single cardiomyocytes with the atomic force microscope. *Eur. Biophys. J.* **28**, 179–186 (1999).
195. Chang, W. T., Yu, D., Lai, Y. C., Lin, K. Y. & Liao, I. Characterization of the mechanodynamic response of cardiomyocytes with atomic force microscopy. *Anal. Chem.* **85**, 1395–1400 (2013).
196. Engler, A. J., Griffin, M. A., Sen, S., Bönnemann, C. G., Sweeney, H. L. & Discher, D. E. Myotubes differentiate optimally on substrates with tissue-like stiffness: pathological implications for soft or stiff microenvironments. **166**, 877–887 (2004).
197. Engler, A. J., Sen, S., Sweeney, H. L. & Discher, D. E. Matrix Elasticity Directs Stem Cell Lineage Specification. *Cell* **126**, 677–689 (2006).

198. Liu, L., You, Z., Yu, H., Zhou, L., Zhao, H., Yan, X., Li, D., Wang, B., Zhu, L., Xu, Y., Xia, T., Shi, Y., Huang, C., Hou, W. & Du, Y. Mechanotransduction-modulated fibrotic microniches reveal the contribution of angiogenesis in liver fibrosis. *Nat. Mater.* **16**, 1252–1261 (2017).
199. Herman-Bausier, P., Valotteau, C., Pietrocola, G., Rindi, S., Alsteens, D., Foster, T. J., Speziale, P. & Dufrêne, Y. F. Mechanical Strength and Inhibition of the *Staphylococcus aureus*. *MBio* **7**, 1–11 (2016).
200. Mohammed, D., Versaevol, M., Bruyère, C., Alaimo, L., Luciano, M., Vercruysse, E., Procès, A. & Gabriele, S. Innovative tools for mechanobiology: Unraveling outside-in and inside-out mechanotransduction. *Front. Bioeng. Biotechnol.* **7**, (2019).
201. O'Shea, C., Holmes, A. P., Winter, J., Correia, J., Ou, X., Dong, R., He, S., Kirchhof, P., Fabritz, L., Rajpoot, K. & Pavlovic, D. Cardiac optogenetics and optical mapping – Overcoming spectral congestion in all-optical cardiac electrophysiology. *Front. Physiol.* **10**, 182 (2019).
202. Caluori, G., Pribyl, J., Cmiel, V., Pesl, M., Potocnak, T., Provaznik, I., Skladal, P. & Rotrekl, V. Simultaneous study of mechanobiology and calcium dynamics on hESC-derived cardiomyocytes clusters. *J. Mol. Recognit.* **32**, e2760 (2019).
203. Gaub, B. M. & Müller, D. J. Mechanical Stimulation of Piezo1 Receptors Depends on Extracellular Matrix Proteins and Directionality of Force. *Nano Lett.* **17**, 2064–2072 (2017).
204. Rohr, S. & Salzberg, B. M. Multiple site optical recording of transmembrane voltage (MSORTV) in patterned growth heart cell cultures: assessing electrical behavior, with microsecond resolution, on a cellular and subcellular scale. *Biophys. J.* **67**, 1301–1315 (1994).
205. Cogollo, J. F. S., Tedesco, M., Martinoia, S. & Raiteri, R. A new integrated system combining atomic force microscopy and micro-electrode array for measuring the mechanical properties of living cardiac myocytes. *Biomed. Microdevices* **13**, 613–621 (2011).
206. Tian, J., Tu, C., Huang, B., Liang, Y., Zhou, J. & Ye, X. Study of the union method of microelectrode array and AFM for the recording of electromechanical activities in

- living cardiomyocytes. *Eur. Biophys. J.* **46**, 495–507 (2017).
207. Upadhye, K. V., Candiello, J. E., Davidson, L. A. & Lin, H. Whole-cell electrical activity under direct mechanical stimulus by AFM cantilever using planar patch clamp chip approach. *Cell. Mol. Bioeng.* **4**, 270–280 (2011).
  208. Pamir, E., George, M., Fertig, N. & Benoit, M. Planar patch-clamp force microscopy on living cells. *Ultramicroscopy* **108**, 552–557 (2008).
  209. Meister, A., Gabi, M., Behr, P., Studer, P., Vörös, J., Niedermann, P., Bitterli, J., Polesel-Maris, J., Liley, M., Heinzelmann, H. & Zambelli, T. FluidFM: Combining atomic force microscopy and nanofluidics in a universal liquid delivery system for single cell applications and beyond. *Nano Lett.* **9**, 2501–2507 (2009).
  210. Guillaume-Gentil, O., Potthoff, E., Ossola, D., Franz, C. M., Zambelli, T. & Vorholt, J. A. Force-controlled manipulation of single cells: From AFM to FluidFM. *Trends Biotechnol.* **32**, 381–388 (2014).
  211. Ossola, D., Amarouch, M.-Y., Behr, P., Vörös, J., Abriel, H. & Zambelli, T. Force-Controlled Patch Clamp of Beating Cardiac Cells. *Nano Lett.* **15**, 1743–1750 (2015).
  212. Linley, J. E. Perforated whole-cell patch-clamp recording. *Methods Mol. Biol.* **998**, 149–157 (2013).
  213. Desbiolles, B. X. E., De Coulon, E., Maino, N., Bertsch, A., Rohr, S. & Renaud, P. Nanovolcano-microelectrode-arrays: Controlled electroporation enables long-term on-demand registration of transmembrane action potentials. *Submitted* (2020).
  214. Almquist, B. D. & Melosh, N. A. Fusion of biomimetic stealth probes into lipid bilayer cores. *Proc. Natl. Acad. Sci.* **107**, 5815–5820 (2010).
  215. Almquist, B. D., Verma, P., Cai, W. & Melosh, N. a. Nanoscale patterning controls inorganic-membrane interface structure. *Nanoscale* **3**, 391–400 (2011).
  216. Almquist, B. D. & Melosh, N. A. Molecular structure influences the stability of membrane penetrating biointerfaces. *Nano Lett.* **11**, 2066–2070 (2011).
  217. Verma, P. & Melosh, N. A. Gigaohm resistance membrane seals with stealth probe electrodes. *Appl. Phys. Lett.* **97**, 10–13 (2010).

218. VanDersarl, J. J. & Renaud, P. Biomimetic surface patterning for long-term transmembrane access. *Sci. Rep.* **6**, (2016).
219. Hansma, P. K., Drake, B., Grigg, D., Prater, C. B., Yashar, F., Gurley, G., Elings, V., Feinstein, S. & Lal, R. A new, optical-lever based atomic force microscope. *J. Appl. Phys.* **76**, 796–799 (1994).
220. Desbiolles, B. X. E., Bertsch, A. & Renaud, P. Ion beam etching redeposition for 3D multimaterial nanostructure manufacturing. *Microsystems Nanoeng.* **5**, (2019).
221. Huebsch, N., Loskill, P., Mandegar, M. A., Marks, N. C., Sheehan, A. S., Ma, Z., Mathur, A., Nguyen, T. N., Yoo, J. C., Judge, L. M., Spencer, C. I., Chukka, A. C., Russell, C. R., So, P. L., Conklin, B. R. & Healy, K. E. Automated video-based analysis of contractility and calcium flux in human-induced pluripotent stem cell-derived cardiomyocytes cultured over different spatial scales. *Tissue Eng. - Part C Methods* **21**, 467–479 (2015).
222. Hoang, P., Jacquir, S., Lemus, S. & Ma, Z. Quantification of Contractile Dynamic Complexities Exhibited by Human Stem Cell-Derived Cardiomyocytes Using Nonlinear Dimensional Analysis. *Sci. Rep.* **9**, (2019).
223. Lugstein, A., Bertagnolli, E., Kranz, C., Kueng, A. & Mizaikoff, B. Integrating micro- and nanoelectrodes into atomic force microscopy cantilevers using focused ion beam techniques. *Appl. Phys. Lett.* **81**, 349–351 (2002).
224. Franks, W., Schenker, I., Schmutz, P. & Hierlemann, A. Impedance characterization and modeling of electrodes for biomedical applications. *IEEE Trans. Biomed. Eng.* **52**, 1295–1302 (2005).
225. Natarajan, A., Stancescu, M., Dhir, V., Armstrong, C., Sommerhage, F., Hickman, J. J. & Molnar, P. Patterned cardiomyocytes on microelectrode arrays as a functional, high information content drug screening platform. *Biomaterials* **32**, 4267–4274 (2011).
226. Shimada, J. & Kaneko, T. Development of Single Cardiomyocyte Measurement of Extracellular Potential. *Biophys. J.* **110**, 169 (2016).
227. Zhao, Y., You, S. S., Zhang, A., Lee, J.-H., Huang, J. & Lieber, C. M. Scalable ultrasmall three-dimensional nanowire transistor probes for intracellular recording. *Nat.*

*Nanotechnol.* **14**, 783–790 (2019).

- 228. Rothe, J., Frey, O., Madangopal, R., Rickus, J. & Hierlemann, A. Robust functionalization of large microelectrode arrays by using pulsed potentiostatic deposition. *Sensors (Switzerland)* **17**, (2017).
- 229. Carbona, S., Goff, C. & Goff, X. Fission yeast cytoskeletons and cell polarity factors: connecting at the cortex. *Biol. Cell* **98**, 619–631 (2006).
- 230. Kume, K., Koyano, T., Kanai, M., Toda, T. & Hirata, D. Calcineurin ensures a link between the DNA replication checkpoint and microtubule-dependent polarized growth. *Nat. Cell Biol.* **13**, 234–242 (2011).
- 231. Geitmann, A. & Dumais, J. Not-so-tip-growth. *Plant Signal. Behav.* **4**, 136–138 (2009).
- 232. Shaw, S. L., Dumais, J. & Long, S. R. Cell surface expansion in polarly growing root hairs of *Medicago truncatula*. *Plant Physiol.* **124**, 959–969 (2000).
- 233. Bernal, R., Rojas, E. & Dumais, J. The mechanics of tip growth morphogenesis: what we have learned from rubber balloons. *J. Mech. Mater. Struct.* **2**, 1157–1168 (2007).
- 234. Davì, V. & Minc, N. Mechanics and morphogenesis of fission yeast cells. *Curr. Opin. Microbiol.* **28**, 36–45 (2015).
- 235. Davì, V., Tanimoto, H., Ershov, D., Haupt, A., De Belly, H., Le Borgne, R., Couturier, E., Boudaoud, A. & Minc, N. Mechanosensation Dynamically Coordinates Polar Growth and Cell Wall Assembly to Promote Cell Survival. *Dev. Cell* **45**, 170-182.e7 (2018).
- 236. Lee, Y. J. & Yang, Z. Tip growth: signaling in the apical dome. *Curr. Opin. Plant Biol.* **11**, 662–671 (2008).
- 237. Dumais, J., Shaw, S. L., Steele, C. R., Long, S. R. & Ray, P. M. An anisotropic-viscoplastic model of plant cell morphogenesis by tip growth. *Int. J. Dev. Biol.* **50**, 209–222 (2006).
- 238. Brand, A. Hyphal Growth in Human Fungal Pathogens and. **2012**, (2012).
- 239. Bastmeyer, M., Deising, H. B. & Bechinger, C. Force exertion in fungal infection.

*Annu. Rev. Biophys. Biomol. Struct.* **31**, 321–341 (2002).

- 240. Thacker, V. V, Dhar, N., Sharma, K., Barrile, R., Karalis, K. & McKinney, J. D. A lung-on-chip model reveals an essential role for alveolar epithelial cells in controlling bacterial growth in early tuberculosis. *bioRxiv* 2020.02.03.931170 (2020). doi:10.1101/2020.02.03.931170
- 241. Popov, V. L., Heß, M. & Willert, E. *Handbook of Contact Mechanics. Handb. Contact Mech.* (2019). doi:10.1007/978-3-662-58709-6
- 242. Ding, Y., Wang, J., Xu, G. K. & Wang, G. F. Are elastic moduli of biological cells depth dependent or not? Another explanation using a contact mechanics model with surface tension. *Soft Matter* **14**, 7534–7541 (2018).
- 243. Pitrone, P. G., Schindelin, J., Stuyvenberg, L., S., P., M., W., K.W., E., J., H., P., T., Preibisch, S., Weber, M., Eliceiri, K. W., Huisken, J. & Tomancak, P. OpenSPIM - an open access platform for light sheet microscopy. *Nat. Methods* **10**, 598–599 (2013).

# Curriculum Vitae

## 1. Personal information

**Name** Melanie Hannebelle

**Office** EPFL STI IBI-STI LBNI / BM 5126 (Bâtiment BM) Station 17 /CH-1015 Lausanne

**Phone** +41 21 693 64 26

**Email** melanie.hannebelle@epfl.ch / melanie.hannebelle@gmail.com

**ORCID** <https://orcid.org/0000-0002-3769-1437>

**Nationality** French

**Date of birth** August 11, 1991

## 2. Education

**PHD in bioengineering**, Prof. G. Fantner & Prof. J. McKinney, EPFL, June 2015-2020

**Master in microengineering**, EPFL, September 2013 – March 2015

**Bachelor and Master in electrical engineering**, ENS Cachan, France, September 2010 – August 2013

**Classes préparatoires aux grandes écoles**, Lycee Lakanal, France, September 2008-July 2010

## 3. Employment history

**PHD** in bioengineering, EPFL, June 2015 – 2020

**Master thesis**, Debiotech, Switzerland, September 2014 - March 2015

**Student assistant**, Prof. Kippenberg, EPFL, July – December 2014

**Consulting for EPFL junior enterprise**, February – March 2014

## 4. Research projects

**PHD** in bioengineering, EPFL, June 2015 – June 2020

*Long-term time-lapse imaging of live mycobacteria with atomic force microscopy and superresolution microscopy*

**Master thesis**, *Design and microfabrication of a shunt implant for hydrocephalus treatment*, Debiotech & LMIS4 (Prof. Renaud), Switzerland, September 2014 - March 2015

**Semester project** *Low-cost impedance-based microfluidic bacteria counter for early detection of contaminated raw milk*, Prof. Braschler & Prof. Renaud, EPFL, January – August 2014

**Semester project** *Labview control and interfacing of a test bench for stretchable electronic devices*, Prof. Lacour, EPFL, September – December 2013

**Research internship** *Atomic Force Microscopy imaging of live immobilized bacteria*, Prof. Fantner, EPFL, May – July 2013

**Research internship** *Experimental characterization of magneto-impedance micro-sensors*, Prof. Moulin, Université Paris 11, France, June - August 2012

## 5. Supervision of students/junior researchers

Camille Roche  
Nicolas Bichon  
Clara Bonnet  
Clement Chenevas-Paule  
Florian Lemarignier

## 6. Teaching activities

Structural mechanics for biology students (teaching assistant at EPFL, 3 semesters)

Advanced Bioengineering Methods Laboratory (teaching assistant at EPFL, 2 semesters)

*total: 323 hours*

## 7. Organisation of conferences

We scientists 2035, workshop on research culture (co-organizer), EPFL, 2019

## 8. Prizes, awards, fellowships

**Excellence scholarship from ENS Cachan**, September 2010 – August 2014 (admission to ENS Cachan after selection through a national exam grants the status of “fonctionnaire stagiaire” and a monthly salary during 4 years)

**EPFL Fusebox challenge**: “Biomimicry – innovation inspired by nature”, 2<sup>nd</sup> prize

## 9. Personal skills (e.g. language skills, digital competences)



**Languages** French (native), English (professional)

**Programming** Matlab, Labview

**Softwares** Comsol, Solidworks, ImageJ, Clewin

## 10. Publications

Kroo, L., Kothari, A., **Hannebelle, M.**, Herring, G., Pollina, T., Chang Md, R., Banavar, S. P., Flaum, E., Soto-Montoya, H., Li, H., Combes, K., Pan, E., Vu, K., Yen, K., Dale, J., Kolbay, P., Ellgas, S., Konte, R., Hajian, R., Zhong, G., Jacobs, N., Jain, A., Kober, F., Ayala, G., Allinne, Q., Cucinelli, N., Kasper, D., Borroni, L., Gerber, P., Venook, R., Baek Md, P., Arora M.D, N., Wagner Md, P., Miki Md, R., Kohn Md, J., Kohn Bitran Md, D., Pearson Md, J., Herrera Md, C. M. & Prakash, M. (2020). Pneumask: Modified Full-Face Snorkel Masks as Reusable Personal Protective Equipment for Hospital Personnel. medRxiv. <https://doi.org/10.1101/2020.04.24.20078907>

Desbiolles, B. X. E., **Hannebelle, M. T. M.**, de Coulon, E., Bertsch, A., Rohr, S., Fantner, G. E., & Renaud, P. (2020). Volcano-shaped SPM probe for combined force-electrogram recordings from excitable cells. *Nano Letters*. <https://doi.org/10.1021/acs.nanolett.0c01319>

**Hannebelle, M. T. M.**, Ven, J. X. Y., Toniolo, C., Eskandarian, H. A., Vuaridel-Thurre, G., McKinney, J. D., & Fantner, G. E. (2020). *A biphasic growth model for cell pole elongation in mycobacteria*. *Nature Communications*, 11(1). <https://doi.org/10.1038/s41467-019-14088-z>

Odermatt, P. D., **Hannebelle, M. T. M.**, Eskandarian, H. A., Nievergelt, A. P., McKinney, J. D., & Fantner, G. E. (2019). *Overlapping and essential roles for molecular and mechanical mechanisms in mycobacterial cell division*. *Nature Physics*. <https://doi.org/10.1038/s41567-019-0679-1>

Eskandarian, H. A., Odermatt, P. D., Ven, J. X. Y., **Hannebelle, M. T. M.**, Nievergelt, A. P., Dhar, N., McKinney, J. D., & Fantner, G. E. (2017). *Division site selection linked to inherited cell surface wave troughs in mycobacteria*. *Nature Microbiology*, 2(9), 17094. <https://doi.org/10.1038/nmicrobiol.2017.94>

Peric, O., **Hannebelle, M.**, Adams, J. D., & Fantner, G. E. (2017). *Microfluidic bacterial traps for simultaneous fluorescence and atomic force microscopy*. *Nano Research*, 3896–3908. <https://doi.org/10.1007/s12274-017-1604-5>

Chappel, E., **Hannebelle, M.**, Cornaggia, L., Dumont-Fillon, D., & Momjian, S. (2017). *Hybrid hydrodynamic characteristic for hydrocephalus valve: A numerical investigation using electrical equivalent networks*. *Cogent Engineering*, 4(1). <https://doi.org/10.1080/23311916.2017.1415103>

Cornaggia, L., Conti, L., **Hannebelle, M.**, Gamper, S., Dumont-Fillon, D., van Lintel, H., Renaud, P., & Chappel, E. (2017). *Passive flow control valve for protein delivery*. *Cogent Engineering*, 4(1). <https://doi.org/10.1080/23311916.2017.1413923>

Nievergelt, A. P., Andany, S. H., Adams, J. D., **Hannebelle, M. T.**, & Fantner, G. E. (2017). *Components for high-speed atomic force microscopy optimized for low phase-lag*. 2017 IEEE

International Conference on Advanced Intelligent Mechatronics (AIM), 731–736.  
<https://doi.org/10.1109/AIM.2017.8014104>

Dumont-Fillon, D., **Hannebelle, M.**, Van Lintel, H., & Chappel, E. (2016). *Design of a Passive Flow Regulator Using a Genetic Algorithm*. *Procedia Engineering*, 168, 1016–1019.  
<https://doi.org/10.1016/j.proeng.2016.11.329>

## 11. Contributions to conferences

**Hannebelle, M. T. M.**, Odermatt, P., Eskandarian, H. A., Ven, J. X. Y., Toniolo, C., Vuaridel-Thurre, G., McKinney, J. D., & Fantner, G. E. (2020). *Exploring the Biophysics of Bacterial Growth and Division with Time-lapse Optical and Atomic Force Microscopy*. NanoBioMed online conference (oral presentation)

**Hannebelle, M. T. M.**, Ven, J. X. Y., Toniolo, C., Eskandarian, H. A., Vuaridel-Thurre, G., McKinney, J. D., & Fantner, G. E. (2019). *Exploring the Biophysics of Bacterial Growth and Division with Time-lapse Optical and Atomic Force Microscopy*. International Scanning Probe Microscopy conference, Belgium (oral presentation)

**Hannebelle, M. T. M.**, Ven, J. X. Y., Toniolo, C., Eskandarian, H. A., Vuaridel-Thurre, G., McKinney, J. D., & Fantner, G. E. (2019). *Pole elongation in mycobacteria resembles “new end take off” (NETO) dynamics in fission yeast*. EMBO Bacterial cell division: closing the gap, Sweden (poster)

**Hannebelle, M. T. M.**, Ven, J. X. Y., Toniolo, C., Eskandarian, H. A., Vuaridel-Thurre, G., McKinney, J. D., & Fantner, G. E. (2019). *Pole elongation in mycobacteria resembles “new end take off” (NETO) dynamics in fission yeast*. Swiss microbiology society SPB meeting, Switzerland (oral presentation)

**Hannebelle, M. T.**, Ven, J. X., Eskandarian, H. A., Toniolo, C., Nievergelt, A. P., McKinney, J. D., & Fantner, G. E. (2019). *Time-Lapse Atomic Force Microscopy Reveals New End Take Off (NETO) Dynamics in Mycobacteria*, Biophysical Society Meeting, USA (oral presentation)

**Hannebelle, M. T. M.**, Ven, J. X. Y., Eskandarian, H. A., Odermatt, P. D., Nievergelt, A. P., McKinney, J. D., Fantner, G. E. (2017). *Long term, correlative AFM and fluorescence imaging of bacterial growth and division*, NanoBioTech conference, Switzerland (oral presentation)

**Hannebelle, M. T. M.**, Eskandarian, H. A., Ven, J. X. Y., Chenevas, C., Odermatt, P. D., McKinney, J. D., Fantner, G. E. (2016) *Long-term correlated AFM and fluorescence microscopy for live-cell imaging*, International Scanning Probe Microscopy conference, Switzerland (poster)